Molecular Beam Epitaxial Growth, Characterization and Device Applications of III-Nitride Nanowire Heterostructures

Hieu Pham Trung Nguyen



Department of Electrical and Computer Engineering
Faculty of Engineering
McGill University
Montreal

February 2012

A thesis submitted to McGill University in partial fulfilment of the requirements of the degree of Doctor of Philosophy



Abstract

Recently, group III-nitride nanowire heterostructures have been extensively investigated. Due to the effective lateral stress relaxation, such nanoscale heterostructures can be epitaxially grown on silicon or other foreign substrates and can exhibit drastically reduced dislocations and polarization fields, compared to their planar counterparts. This dissertation reports on the achievement of a new class of III-nitride nanoscale heterostructures, including InGaN/GaN dot-in-a-wires and nearly defect-free InN nanowires on a silicon platform. We have further developed a new generation of nanowire devices, including ultrahigh-efficiency full-color light emitting diodes (LEDs) and solar cells on a silicon platform.

We have identified two major mechanisms, including poor hole transport and electron overflow, that severely limit the performance of GaN-based nanowire LEDs. With the incorporation of the special techniques of p-type modulation doping and AlGaN electron blocking layer in the dot-in-a-wire LED active region, we have demonstrated phosphor-free white-light LEDs that can exhibit, for the first time, internal quantum efficiency of > 50%, negligible efficiency droop up to ~ 2,000A/cm², and extremely high stable emission characteristics at room temperature, which are ideally suited for future smart lighting and full-color display applications.

We have also studied the epitaxial growth, fabrication and characterization of InN:Mg/i-InN/InN:Si nanowire axial structures on n-type Si(111) substrates and demonstrated the first InN nanowire solar cells. Under one-sun (AM 1.5G) illumination, the devices exhibit a short-circuit current density of $\sim 14.4~\text{mA/cm}^2$, open circuit voltage of 0.14 V , fill factor of 34.0%, and energy conversion efficiency of 0.68%. This work opens up exciting possibilities for InGaN nanowire-based, full solar-spectrum third-generation solar cells.

Abrégé

Récemment, les hétérostructures à base de nitride et de groupe III ont fait l'objet de recherches intensives. Grâce à la relaxation latérale effective du stress, de telles hétérostructures d'échelle nanométrique peuvent être déposés sur du Silicium ou d'autres substrats. Celles-ci démontrent une réduction dramatique des dislocations et des champs de polarisations comparativement à leurs contreparties planes. Cette dissertation rapporte l'accomplissement d'une nouvelle classe de matériau nanométrique, soit des hétérostructures III-nitride incluant InGaN/GaN point dans fils ainsi que des nanofils d'InN presque sans défauts sur du Silicium. De plus, nous avons développé une nouvelle génération de dispositifs à base de nanofils, incluant des diodes émettrices de lumière (LEDs) à efficacité ultra haute et spectre visible complet ainsi que des cellules solaires sur une gaufre de Silicium.

Nous avons identifié 2 mécanismes majeurs, incluant le faible transport des trous et le surplus d'électrons, qui limitent sérieusement la performance des LEDs à base de nanofils de GaN. Avec l'ajout de certaines techniques spéciales de modulation de type p, et une couche bloquante d'électrons faite de AlGaN dans la région active de la LED point dans fil. Par ailleurs, nous avons démontré des LEDs blanche sans phosphore qui démontrent, pour la première fois, une efficacité quantique supérieure à 50% ainsi qu'une baisse d'efficacité négligeable jusqu'à ~ 2,000A/cm² et des caractéristiques d'émissions très hautes et stables à température pièce. Celles-ci sont donc toutes désignées pour des applications d'illumination intelligentes et des écrans pleines couleurs.

La croissance par épitaxie, la fabrication et la caractérisation des nanofils d'InN:Mg/i-InN/InN:Si axiaux sur des substrats de Si(111) de type n et démontré la première cellule solaire à base d'InN. Sous l'illumination d'un soleil (AM 1.5G), les dispositifs démontrent une densité de courant de ~ 14.4 mA/cm² en court-circuit, un voltage de circuit ouvert de 0.14V, un facteur de remplissage de 34.0% et une efficacité

de conversion d'énergie de 0.68%. Ce travail ouvre des portes excitantes pour des cellules solaires plein spectre de troisième génération à base de nanofils d'InGaN.

Acknowledgement

This doctoral dissertation would not be finished without the supervision, support and encouragement from many people. The author wishes to express his sincere appreciation to those who have involved in his work in this dissertation.

First of all, I would like to present my deep gratitude to my brilliant supervisor Professor Zetian Mi who offered me a great opportunity to study and do research in McGill University. Under his supervision, support, and encouragement, I have had a really good opportunity to build up my research experience which is certainly useful for my future career. All of my achievements presented in this thesis will not be done without his support. I would also like to thank Professors Ishiang Shih and Nathaniel Quitoriano for their guidance, suggestion, and evaluation for my research topics. I also wish to acknowledge my PhD defense committee members, Professors Roni Khazaka, Kirk Bevan, Vamsy Chodavarapu, Pat Kambhampati, and Dayan Ban for their interest, evaluation, and valuable suggestions.

I also would like to send my special thanks to my colleagues of the MBE group for their assistance and discussions with my experiment, including Dr. Saeed Fathololoumi for his kindly assistance in the PL set up and advice, Dr. Kai Cui for his generous aid in the MBE growth and TEM imaging, my coworkers Shaofei Zhang, Mehrdad Djavid and Ruofan Wu with their help in some measurements and simulations, and other members including Dr. Pablo Bianucci, Dr. Mohammad Harati, Md Golam Kibria, Songrui Zhao, Mohammad H. T. Dastjerdi, Yukun Li, Bandar AlOtaibi, Shizhao Fan, Chenxu Shao, and Shouvik Mukherjee for their discussion and encouragement.

I would like to appreciate Professor. Thomas Szkopek for his advises and suggestions in my experiment. Thanks Peter Gaskell, Jonathan Guillemette, Shahriar Al Imam, Elizabeth Ledwosinska, Shadi Sabri, Helgi Skuli Skulason, and Tejas Deshpande for yours kind discussion and encouragement throughout my PhD life. I

would also like to thank Jonathan for helping me with abstract translation and Hadley Myers for his partially help in showing me how to take very nice LED images.

Special thanks and appreciation I would like to send to McGill nanotools microfab members including Dr. Matthieu Manini, Donald Berry, Jun Lee, and Dr. Lino Eugene, for their technical support, training and discussions related to my research topic and for helping me speed up the fabrication processes.

I also would like to thank Prof. Liet Van Dang, and Prof. Tao Van Chau for their assistances and recommendations during my study. Thanks Prof. Dang who gave me a good chance to familiar with research society. I would also like to thank Prof. Hanjo Lim, and Prof. Jaejin Lee for their guidance and support during my master program study when I could build up the fundamental knowledge for higher education and research activities.

Last but never least, I would like to thank my parents, Nam Van Nguyen and Hoa Thi Pham and my brothers and sisters for their love, encouragement and always believe on my study. I also wish to thank my parents-in-law, Biet Van Nguyen and Tay Thi Vo for their love and encouragement. Special thanks are dedicated to my wife, Ngoc Thi Ai Nguyen, who is always beside me when I face with difficulties, thanks for her support, patience, confidence and endless love.

This work would not be possible without financial support for instruments and facilities. I wish to send my deep appreciation to the Natural Sciences and Engineering Research Council of Canada (NSERC), the Fonds de recherché sur la nature et les technologies, Canada Foundation for Innovation, and the Hydro-Quebec Nano-Engineering Program at McGill University for their supports on my research.

Table of Content

Abs	tract	i
Abr	égé	ii
Ack	nowledgements	iv
Tab	le of Content	vi
List	of Figures	X
List	of Tables	xix
List	of Acronyms	XX
Con	tributions of Authors	xxii
Stat	ement of Originality	xxiii
Cha	pter 1: Introduction	1
1.1	Overview	1
1.2	Recent Developments of III-Nitride Nanowire Based Devices	2
	1.2.1 Sensors	2
	1.2.2 Photodetectors	3
	1.2.3 Solar Cells	3
	1.2.4 Laser Diodes (LDs)	6
	1.2.5 Light Emitting Diodes (LEDs)	7
1.3	Key Factors Limiting the Performance of InGaN Based LEDs	8
	1.3.1 Polarization	10
	1.3.2 Crystal Defects and Dislocations	11
	1.3.3 Spontaneous Emission	12
	1.3.4 Auger Recombination	12

	1.3.5 Inhomogeneous Carrier Distribution	13
	1.3.6 Electron Overflow	14
1.4	Dissertation Preview	16
Cha	pter 2: Molecular Beam Epitaxial Growth and Characterization of High	
Qua	ality III-Nitride Nanowire Heterostructures	18
2.1	Introduction	18
2.2	III-Nitride Nanowire Growth Mechanisms	18
	2.2.1 VLS Growth	18
	2.2.2 Spontaneous Formation	20
	2.2.3 Selective Area Growth	22
2.3 1	Plasma Assisted Molecular Beam Epitaxial Growth of High Crystalline Quality I	II-
Nitr	ide Nanowire Semiconductors	23
2.4	Molecular Beam Epitaxial Growth and Characteristics of InN Nanowires	28
	2.4.1 Surface Charge Properties of InN	30
	2.4.2 MBE growth and properties of InN nanowires	33
	2.4.3 Si and Mg-Doped InN Nanowires	37
2.5.	MBE Growth and Characteristics of GaN Nanowires and InGaN/GaN Dot-in-a-	
Wire	e Heterostructures	40
	2.5.1 Review on the MBE Growth and Characteristics of GaN Nanowires	40
	2.5.2 MBE Growth and Characterization of InGaN/GaN Dot-in-a-Wire	
	Nanoscale Heterostructures	43
2.6	Conclusion	49
Cha	pter 3: Full-Color InGaN/GaN Dot-in-a-Wire Light Emitting Diodes on	
Silio	con	50
3.1	Introduction	50

3.2 I	High Efficiency InGaN/GaN Dot-in-a-Wire Red Light Emitting Diodes	.51
	3.2.1 Molecular Beam Epitaxial Growth and Characterization of InGaN/GaN Dot-in-a-Wire Red Light Emitting Diodes	.52
	3.2.2 LED Fabrication Process	.55
	3.2.3 Device Characterization and Results Analysis	.56
3.3 I	Full-Color InGaN/GaN Dot-in-a-Wire LEDs on Silicon	.64
	3.3.1 Design and MBE Growth of InGaN/GaN Dot-in-a-Wire White-Light LEI)s64
	3.3.2 Device Characterization and Results Analysis	.68
3.4 (Conclusion	.75
Cha	pter 4: p-Type Modulation Doped InGaN/GaN Dot-in-a-Wire White Light-	
Emi	tting Diodes Monolithically Grown on Si(111)	76
4.1 I	Introduction	.76
4.2 I	Design, Growth and Fabrication of p-doped InGaN/GaN Dot-in-a-Wire LEDs	.80
4.3 I	Results and Discussion	.82
4.4 (Conclusion	.92
Cha	pter 5: Controlling Electron Overflow in Phosphor-Free InGaN/GaN	
Nan	owire White-Light-Emitting Diodes	.93
5.1 I	Introduction	.93
5.2 I	Design, Growth and Fabrication of InGaN/GaN Dot-in-a-Wire LEDs	.94
5.3 I	Results and Discussions	100
	5.3.1 Measurement and Simulation of Electron Overflow in Nanowire LEDs	100
	5.3.2 Reduced Electron Overflow with the Incorporation of AlGaN	
	Electron Blocking Layer	109
5 4	Conclusion	114

Chapter 6: Temperature-Dependent Nonradiative Recombination Processes in	
GaN-Based Nanowire White-Light-Emitting Diodes on Silicon11	
6.1 Introduction 11:	
6.2 Experimental Details	
6.3 Results and Discussion	
6.4 Conclusion	
Chapter 7: InN Nanowires for Photovoltaic Applications	
7.1 Introduction	
7.2 Growth and Characterization of InN Nanowires	
7.3 Design and Fabrication of InN Nannowire Solar Cells on Si	
7.4 Results and Discussions	
7.5 Conclusion	
Chapter 8: Conclusion and Future Work14	
8.1 Summary of the Thesis Work	
8.2 Suggested Future Work	
8.2.1 High Performance LEDs with Coaxial Nanowire Heterostructures143	
8.2.2 Nanowire LEDs with Significantly Improved Light Extract Efficiency 14-	
8.2.3 High Efficiency Ultraviolet Nanowire LEDs	
8.2.4 High Efficiency III-N Nanowire Solar Cells	
List of Publications and Copyrights149	
Bibliography	

List of Figures

Figure 1.1: Schematics of (a) p-GaN/i-In _x Ga _{1-x} N/n-GaN and (b) p-GaN/n-GaN nanowire structure and the corresponding energy band diagrams. (c) Current-voltage characteristics of single nanowire solar cells with different In contents in the active region under dark and illumination conditions [85]
Figure 1.2: (a) SEM image of p-GaN nanorods grown on n-Si substrate by CVD. Cross-sectional view is shown in the inset. (b) I-V characteristics of a p-GaN/n-Si solar cell under dark and illumination conditions [86]
Figure 1.3: Schematic of current components injected into the LED device 9
Figure 1.4: Crystal structure of GaN semiconductor [139]
Figure 1.5: Simulated band-diagram and hole concentration of the InGaN/GaN multi-quantum well LEDs under +6V bias at room temperature. Quasi-Fermi levels are presented as the dashed lines [163]
Figure 1.6: Illustration of carrier capture in the InGaN/GaN quantum well (left) and carrier leakage out of the quantum well (right) under large polarization field [152].
Figure 1.7: Energy band diagram of InGaN/GaN multi-quantum well heterostructures under polarization (solid lines) and without polarization (dashed lines) [151].
Figure 2.1: Illustration of the VLS growth process: I) semiconductor in vapour phase is introduced into the system with metal catalyst on the substrate surface, II) the formation of liquid droplets on the substrate surface near or above the eutectic temperature, and III) the formation of nucleation sites and the nanowire axial growth.
Figure 2.2: Schematic illustration of the spontaneous growth of III-nitride nanowires by molecular beam epitaxy, including adatom absorption, desorption, diffusion, and nucleation processes [113]
Figure 2.3: Scanning electron microscopy image of GaN nanowires grown by metal-organic chemical vapour deposition using the selective area growth process [200].

Figure 2.4: A Veeco Gen II MBE system equipped with a radio-frequency plasma-assisted nitrogen source	:5
Figure 2.5: Schematic of the MBE chamber [201]	6
Figure 2.6: The density of states for the stable surface structures found on selected InN surfaces: a) structure stable at moderate In/N ratios on polar c-plane surface, and b) In–N dimer structure stable at moderate In/N ratios on nonpolar m-plane surface [207].	32
Figure 2.7: SEM images of InN nanowires (a) grown directly on Si(111) at 480 °C and (b) grown on Si(111) at 480 °C with the use of an in situ deposited In seeding layer.	5
Figure 2.8: Photoluminescence spectra of nondoped InN nanowires on Si(111) measured at 5K under various laser powers	7
Figure 2.9: Photoluminescence spectra of InN nanowires on Si(111) substrates for Si doping concentrations of $\sim 1 \times 10^{18}$ cm ⁻³ (dashed and dotted line), 2×10^{17} cm ⁻³ (dotted line), 5×10^{16} cm ⁻³ (dashed line), nondoped (solid line), measured at 5K.	88
Figure 2.10: Scanning electron microscopy image of InN nanowires grown on Si(111) substrates with a relatively high Mg doping concentration. The wires show deteriorated structural properties, with the presence of slightly tapered surface morphology.	39
Figure 2.11: 5 K photoluminescence spectra of InN:Mg nanowires grown at different Mg effusion cell temperatures	.0
Figure 2.12: The scanning electron microscopy (SEM) image of InGaN/GaN nanowire heterostructures on Si(111)	.5
Figure 2.13: A low magnification bright field scanning transmission electron microscopy image showing the position and vertical alignment of the InGaN dots in a GaN nanowire.	÷5
Figure 2.14: Room temperature photoluminescence spectra of various InGaN/GaN dot-in-a-wire heterostructures grown on Si(111). The green, yellow and orange emission spectra from the dot-in-a-wire heterostructures were grown under different conditions.	ŀ7
Figure 2.15: Room temperature photoluminescence spectra of the InGaN/GaN dot-in-a-wire sample under different optical power excitations varying from 60 μ W to 16 mW.	8

Figure 2.16: Internal quantum efficiency of the InGaN/GaN dot-in-a-wire measured under optical injection condition ($\lambda \sim 405$ nm)
Figure 3.1: (a) Schematic illustration of InGaN/GaN dot-in-a-wire LED heterostructures. (b) A 45 degree tilted SEM image showing the morphology of the InGaN/GaN dot-in-a-wire heterostructures grown on a Si(111) substrate 53
Figure 3.2: (a) HAADF image in pseudo-color scale showing the alignment of three InGaN quantum dots in a GaN nanowire. The solid arrows point out the location of three dots and the dashed arrow indicates the growth direction. The pseudo-color scale bar shows the intensity for each color in the image. (b) HAAADF images and EDXS analysis of the In composition in the InGaN dots. The inset shows the HAADF image and EDXS signal variations of Ga and In along the yellow line.
Figure 3.3: Fabricated devices with different sizes $(1\times1~\text{mm}^2,~0.5\times0.5~\text{mm}^2,~0.3\times0.3~\text{mm}^2,~\text{and}~0.1\times0.1~\text{mm}^2)$ and the use of metallic contact grid pattern for current spreading.
Figure 3.4: Current-voltage characteristics of InGaN/GaN dot-in-a-wire LED devices.
Figure 3.5: Room temperature electroluminescence spectra of the InGaN/GaN dot-in-a-wire LED measured under various injection currents Optical image of the red LED device under 100 mA injection current is shown in the inset
Figure 3.6: Variations of the peak wavelength and spectral linewidth measured under different injection currents.
Figure 3.7: Room temperature IQE of the InGaN/GaN dot-in-a-wire red LED versus injection current. The inset shows the IQE of the red LED device under optical excitation ($\lambda \sim 405$ nm).
Figure 3.8: Room temperature electroluminescence spectra measured under different injection currents up to 1.2 A (~ 480 A/cm²) for the 2 nd red-emitting LED device with enhanced inhomogeneous broadening
Figure 3.9: Variations of the peak wavelength and spectral linewidth with injection current were measured for the 2 nd red-emitting LED device with enhanced inhomogeneous broadening.
Figure 3.10: CIE chromaticity coordinates for red InGaN/GaN dot-in-a-wire LED devices with relatively small (1 st device) and large (2 nd device) inhomogeneous broadening. The current was varied from 100 to 300 mA for the 1 st device (dots) and from 400 to 1.200 mA for the 2 nd device (squares)

Figure 3.11: Variations of the relative external quantum efficiency versus injection current for the InGaN/GaN red-emitting dot-in-a-wire LED measured at room temperature.
Figure 3.12: A 45 degree tilted scanning electron microscopy image of the InGaN/GaN dot-in-a-wire heterostructures grown on a Si(111) substrate by molecular beam epitaxy.
Figure 3.13: A high-resolution HAADF image in a pseudo-color display showing the atomic number contrast between InGaN dots and GaN barriers 66
Figure 3.14: An energy dispersive x-ray spectrometry spectrum image showing the quantitative variation of In along the centers of seven InGaN dots. The inset shows the qualitative In and Ga signal variation along the green line
Figure 3.15: An electron energy loss spectrometry spectrum image showing the integrated In and Ga signal along the lateral direction of GaN nanowire and an InGaN dot. The inset shows the line along which the electron energy loss spectrometry spectrum image is taken.
Figure 3.16: Room-temperature current-voltage characteristics of an InGaN/GaN dot-in-a-wire LED on silicon
Figure 3.17: Room temperature electroluminescence spectra of green, yellow and orange LED devices measured at 120 A/cm² current injection and the corresponding optical microscopy images (inset).
Figure 3.18: Variations of the peak wavelengths of the green (square), yellow (circle), and orange (triangle) InGaN/GaN dot-in-a-wire LEDs with injection current. Blueshifts of ~3.5 nm, 6.4 nm, and 17.2 nm were observed for the green, yellow, and orange LED devices, respectively
Figure 3.19: Normalized electroluminescence spectra of InGaN/GaN dot-in-a-wire white-emitting LEDs under different injection currents at room temperature. Shown in the inset is the optical microscopy image of the device 72
Figure 3.20: Room-temperature internal quantum efficiency of the white InGaN/GaN dot-in-a-wire LED device measured under electrical injection
Figure 3.21: Room temperature relative external quantum efficiency of the white LED device, showing negligible efficiency droop up to 200 A/cm ² injection current
Figure 3.22: CIE chromaticity coordinates of the light emission from InGaN/GaN dot-in-a-wire white LEDs

Figure 4.1: Room temperature peak position and full-width-half-maximum of electroluminescence spectra measured from the InGaN/GaN dot-in-a-wire white LEDs
Figure 4.2: Simulated hole concentration across the InGaN/GaN quantum dot active regions for LEDs without (a) and with (b) the usage of p-type modulation doping in InGaN/GaN active regions under 1,000 A/cm² injection current
Figure 4.3: Schematic of the p-doped InGaN/GaN dot-in-a-wire LED with the flat band energy shown on the right side.
Figure 4.4: Room temperature photoluminescence spectra of p-doped and undoped white LED heterostructures measured under the same optical excitation conditions.
Figure 4.5: Current-voltage characteristics of undoped- and p-doped dot-in-a-wire LEDs measured at room temperature. The optical microscopy image of the fabricated dot-in-a-wire LED is shown in the inset.
Figure 4.6: Electroluminescence spectra of a p-doped InGaN/GaN dot-in-a-wire LED measured at injection currents from 100 to 500 mA under pulsed bias conditions at room temperature. The optical image of the device is shown in the inset.
Figure 4.7: Room temperature electroluminescence spectra of p-doped and undoped white LED under an injection current of 300 mA
Figure 4.8: 1931 Commission International de l'Eclairage chromaticity diagrams. Location of the light emission for the undoped (triangles) and p-doped (circles) dot-in-a-wire LEDs are shown at injection currents from 100 mA to 400 mA.
Figure 4.9: Variation of the room temperature internal quantum efficiency of the undoped and p-doped dot-in-a-wire LEDs versus injection currents
Figure 4.10: Variation of the room temperature internal quantum efficiency of the undoped and p-doped dot-in-a-wire LEDs under different optical pumping power ($\lambda = 405 \text{ nm}$).
Figure 4.11: Variation of the relative external quantum efficiency versus current density for a p-doped dot-in-a-wire LED measured at room temperature 89
Figure 4.12: Variation of the relative external quantum efficiency versus current density for a p-doped dot-in-a-wire LED measured at 5K

Figure 4.13: Variations of the relative external quantum efficiency with current at relatively low injection levels for the undoped LED
Figure 4.14: Variations of the relative external quantum efficiency with current at relatively low injection levels for the p-doped LED
Figure 5.1: (a) Schematic illustration of InGaN/GaN dot-in-a-wire LEDs grown on Si(111) substrates. (b) Illustration of three LED designs. From left to right: InGaN/GaN dot-in-a-wire LEDs with the incorporation of an InGaN test well (LED I), an AlGaN electron blocking layer and an InGaN test well (LED II), and an AlGaN electron blocking layer but no test well (LED III) between the quantum dot active region and the p-GaN section. Flat energy band diagrams for the three LED structures are shown in the insets
Figure 5.2: Room-temperature photoluminescence spectra of the three LED device heterostructures. The emission peak at ~ 439 nm is due to the presence of the InGaN test well, which can be clearly measured for LEDs I and II 97
Figure 5.3: A 45° tilted SEM image of the InGaN/GaN dot-in-a-wire LED heterostructure grown on Si(111) substrate
Figure 5.4: (a) Bright field TEM image of InGaN/GaN dot-in-a-wire LED II, wherein the InGaN quantum well (QW), quantum dots (QDs), and AlGaN electron blocking layer (EBL) are identified. (b) Annular dark field TEM image and energy dispersive x-ray spectrometry signals for In, Ga, and Al of LED II 99
Figure 5.5: Normalized electroluminescence spectra of LED I. This design incorporates ten InGaN/GaN quantum dots in the active region and a GaN/InGaN/GaN test quantum well between the LED active region and p-GaN. 101
Figure 5.6: Normalized electroluminescence spectra of the InGaN/GaN dot-in-a-wire LED with only ten quantum dots in the active region measured at room temperature.
Figure 5.7: Relative external quantum efficiency for emission from the quantum dot active region and from the test well for LED I measured at room temperature.
Figure 5.8: Electroluminescence spectra of LED I at 300 K (solid line) and 80 K (dash dot curve) under 450 A/cm ² injection current
Figure 5.9: Variations of the relative external quantum efficiency (EQE) related to the emission from the quantum dot active region measured at 80, 200, and 300 K. The simulated internal quantum efficiency (IQE) based on the ABF model is also shown for comparison. The dotted blue line is the calculated IQE versus injection currents in the absence of any 3 rd or higher order carrier loss mechanisms.

Figure 5.10: Current-voltage characteristics of LED I measured at 300 K, 200K, and 80K, respectively.	105
Figure 5.11: Simulated electron current density across the InGaN/GaN quantum dot active region using the APSYS simulation package (Crosslight Software, 2011) with (red dashed curve) and without (black curve) the incorporation of an AlGaN electron blocking layer (EBL).	107
Figure 5.12: The electron density distribution across the near surface GaN region of the nanowire LEDs with (red dashed curve) and without (black curve) the incorporation of an AlGaN electron blocking layer	108
Figure 5.13: Electroluminescence spectra of LED II measured under 1200 mA injection current at 80, 200, and 300 K. Emission peak from the test well is not observed, confirming the drastically reduced, or the absence of electron overflow in the LED devices with the incorporation of an electron blocking layer.	110
Figure 5.14: Variations of the measured relative external quantum efficiencies of LED III with injection current at 80 K, 200 K, and 300 K. The simulated IQE using the ABF model shows a good agreement with experimental results	111
Figure 5.15: Relative external quantum efficiency measured at room temperature for the InGaN/GaN dot-in-a-wire LED with the incorporation of an AlGaN electron blocking layer and p-type modulation doping in the device active region	112
Figure 5.16: the 1931 Commission International de l'Eclairage chromaticity diagram. The device exhibits highly stable emission characteristics, with x and y in the ranges of $\sim 0.33-0.35$, and $0.36-0.38$, respectively	113
Figure 6.1: Bright field TEM image and EDXS analysis of a single InGaN/GaN dot-in-a-wire structure, wherein the AlGaN EBL and InGaN/GaN quantum dots are identified.	118
Figure 6.2: Room-temperature photoluminescence spectrum of the dot-in-a-wire LED heterostructure.	118
Figure 6.3: Electroluminescence spectra of a phosphor-free InGaN/GaN dot-in-a-wire white LED measured under various injection currents at room temperature.	119
Figure 6.4: Locations of the light emission characteristics shown in the 1931 Commission International de l'Eclairage chromaticity diagram at injection currents from 300 mA to 800 mA. The optical image of the white LED is shown in the inset	119

Figure 6.5: Variations of the relative external quantum efficiencies (EQE) with injection current measured in the temperature range of 6 K to 440 K. The simulated internal quantum efficiencies (IQE) using the ABF model are also shown for comparison.	120
Figure 6.6: Plot of the current densities (solid squares) at which the quantum efficiency reaches ~ 80% of its peak value as a function of temperature. The current densities at which conventional GaN-based quantum well LEDs (solid circles and triangles) and other reported GaN-based nanowire LEDs (star) reach their peak quantum efficiencies are also shown for comparison. The solid circles, upward triangles, downward triangles, and star denote the data obtained from references 126, 347, 349, and 329, respectively.	121
Figure 6.7. Plot of the SRH recombination contribution versus injection current in the temperature range of 6 K to 440 K	124
Figure 6.8: Variation of the SRH nonradiative recombination coefficient with temperature.	125
Figure 6.9: The corresponding nonradiative recombination lifetime at different temperatures and the theoretical fit using a trap energy of ~ 0.063 eV separated from the intrinsic Fermi level.	126
Figure 7.1: Schematic illustrations of (a) InN:Si/i-InN nanowire solar cells grown on p-type Si substrates, (b) InN:Mg/i-InN/InN:Si nanowire solar cells grown on n-type Si substrates, and (c) CdS-passivated InN:Mg/i-InN/InN:Si nanowire solar cells grown on n-type Si substrates.	132
Figure 7.2: 45° scanning electron microscopy images of (a) the InN nanowire ensemble spin-coated with a polyimide layer, with the top region of the wires exposed by dry etching and (b) the polyimide immersed wire ensemble after the deposition of Ni/Au contact layers.	133
Figure 7.3: (a) I-V response of InN:Si/i-InN nanowire devices on p-Si(111) measured under dark conditions. (b) Schematic of the energy band diagram of the InN:Si/i-InN/p-Si heterojunction under thermal equilibrium. The presence of a thin (\sim 2-3 nm) amorphous SiN _x layer is also illustrated.	135
Figure 7.4: (a) I-V characteristics of InN:Mg/i-InN/InN:Si nanowire solar cells grown on n-type Si(111) substrates under dark and illumination (1-sun at AM 1.5G) conditions. (b) Illustration of the corresponding energy band diagram of the nanowire junction under thermal equilibrium.	137
Figure 7.5: I-V characteristics of CdS-passivated InN:Mg/i-InN/InN:Si nanowire solar cells grown on n-type Si(111) substrates under dark and light (1-sun at AM 1.5G) illumination conditions	138

Figure 8.1: Proposed coaxial nanowire heterostructure for high efficiency nanowire based LEDs	143
Figure 8.2: Schematic illustration of the proposed AlGaInN/AlGaN deep UV LEDs with the incorporation of the special techniques of electron blocking and modulation p-doing in the device active region for reducing electron overflow and enhancing hole transport, respectively.	146
Figure 8.3: Proposed high efficiency single (left) and multi-junction (right) solar cells based on InGaN material system	147
Figure 8.4: (a) Illustration of the energy band diagram in the active region of an intermediate band solar cell. (b) Proposed InGaN based intermediate band solar cells with the utilization of dot-in-a-wire heterostructure	148

List of Tables

Table 6.1: List of commonly reported Auger coefficients in InGaN/GaN	
heterostructures	3

List of Acronyms

Am-MBE Ammonia-Molecular Beam Epitaxy

CBE Chemical Beam Epitaxy

CIE The 1931 Commission International De L'eclairage Chromaticity

Diagrams

CVD Chemical Vapour Deposition

EBL Electron Blocking Layer

EDXS Energy Dispersive X-Ray Spectrometry

EL Electroluminescence

HAADF High Angle Annular Dark Field

HVPE Hydride Vapor Phase Epitaxy

IQE Internal Quantum Efficiency

ITO Indium Tin Oxide

LED Light Emitting Diode

LD Laser Diode

MBE Molecular Beam Epitaxy

MOCVD Metal-Organic Chemical Vapor Deposition

MQW Multi-Quantum Well

NW Nanowire

PAMBE Plasma Assisted-Molecular Beam Epitaxy

PL Photoluminescence

QCSE Quantum Confined Stark Effect

QD Quantum Dot

QW Quantum Well

RF Radio Frequency

RHEED Reflection High Energy Electron Diffraction

SAE Selective Area Epitaxy

SEM Scanning Electron Microscopy

SRH Shockley-Read-Hall

SSL Solid State Lighting

STEM Scanning Tunneling Electron Microscope

TDPL Temperature Dependent Photoluminescence

TEM Transmission Electron Microscopy

UV Utraviolet

VLS Vapour-Liquid-Solid

XRD X-Ray Diffraction

XTEM Cross-Sectional Transmission Electron Microscopy

Contributions of Authors

This thesis includes a collection of manuscripts written by the candidate and his supervisor, Prof. Zetian Mi. The results presented in the manuscripts are the collaboration of many coauthors with their contributions evaluated. The molecular beam epitaxial growth of the light emitting diode heterostructures and solar cells were performed by the candidate and Dr. Kai Cui. The TEM imaging was carried out by M. Couillard, Prof. G. A. Botton, and Dr. Kai Cui at the Canadian Centre for Electron Microscopy, a National facility supported by NSERC and McMaster University. Some of the TEM images were also captured by Dr. Kai Cui and the candidate using the TEM facility at McGill University. The LED and solar cell device fabrication was performed by the candidate. The simulation based on the ABF mode and APSYS software were done by Mehrdad Djavid, and Shaofei Zhang. Dr. Saeed Fathololoumi contributed to the photoluminesence set up. The photoluminesence results were measured by the candidate and Shaofei Zhang. Electroluminesence measurements were performed primarily by the candidate, with some assistance from Shaofei Zhang. The solar cell fabrication and characterization was completed by the candidate. Prof. Zetian Mi was listed as the co-author on the manuscripts showing his supervision role throughout the candidate's work and manuscript preparation.

Statement of Originality

This thesis is the collection of seven journal papers which are published/accepted for publication in Nano Letters, Nanotechnolgy, IEEE Photonics Technology Letters, Journal of Selected Topics in Quantum Electronics, and ECS Transactions. Many first demonstrations have been accomplished and are included in this thesis.

We have developed, for the first time, highly stable white light emitting diodes using catalyst-free InGaN/GaN dot-in-a-wire nanoscale heterostructures on Si(111) substrates, with the quantum dots aligned near-perfectly at the center of the nanowires. In addition, by significantly enhancing the hole transport in the device active region using p-type modulation doping, we have demonstrated the most efficient phosphorfree white light LEDs ever reported, which exhibit an internal quantum efficiency of \sim 56.8% at room temperature relative to that measured at 5 K. The p-doped dot-in-a-wire LEDs also show many desired properties, including highly stable white light emission, nearly zero efficiency droop at injection current densities up to \sim 640 A/cm², and relatively high color rendering properties, that are ideally suited for future smart lighting applications. This work constitutes a significant progress for achieving low cost, high performance phosphor-free white LEDs utilizing nanowire heterostructures.

We have also demonstrated that electron leakage and overflow, rather than Auger recombination, directly limit the maximum quantum efficiency of GaN-based nanowire LEDs. We found that efficiency droop in nanowire LEDs becomes more severe at low temperatures, which is directly correlated with the relatively enhanced electron overflow with decreasing temperature. We have further achieved, for the first time, an effective control of electron overflow in phosphor-free InGaN/GaN dot-in-a-wire white LEDs by incorporating a p-doped AlGaN electron blocking layer between the quantum dot active region and the p-GaN. The resulting nanowire LEDs exhibit remarkably stable white-light emission and are virtually free of any efficiency degradation up to ~ 2.200 A/cm². This work has identified and addressed one of the major obstacles of

nanowire LEDs for applications in future high power phosphor-free, all-semiconductor based solid state lighting.

We have further demonstrated that Shockley-Read-Hall (SRH) nonradiative recombination, due to the large surface-to-volume ratios and the presence of surface states and defects, can severely degrade the performance of nanowire LEDs. The slow rising trend of the quantum efficiency observed in nanowire LEDs is directly related to the large SRH recombination. The quantum efficiency reaches its peak value at higher current injection with increasing SRH recombination, which further limits the maximum achievable efficiency at high injection levels. The LED device can be significantly enhanced by embedding the InGaN/GaN dot-in-a-wires in a large bandgap AlGaN shell structure to minimize nonradiative recombination on the wire surfaces.

We also reported the first experimental demonstration of InN nanowire solar cells, directly grown on Si(111) substrates by molecular beam epitaxy. With the use of a CdS surface passivation, InN:Mg/i-InN/InN:Si nanowire homojunction solar cells exhibit a promising short-circuit current density of $\sim 14.4~\text{mA/cm}^2$ and power conversion efficiency of $\sim 0.68\%$ under simulated one-sun (AM 1.5G) illumination. This work suggests the first successful demonstration of p-type doping in InN nanowires and also constitutes important progress for the development of InGaN-based, full-solar-spectrum photovoltaics.

In conclusion, work presented in this thesis has contributed significantly to the understanding and development of III-nitride nanowire-based high performance optoelectronic devices.

Chapter 1: Introduction

1.1 Overview

In the recent years, optoelectronic devices that are made of III-nitride materials have been intensively studied, due to the tremendous advantages offered by this materials system. Group III-nitride compound semiconductors exhibit unique electrical and optical properties, such as high electron mobility, large saturation velocity, high breakdown electric field, extreme chemical stability, and good thermal conductivity [1-9]. The direct energy bandgap III-nitride semiconductors can absorb and emit light very efficiently over a very broad spectrum, ranging from ~ 0.65 eV (InN) to 6.4 eV (AlN), which encompasses nearly the entire solar spectrum [1, 6, 8-10]. However, due to the lack of native substrates, conventional III-nitride planar heterostructures generally exhibit very high dislocation densities that severely limit the device performance and reliability. On the other hand, nanowire heterostructures can be grown on lattice mismatched substrates with drastically reduced dislocation densities, due to the highly effective lateral stress relaxation [11, 12]. In this context, tremendous progress has been made in the development of III-nitride nanowire heterostructures [13-15]. The growth of nearly defect-free III-nitride nanowire heterostructures has been reported on various substrates, including Si and sapphire [16-19]. In addition, nanowires offer many extraordinary advantages for applications in future nanophotonic and nanoelectronic devices. For example, when designed as solar cells, nanowires provide several distinct advantages, including a direct path for charge carrier transport, a large surface area for better light absorption, and a high possibility for multi-exciton phenomena [20-23]. At the present time, the use of IIInitride nanowires for applications in various optoelectronic devices, including solar cells [24-33], light emitting diodes [34-38], lasers [39-43], sensors [44-47], and photodetectors [48-55] have been extensively investigated worldwide.

1.2 Recent Developments of III-Nitride Nanowire Based Devices

In what follows, a brief overview is provided for the recent developments of IIInitride nanowire sensors, photodetectors, solar cells, lasers, and LEDs.

1.2.1 Sensors

An emerging application of III-nitride nanowires is to sense traces of gasses and biomolecules. Advantages of III-nitrides for such applications include the extreme chemical stability and the suitability for high temperature operation. For example, GaN has the ability to detect gases at temperatures up to ~600 °C. In this regard, many sensing applications using III-nitride thin film structures have been demonstrated [47, 56-58]. Compared to thin film structures, the use of III-nitride nanowires can significantly improve the device sensitivity, due to the large surfaceto-bulk ratios [59, 60]. Lim et al. demonstrated highly sensitive hydrogen sensors using GaN nanowires [61]. In this approach, the nanowire diameters and lengths were in the ranges of 15 nm to 60 nm and 1 µm to 20 µm, respectively. The nanowires were functionalized with thin Pd or Pt layers, which can drastically increase the device sensitivity, compared to the uncoated devices, due to the enhanced catalytic dissociation of molecular hydrogen. High performance hydrogen sensors based on other nanowire heterostructures, including In₂O₃, ZnO and SnO₂ nanowires have also been reported [62-66]. Additionally, III-nitride nanowires have been employed for DNA sensors [67-69]. Simpkins et al. tested three different samples for DNA sensing using fluorescence imaging, including silane/glutaraldehyde GaN thin film, silane/glutaraldehyde GaN nanowire structure, and GaN film control sample without glutaraldehyde deposition. Florescence was observed for the GaN thin film and nanowire samples, and no detectable emission was recorded for the GaN sample without glutaraldehyde deposition. Significantly stronger fluorescence was measured for the GaN nanowire sample, compared to the GaN thin film, which was attributed to the significantly larger surface area of GaN nanowires.

1.2.2 Photodetectors

III-N material system has also been employed in photodetector applications, due to its widely tunable bandgap and high conductivity achieved in small nanowire geometry [70]. For example, wide bandgap AlGaN and GaN nanowires have been considered as the best candidates for UV light detection. Calarco et al. [71] found that, both in the dark and under UV illumination, electrical transport of GaN nanowires depends on the nanowire diameters, suggesting that the photoconduction is influenced by the wire surface. The nanowires in Calarco's work were grown using plasma-assisted molecular beam epitaxy, with the diameters ranging from 20 to 500 nm. The diameter of the nanowires was controlled by varying the III/V flux ratio. Nanowire with smaller diameters exhibit faster photoresponse compared to the thicker ones. Detailed studies suggested that there was spatial separation between electrons and holes in GaN nanowires. The depletion space charge layer originates from the Fermi-level pinning at the surface of nanowires and plays an important role in the dark and photocurrents of these GaN nanowires. This phenomenon results in the size dependent photocurrent behaviour in GaN nanowires. Rigutti et al. [72, 73] reported that a single GaN/AlN nanowire UV photodetector with embedded quantum disks enhanced the sensitivity and lowered the dark current. High responsivity at $\lambda=300$ nm at room temperature was measured for this type of photodetectors.

1.2.3 Solar Cells

Applications of III-nitride nanowire heterostructures in solar cells can significantly enhance the device performance, due to the direct path for charge carrier transport, large surface area for better light absorption, and potentially high efficiency for multi-exciton process [20, 22, 23, 74]. Zhu et al. [75] reported nanowire solar cells with enhanced absorption over a wide wavelength and angle range, compared to planar devices. They claimed that the improvement of efficiency stemed mainly from the very low surface reflection, which can let more photons pass through. Another important parameter in increasing the solar efficiency is the ability to engineer the bandgap of the nanowire materials for matching with the solar spectrum. InGaN, with

bandgap energy varying from ~ 0.65 eV (InN) to ~ 3.4 eV (GaN), is one of the best candidates for full-solar spectrum photovoltaic devices [76-78]. Due to the highly efficient strain relaxation, InGaN nanowires can offer tunable bandgap over a wide range of In content without the generation of misfit dislocations, thereby rendering it feasible to design and grow solar cell heterostructures with desired bandgap combinations [15, 79-81]. In recent years, extensive research has been performed for such devices. Many simulation results have shown high conversion efficiency values: such as an energy conversion efficiency of ~ 20% for In_{0.65}Ga_{0.35}N single junction solar cells (Zhang et al. [82]), 31% for In_{0.46}Ga_{0.54}N/Si double junction solar cells (Hsu et el [83]), and ~ 35.1% for InGaN double junction solar cell with energy bandgap of the top and bottom cells being 1.74 eV and 1.15 eV, respectively [84]. The first coaxial III-nitride nanowire photovoltaic devices, with an engineered bandgap for wide wavelength absorption range, were reported by Dong et al. in 2009 [85]. The coaxial n-GaN/i-In_xGa_{1-x}N/p-GaN nanowire heterostructures, shown in figures 1.1(a) and (b), were synthesized by metal-organic chemical vapor deposition (MOCVD). The In content was varied to achieve the designed bandgap by changing the shell growth temperature. For these devices, the open circuit voltage (Voc) and short circuit current density (J_{sc}) were measured in the ranges of 1.0 to 2.0 V and 0.39 to 0.059 mA/cm² when the In content was varied from 0.27 to 0, respectively. The maximum conversion efficiency for these solar cells is ~0.19 %. Figure 1.1(c) shows the measured current-voltage characteristics, for devices with different active layer bandgap energies. It is seen that the V_{oc} increases when In concentration is lowered from 0.27 to zero, due to the widening of the bandgap. The devices with lower In content also showed lower J_{sc}, due to the blue shift of the absorption spectrum to the region with less solar spectral overlap. It is expected that high efficiency solar cells can be achieved if the optimal conditions for the In content in the active regions can be successfully implemented.

Tang et al. [86] proposed a combination of p-GaN nanowire on n-Si substrate to form a heterostructure solar cell which exhibited a relatively high J_{sc} of 7.6 mA/cm² and high conversion efficiency of ~ 2.73% (AM1.5, 100mW/cm^2). In this study, GaN nanorods were grown on Si substrates by chemical vapour deposition (CVD) method with Au as a catalyst. Figure 1.2(a) shows the SEM image of the as-grown GaN nanorods on a Si substrate with the cross-sectional view shown in the inset. Current–voltage characteristic of the p-GaN/n-Si heterostructure is illustrated in figure 1.2(b). It was concluded in this study that nanorod structures can be used as an anti-reflection layer to reduce light reflection at the solar cell surface.

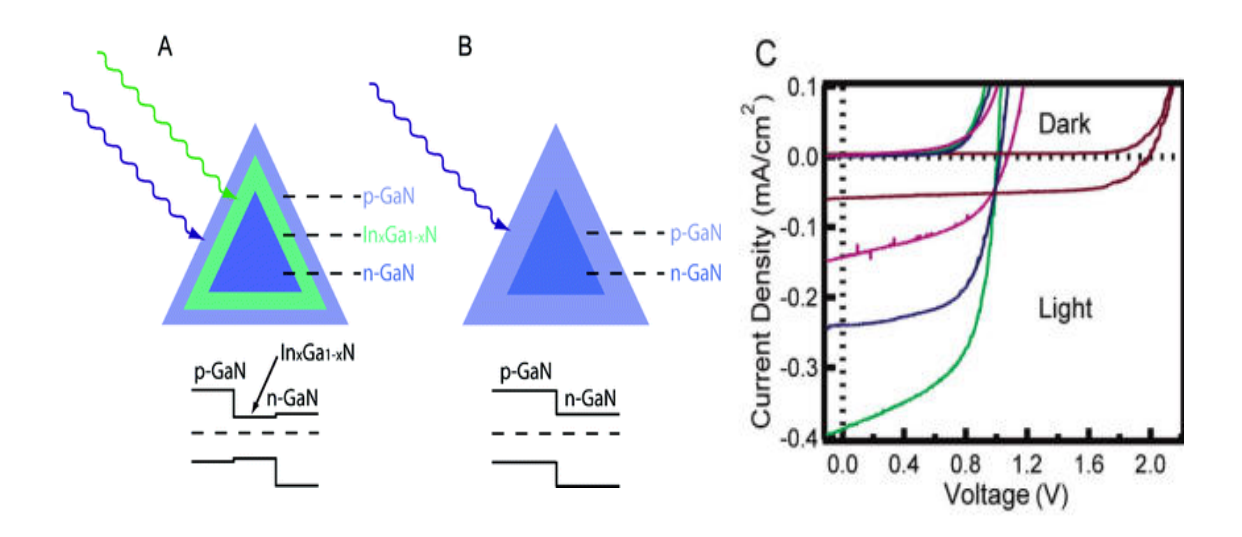
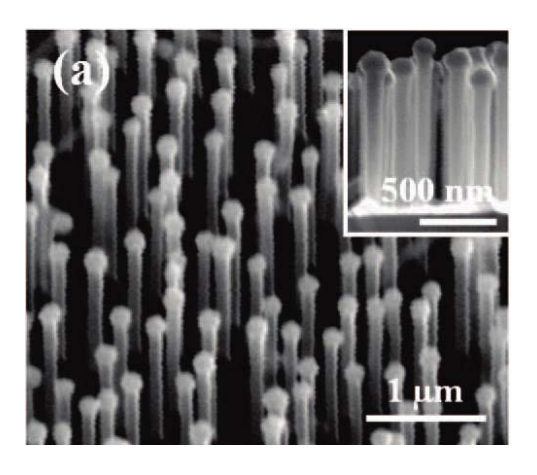


Figure 1.1: Schematics of (a) p-GaN/i-In_xGa_{1-x}N/n-GaN and (b) p-GaN/n-GaN nanowire structure and the corresponding energy band diagrams. (c) Current-voltage characteristics of single nanowire solar cells with different In contents in the active region under dark and illumination conditions [85].



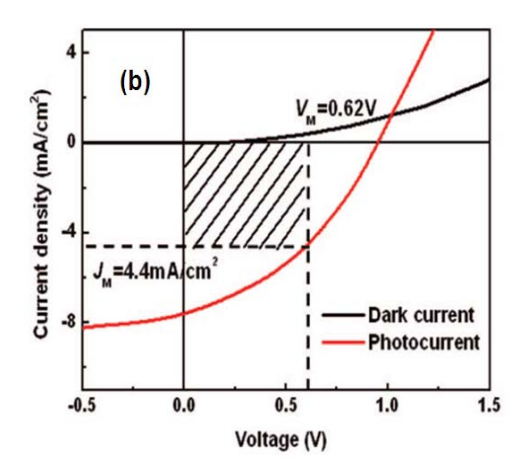


Figure 1.2: (a) SEM image of p-GaN nanorods grown on n-Si substrate by CVD. Cross-sectional view is shown in the inset. (b) I-V characteristics of a p-GaN/n-Si solar cell under dark and illumination conditions [86].

1.2.4 Laser Diodes (LDs)

III-nitride nanowire lasers have also been intensively investigated [87-90]. They offer many potential advantages, including ultralow threshold, low power consumption, and high-speed modulation. Additionally, high performance InGaN nanowire lasers that can be fabricated on a Si-platform and can exhibit emission wavelengths in the range of 1.3 to 1.55 µm are in demand for future chip-level optical communications. Single GaN nanowire lasers with lengths greater than 16 µm [91] and diameters ranging from 150 nm to 400 nm were reported by Johnson *et al.* [89]. The measured laser threshold power was ~500 nJ/cm², and the nanowire cavities exhibited Q factors of ~ 500 to 1500. In another work, GaN nanowire lasers with lasing threshold power ~ 22 kW/cm² was reported by Gradecak *et al.* [87]. Choi *et al.* grew single crystal GaN nanowires with triangular cross sections by using MOCVD and demonstrated UV laser emission at ~384 nm with relatively low threshold [90]. At the present time, the major challenges for III-nitride nanowire lasers include the demonstration of such devices operating in the near-infrared wavelength range and the achievement of high performance lasing under electrical injection.

1.2.5 Light Emitting Diodes (LEDs)

There has been a growing demand for low-cost, high-efficiency and phosphor-free white LEDs that can be fabricated on a single chip. In this regard, it is important to achieve high efficiency InGaN/GaN LEDs with emission wavelengths in the green, yellow and red wavelength range. The performance of conventional planar InGaN/GaN quantum well based LEDs has been limited, to a large extent, by the presence of large dislocation densities and strain-induced polarization field associated with the large inter-layer lattice mismatch. As discussed before, nanowire heterostructures offer reduced defect densities and strain distribution, due to the effective lateral stress relaxation [11, 12]. The nanoscale structures can improve light extraction efficiency and reduced light absorption, due to the large surface-to-volume ratios [92, 93]. III-nitride nanowire heterostructures have been employed as the active region material for LEDs over a full range of colors, including red, organ, yellow, green, blue, UV and even white colors [16, 17, 37, 80, 94-97]. Such nanowire LEDs can be realized using either the top-down and bottom-up fabrication methods.

In the top-down approach, the nanowire structures are fabricated by etching the as-grown planar heterostructures using focused-ion-beam, induced couple plasma, wet-chemical, and/or reactive ion beam etching [98-101]. Etch-induced defects can be reduced by using an *ex situ* annealing process [102]. During the subsequent device fabrication, surface planarization and passivation processes, with the use of SU-8, polyimide, or spin-on-glass, have been developed, which can prevent metal falling down on the bottom of the nanowires [38, 103, 104]. Using the method of silica nanoparticle lithography, Wang *et al.* reported nanorod LEDs with nearly constant emission wavelengths [104]. Reduced polarization fields in the nanorod structures were also confirmed by Raman scattering measurements. By combining both dry and wet etching processes, Li *et al.* reported highly uniform, nearly dislocation-free InGaN/GaN nanorod LEDs, which exhibited a significant enhancement (a factor of ~ 10, or larger) in the PL intensity, compared to the planar LED heterostructures [105]. Chen *et al.* also reported nanowire LEDs with relatively high output power (~ 6.8

W/cm² at an injection current of 32A/cm²) and external quantum efficiency (~ 16.6% at 1.6 A/cm²) using the top-down fabrication method [106].

In spite of the significant improvements made in nanowire LEDs fabricated by the top-down method, the performance of such devices has been severely limited by the presence of dislocations in the bulk of nanowires and etch-induced defects on the lateral surfaces. Additionally, the achievement of long-wavelength LEDs has been restricted by the epitaxial growth of planar heterostructures. In this regard, nanowire LEDs fabricated by the bottom-up approach have been intensively investigated. Such devices can be realized by using various growth techniques, including direct reaction of Ga or In metals with NH₃ [107, 108], chemical vapour deposition [15, 109, 110], molecular beam epitaxy [91, 111-113], chemical beam epitaxy [114], and hydride vapour phase epitaxy [115]. The underlying growth mechanisms have been extensively investigated, which may involve the use of catalysts in the vapour-liquidsolid growth mode, the spontaneous formation (self-organization) under nitrogen rich conditions, or the selective area epitaxy on nano-patterned substrates. Various bottom-up nanowire LEDs include core-shell nanowire [116-118], well/disk-in-a-wire [119-121], ternary nanowire [17, 115], and dot-in-a-wire nanoscale heterostructures have been developed [38].

1.3 Key Factors Limiting the Performance of InGaN Based LEDs

Significant progress has been made on InGaN based LEDs since the first demonstration of such devices by Nakamura et al. in 1993 [122]. To date, most of the improvements have been focused on the enhancement of material quality and the improvement of device fabrication techniques, which have led to the commercialization of InGaN based LEDs for lighting applications. However, luminescence efficiency of these LEDs has been observed to degrade considerably at high injection current which is referred to as "efficiency droop". As a consequence, it is difficult to achieve high brightness and high power lighting application even when the devices are operated at high injection current. The underlying mechanism has been extensively investigated. Defects and carrier delocalization [123], polarization

field [124, 125], Auger recombination [126], carrier leakage [127], and poor hole transport [128, 129] have been identified as some of the most probable causes. However, the main factor that leads to the efficiency droop is still not clear and being intensively investigated. Figure 1.3 shows the schematic of the LED current components injected into the device active region. If we assume unity electrical injection efficiency, the internal quantum efficiency (η_i) is typically modeled by the ABC model:

$$\eta_i = \frac{BN^2}{AN + BN^2 + CN^3 + f(N)} \tag{1.1}$$

Where N is the carrier density and A, B, and C are the Shockley-Read-Hall nonradiative recombination, radiative recombination, and Auger recombination coefficients, respectively [130, 131] . f(N) represents the carrier leakage outside of the active region.

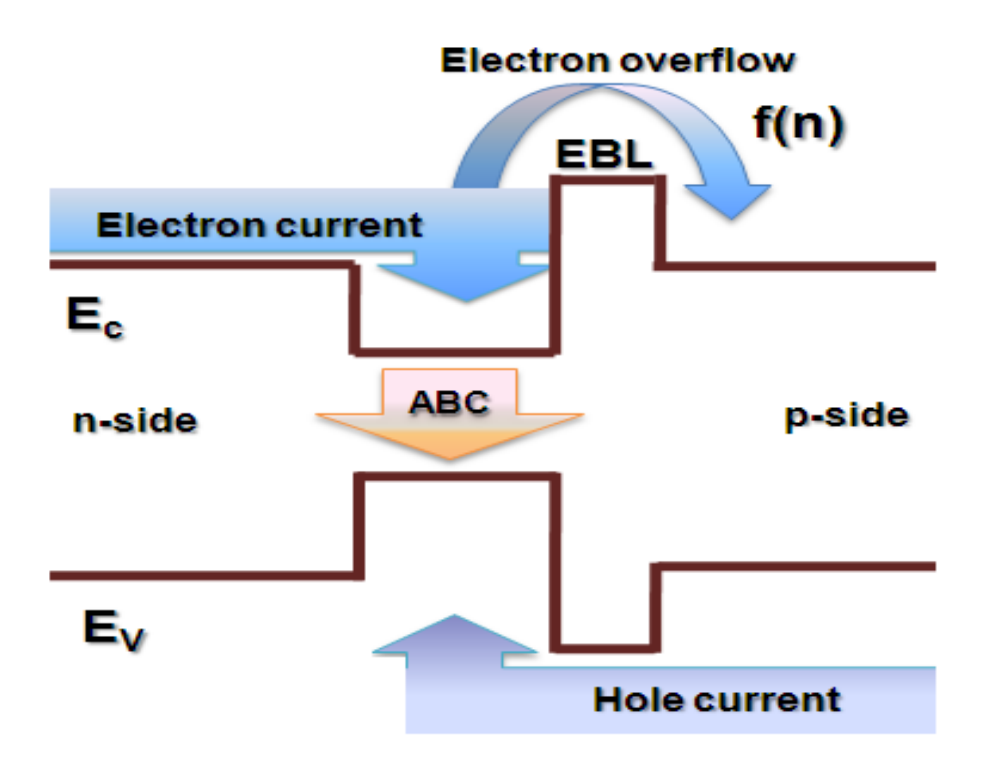


Figure 1.3: Schematic of current components injected into the LED device.

1.3.1 Polarization

Polarization field is one of the dominant issues in nitride semiconductors and plays an important role in determining the performance of nitride based devices. III-nitride semiconductors exhibit wurtzite crystal structure. Such hexagonal structures are defined by the edge length a of the basal hexagon, the height c of the hexagonal prism, and an internal parameter u as the anion-cation bond length along the (0001) axis in units of c as shown in figure 1.4. The polarization field is attributed to the asymmetric wurtzite crystal structure. Spontaneous and strained-induced piezoelectric polarizations, therefore, exist in this material system. These polarization fields are stronger in c-face nitride compared to other III-N alloys [132]. Piezoelectric polarization is also considered as strain induced polarization which is present due to the displacement of anion sub-lattice and the canion sub-lattice based on the interface strain. Piezoelectric polarization plays a more important role in GaN based LEDs than the spontaneous polarization [133-135]. Polarization field increases as the lattice mismatch between epilayers increases, leading to the spatial separation of electron and hole. Therefore, the radiative carrier recombination efficiency is also reduced. Additionally, the built-in electric field significantly impacts the properties of the quantum well active regions. Electron-hole separation is more dominant in wider wells, compared to narrower ones. As a consequence, optical gain and spontaneous emission rate are smaller in wider wells [134, 135]. Due to the built-in electric field, the transition energy of the carriers is decreased, resulting in a red-shift of the emission spectra. In contrast, the built-in electric field can be reduced with increasing injection current into the quantum well by the phenomenon of charge screening [136, 137]. A blue-shift in the peak emission wavelength is commonly observed due to this charge screening effect [138].

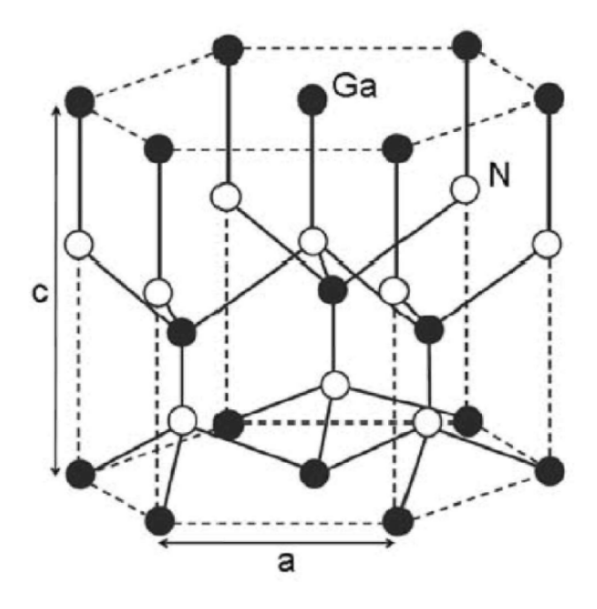


Figure 1.4: Crystal structure of GaN semiconductor [139].

1.3.2 Crystal Defects and Dislocations

The large lattice mismatch (~ 11%) between InN and GaN and the lack of suitable substrates generally lead to the generation of very large densities of crystalline defects and dislocations in LED heterostructures. The dislocation density for GaN based heterostructures is typically reported in range of ~ 10⁸ to 10¹⁰ cm⁻² [140-143]. The defect formation mostly depends on the substrate and buffer layers [144-147], growth conditions [143], carrier concentration [148], and type of impurities [149, 150]. The defects can form intermediate energy levels in the bandgap. The resulting nonradiative recombination at these defect energy levels is called as the Shockley-Read-Hall nonradiative recombination. Nonradiative recombination can significantly degrade the device efficiency. Based on the ABC model, the parameter A is related to the crystal defects which generally influence the maximum achievable efficiency [151]. However, recent studies have shown that defect-related nonradiative recombination may also cause efficiency droop, depending on the quantum well carrier density or the carrier localization related to the non-uniform indium

distribution in the quantum well active regions [152]. Therefore, the exact role of defects in the efficiency droop of GaN-based LEDs has remained a subjective of debate and is being intensively investigated.

1.3.3 Spontaneous Emission

To achieve high power, high brightness LEDs, it is required to eliminate or greatly reduce the efficiency droop at high injection currents. While many techniques have been developed to effectively address efficiency degradation at high injection levels, some recent studies have also shown that the spontaneous emission, described by the parameter B in the ABC model, may also play a role in the commonly observed LED efficiency degradation. Recently, David et al. [153] reported that radiative recombination can contribute to the probability of efficiency droop in InGaN LEDs. This has also been confirmed by Shim et al. [154]. Owing to the saturation of the radiative recombination rate with increasing current, the total carrier recombination rate may become smaller than the carrier injection rate even at a relatively low current density. As a consequence, the carrier density in InGaN quantum wells is increased, due to the saturation of the radiative recombination with increasing injection current. This problem may increase the nonradiative carrier losses, thereby leading to quantum efficiency droop with increasing current.

1.3.4 Auger Recombination

Auger recombination in semiconductors, typically involves the transfer of the excess energy released from the nonradiative recombination of an electron-hole pair to a third particle which is then excited to a higher energy level in the same energy band [155]. This carrier can be an electron or hole, which can subsequently release its energy and relax to the band edge. Auger coefficient C is used to describe the probability of the Auger recombination process. Wide bandgap semiconductors generally exhibit a smaller Auger recombination rate, compared to semiconductors with a narrower bandgap. For GaN (bandgap ~ 3.4 eV), the expected Auger coefficient C is ~ 10^{-34} cm⁶s⁻¹ [156]. However, much higher values (in the range of ~ 10^{-30} cm⁶s⁻¹) have been reported for InGaN alloys [157-159]. With these values,

efficiency droop can be explained [151] even we when assume that the carrier leakage is nearly zero in the ABC model with A and B values being $10^7 \, \text{s}^{-1}$ and $2 \times 10^{-11} \, \text{cm}^3 \cdot \text{s}^{-1}$, respectively. Evidently, efficiency droop increases as the Auger coefficient C becomes larger.

1.3.5 Inhomogeneous Carrier Distribution

Due to the heavy effective mass and low mobility of holes, the hole transport in LED active regions may be highly inefficient [160, 161]. As a consequence, injected holes are located mostly close to the p-doped GaN layer and the hole concentration is significantly reduced toward the n-doped GaN side, while the electron distribution is expected to be more uniform, thereby leading to the highly inhomogeneous carrier distribution throughout the LED device active regions [128, 129, 161-163]. Figure 1.5 shows the simulated band-diagram and hole concentration for an InGaN/GaN multiquantum well LED structure with an emission peak at ~ 400-410 nm and the barrier thickness of the quantum well being ~ 12 nm under +6V bias [163]. The hole density decreases rapidly from the p-GaN to the n-GaN, resulting in the nonuniform hole distribution in the multi-quantum wells. The hole concentration uniformity can be improved by varying the barrier thickness [163]. Tsai et al.[164] observed that a thinner barrier located near to the p-type layers can increase the hole injection, therefore reducing the electron leakage. The highly nonuniform carrier distribution also leads to significantly enhanced Auger recombination and increased electron overflow, further limiting the optical emission efficiency at high injection levels. In this regard, special techniques, including p-doped active region, and thin InGaN barrier, have been implemented to improve the performance of conventional InGaN/GaN quantum well LEDs [124, 128, 163].

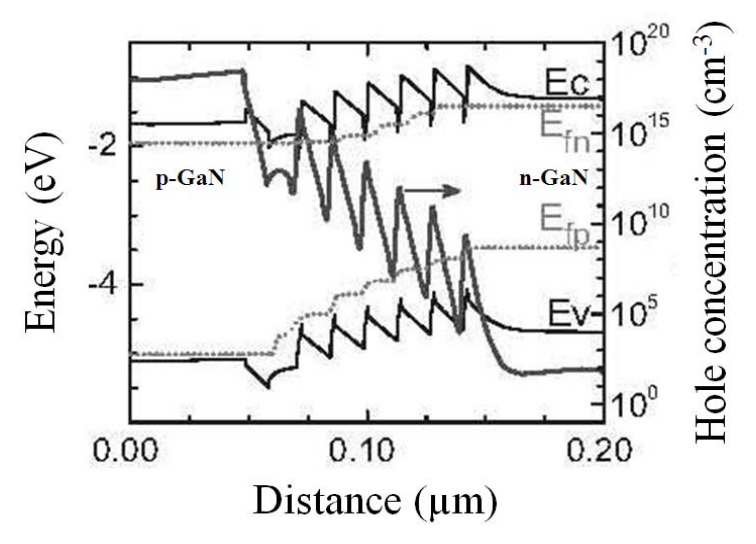


Figure 1.5: Simulated band-diagram and hole concentration of the InGaN/GaN multiquantum well LEDs under +6V bias at room temperature. Quasi-Fermi levels are presented as the dashed lines [163].

1.3.6 Electron Overflow

The above factors causing efficiency droop are related to the carrier losses inside the LED active region. However, the current flow out of the active region is also an important element responsible for efficiency degradation [165-169]. Figure 1.6 illustrates the carrier capture (left) and leakage inside and outside the LED active regions, respectively.

Figure 1.6: Illustration of carrier capture in the InGaN/GaN quantum well (left) and carrier leakage out of the quantum well (right) under large polarization field [152].

Polarization field causes the band energy to tilt, resulting in the separation of electrons and holes. Therefore, carrier recombination is also reduced. Polarization field associated with the nonuniform carrier distribution can cause electron leakage out of the LED active region, which can recombine with holes in the p-GaN region before they can reach the active region, resulting in the degradation of radiative recombination in the active region [151]. One of the primary reasons for electron overflow is the reduction of energy barrier due to the built-in polarization field [170]. Shown in figure 1.7 is the energy band diagram of a typical InGaN/GaN multiquantum well LED [171] with polarization (solid lines) and without polarization (dashed lines). With the presence of polarization field, the band gap is tilted downward near the p-GaN region. However, this phenomenon is not observed in the case of zero-polarization [151]. This problem normally occurs in Ga-polar III-Nitride LEDs. In this regard, the technique of electron blocking layer (EBL) with a high bandgap energy material such as AlGaN is used to prevent the electron overflow [172]. Nevertheless, at relatively high carrier injection, the EBL usually can not completely block the electron overflow in GaN LEDs and, as a result, efficiency droop can still be observed [166, 169, 173]. Experimental measurement results of electron leakage beyond the EBL was recently reported by measuring the spontaneous emission from the p-side of the LED [127].

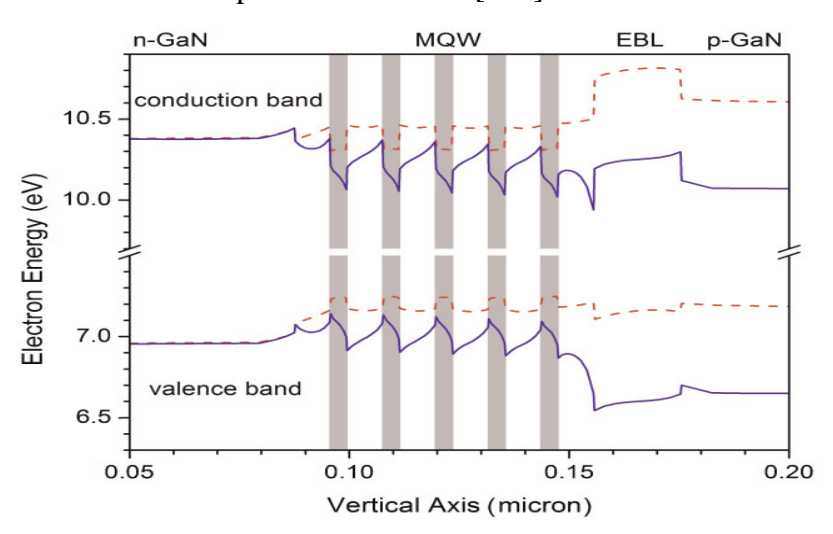


Figure 1.7: Energy band diagram of InGaN/GaN multi-quantum well heterostructures under polarization (solid lines) and without polarization (dashed lines) [151].

1.4 Dissertation Preview

This thesis focuses on the development of novel InGaN nanowire heterostructures on a silicon platform as well as their applications in high performance LEDs and solar cells. In this thesis, we have first studied the MBE growth, fabrication and characterization of superior quality InGaN/GaN dot-in-a-wire and In(Ga)N nanowire heterostructures on Si(111) substrates. A large part of the research has been focused upon the development of full-color, catalyst-free InGaN/GaN dot-in-a-wire nanoscale heterostructures, which provide superior three-dimensional carrier confinement required for ultrahigh efficiency emission. Additionally, the color chromaticity and temperature can be well controlled by varying the compositions and/or sizes of the dots in a single epitaxial growth step. High efficiency green, red, and white InGaN/GaN nanowire LEDs has been demonstrated. In addition, we report on the achievement of nanowire solar cells on Si using InN based material system.

Chapter 1 provides an overview of III-N nanowires and their advantages for device applications. The recent developments of III-N nanowire based sensors, photodetectors, biosensor, solar cells, laser diodes, and LEDs are briefly described. Additionally, the key factors that limit the LED performance are presented in detail, which include polarization, crystalline defect and dislocation, spontaneous emission, Auger recombination, inhomogeneous carrier distribution, poor hole transport, and electron overflow.

In Chapter 2, the growth mechanism of high quality III-N nanowires and dot-in-a-wire heterostructures are discussed. The characterization of GaN and InN nanowires and InGaN/GaN dot-in-a-wire heterostructures are presented.

Chapter 3 is related to the development of high efficiency LEDs with operation wavelengths varying across nearly the entire visible wavelength range, from green, yellow, orange, to red. The realization of phosphor-free white-light LEDs is also described.

In Chapter 4, we report on the achievement of p-doped InGaN/GaN dot-in-a-wire white LEDs, which can exhibit a record-high internal quantum efficiency (>50%). The use of p-type modulation doping in the nanowire LED active region can significantly enhance the hole transport and injection process, thereby drastically increasing the LED quantum efficiency and emission stability.

The first observation of electron overflow in nanowire LEDs is presented in Chapter 5. We have also designed, grown, fabricated, and characterized InGaN/GaN dot-in-a-wire LEDs with the use of an AlGaN electron blocking layer, which can largely prevent electron overflow, leading to nanowire LEDs with virtually zero efficiency droop.

In Chapter 6, we have studied the role of nonradiative recombination on the performance limit of nanowire LEDs, which offers critical insight for the future development of practical nanowire photonic devices. We have demonstrated that Shockley-Read-Hall nonradiative recombination, due to the large surface-to-volume ratios and the presence of surface states and defects, largely limits the performance of GaN-based nanowire LEDs.

In Chapter 7, we have investigated the MBE growth and characterization of superior quality InN nanowire solar cell heterostructures. We have demonstrated the first InN nanowire solar cells consisting of InN:Si/i-InN/InN:Mg nanowire homojunctions on n-type Si(111) substrates, which exhibit a promising short-circuit current density of $\sim 14.4 \text{ mA/cm}^2$ and an energy conversion efficiency of $\sim 0.68\%$ under one-sun (AM 1.5G) illumination.

Finally, the summary of this thesis, future work, and outlook are presented in Chapter 8.

Chapter 2: Molecular Beam Epitaxial Growth and Characterization of High Quality III-Nitride Nanowire Heterostructures

2.1 Introduction

The techniques commonly used for the growth/synthesis of III-nitride nanowires include dry etching[101, 174, 175], direct reaction between Ga or In metals and NH₃ [107, 108], chemical vapor deposition (CVD) [109], molecular beam epitaxy (MBE) [111, 176, 177], chemical beam epitaxy (CBE) [114], and hydride vapor phase epitaxy (HVPE) [115]. The underlying growth mechanisms have been extensively investigated, which may involve the use of catalyst drops in the vapour-liquid-solid (VLS) growth mode, the spontaneous formation under nitrogen rich conditions, or the selective area epitaxy (SAE) on nano-patterned substrates. Additionally, sophisticated nanowire heterostructures, including core-shell and dot-in-a-wire nanoscale heterostructures, can be achieved by using one or two of the afore-described growth processes.

In this chapter, the growth mechanisms of III-N nanowires are first discussed. The MBE growth and characterization of high quality GaN, InN, and InGaN dot-in-a-wire nanoscale structures are investigated in detail.

2.2 III-Nitride Nanowire Growth Mechanisms

Nanowires with controlled properties can be achieved by using either the VLS, the spontaneous formation under nitrogen rich conditions, or the selective area growth process. The growth mechanisms of these processes are described below.

2.2.1 VLS Growth

The growth of nanowire structures by the VLS process was reported in the 1960s by Wagner and Ellis [178]. The VLS growth generally requires a metal particle such as

Au, Ni, and Fe to serve as catalyst and assist nanowire formation [179]. The growth process typically involves three main phases: I) the deposition of metal alloys and matrices, followed by the formation of liquid droplets on the substrate surface, II) crystal nucleation, and III) axial growth of nanowires, where the vapour reaches supersaturation with respect to the solid phase. The low solubility of metal particles in growing semiconductor structures results in a low melting temperature (eutectic point) in the alloy phase diagram, which allows for VLS growth at temperatures of around or higher than the eutectic melting temperature. Figure 2.1 shows the schematic of VLS growth processes. The position and diameter of nanowires grown by the VLS method depend on the position and size of the metal particles and other growth parameters such as temperature and pressure. The nanowire length is usually determined by growth rate and time. The growth rate depends on the supersaturation of the vapour, which is affected by the source concentration as well as the substrate temperature. The growth kinetics affect the nanowire orientation, morphological configuration, and other structural properties [180]. Due to the reduction of the surface energy on the exposed sidewall facets, the growth along the <111> crystal orientation is generally preferred, as commonly observed in the growth of III-V and group IV nanowires [181]. Nanowires grown along the <001> direction have also been reported with catalyst sizes of less than 10 nm [182]. The growth of III-nitride nanowire structures by the VLS technique has been reported using a quartz tube furnace [183], low pressure metal-organic vapour phase epitaxy [184], and thermal chemical vapour deposition [185]. Kang et al. obtained highly uniform and vertically aligned GaN nanowires on c-Al₂O₃ substrates by thermal chemical vapour deposition process using Ni catalysts [186]. III-nitride nanowires can also be grown on many other substrates, including silicon, GaAs and GaP [184]. For metal catalyst assisted nanowires, the metal catalyst generally remains on the tip of nanowires after growth and can be subsequently removed. However, the metal catalyst atoms can diffuse into semiconductor nanowires during growth and therefore may introduce impurities in the nanowires [187, 188]. Such impurities impose deep level trap states in nanowire semiconductors and reduce minority carrier lifetime. Consequently, the carrier collection or emission efficiency may be reduced, limiting the performance of these nanowire devices [189, 190].

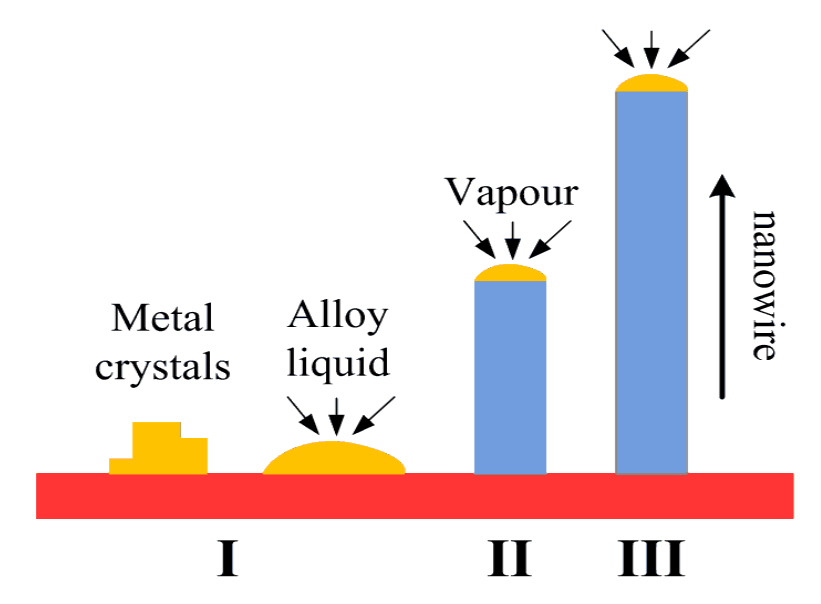


Figure 2.1: Illustration of the VLS growth process: I) semiconductor in vapour phase is introduced into the system with metal catalyst on the substrate surface, II) the formation of liquid droplets on the substrate surface near or above the eutectic temperature, and III) the formation of nucleation sites and the nanowire axial growth.

2.2.2 Spontaneous Formation

Group III-nitride nanowires can also be formed spontaneously under nitrogen rich conditions without using any foreign metal catalysts [191, 192]. In this growth process, the metal catalyst is not used and hence there is no catalyst droplet at the top of nanowires [193]. The technique of molecular beam epitaxy has been commonly used for the spontaneous or self-organized growth of III-nitride nanowires. However, the mechanism of the spontaneous formation, or self-organization of InN and GaN nanowire heterostructures has not been fully understood. It has been suggested that the spontaneous formation of InN or GaN nanowires may involve a self-catalytic growth process, wherein Ga and In droplets can serve as catalysts to assist the nanowire formation [91, 111, 194]. The presence of Ga (or In) droplets on the tip or sidewall of the nanowires, however, has not been observed experimentally [191-193, 195]. Alternatively, diffusion-induced growth has been suggested as the major driving

force for the spontaneous formation of III-nitride nanowires by molecular beam epitaxy [113]. In this model, the growth of nanowires is initiated by the differences in surface energies, sticking coefficients, and diffusion coefficients on different crystal planes. Illustrated in figure 2.2, adatoms diffuse from the nanowire sidewall to the top, due to the lower chemical potential at the top surface. The sticking coefficient at the tip of nanowires is much higher than that on the sidewalls. As a result, Ga adatoms impinging directly on or within a surface diffusion length of the nanowire tip can be incorporated on the nanowire tip, leading to the axial growth of nanowires. The diffusion-induced mechanism is consistent with the observation that the nanowire axial growth rate increases rapidly with the increase of substrate temperature, due to the significantly enhanced adatom surface migration [177, 191]. Self-organized III-nitride nanowires generally exhibit excellent crystalline quality and uniformity, rendering them an excellent candidate for applications in optoelectronic devices.

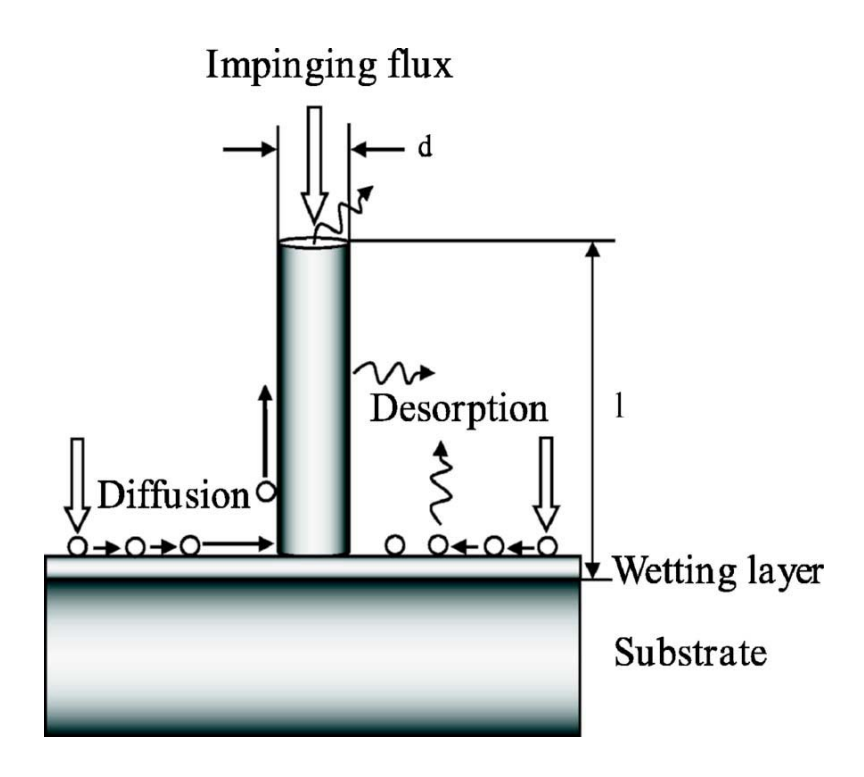


Figure 2.2: Schematic illustration of the spontaneous growth of III-nitride nanowires by molecular beam epitaxy, including adatom absorption, desorption, diffusion, and nucleation processes [113].

2.2.3 Selective Area Growth

An alternative approach for nanowire growth is to use selective area epitaxy [196-200]. In this approach, nanowire growth takes place on pre-patterned substrates. Various selective area growth masks, including SiO₂, Ti, Al and Au templates have been utilized [196, 200]. The selective area growth provides a better control over the nanowire position, size, and aspect ratio and hence is capable of growing materials with controlled emission wavelengths. In this approach, nanowire growth is largely determined by adatom migration, adsorption, and desorption on the exposed substrate surface as well as the masked region, which can be controlled by varying the growth conditions including the substrate temperature and III/V flux ratios. The size and position of the patterns on the mask can be designed to achieve desired nanowire structures. However, effects associated with the profile of the nanoscale masks, the anisotropic lateral overgrowth, and faceting should be considered. High-quality and uniform GaN nanowires with precisely controlled positions and diameters were grown by metal-organic chemical vapour deposition through a selective growth mask [196]. Highly uniform GaN nanocolumns were also grown through a set of nanohole arrays arranged in a triangular lattice, which were prepared on a Ti (5 nm) film by focused-ion-beam etching [200]. Figure 2.3 shows the scanning electron microscopy image of the resulting GaN nanocolumn arrays which exhibit highly uniform diameters (~ 417 nm).

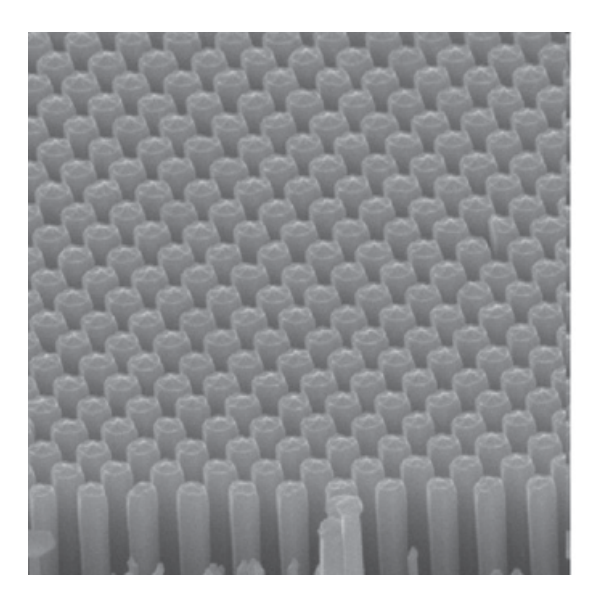


Figure 2.3: Scanning electron microscopy image of GaN nanowires grown by metalorganic chemical vapour deposition using the selective area growth process [200].

2.3 Plasma Assisted Molecular Beam Epitaxial Growth of High Crystalline Quality III-Nitride Nanowire Semiconductors

The current dominant techniques for growing high quality III-Nitride optoelectronic materials are MOCVD and MBE. Historically, MOCVD has been widely used to produce large scale, commercial LEDs and LDs compared to MBE due to the lack of efficient nitrogen sources in the MBE growth. However, MBE has reached a high level of maturity and now offers several i mportant advantages compared to the MOCVD growth method, such as better interface control and the suitability for exploring new material structures or achieving high quality crystalline materials. MBE can provide the highest control of the epitaxial growth of various nanostructures. Compare to MOCVD, MBE exhibits several advantages including ultra-high vacuum environment (~10⁻⁸ to 10⁻¹⁰ Pa) and a slow deposition rate (typically less than 1000 nm/hr), which is useful to minimize impurity incorporation in the epitaxial layers. The MBE growth temperature is also much lower than that of MOCVD, which can enhance indium incorporation, leading to the realization of high

indium content InGaN structures. By using the MBE growth technique, the composition and thickness of the epilayer can be controlled precisely to mono-atomic layer level. Its in-situ monitoring capability can also greatly assist researchers to manage the growth quality and to develop new materials.

The MBE growth process of III-Nitride structures can be divided into two categories, based on the nitrogen sources, including ammonia-molecular beam epitaxy (Am-MBE) and plasma-assisted molecular beam epitaxy (PAMBE), respectively. Am-MBE involves the use of ammonia (NH₃) gas as group V source while high purity N₂ gas is used as group V element in the case of PAMBE. Because N₂ molecule has a high thermal stability, radio frequency (RF) plasma is often used to break the N₂ and create atomic N. For both approaches, solid group III sources, including In, Ga, and Al are generally used. In the Am-MBE system, the NH₃ breaking efficiency depends on the growth temperature and the efficiency values remains relatively low. Therefore, a large amount of NH₃ is required for the growth. In addition, the remaining NH₃ which is not decomposed during growth can react with the chamber and the effusion cell materials at high temperatures. The resulting corrosive problem and chamber cleaning are big issues with this type of MBE growth method. However, in the case of PAMBE, a plasma source of high purity inert N₂ gas is used to supply the group V element. The active nitrogen plasma includes ionized molecules (N2+), atoms (N), and ionized atoms (N+), which are introduced into the chamber for the In(Ga)N deposition. The amount of active nitrogen plasma can be well controlled by adjusting the nitrogen flow rate and the plasma power (the maximum power is generally ~ 500 W). RF-plasma assisted MBE growth technique, therefore, is more efficient compared to the Am-MBE approach.

In this thesis, III-Nitride nanowire heterostructures were grown by a Veeco Gen II MBE system equipped with a RF plasma-assisted nitrogen source. Figure 2.4 shows the MBE system in the Department of Electrical and Computer Engineering. The MBE system consists of three main vacuum chambers including an introchamber, a buffer chamber, and a growth chamber. Si substrates are first cleaned by standard cleaning techniques such as hydrogen fluoride (HF) acid treatment or RCA

technique. They are subsequently loaded into the intro-chamber and degassed at ~ 200 °C before transferring to the buffer chamber. The buffer chamber is used for preparation and storage of samples. A second degassing process is applied in the buffer chamber to make the samples extremely clean before they are transferred to the growth chamber which requires a very clean and high purity environment. Figure 2.5 shows the typical structure of an MBE chamber. Group III elements which are contained in the effusion cells can be thermally evaporated by heating the effusion cells. Group III atoms then impinge onto the heated sample surface and react with the active nitrogen species for the formation of In(Ga)N materials. Group III fluxes can be controlled by varying the group III effusion cell temperature.

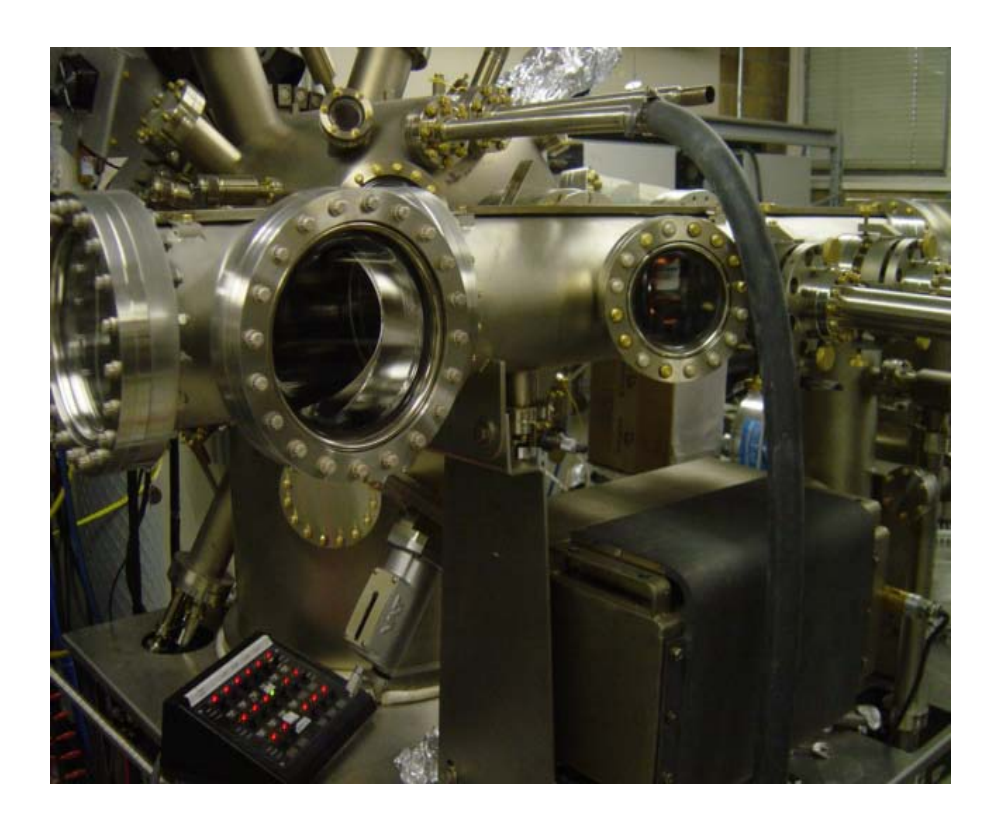


Figure 2.4: A Veeco Gen II MBE system equipped with a radio-frequency plasma-assisted nitrogen source.

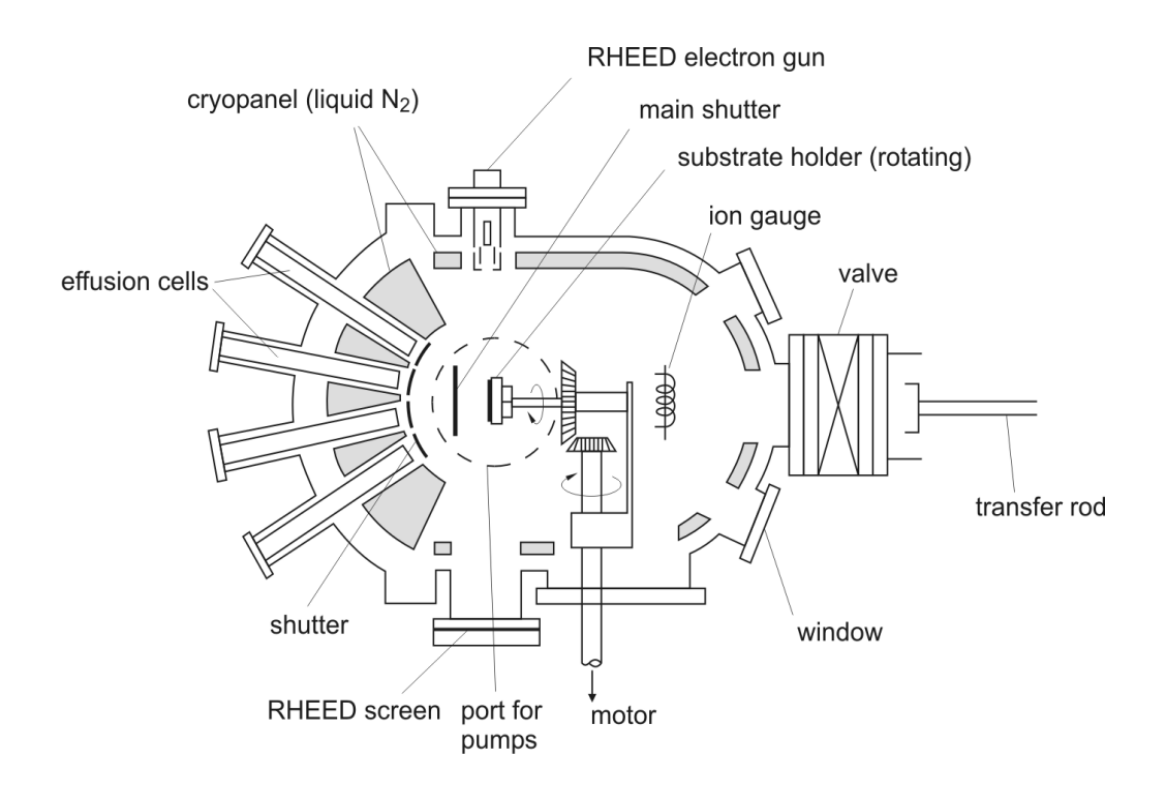


Figure 2.5: Schematic of the MBE growth chamber [201].

The challenges of nanowire growth include the control of the wire uniformity, height, diameter, shape, density, and orientation/alignment, as well as the elimination of stacking faults and other defects. The growth conditions, including the substrate temperature, III/V fluxes, and growth rate, can be optimized to address the above issues. For instance, higher density nanowire arrays can be obtained by decreasing the growth temperature. On the other hand, when grown at higher temperatures, the density of nanowires is generally reduced. This can be explained by the enhanced adatom surface migration at high temperatures [202]. Additionally, the nanowire density can be increased by increasing the growth rate. The size of nanowires depends strongly on the size of the metal catalyst, in the case of VLS growth technique, or the size of the patterned area in the SAE approach as mentioned above. The substrate orientation also plays an important role in the nanowire alignment. Due to the reduction of surface energy of the exposed sidewall facet during growth, the <111>

growth direction is commonly used in the growth of III-N and group IV nanowires rather than that the <001> direction [181].

MBE systems are generally equipped with a reflection high energy electron diffraction (RHEED) system, which enables an in situ monitoring of the surface properties and the quality of nanowire structures. In the RHEED system, a beam of electrons, generated from an electron gun, strikes the sample surface in a very small angle to the sample surface. The interaction of electrons and atoms on the sample surface leads to the formation of regular patterns on the phosphorous detector screen. Therefore, the sample surface properties can be revealed in the RHEED pattern. In addition, the RHEED pattern can be used as a powerful tool to monitor the in situ oxide desorption of the substrate surface. During the nanowire growth, spotty patterns (an array of dots) are displayed on the RHEED screen. The general information of the nanowires, including the size, shape, orientation, and density can be derived from the size, shape and density of the dots on the RHEED screen. Nanowires with small diameters and high densities are displayed as an array of tightly spaced small dots on the RHEED. In contrast, an array of well-spaced, large dots on the RHEED screen indicates the growth of low density and thick nanowires. In general, when the growth starts with a few monolayers of In or Ga seeding layer prior to the introduction of any nitrogen species, the RHEED pattern shows bright array of circular dots. At the beginning of nanowire growth, the dot arrays are still bright. During the subsequent growth, the dot arrays may become significantly dimmer while maintaining the dot shape. The dimmer RHEED patterns as growth continues may be explained by the nonuniformity in nanowire heights, which leads to destructive interference as electrons are being deflected off the wire structures in alternate paths. The orientation of the wires may also be obtained by examining the shape of the dots shown on the RHEED pattern. Circular dots generally indicate that nanowires are grown perpendicular to the substrate. The appearance of elliptical dots, however, suggests that nanowires are tilted and oriented in various directions.

2.4 Molecular Beam Epitaxial Growth and Characterization of InN Nanowires

InN material has been intensively studied in the past decade due to its various distinctive properties. InN exhibits a direct band gap in the infrared range and has the largest electron mobility and drift velocity among all III-nitrides due to its low electron effective mass, making it an excellent candidate for a new generation of nanophotonic and nanoelectronic devices, including terahertz emitters, detectors, nanoscale lasers and high-speed field-effect transistors as well as high efficiency solar cells. The bandgap of InGaN material can be varied from ~ 0.7 to 3.4 eV, which practically includes the whole solar spectrum and yields the possibility of multijunction solar cells. InN exhibits unique electronic band structure, with a very large electron affinity (~ 5.9 eV), which is the largest value among all known semiconductors. As a consequence, the presence of impurities, defects and dislocations generally leads to very high electron concentrations (>1×10¹⁸ cm⁻³) even for nominally undoped InN, which significantly affect its electrical and optical properties [6].

Nearly forty years after the first demonstration of InN using RF sputtering of metallic In in nitrogen environment, there still exist many challenges for growing high quality InN and for understanding its many fundamental properties. The material deposited using the RF sputtering method consisted of polycrystalline grains and showed an absorption band edge of 1.9 eV [203]. For a long time, the bandgap of InN was believed to be ~ 1.9 eV. It was later found that the bandgap of InGaN alloys with ~ 50% In was below 2 eV, suggesting a much smaller bandgap for InN [204]. Recently, the technological breakthrough in growing InN materials using PA MBE has led to high quality InN films with reasonably low free electron concentrations (~ 3×10¹⁷ cm⁻³) and high electron mobility (>2000 cm²/Vs) [205]. From both the optical absorption and photoluminescence (PL) studies, it was concluded that the energy bandgap of InN is ~ 0.65 eV [205]. The large discrepancy with previous reports is believed to be related to the Burstein-Moss effect. The optical absorption/emission is largely forbidden for the energy levels below the Fermi level in degenerate semiconductors and, as a result, the observation of the band edge absorption/emission

in InN may not be possible, if the material is plagued with very high concentrations of electrons.

InN generally exhibits very high background electron concentrations, due to the presence of high densities of native defects, impurities, and surface states [206]. For a long time, the main source for unintentional doping was believed to be nitrogen vacancies, which, however, was not supported by recent first principle calculations [207]. The high residual electron density was also attributed to threading dislocations [208]. But Gullinat *et al.* studied the effect of threading dislocation densities in various InN films on the carrier concentrations and found there was lack of correlation [209]. It was observed that threading dislocations mainly reduced the electron mobility by introducing scattering sites.

Later studies showed the presence of high levels of oxygen and hydrogen in asgrown InN samples, suggesting that controlling impurity incorporation is very important in eliminating the unintentional doping in InN [207]. Oxygen occupies the nitrogen site (O_N) , and it is a shallow donor with the formation energy much lower than that of V_N . If oxygen is present in the growth environment, then high donor densities in InN is expected. It may also be noted that hydrogen is present in most growth environments. Hydrogen can exist in InN lattice as either interstitial (H_i) or substitutional on nitrogen site (H_N) , both of which would act as donors [207]. Pettinary *et al.* introduced hydrogen atoms to as-grown InN film using a remote plasma and observed that the electron concentration was increased by more than two orders of magnitude (from $\sim 10^{17}$ cm⁻³ to 10^{19} cm⁻³) [210]. Ruffenach *et al.* experimentally observed that by annealing the as-grown InN films in nitrogen environment at high temperatures, the hydrogen out diffused and the free electron concentration dropped significantly [211].

For practical device applications, it is important to develop p-type InN. As discussed above, while it has been relatively easy to achieve n-type doping in InN, it has remained a dominating task to grow nearly defect- and impurity-free InN and to demonstrate p-type conductivity. Mg is a commonly used acceptor dopant for InN,

and it mostly substitutes the In site [212]. Jones *et al.* reported the evidence of p-type doping in InN [213]. However, with the presence of strong surface electron accumulation, it has been difficult to directly probe the p-type bulk using conventional electrical measurement techniques. It was later determined that the acceptor ionization energy was approximately 60 meV for Mg in InN using low-temperature PL measurements [214, 215]. Wang *et al.* found that p-type InN can be grown if the Mg acceptor concentration is in the range of $\sim 1 \times 10^{18}$ cm⁻³ to 3×10^{19} cm³ and any doping concentrations lower than these values may not be sufficient to compensate the background donors [214]. More recently, using electrolyte capacitance-voltage measurements, Yim *et al.* measured the carrier concentrations below the accumulation surface of both n-type and p-type InN [216].

The lattice parameters of wurtzite InN was measured to be a = 3.53 Å and c = 5.7 Å [77]. Theoretical studies have shown that InN can have relatively high electron motilities of ~ 4,400 cm²/Vs and 30,000 cm²/Vs at 300 K and 77 K, respectively [217]. Experimentally, however, it was observed that InN films with high free electron concentrations were characterized by greatly reduced electron mobility. The growth of p-type InN is a crucial step towards achieving many practical devices, which has remained very difficult, due to the presence of large bulk and surface electron concentrations. This has become even more challenging for InN nanowires, since they have high surface-to-volume ratios and consequently more electrons to compensate in order to achieve p-type conductivity, due to the commonly observed surface electron accumulation.

2.4.1 Surface Charge Properties of InN

The surface and interface charge properties play a vital role in the formation, physical structure, and characterization of nitride nanoscale heterostructures as well as their emerging applications in high performance electronic, photonic, and biochemical devices. It has been generally observed that there is a very high electron concentration ($\sim 10^{13} - 10^{14} \text{ cm}^{-2}$) on the polar and nonpolar growth surfaces of InN films and the surface Fermi-level pins deep in the conduction band [218-221]. However, the origin

of the surface electron accumulation of InN has remained a subject of intensive debate. Although it has been explained by the unusual positioning of the Branch point energy (E_B) well above the conduction band minimum at the Γ -point and the resulting surface Fermi-level pinning deep in the conduction band (near E_B) [218], recent studies strongly suggest that the surface electron accumulation depends critically on the surface states and polarity as well [207, 222].

Van de Walle et al. calculated the bulk and surface energy states of InN using the density functional theory with appropriate modifications to the pseudopotentials [207, 222]. The calculated results are shown in figure 2.6 for polar c-plane (0001) and nonpolar m-plane $(1\bar{1}00)$ surfaces. The polar surface with moderate In/N ratios has a stable surface reconstruction, where an In adatom binds to three In atoms on the surface. For such a surface reconstruction, the calculated density of states, illustrated in figure 2.6(a), show two sets of surface states, with the lower set and upper set being fully occupied and empty, respectively [207]. Since the occupied surface states have an areal density of $\sim 5 \times 10^{14}$ cm⁻², significantly larger than the number of bulk states in the near-surface region, the surface Fermi level is approximately positioned at the highest occupied energy states, i.e. ~ 0.6 eV above the conduction band minimum. The derived surface level position and the associated surface electron accumulation are in qualitative agreements with experimental results for the InN polar surface. For the non-polar surface with moderate In/N ratios, the In adlayer is mostly absent and the surface consists of largely In-N dimers. Illustrated in figure 2.6(b), there exist two dangling bonds in the surface electronic structure in this case, including the occupied N dangling-bond state and the unoccupied In dangling-bond state that are positioned close to the valence band maximum and above the conduction band minimum, respectively. Consequently, surface accumulation and Fermi level pinning is not expected for nonpolar InN surfaces. Wu et al. confirmed the calculation results by probing a freshly cleaved nonpolar InN surface, which showed the absence of surface electron accumulation [223].

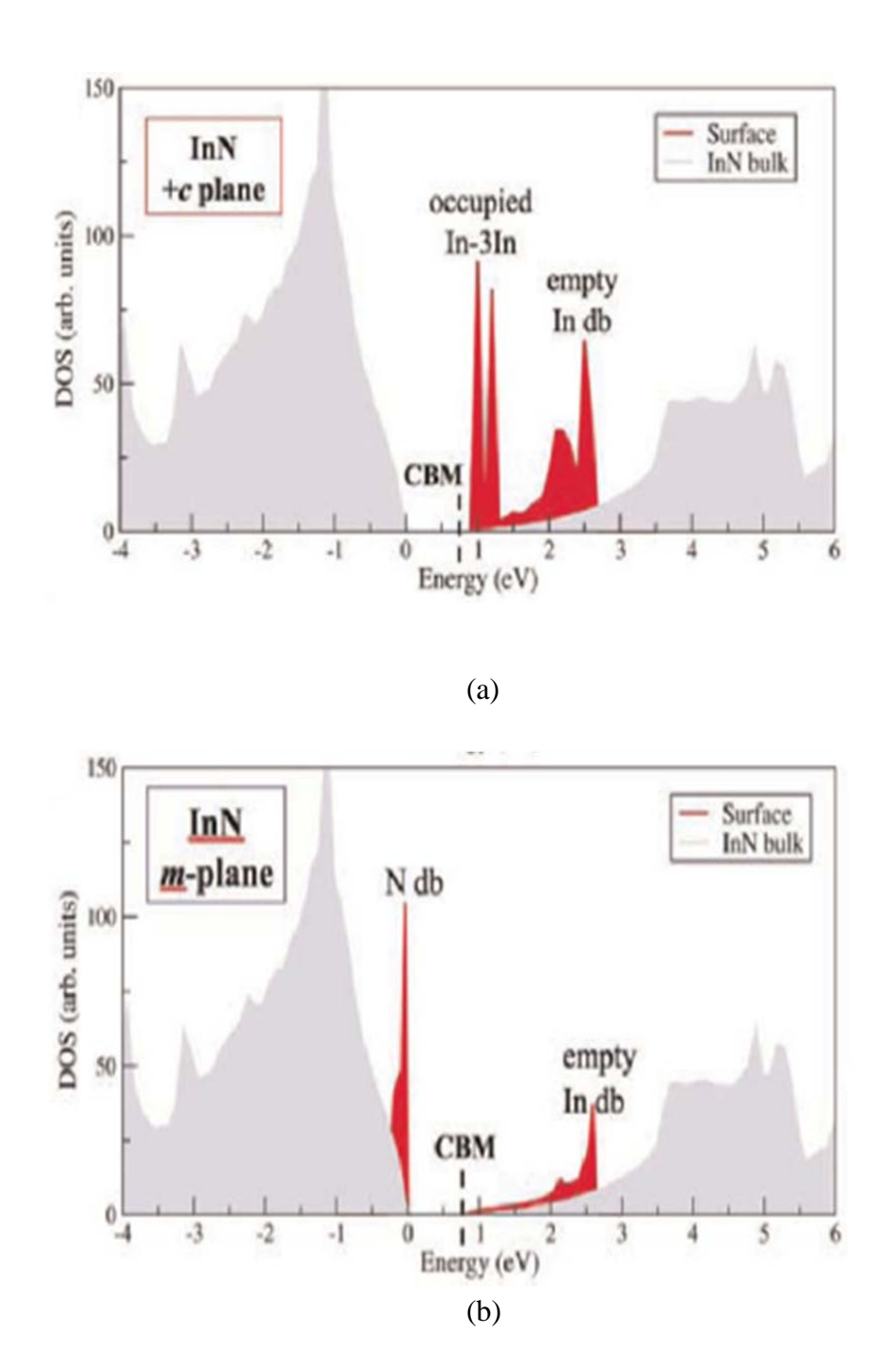


Figure 2.6: The density of states for the stable surface structures found on selected InN surfaces: a) structure stable at moderate In/N ratios on polar c-plane surface, and b) In–N dimer structure stable at moderate In/N ratios on nonpolar m-plane surface [207].

Knowing the Fermi level position at the surface and the energy band structure of the bulk, one can calculate the band bending at the surface by solving the Poisson's equation. For simplicity, Yim *et al.* neglected the quantum effects but included the non-parabolicity of the band and assumed that E_{FS} is located 1.5 eV above the valence band maximum [216]. The calculated results are similar to that estimated by Van de Walle *et al.* [207]. Calculations also showed that large surface electron accumulation was present in p-type InN, which was experimentally observed by electric field measurement using second harmonics [224].

Recently, the surface electron accumulation profile has been measured at the lateral, nonpolar surfaces of [0001] oriented wurtzite InN nanowires, which may be explained by the presence of surface impurities and defects [207, 225-227]. There is also evidence that the surface electron concentration is correlated with the bulk electron density as well [228]. Further studies are required in order to fully understand the surface charge properties of InN nanowires.

2.4.2 MBE Growth and Properties of InN Nanowires

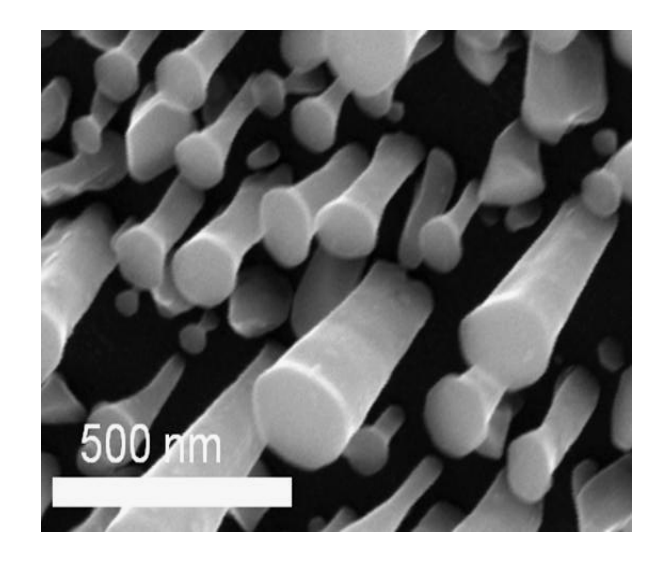
InN nanowires have been grown using a foreign metal catalyst via the VLS mechanism [229, 230] or spontaneously under nitrogen rich conditions [231]. The resulting InN nanowires generally exhibit severely tapered morphology [202, 232, 233]. There are generally large variations in the wire diameters and amongst the wire heights [232, 233]. The poorly defined surface morphology adversely affects the structural, optical and electrical properties of InN nanowires and severely limits their practical device applications [205, 234-237]. In this regard, we have developed a novel growth technique to obtain nontapered, highly uniform, and nearly homogeneous InN nanowire by using an *in situ* deposited In seeding layer prior to growth initiation.

In this experiment, electronically pure InN nanowires are grown on Si(111) substrates by plasma-assisted MBE under nitrogen-rich conditions. To achieve high-quality InN nanowires with controllable structural properties, we investigated the self-catalytic growth of InN nanowires. In this process, a thin ($\sim 0.5-1.6$ nm) In

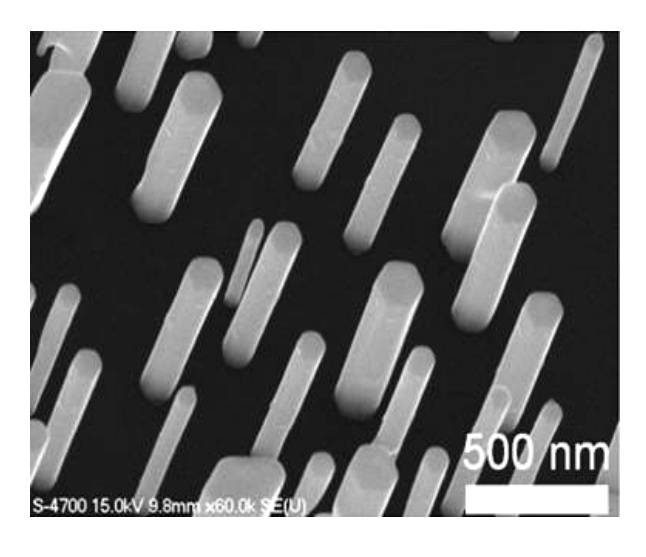
seeding layer is first deposited on the Si substrate surface prior to growth initiation [238, 239]. The thin In layer forms nanoscale liquid droplets at elevated temperatures, which provides well-defined nucleation centers for the formation and growth of InN nanowires. Subsequently, the InN nanowire growth is carried out at a nominal growth rate of 0.6 Å/sec, nitrogen flow rate of 1.0 - 2.0 sccm, growth temperature of 440 - 520 °C, and RF plasma forward power of $\sim 400 \text{ W}$.

The scanning electron microscopy images of InN nanowires grown on Si without and with the use of In seeding layer are shown in figures 2.7 (a) and (b), respectively. It is evident that significantly improved structural properties, with a nontapered surface morphology and nearly identical heights, can be obtained by using an *in situ* deposited In seeding layer. The wires are of wurtzite structure and well-separated, with the c-axis oriented vertically to the Si(111) substrate surface. With increasing growth temperature, InN nanowires generally exhibit reduced areal densities and larger diameters.

This study indicates that the formation of InN nanowires may involve a self-catalytic process, as suggested by recent experiments [240-242]. In this process, InN nanowires nucleate and grow from nanoscale In droplets created on the growing surface. During the conventional spontaneous growth of InN nanowires, there are no well-defined nucleation centers, and, consequently, the continuously random nucleation of nanowires leads to InN nanowires on Si with a large variation in height and diameter. Also due to the large diffusion rate of In adatom and their preferential incorporation near the wire top, conventional InN nanowires generally exhibit severely tapered morphology [202, 233]. On the other hand, in the present approach, the *in situ* deposited In layer prior to growth initiation forms nanoscale liquid droplets on the Si surface at elevated temperatures, which can therefore act as seeds to promote the nucleation of InN nanowires. As a result, the nanowire density is largely pre-determined, and the size uniformity is significantly enhanced. It is therefore evident that the use of an *in situ* deposited In seeding layer can provide an additional dimension to effectively control the growth and properties of InN nanowires.



(a)



(b)

Figure 2.7: SEM images of InN nanowires (a) grown directly on Si(111) at $480\,^{\circ}C$ and (b) grown on Si(111) at $480\,^{\circ}C$ with the use of an *in situ* deposited In seeding layer.

Important for practical device applications is a precise control of the carrier concentration and conductivity of InN nanowires. The residual electron density of InN can be derived from a Hall-effect measurement or by analyzing the photoluminescence spectral linewidth measured at low temperatures [243, 244]. For conventional n-type degenerate InN, the measured photoluminescence linewidths are generally in the range of 50 to 100 meV, which correspond to residual electron densities of $\sim 10^{18}$ cm⁻³, or higher [245]. Illustrated in figure 2.8 are the photoluminescence spectra for the presently achieved nontapered InN nanowires measured under various laser powers at 5 K. An extremely narrow spectral linewidth of 8 meV was obtained under low excitation conditions. Detailed analysis revealed that the electron density in the undoped InN nanowires is $\sim 2 \times 10^{15}$ cm⁻³, or less, which is nearly a factor of 500 times smaller than the commonly reported values [228, 245-249], suggesting, for the first time, the achievement of nearly intrinsic InN. The presence of an extremely low level of carrier concentration in the undoped InN nanowires is also directly reflected in the power-dependent photoluminescence emission, shown in figure 2.8. With increasing excitation power, there is a considerable blueshift in the photoluminescence peak energy, accompanied by a significant broadening of the spectral linewidth. Such a clear band filling effect has not been previously observed in the photoluminescence emission of n-type degenerate InN.

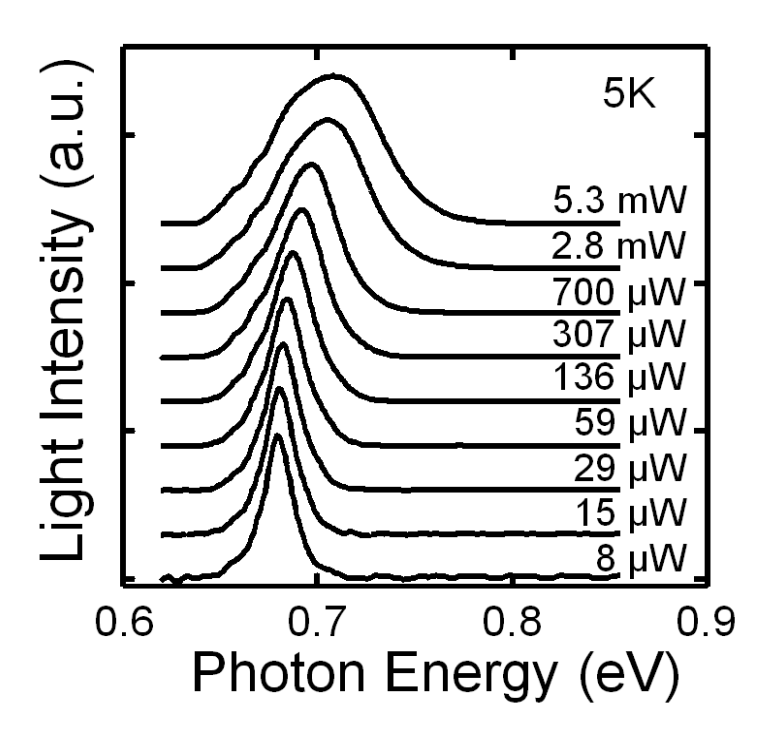


Figure 2.8: Photoluminescence spectra of nondoped InN nanowires on Si(111) measured at 5K under various laser powers.

2.4.3 Si and Mg-Doped InN Nanowires

With the achievement of nearly intrinsic InN nanowires [250], we have subsequently investigated the growth and optical properties of Si- and Mg-doped InN nanowires. These nanowires are grown by introducing the respective dopants during nanowire growth without any modifications to the previously described growth conditions. Due to the significantly enhanced In adatom surface migration and the preferred growth along the nanowire length direction, the resulting doping level is generally smaller, compared to that of planar heterostructures. It is expected that the local dopant fluctuation in the wires may also be negligible, due to the relatively large (> 100 nm) wire diameters. For the Si doping concentrations considered (< $\sim 1 \times 10^{18}$ cm⁻³), no morphological changes to the InN nanowires were observed. However, the incorporation of Si-dopant can significantly modify the optical properties of InN nanowires. Illustrated in figure 2.9 are the photoluminescence spectra of InN:Si nanowires measured at 5 K for various Si doping levels. It is seen that, with increasing Si-doping concentration, InN nanowires exhibit a considerable blueshift in

the photoluminescence peak energy, a drastic increase in the spectral linewidth, and a significant decrease in the luminescence efficiency. Such effects have also been observed at elevated temperatures and under various laser powers. The observed Burstein-Moss shift, *i.e.* the significant increase in the photoluminescence peak energy and broadening of the spectral linewidth, can be well explained by the increased electron densities with increasing Si doping concentrations. However, the exact origin of the drastically reduced luminescence efficiency with increasing Si doping concentration remains unclear. One possible explanation is the increasing surface electron accumulation that leads to a significantly increased spatial separation of charge carriers in the wires. As a consequence, the radiative efficiency is reduced with increasing Si doping concentration.

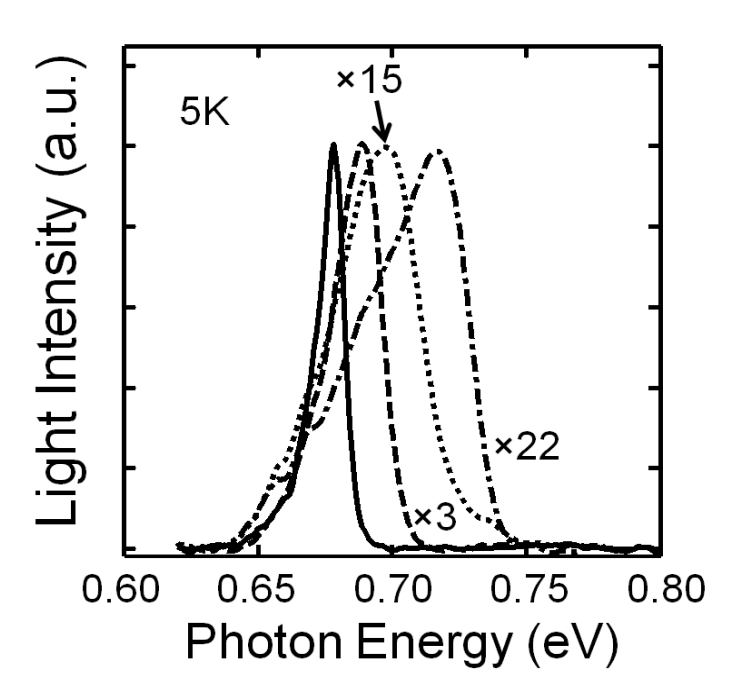


Figure 2.9: Photoluminescence spectra of InN nanowires on Si(111) substrates for Si doping concentrations of $\sim 1 \times 10^{18} \text{ cm}^{-3}$ (dashed and dotted line), $2 \times 10^{17} \text{ cm}^{-3}$ (dotted line), $5 \times 10^{16} \text{ cm}^{-3}$ (dashed line), nondoped (solid line), measured at 5K.

From photoluminescence measurements of InN:Mg films, it was determined that the Mg acceptor activation energy was about 61 meV [251]. However, to the best of our knowledge, the growth and properties of InN:Mg nanowires have not been reported. In this study, InN:Mg nanowires, with Mg effusion cell temperatures

varying from 185 °C to 235 °C, are grown and characterized. It was observed that, for relatively low Mg concentrations, InN nanowires with excellent surface morphology and structural properties can be obtained. However, with increasing Mg flux, the wires show increasing diameter and reducing length, potentially due to the reduced adatom surface migration. Similar effects have also been observed for GaN:Mg nanowires [252, 253]. A further increase of the Mg concentration generally leads to a tapered surface morphology, shown in figure 2.10, and the generation of dislocations.

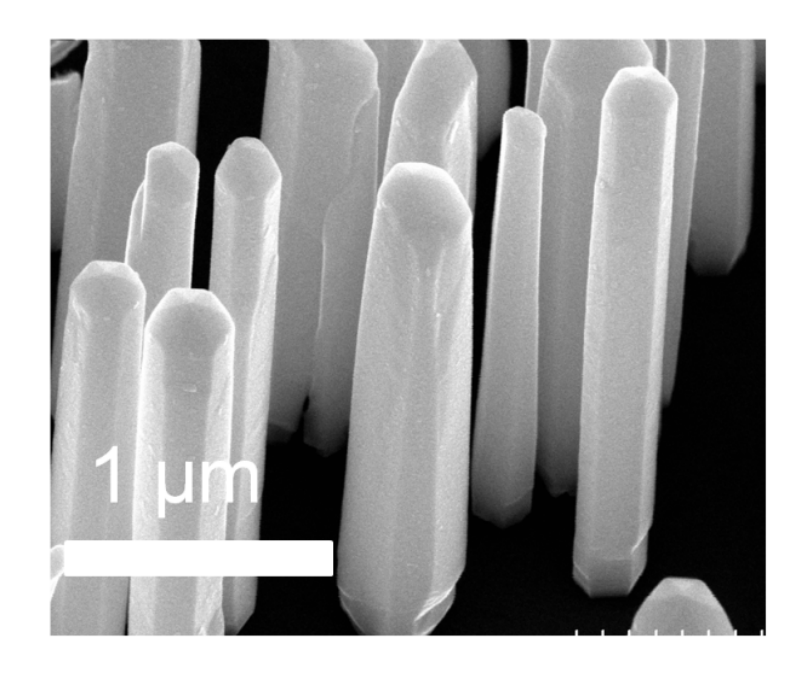


Figure 2.10: Scanning electron microscopy image of InN nanowires grown on Si(111) substrates with a relatively high Mg doping concentration. The wires show deteriorated structural properties, with the presence of slightly tapered surface morphology.

Illustrated in figure 2.11 are the photoluminescence spectra of InN:Mg nanowires measured at 5 K for various Mg effusion cell temperatures. It is observed that the photoluminescence peak intensity decreases considerably with increasing Mg incorporation, which may be directly related to the formation of Mg-related defects.

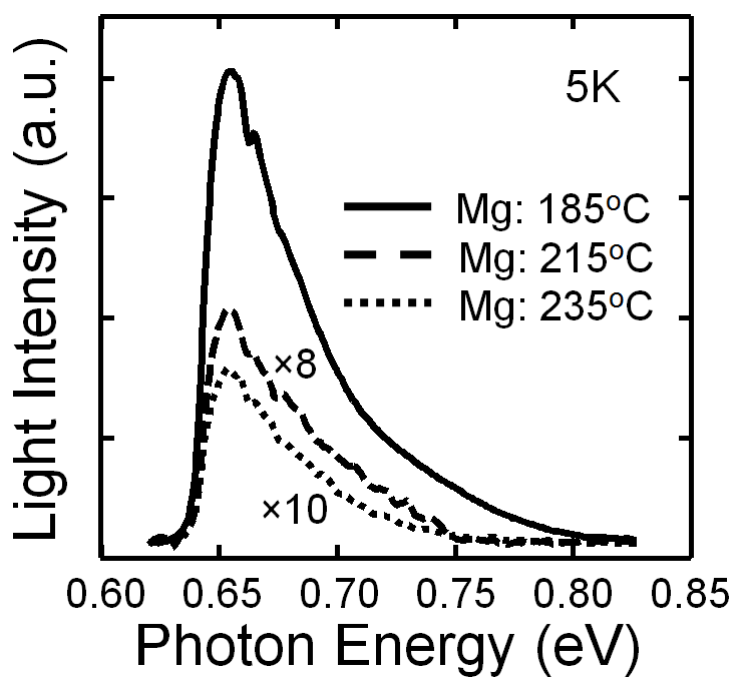


Figure 2.11: 5 K photoluminescence spectra of InN:Mg nanowires grown at different Mg effusion cell temperatures.

2.5 MBE Growth and Characteristics of GaN Nanowires and InGaN/GaN Dot-in-a-Wire Heterostructures

2.5.1 Review on the MBE Growth and Characteristics of GaN Nanowires

GaN and related nitrides have been intensively studied due to their unique properties, including chemical stability, direct band gap, and large breakdown electric field. Applications of GaN nanowires include violet lasers, ultraviolet photodetectors, high electron mobility transistors, high-speed heterojunction bipolar transistors, as well as visible LEDs. GaN nanowires offer superior emission properties for LED applications, compared to GaN thin films, due to the efficient light extraction and drastically reduced dislocation densities. Densely packed GaN nanowire arrays can be designed as high brightness LEDs, while isolated, low density nanowires may be fabricated for single nano-devices and for the study of electronic, optical and mechanical properties of the materials.

While most III-V compound nanowires are grown via the VLS process with metallic nano-particles as catalysts [254-257], GaN nanowires have shown a strong

anisotropic property that permits spontaneous growth via PAMBE under N-rich conditions (for the reduction of Ga surface diffusion [258]). In the past several years, a number of groups have investigated GaN nanowires grown on Si(111) using PAMBE, and it has been shown that the nanowires exhibit a hexagonal crystalline structure with vertical faceted sidewalls and the *c*-axis perpendicular to the surface of the substrate [259-263]. Despite the large mismatch (~17%) between GaN and Si, the grown nanowires are shown to be fully relaxed, producing high quality single crystals that are free of strain and dislocations. In some cases, even the nanowires base region next to the Si substrate shows very low densities of defects or stacking faults [263]. It may be noticed that GaN nanowires can also be grown on Si(111) substrates using the CVD technique, which can yield high quality, single crystalline, and hexagonal wurtzite structured nanowires. However, the diameter distribution is often quite large, and the nanowires are typically not vertically aligned to the substrates [264-268].

Recently, Cerutti et al. have demonstrated the growth of GaN nanowires on Si(001) substrates via PAMBE and realized wurtzite single crystal structure with diameters in the range of 20-40 nm along the [0001] direction [269]. In addition, their PL measurements showed intense and narrow excitonic emissions which indicated high crystal quality, and the Raman scattering analysis suggested the wires are strainfree. Calarco et al. have also recently grown GaN nanowires via PAMBE on Si(111) substrates. They found that a linear dependence of the mean values of diameter and length on deposition time occurred during the nucleation state, which is in direct contrast to the previous observation of an inverse dependence of the nanowire length on its diameter. This property was attributed to the diffusion-induced growth mechanism [177]. Debnath et al. have also examined the growth mechanism of GaN nanowires on Si(111) utilizing catalyst-free PAMBE recently [177]. They reported that at the initial stage of growth, a nucleation process occurred where the densities of nanowires as well as their diameters increased gradually with growth time. For growth beyond the initial nucleation stage, the nanowire length decreased with increasing diameter, which was explained by the adatom diffusion on the nanowire sidewalls towards the tip. They stated that for thin wires (diameters ~10-80 nm),

growth was driven by adatom diffusion on the nanowire lateral surfaces, while for the case of thicker wires this adatom diffusion process was less prominent and the adsorption at the nanowire top became more dominant. Tchernycheva et al. have also grown GaN nanowires on Si(111) substrate via PAMBE and examined their structural and optical characteristics [263]. They reported that the nanowires growth followed the Gibbs Thomson's mechanism where the length of the nanowires increased as a function of nanowire diameter. In addition, they showed that the nanowires exhibited a strong near band-edge PL up to room temperature, and their micro-PL measurements for a single nanowire yielded a peak at 3.478 eV with 6-10 meV broadening, which was close to the luminescence of the nanowire ensembles, indicating the strain homogeneity amongst the wires. GaN nanowires growth via catalyst-free PAMBE on Si(111) was also done by Robins et al. for the investigation of the nanowire optical properties and electronic structures [270]. Using the same technique, Averett et al. have performed epitaxial GaN film overgrowth on top of the nanowires grown on Si(111) and observed a significant improvement in crystal quality [271]. In addition, they have demonstrated that under Ga-rich conditions at high substrate temperatures, the Ga adatom desorption rate increased with increasing V/III flux ratio, hence the formation of GaN nanowire was enhanced. This was also shown to be the case by Park et al.[272].

There have been other reports on the growth of GaN nanowires on Si substrates as well. Seo et al. have conducted the growth of periodic arrays of GaN nanowires on Si(111) where periodic patterns were made first by conventional UV lithography before self-implantation of Si ions [273]. They claimed that the modification of Si substrate surface morphology prior to deposition via ion bombardments can enhance the nanowire nucleation and growth, where nano-capillary condensation of Ga droplets acted as catalysts in VLS process to assist the nanowires to elongate out of the supporting thin film matrix. SAE growths have also been done by employing patterned substrates on Si [274]. Ishizawa et al. have used patterned, pre-deposited thin Al layers on n-type Si(111) substrates to grow GaN nanowires [274]. The patterned Al disc layers were nitrided in PAMBE, thereby producing AlN crystals

that served as nucleation sites for the nanowire selective growth. Kishino et al. have also demonstrated SAE growth of GaN nanowires via Ti-mask-patterned Si(111) substrates [275]. They observed that the GaN nanowires grew only on the stripe areas of exposed Si, with no growth on the Ti surface, at a deposition temperature of 935 °C. Below 900 °C, nanowire growth on the Ti surface occurred hence SAE growth was not obtained. The use of buffer layers to assist GaN nanowire growth on Si substrates has also been investigated [276, 277]. Hsiao et al. have demonstrated the growth of GaN nanowires on Si(111) with the insertion of a thin GaN buffer layer [276]. They stated that the crystal seed grown at the wall of the openings in the buffer layer induced nano-capillary condensation effect, which assisted the GaN nanowire growth. In addition, they showed that the nanowire density and diameter may be controlled by the N/Ga flux ratios. Songmuang et al. have also shown the growth of GaN nanowires on Si(111) with the use of thin AlN buffer layers, and showed considerable improvements in the orientation of the nanowires [278]. Furthermore, they showed that well-spaced nanowires were formed due to a large diffusion length of Ga atoms, which occured under high deposition temperatures where the actual amount of grown material was less.

2.5.2 MBE Growth and Characterization of InGaN/GaN Dot-in-a-Wire Nanoscale Heterostructures

For practical device applications, it is highly desired and essential that axial and radial nanowire heterostructures, with well-controlled layer thicknesses and compositions and well-defined interfaces, can be grown and fabricated. To achieve such heterostructures using the VLS growth mechanism, it is required that the catalyst nanocluster is apposite for the growth of the various nanowire materials under similar growth conditions. Alternatively, III-nitride nanowire heterostructures can be grown spontaneously under nitrogen rich conditions. In what follows, we have developed, for the first time in the world, InGaN/GaN dot-in-a-wire nanoscale heterostructures. Such novel nanoscale heterostructures are grown on Si(111) substrates. They can exhibit high efficiency emission in the blue, green, and red wavelength range. Compared to InGaN ternary nanowire structures, the incorporation of InGaN dots in

GaN nanowires can provide a promising approach for realizing high efficiency green and red emission, due to the three-dimensional carrier confinement.

In this study, catalyst-free, vertically aligned InGaN/GaN dot-in-a-wire heterostructures are grown on Si(111) substrates by RF-PAMBE. The oxide on the substrate surface is removed in situ at ~ 770 °C. Subsequently, GaN nanowires are formed under nitrogen rich conditions without the use of any external catalyst. The growth conditions for GaN nanowires include a growth temperature of ~ 750°C, nitrogen flow rate of 1.0 sccm, a forward plasma power of ~ 350 - 400 W, and a Ga beam equivalent pressure of ~ 6×10⁻⁸ Torr. To realize visible light emission, InGaN quantum dots are incorporated in GaN nanowires, which are formed by the straininduced self-organization. The InGaN quantum dots are grown at relatively low temperatures (~ 600 °C) to enhance the In incorporation. The In composition in the dots can be well controlled by varying the In and Ga beam flux. Each quantum dot layer is subsequently capped by a GaN layer. Both the InGaN dots and GaN barrier layers are grown using the same plasma power (~ 400 W) and nitrogen flow rate (1.0 sccm). The dot height and barrier layer thickness can be controlled by the growth time. In this experiment, ten InGaN/GaN quantum dots are incorporated in each GaN nanowire. Shown in figure 2.12 is a 45 degree-titled scanning electron microscopy (SEM) image of the InGaN dot-in-a-wire heterostructures grown on Si (111) substrate. The areal density of the nanowires is estimated to be $\sim 1 \times 10^{10}$ cm⁻². The wires are vertically aligned to the substrate and exhibit a high degree of size uniformity. A bright field scanning transmission electron microscopy (STEM) image (FEI Titan 80-300 cubed equipped with an aberration corrector of the probe-forming lens and a high-brightness electron source) of a single InGaN/GaN dot-in-a-wire is shown in figure 2.13, wherein vertically aligned multiple InGaN quantum dots can be identified. The nanowires are of wurtzite crystal structure, with the c-axis aligned along the growth direction. The dot widths are in the range of 20 to 40 nm, and the dot heights, depending on the growth time, can be varied from ~ 3 nm to 10 nm. Compared to conventional well/disk-in-a-wire heterostructures, the dots are completely embedded in the center region of the wires, thereby leading to superior 3dimentional carrier confinement. It is also interesting to notice that the InGaN dots alignment is correlated along the growth direction, due to strain-induced selforganization, which is indicated by the white arrow shown in figure 2.13.

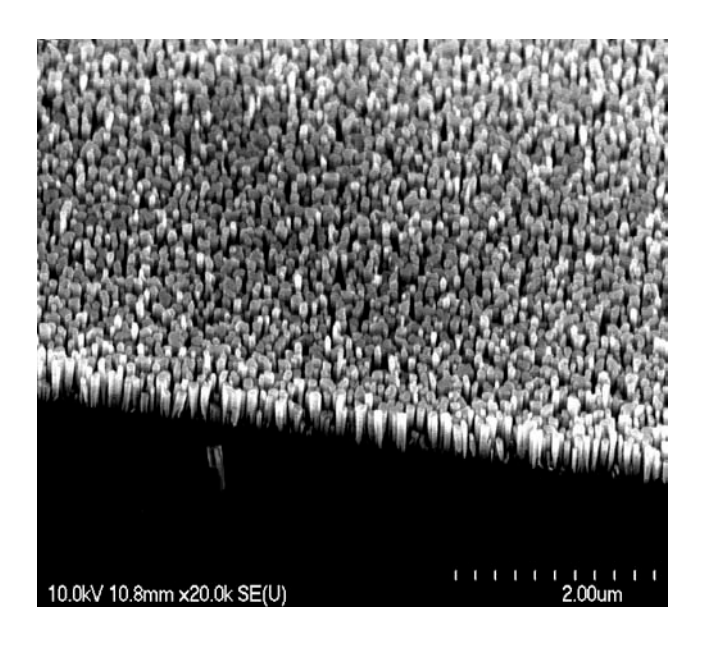


Figure 2.12: The scanning electron microscopy (SEM) image of InGaN/GaN nanowire heterostructures on Si(111).

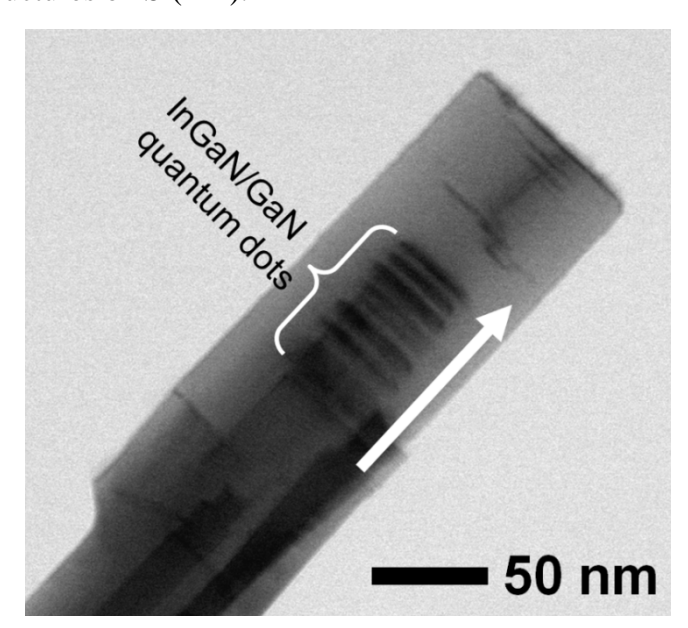


Figure 2.13: A low magnification bright field scanning transmission electron microscopy image showing the position and vertical alignment of the InGaN dots in a GaN nanowire.

Shown in figure 2.14, the photoluminescence spectra of InGaN/GaN dot-in-awire heterostructures grown under different conditions are measured at room temperature. Their optical properties are determined by the sizes and compositions of the dots and, to some extent, the wire diameters as well. Consequently, multicolor emission, illustrated in figure 2.14, can be controllably achieved by varying the growth conditions, including the substrate temperature, growth duration, and In/Ga flux ratio. Defect-related yellow luminescence, that is commonly observed in GaN films, is absent in catalyst-free GaN nanowires. Compared to previously reported InGaN/GaN quantum wells [279, 280], InGaN ternary nanowires [17, 115], or InGaN/GaN well/disk-in-a-wire heterostructures [119-121], the use of self-organized quantum dots can enable ultrahigh emission efficiency in the entire visible spectrum, due to the superior three-dimensional carrier confinement and a high degree of tunability offered by the dots [16]. Depending on the dot compositions and sizes, strong photoluminescence emission in the green (dashed line), yellow (dotted line) and orange (dashed-dotted-line) wavelength range can be obtained from the dot-in-awire heterostructures, shown in figure 2.14. Moreover, intrinsic white light can be achieved by light mixing of the blue, green and red emission from multiple selforganized quantum dots incorporated in single GaN nanowires. This is evidenced by the photoluminescence spectrum (solid line) shown in figure 2.14 for GaN nanowires that incorporate ten vertically aligned InGaN/GaN quantum dots with various In compositions. The emission peak is centered at ~ 545 nm and spans nearly the entire visible wavelength range.

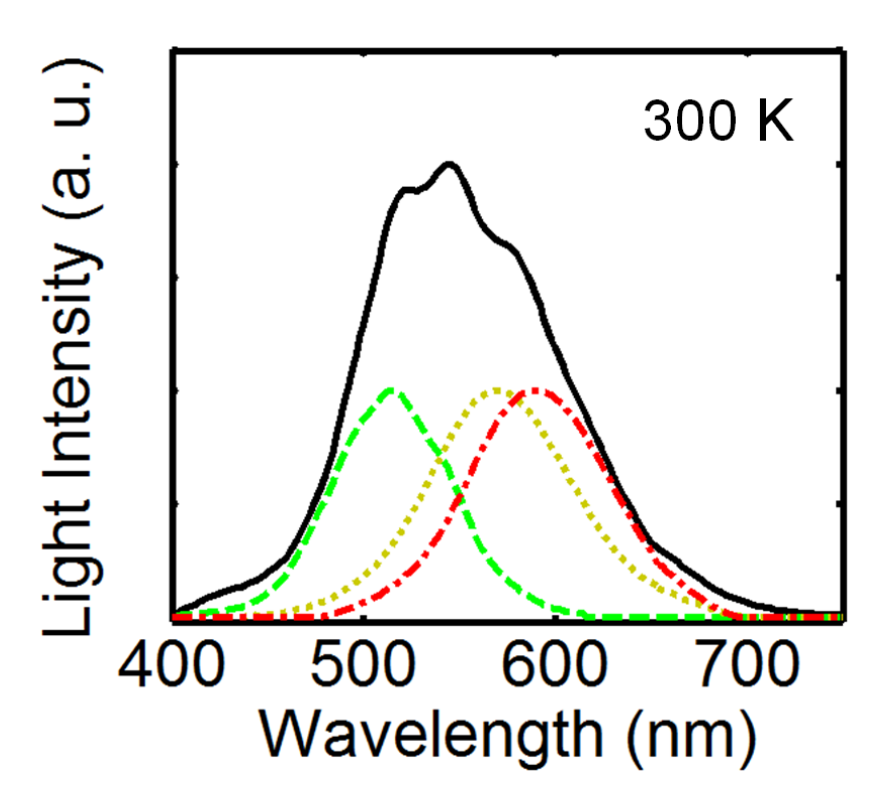


Figure 2.14: Room temperature photoluminescence spectra of various InGaN/GaN dot-in-a-wire heterostructures grown on Si(111). The green, yellow and orange emission spectra from the dot-in-a-wire heterostructures were grown under different conditions.

Luminescence emission from the GaN nanowires can also be observed as shown in figure 2.15. Their intensity, however, is significantly smaller than that of the InGaN quantum dots, in spite of the thick GaN segments surrounding the dot layers. This further confirms the excellent optical quality of InGaN quantum dots. Moreover, the peak positions of the InGaN quantum dot emission are nearly power independent, which suggests the presence of a very small quantum-confined Start effect due to the much reduced polarization fields in the wires associated with the reduced strain field.

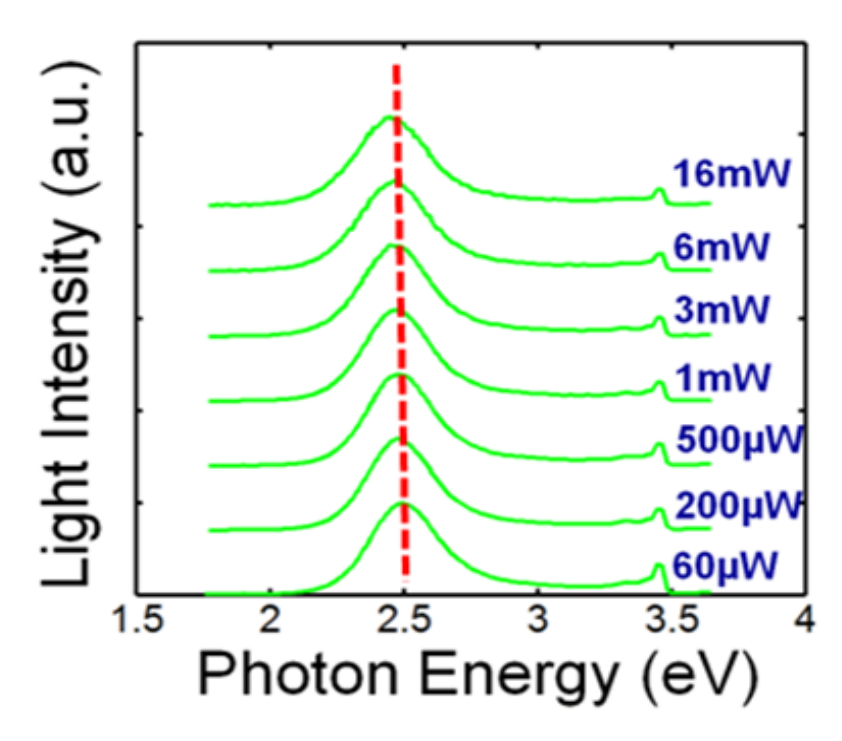


Figure 2.15: Room temperature photoluminescence spectra of the InGaN/GaN dot-in-a-wire sample measured under different optical power excitations from 60 μW to 16 mW.

We have further studied the internal quantum efficiency of the InGaN/GaN dotin-a-wire heterostructure under optical injection (λ = 405 nm). In this experiment, the room-temperature internal quantum efficiency, relative to that at 5 K, is derived by comparing the light intensity measured at these temperatures under the same optical injection power, assuming that the internal quantum efficiency at 5 K is ~ 100%. As shown in figure 2.16, a relatively high internal quantum efficiency of ~ 22% was measured for the ten InGaN/GaN quantum dots embedded in GaN nanowire samples. These values are significantly higher than the internal quantum efficiencies of previously reported nanowire LEDs with emission in the green or longer wavelength range [17, 281].

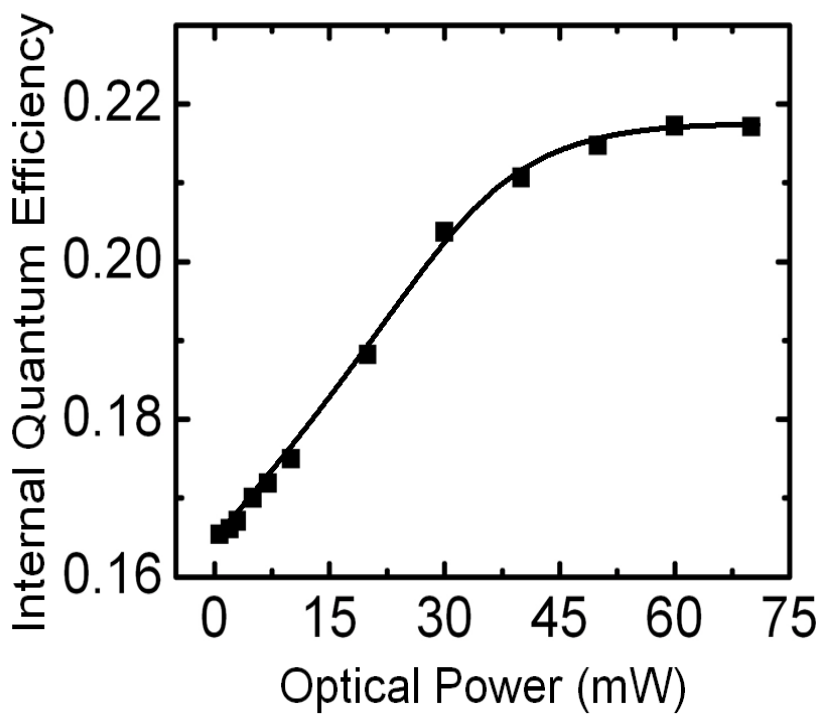


Figure 2.16: Room temperature internal quantum efficiency of the InGaN/GaN dotin-a-wire measured under optical injection condition ($\lambda \sim 405$ nm).

2.6 Conclusion

In this chapter, an overview of the growth/synthesis and properties of III-nitride nanowires, including InN and GaN nanowires are first presented. We then describe the MBE growth and characteristics of high quality, nontapered InN nanowires with the use of an *in situ* deposited In seeding layer prior to growth initiation. In addition, we have achieved catalyst-free InGaN/GaN dot-in-a-wire nanoscale heterostructures on Si(111) substrates. Their structural and optical properties can be controlled by varying the growth conditions in a single epitaxial step. Such novel nanoscale heterostructures provide the basic building blocks for the realization of a host of high performance optoelectronic devices, including LEDs and solar cells, which are described in the following chapters.

Chapter 3: Full-Color InGaN/GaN Dot-in-a-Wire Light Emitting Diodes on Silicon

3.1 Introduction

GaN-based nanowire light emitting diodes (LEDs), with emission wavelengths in the green, yellow, and red spectral region have been intensively investigated for applications in future phosphor-free solid state lighting and full-color displays. Compared to conventional InGaN/GaN quantum well LEDs, the use of nanowire heterostructures offers many distinct advantages, including drastically reduced dislocation densities and polarization fields in the device active region, thereby promising high efficiency LEDs with emission color in the green, yellow, and red wavelength range. Additionally, the use of nanowires can significantly enhance the light extraction efficiency and offers the compatibility with low-cost, large-area Si substrates [15, 115, 119, 176, 269, 282, 283].

GaN-based nanowire LEDs can be fabricated by using either top-down [4] or bottom-up approach [120] as discussed in Chapters 1 and 2. In the commonly reported III-nitride nanowire LEDs, the device active regions often consist of well-in-a-wire [120, 284] heterostructures or ternary InGaN wires [17, 281]. The internal quantum efficiency of such devices, however, may be severely limited by nonradiative carrier recombination on the nanowire surfaces [285, 286], due to the lack of effective lateral confinement [285, 287]. Additionally, with the formation of In-rich nanoclusters, a precise control of the emission wavelength is often difficult to realize. To improve the performance of nanowire LEDs, we have recently developed InGaN/GaN dot-in-a-wire nanoscale heterostructures, which provide superior three-dimensional carrier confinement [16]. Moreover, controlled emission can be realized by varying the compositions and/or the sizes of the dots.

3.2 High Efficiency InGaN/GaN Dot-in-a-Wire Red Light Emitting Diodes

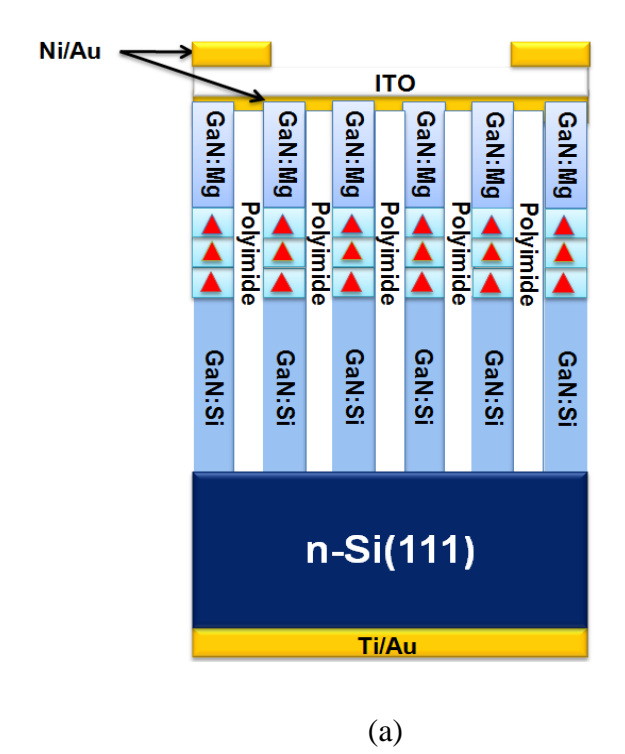
High performance GaN-based light emitting diodes (LEDs), with emission wavelengths in the red spectral range, are essentially required for future phosphorfree solid state lighting and full color displays. The achievement of these devices, however, has been severely limited by the large lattice mismatch (~ 11%) between InN and GaN and the resulting large polarization fields and dislocation densities in the LED heterostructures [288-290]. Moreover, conventional InGaN quantum well LEDs suffer from efficiency degradation at relatively high injection current levels [291, 292]. With the presence of polarization fields and the associated quantumconfined Stark effect (QCSE), emission characteristics of these devices also vary considerably with injection current. To date, the realization of III-nitride-based red LEDs largely rely on the conversion of photons emitted from a high power UV/blue LED using molybdate phosphors such as Na₅Eu(MoO₄)₄ or NaEu(MoO₄)₂ [293] and red-emitting (CdSe)ZnSe or CdSe/ZnS quantum dots [294, 295]. Recently, GaNbased red-emitting LEDs with the use of europium (Eu) doping have also been reported [296, 297]. Such LEDs generally exhibit very low efficiency and/or poor reliability [298]. It is therefore imperative to develop innovative solutions in order to achieve high performance red LEDs.

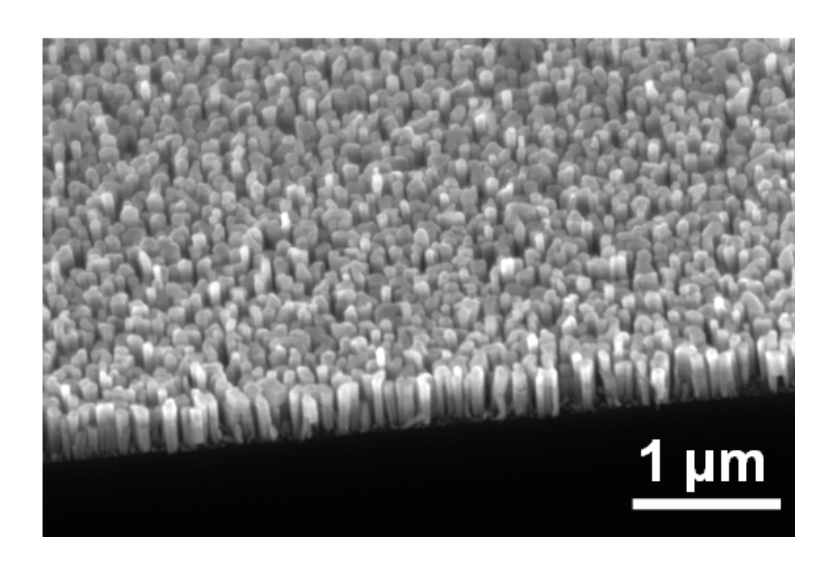
In this regard, significant progress has been made in InGaN/GaN nanowire heterostructures with tunable luminescence emission being realized using core/shell [299], well/disk-in-a-wire [120, 300], as well as InGaN ternary nanowire heterostructures [17, 301]. The realization of red emission from GaN-based nanowire and quantum dot heterostructures has been reported [152, 302, 303]. However, a critical challenge for achieving high efficiency nanowire devices lies in the presence of extensive charged surface states and/or surface defects, which generally result in Femi-level pining and energy band bending at the wire lateral surfaces [304-306]. It is expected that nanowire LEDs with significantly improved performance can be realized by utilizing InGaN/GaN dot-in-a-wire heterostructures, due to the superior three-dimensional carrier confinement provided by the dots [16]. We have therefore investigated the MBE growth, fabrication and characterization of high efficiency red-

emitting LEDs on Si(111) substrates with the incorporation of such nanoscale heterostructures [307]. The devices exhibit relatively high internal quantum efficiency (IQE ~32.2%) under electrical injection, which is derived by assuming the maximum IQE measured at 5 K is ~ 100%. Moreover, no efficiency droop was observed for injection current up to ~ 480 A/cm². We have also demonstrated that, by controlling the inhomogeneous broadening for the dot-in-a-wire heterostructures, the devices can exhibit stable emission characteristics with increasing current.

3.2.1 Molecular Beam Epitaxial Growth and Characterization of InGaN/GaN Dot-in-a-Wire Red LEDs

The InGaN/GaN dot-in-a-wire LED heterostructures, illustrated in figure 3.1(a), were grown on n-type Si(111) substrates under nitrogen rich conditions using a Veeco Gen II MBE system equipped with a RF plasma-assisted nitrogen source. The n- and p-type GaN nanowires were doped with Si and Mg, respectively. The growth conditions for GaN nanowires include growth temperatures of ~ 700 to 750 °C, a nitrogen flow rate of 1-2 sccm, and a forward plasma power of ~ 400 W. The device active region consists of three vertically aligned InGaN dots, separated by 5 nm GaN barrier layers. Described in Chapter 2, we have demonstrated that, by varying the growth conditions, emission wavelengths of the InGaN/GaN dot-in-a-wire heterostructures can be tuned across nearly the entire visible wavelength range. In this experiment, the InGaN/GaN quantum dot heterostructures were grown at relatively low temperatures (535 to 550 °C) to enhance In incorporation. A 45 degree-tilted scanning electron microscopy (SEM) image is illustrated in figure 3.1(b). The wire areal density is in the range of $\sim 1\times10^{10}$ cm⁻².





(b)

Figure 3.1: (a) Schematic illustration of InGaN/GaN dot-in-a-wire LED heterostructures. (b) A 45 degree tilted SEM image showing the morphology of the InGaN/GaN dot-in-a-wire heterostructures grown on a Si(111) substrate.

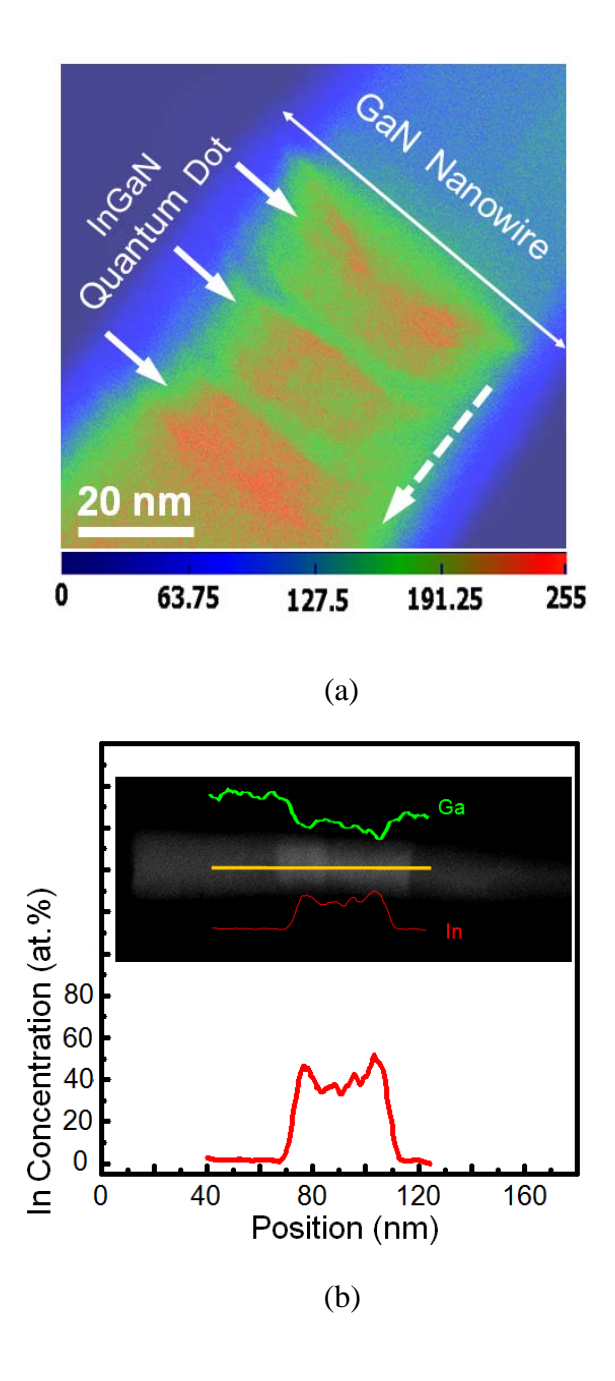


Figure 3.2: (a) HAADF image in pseudo-color scale showing the alignment of three InGaN quantum dots in a GaN nanowire. The solid arrows point out the location of three dots and the dashed arrow indicates the growth direction. The pseudo-color scale bar shows the intensity for each color in the image. (b) HAADF images and EDXS analysis of the In composition in the InGaN dots. The inset shows the HAADF image and EDXS signal variations of Ga and In along the yellow line.

The InGaN quantum dots in a GaN nanowire structure are revealed by the atomic number contrast in the high angle annular dark field (HAADF) transmission electron microscopy (TEM) image, shown in figure 3.2(a). Three InGaN quantum dots are observed in the area with relatively higher intensity (green and red regions), which are pointed out by the solid arrows. These dots are aligned along the growth direction, indicated by the dashed arrow in the GaN nanowire. The dot heights and widths are estimated to be in the ranges of 12 to 15 nm and 30 to 40 nm, respectively. Illustrated in figure 3.2(b), the In content in the InGaN quantum dot is analyzed by the energy dispersive x-ray spectrometry (EDXS) and the In peak corresponds to ~ 55% In content in the dot.

3.2.2 LED Fabrication Process

During the device fabrication process, a polyimide (PI) resist layer was spin-coated to fully cover the GaN nanowires for surface passivation and planarization. Then, reactive-ion etching (RIE) using O2 gas was applied on the sample until the topsection of the nanowires was revealed. The sample was subsequently patterned into cells of various sizes by standard photolithography. p- and n-metal contacts on the nanowire surface and backside of the Si substrate were deposited by e-beam evaporator technique. The p-metal and n-metal contacts consist Ni(5nm)/Au(7nm)/ITO(200nm) and Ti(20nm)/Au(120nm) layers, respectively. To alleviate the hole transport problem, metallic contact grids, illustrated in figure 3.3, were made on the device surface. The fabricated devices with Ni/Au and Ti/Au metal contacts were first annealed at ~ 500 °C for 1 minute in nitrogen ambient. After the deposition of the ITO transparent contact, a second annealing step was performed at 300°C in vacuum for ~ 1 hour. Figure 3.3 shows the fabricated devices with different sizes, including $1\times1 \text{ mm}^2$, $0.5\times0.5 \text{ mm}^2$, $0.3\times0.3 \text{ mm}^2$, and $0.1\times0.1 \text{ mm}^2$.

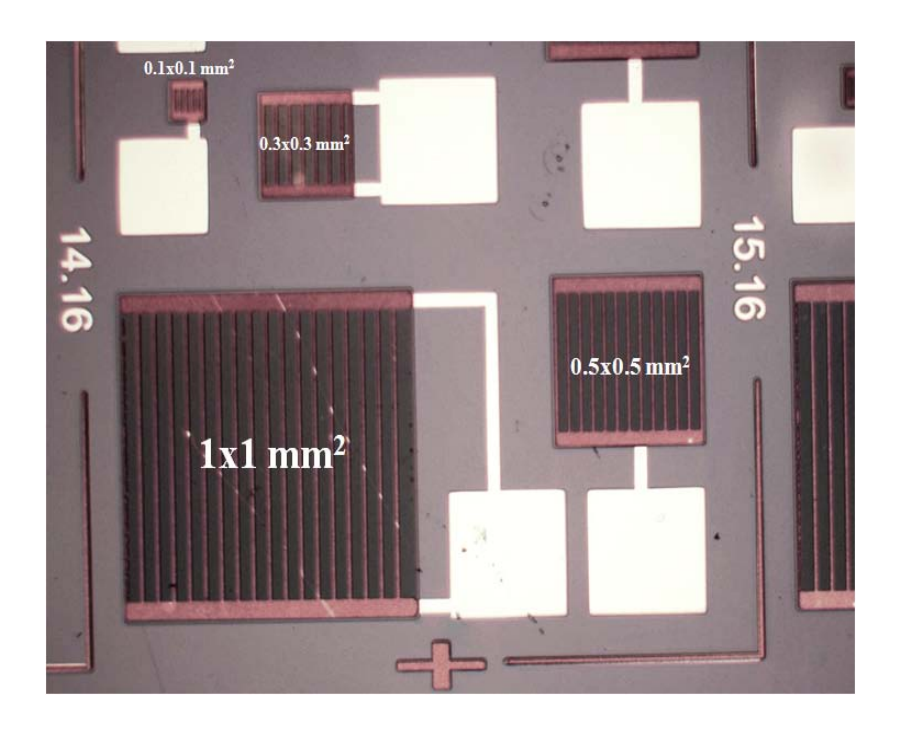


Figure 3.3: Fabricated devices with different sizes $(1\times1~\text{mm}^2, 0.5\times0.5~\text{mm}^2, 0.3\times0.3~\text{mm}^2)$, and $0.1\times0.1~\text{mm}^2$) and the use of metallic contact grid pattern for current spreading.

3.2.3 Device Characterization and Results Analysis

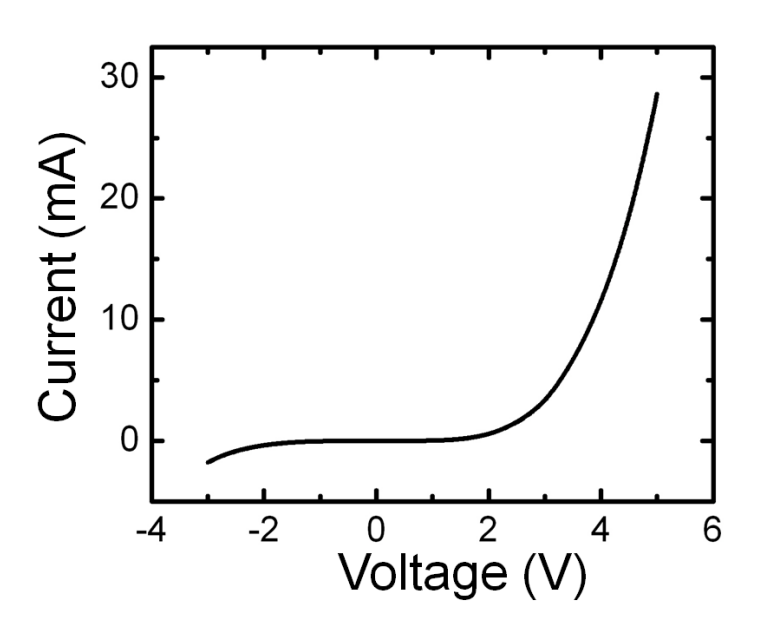


Figure 3.4: Current-voltage characteristics of InGaN/GaN dot-in-a-wire LED devices.

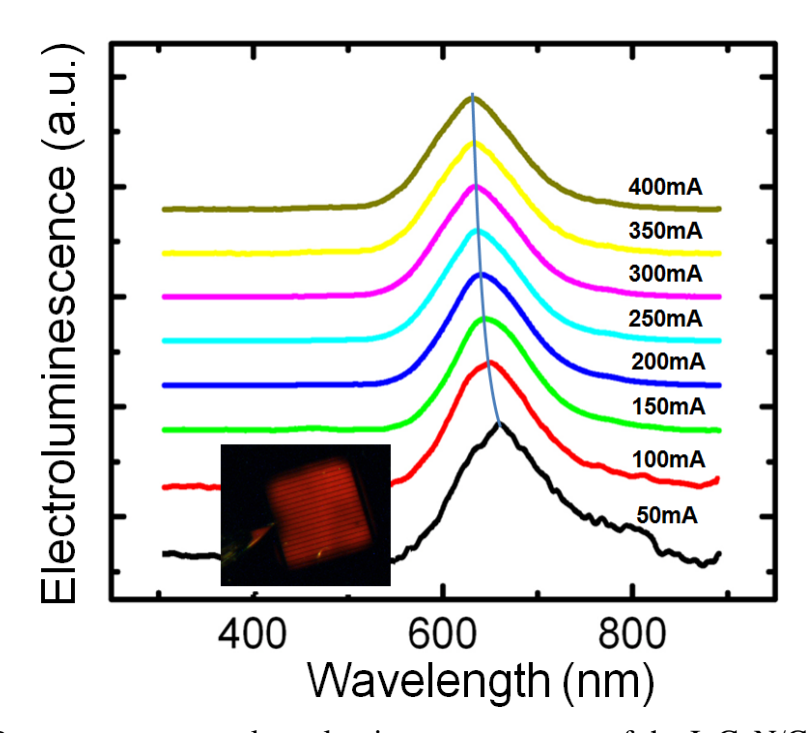


Figure 3.5: Room temperature electroluminescence spectra of the InGaN/GaN dot-in-a-wire LED measured under various injection currents. Optical image of the red LED device under 100 mA injection current is shown in the inset.

Variations of the spectral linewidths and peak emission wavelengths are further shown in figure 3.6. It is seen that, with increasing current, there is a considerable blueshift, accompanied by a small broadening of the spectral linewidth. The peak wavelength shifts to ~ 633 nm and the spectral linewidth broadens to ~ 102 nm when measured at ~ 400 mA. The relatively large blueshift with current is explained by the presence of polarization fields and the associated QCSE, due to the relatively high indium compositions in the red-emitting InGaN/GaN quantum dots. Additionally, the blueshift may be partly explained by the nonuniform turn-on voltage for each nanowire emitter, with lower turn-on voltages expected for nanowires with higher In compositions (longer emission wavelengths).

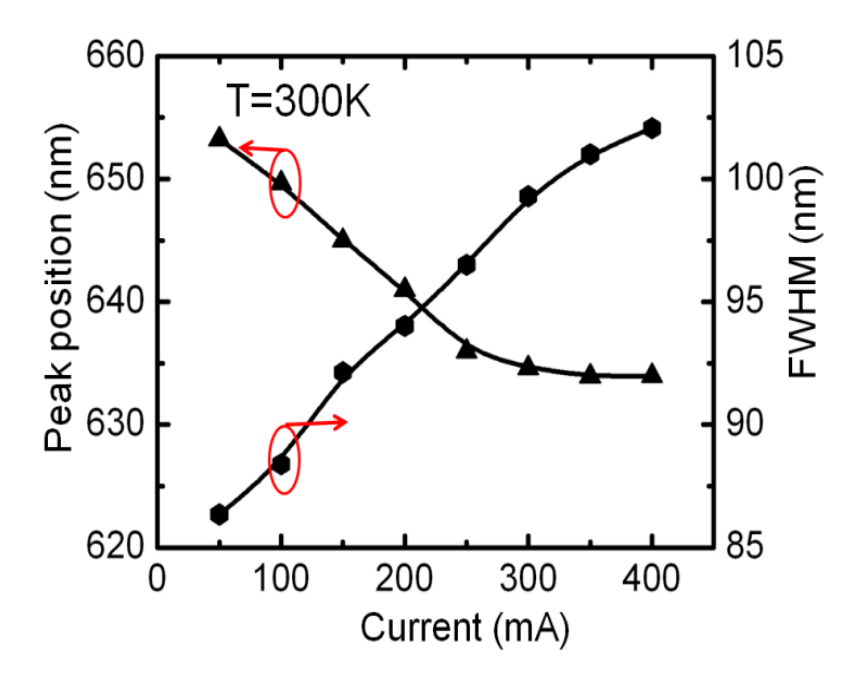


Figure 3.6: Variations of the peak wavelength and spectral linewidth measured under different injection currents.

The LED IQE was measured by comparing the relative external quantum efficiency derived at room temperature to the maximum value measured at 5 K at the same current. In this analysis, it is assumed that the maximum IQE at 5 K is approximately unity. Illustrated in figure 3.7, the LED IQE increases drastically with injection current. For injection current densities of > 300 mA, a relatively high IQE of $\sim 32.2\%$ was recorded. Under optical pumping ($\lambda = 405$ nm), the devices exhibit an IQE of $\sim 18.6\%$, shown in the inset of figure 3.7. The relatively high efficiency is

attributed to the superior three-dimensional carrier confinement provided by the dotin-a-wire nanoscale heterostructures. For comparison, there have been no reports on the IQE of GaN-based red-emitting LEDs to date, to the best of our knowledge.

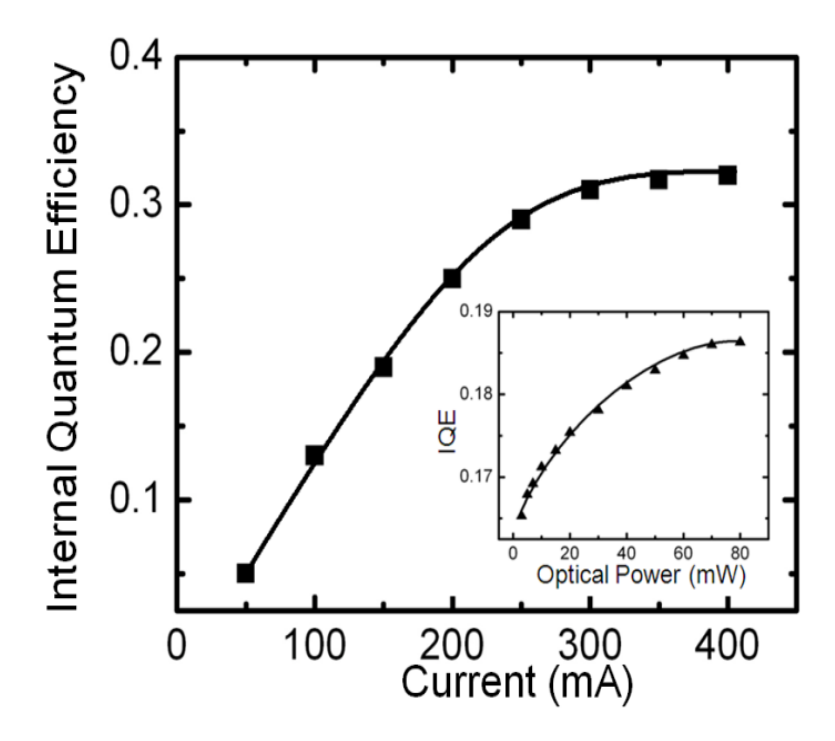


Figure 3.7: Room temperature IQE of the InGaN/GaN dot-in-a-wire red LED versus injection current. The inset shows the IQE of the red LED device under optical excitation ($\lambda \sim 405$ nm).

For practical applications, LEDs with stable emission characteristics, *i.e.* nearly invariant peak wavelength and spectral linewidth with current, are highly desired. In this regard, we have investigated the effect of inhomogeneous broadening on the output characteristics of red-emitting nanowire LEDs. Emission spectra of the dot-in-a-wire heterostructures depend critically on the size and composition of the dots as well as the diameter of the wires. When grown at relatively high temperatures, InGaN dots are characterized by the presence of various In-rich nanoclusters, due to the enhanced In phase separation, which lead to a significantly increased inhomogeneous broadening [16]. Such red-emitting dot-in-a-wire LEDs were fabricated and characterized. Illustrated in figure 3.8 is the electroluminescence spectra measured

under injection currents up to 1.2 A (~ 480 A/cm²) at room temperature. In spite of the significantly increased linewidth, a large part of the emission spectra are still in the red wavelength range. Variations of the spectral linewidth and peak wavelength with current are shown in figure 3.9. It is evident that the resulting output characteristics, in terms of both the peak position and spectral linewidth, are significantly more stable, compared to the LEDs with a smaller inhomogeneous broadening.

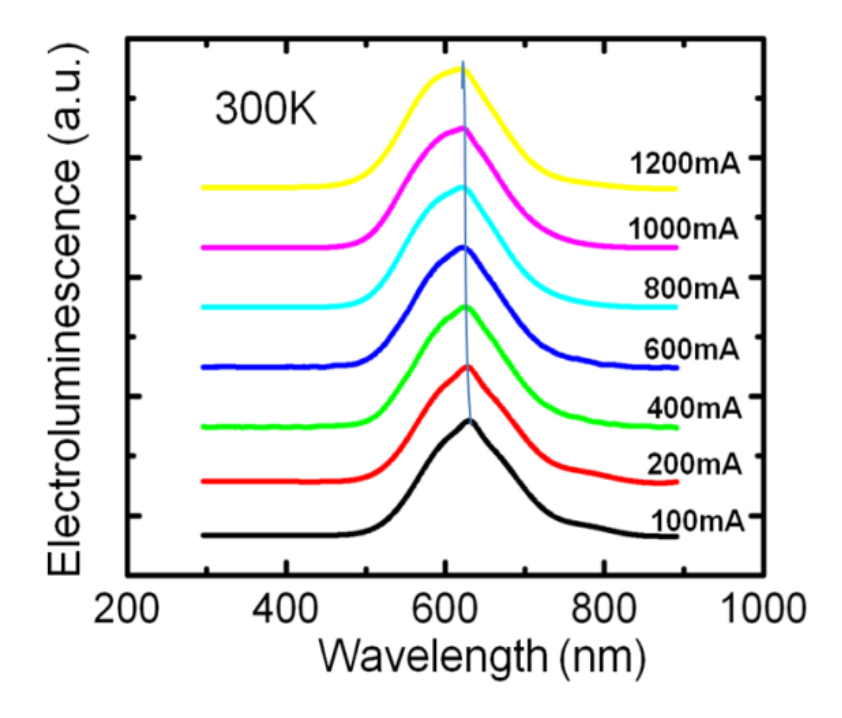


Figure 3.8: Room temperature electroluminescence spectra measured under different injection currents up to 1.2 A ($\sim 480 \text{ A/cm}^2$) for the 2nd red-emitting LED device with enhanced inhomogeneous broadening.

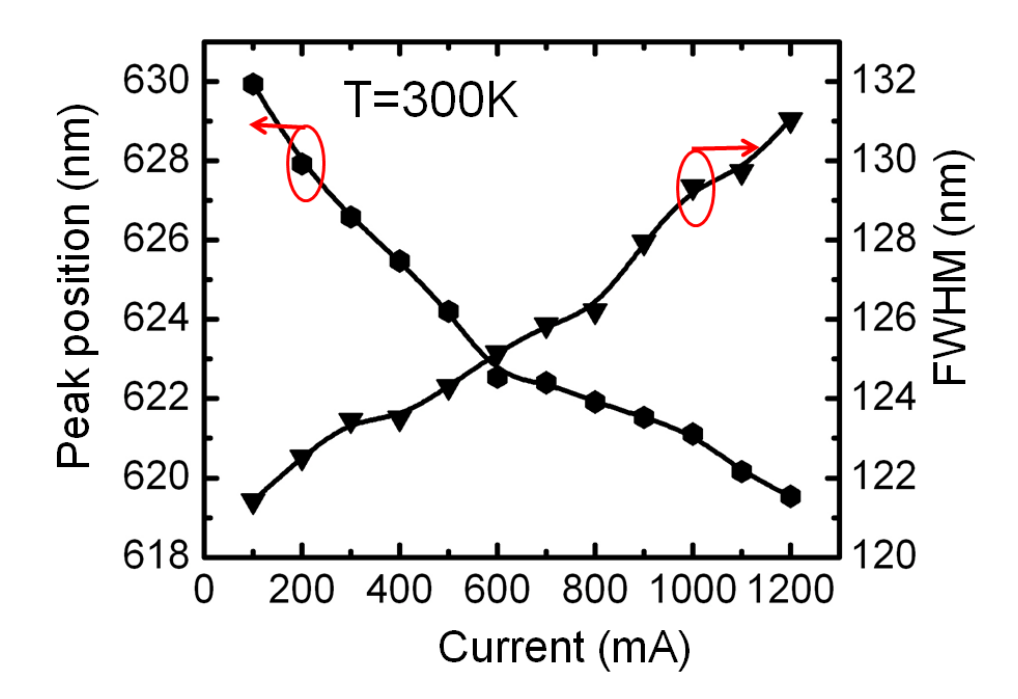


Figure 3.9: Variations of the peak wavelength and spectral linewidth with injection current measured for the 2nd red-emitting LED device with enhanced inhomogeneous broadening.

Emission characteristics of these devices are further depicted in the CIE chromaticity diagram, illustrated in figure 3.10. The CIE chromaticity diagram is the 1931 Commission International de l'Eclairage chromaticity diagrams which determine the emission properties of the LED devices by using color matching function and the chromaticity diagram. The CIE coordinates, x and y are calculated from the tristimulus values X, Y, Z as shown below:

$$\chi = \frac{X}{X + Y + Z} \tag{3.1}$$

$$y = \frac{Y}{X + Y + Z} \tag{3.2}$$

$$z = \frac{z}{x + y + z} = 1 - x - y \tag{3.3}$$

where X, Y, and Z are related to the color matching functions corresponding to the eye sensitivity curves of the red, green, and blue cones, respectively.

$$X = \int_0^\infty I(\lambda)\bar{x}(\lambda)d\lambda \tag{3.4}$$

$$Y = \int_0^\infty I(\lambda)\bar{y}(\lambda)d\lambda \tag{3.5}$$

$$Z = \int_0^\infty I(\lambda)\bar{z}(\lambda)d\lambda \tag{3.6}$$

It is seen that significantly improved emission stability is achieved at much higher injection levels for the 2^{nd} LED device.

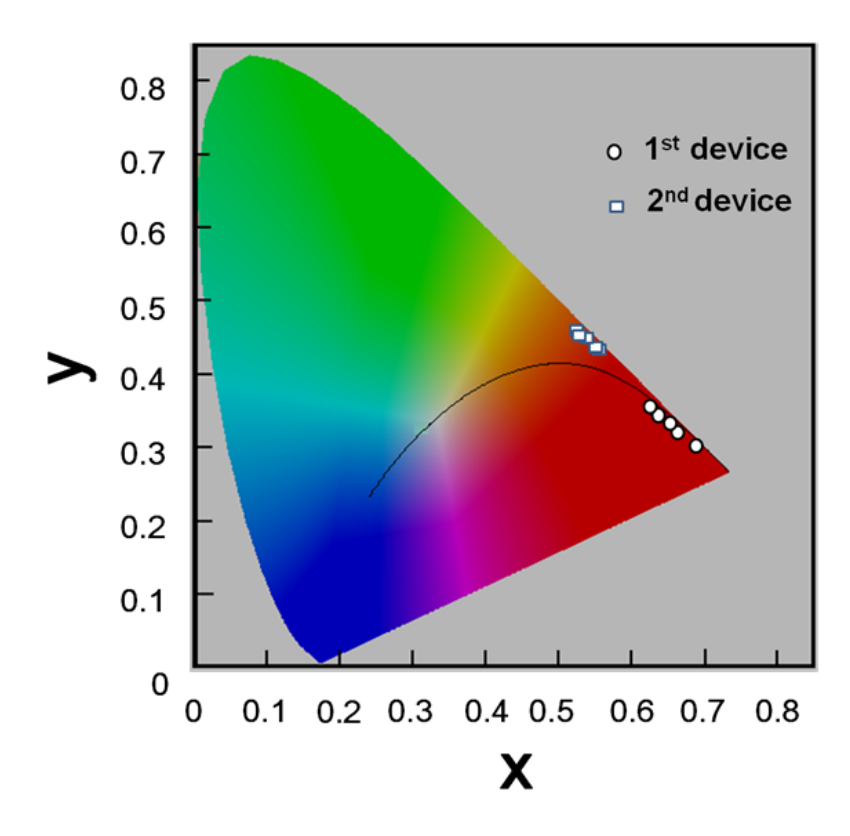


Figure 3.10: CIE chromaticity coordinates for red InGaN/GaN dot-in-a-wire LED devices with relatively small (1st device) and large (2nd device) inhomogeneous broadening. The current was varied from 100 to 300 mA for the 1st device (dots) and from 400 to 1,200 mA for the 2nd device (squares).

We have further studied variations of the external quantum efficiency with injection current at room temperature. Illustrated in figure 3.11, the external quantum efficiency first shows an increasing trend and then stays nearly constant with injection current. No efficiency droop was observed for injection current density as high as ~ 480 A/cm² at room temperature, in spite of the presence of polarization field. This observation suggests that polarization may not be the primary mechanism responsible for the efficiency degradation in GaN-based LEDs, which agrees with recent study on the predominant effect of hot electron and the associated carrier overflow on efficiency droop in InGaN LEDs [308]. Compared to conventional InGaN/GaN quantum well LED heterostructures, the present dot-in-a-wire devices employ relatively thick (~ 12 nm) InGaN dots, which can increase electron injection efficiency by minimizing hot carrier effect and the associated ballistic or quasiballistic transport [308]. Moreover, due to In segregation, the thin (~ 5 nm) barriers consist of InGaN instead of GaN. The reduced energy barrier can further enhance the hole injection process and reduce electron overflow. Consequently, efficiency degradation can be minimized at high injection levels.

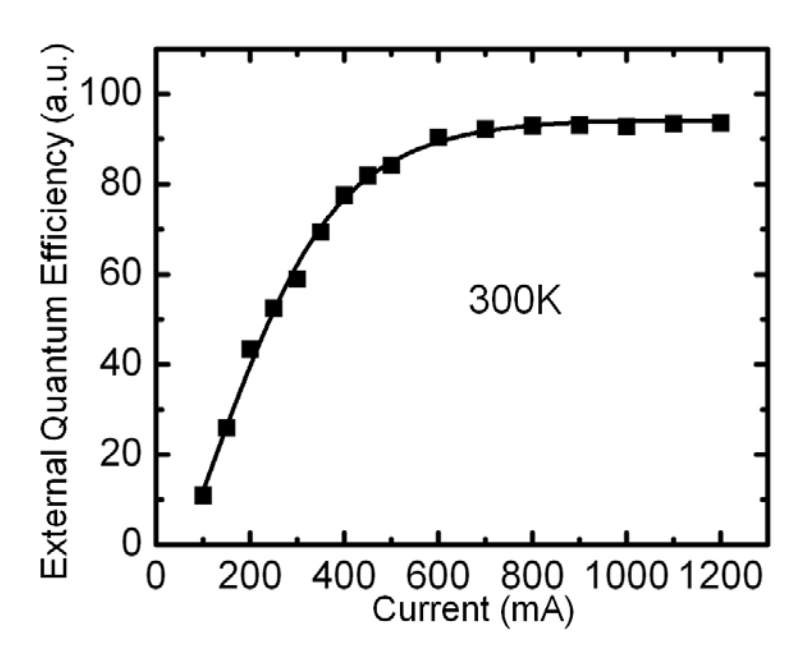


Figure 3.11: Variations of the relative external quantum efficiency versus injection current for the InGaN/GaN red-emitting dot-in-a-wire LED measured at room temperature.

3.3 Full-Color InGaN/GaN Dot-in-a-Wire LEDs on Silicon

With the achievement of red-emitting nanowire LEDs, it is possible to demonstrate phosphor-free white-light LEDs by using the novel InGaN/GaN dot-in-a-wire nanoscale heterostructures on a Si platform. The design, epitaxial growth, fabrication, and characterization of white-light LEDs are described in this section. We have demonstrated phosphor-free InGaN/GaN dot-in-a-wire white LEDs by incorporating multi-color (blue, green, and red) quantum dots in GaN nanowires. Such devices can exhibit a relatively high room-temperature internal quantum efficiency of ~ 22% - 37% of that measured at 5 K and negligible efficiency degradation for injection currents up to ~ 200 A/cm². The strong white light emission is a direct consequence of the large inhomogeneous broadening of the InGaN/GaN quantum dots, due to the variations of In compositions in the dot layers, which are measured to be in the range of 10% to 50%. The emission characteristics of nanowire LEDs in the green and yellow wavelength range are also briefly described.

3.3.1 Design and MBE Growth of InGaN/GaN Dot-in-a-Wire White-Light LEDs

In this experiment, self-organized InGaN/GaN dot-in-a-wire LED heterostructures, with the incorporation of 10 InGaN/GaN vertically coupled quantum dots in the active region, were grown on n-type Si(111) substrates under nitrogen rich condition. The device heterostructures consist of $\sim 0.4~\mu m$ GaN:Si, ten vertically coupled InGaN/GaN dots, and $\sim 0.2~\mu m$ GaN:Mg sections. GaN nanowires were grown at $\sim 750~\rm ^{\circ}C$. During the growth process, the nitrogen flow rate was kept at $\sim 1-2~\rm sccm$, with a forward power of $\sim 400~\rm W$. Figure 3.12 shows the scanning electron microscopy image of typical InGaN/GaN dot-in-a-wire heterostructures grown on Si(111). The nanowires are vertically aligned to the substrate, with the wire diameters and densities in the range of 30 to 100 nm and $\sim 1\times10^{10}~\rm cm^{-2}$, respectively. The InGaN/GaN quantum dot active regions were grown at temperatures of $\sim 550~\rm -600~\rm ^{\circ}C$). For comparison, the InGaN quantum dots in red LED structures, described in Sec. 3.1, were grown at lower temperatures ($< 550~\rm ^{\circ}C$) to enhance the In content in the InGaN dots. However, the emission characteristic of device with high In content

is not stable due to the larger polarization fields and the associated QCSE, as described in Sec. 3.2. For the white-light LED heterostructures, the InGaN/GaN quantum dots were grown at higher substrate temperatures to improve the crystalline quality and to reduce the polarization fields and QCSE. Each quantum dot consists of ~ 3 nm InGaN, which is subsequently capped by ~ 3 nm GaN. Structural properties of the InGaN/GaN dot-in-a-wire heterostructures were characterized by scanning transmission electron microscopy (STEM). Detailed growth mechanism and structural characterizations can be found in Sec. 2.3.

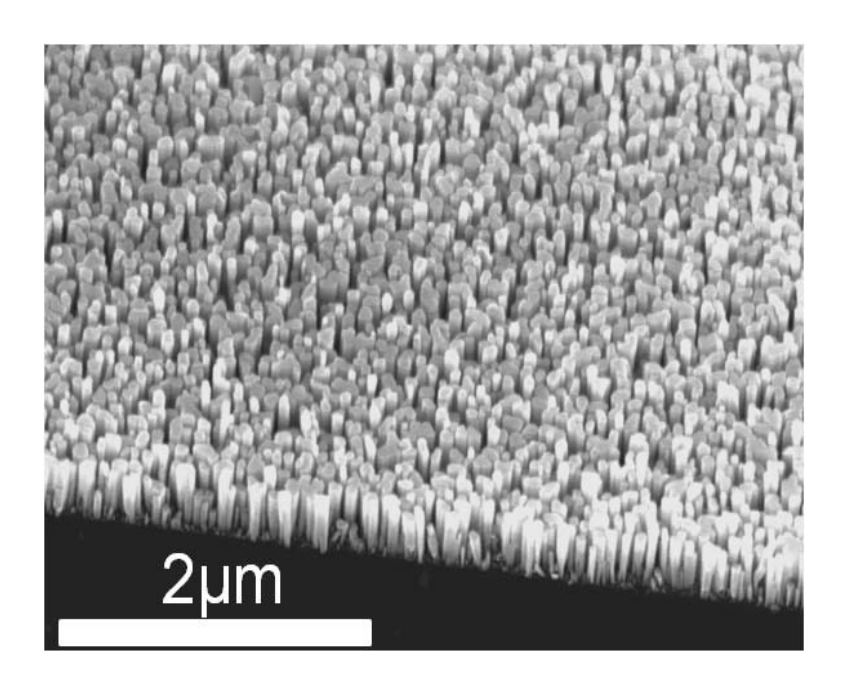


Figure 3.12: A 45 degree tilted scanning electron microscopy image of the InGaN/GaN dot-in-a-wire heterostructures grown on a Si(111) substrate by molecular beam epitaxy.

In order to gain a better understanding of the growth and emission mechanisms, STEM imaging and spectrum imaging were performed on a single nanowire to investigate the structural properties of the InGaN/GaN dot-in-a-wire heterostructures. A HAADF image showing the atomic number contrast is illustrated in figure 3.13. The intensity at each pixel is presented as a pseudo-color display in order to highlight the changes in intensity quantitatively. The InGaN dots are located at the regions with

relatively high intensity (red, yellow and white on the color scale), since the average atomic number in the dot region is larger than that in GaN barriers. Importantly, no extending defects such as dislocations or stacking faults are observed in the InGaN/GaN quantum dot active region.

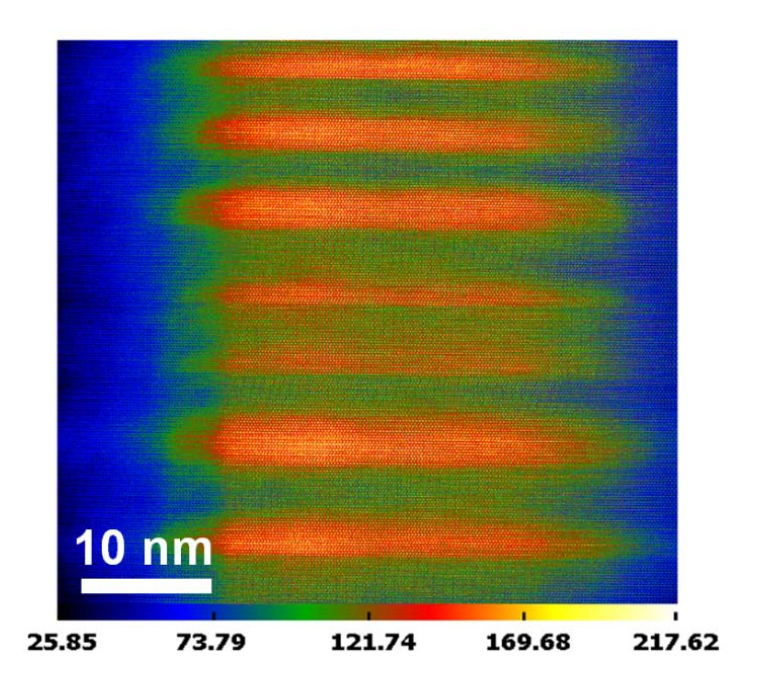


Figure 3.13: A high-resolution HAADF image in a pseudo-color display showing the atomic number contrast between InGaN dots and GaN barriers.

In order to study the elemental distribution in the InGaN dots, energy dispersive X-ray spectrometry spectrum image (EDXS-SI) was performed across the centers of InGaN/GaN quantum dots. From the qualitative variation of the In L_{α} and Ga K_{α} signals shown in the inset of figure 3.14, an In-rich or Ga-deficient region is observed in the InGaN dots. Using the Ga signal from the top GaN capping region as a built-in reference, the In concentration in each $In_xGa_{1-x}N$ dot is quantified and shown as the line profile in figure 3.14. The In composition (x) in each dot is not uniform, and it varies from ~ 10 to 50 atomic percent. Although these values are based on the through-thickness averaging, the compositional variation of the dots is consistent with the large inhomogeneous broadening observed in the photoluminescence spectra (figure 2.14). Since the sub-nm spatial resolution EDXS conditions were used, it may

also be noticed both from the HAADF images and the EDXS data that the barrier layers contain a small percentage of In, due to In segregation, thereby leading to the unique dot-in-a-wire core-shell nanoscale heterostructures.

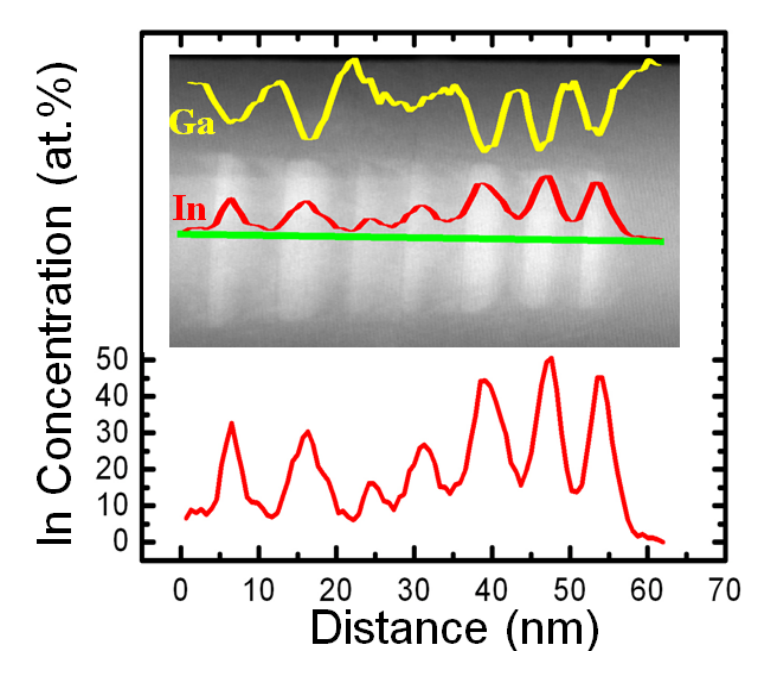


Figure 3.14: An energy dispersive X-ray spectrometry spectrum image showing the quantitative variation of In along the centers of seven InGaN dots. The inset shows the qualitative In and Ga signal variation along the green line.

Besides the EDXS analysis, an electron energy loss spectrometry spectrum image (EELS-SI) was taken along the lateral direction (indicated by the green line) of an individual InGaN dot, illustrated in the inset of figure 3.15. The line profile of the integrated intensity for In $M_{4,5}$ and Ga $L_{2,3}$ edge are also depicted, and a drop/increase of the Ga and In signal is observed in the dot region. The diameter of the dot is estimated to be ~ 40 nm based on the In profile. Consequently, the InGaN/GaN quantum dots are completely embedded in the center region of the wires, leading to superior three-dimensional carrier confinement that was not possible in any previously reported GaN-based nanowire heterostructures [17, 120, 281, 284, 309]. It is also important to notice that the InGaN dots are nearly perfectly aligned along the growth direction, due to strain-induced self-organization.

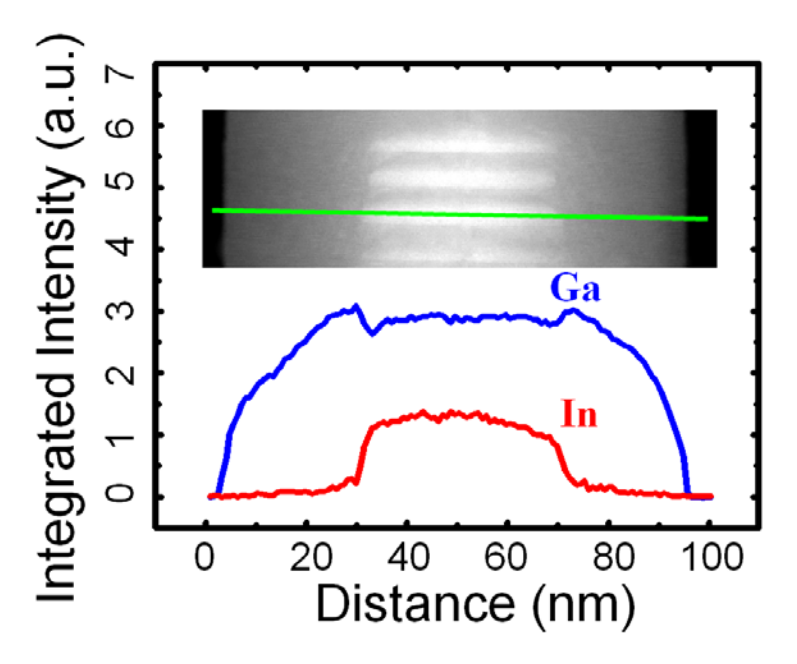


Figure 3.15: An electron energy loss spectrometry spectrum image showing the integrated In and Ga signal along the lateral direction of GaN nanowire and an InGaN dot. The inset shows the line along which the electron energy loss spectrometry spectrum image is taken.

These LED samples were then fabricated. The device fabrication process for is similar to that for the red LEDs discussed in Sec. 3.1.

3.3.2 Device Characterization and Results Analysis

Optical properties of InGaN/GaN dot-in-a-wire nanoscale heterostructures are investigated using temperature variable photoluminescence spectroscopy. Discussed in Sec. 2.5.2, the emission wavelengths can be readily tuned across nearly the entire visible wavelength range, which is achieved by effectively varying the In content in the quantum dots using different growth temperatures and/or In/Ga flux ratios. Moreover, we have demonstrated strong white emission by incorporating multi-color quantum dots in GaN nanowires, shown as the solid line in figure 2.14, which exhibit a peak wavelength at ~ 545 nm and a broad spectral line width (full width half maximum – FWHM) of ~ 150nm. The white light emission is a direct consequence of the large variations of In compositions (~ 10 % to 50 %) in the dots in single GaN nanowires.

Illustrated in figure 3.16, the fabricated dot-in-a-wire LED devices on silicon exhibit excellent current-voltage characteristics, including relatively low series resistance ($\sim 20-50\Omega$) and negligible leakage current under relatively large reverse bias. Such InGaN/GaN dot-in-a-wire LEDs can exhibit strong emission in the green, yellow, and orange wavelength range, depending on the growth condition. Shown in figure 3.17 are the room temperature electroluminescence spectra of some representative dot-in-a-wire LED devices measured under injection currents of ~ 120 A/cm². The peak emission wavelengths are at 522, 589, and 619 nm, leading to the appearance of green, yellow, and orange emission, respectively. The device areas are ~ 300×300 µm². The corresponding optical images are also shown in the insets of figure 3.17. The different emission wavelengths are due to variations of In compositions in the InGaN/GaN quantum dot layers. Higher In compositions (up to ~ 50%) and, consequently, orange/red emission can be achieved by utilizing relatively low substrate temperature and/or high In/Ga flux ratios during the growth of the quantum dot active regions, described in Sec. 3.1. The use of relatively thin (~ 3 nm) InGaN quantum dots also contribute significantly to the relatively high internal quantum efficiency, due to the reduced strain field and the minimization of dislocation formation.

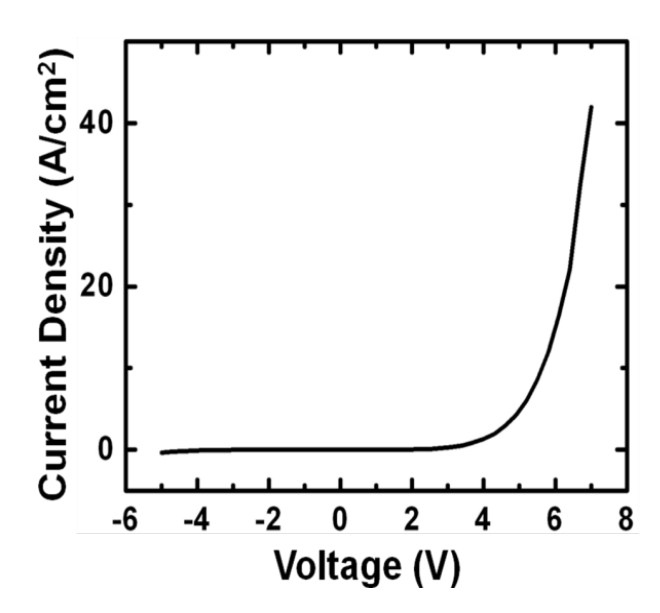


Figure 3.16: Room-temperature current-voltage characteristics of an InGaN/GaN dot-in-a-wire LED on silicon.

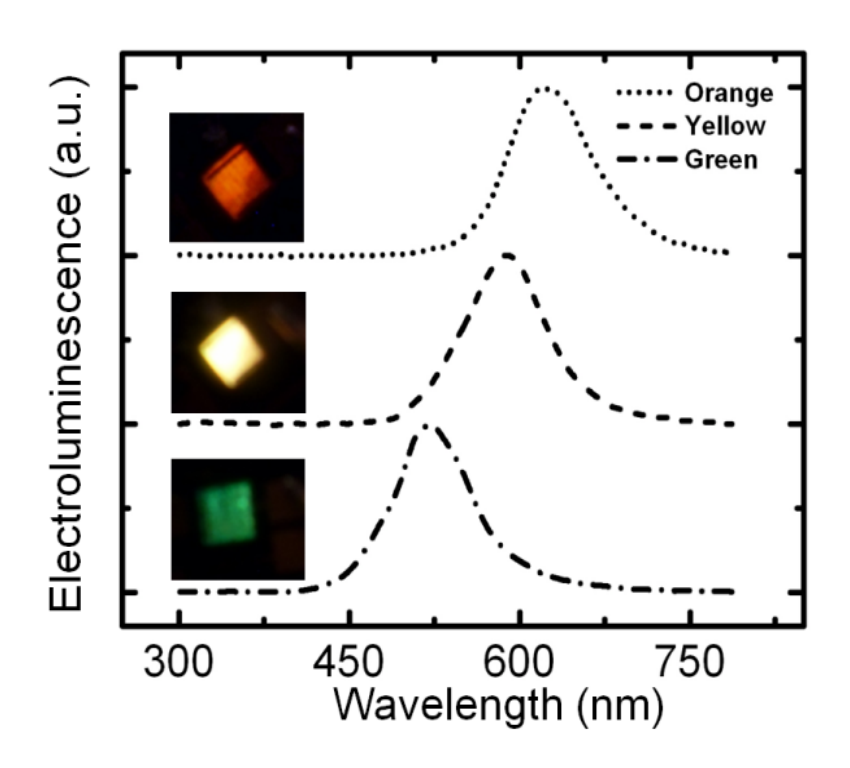


Figure 3.17: Room temperature electroluminescence spectra of green, yellow and orange LED devices measured at 120 A/cm² current injection and the corresponding optical microscopy images (inset).

Variations of the peak emission wavelengths with injection currents are shown in figure 3.18. Relatively small blue shifts of ~ 3.5 nm and 6.4 nm are observed for the green and yellow LEDs for injection currents from 12 A/cm² up to 200 A/cm², respectively. The orange emitting devices, however, exhibit significantly larger blueshift (~ 17.2 nm) in the same current range. The observed blue shifts with increasing current may be explained by the quantum-confined Stark effect [135, 310], which becomes more important in devices with relatively high In compositions.

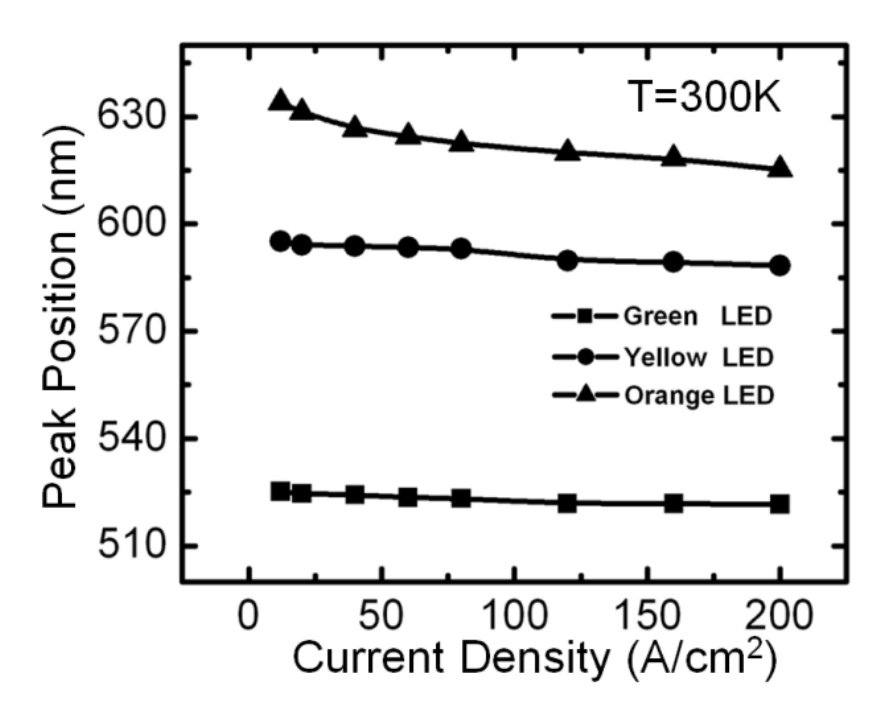


Figure 3.18: Variations of the peak wavelengths of the green (square), yellow (circle), and orange (triangle) InGaN/GaN dot-in-a-wire LEDs with injection current. Blueshifts of ~3.5 nm, 6.4 nm, and 17.2 nm were observed for the green, yellow, and orange LED devices, respectively.

We have further demonstrated phosphor-free white LEDs by incorporating multi-color InGaN quantum dots in single GaN nanowires. Shown in figure 3.19 are the electroluminescence spectra of the white LEDs measured under pulsed bias condition (1% duty cycle) at various injection currents. The emission spectra span from ~430 nm to >700nm, covering nearly the entire visible wavelength range. High brightness emission from the white LED is also displayed in the inset of figure 3.19. A consistent blueshift (up to ~ 8.4 nm) was observed when the injection current was varied from 30 mA to 500 mA.

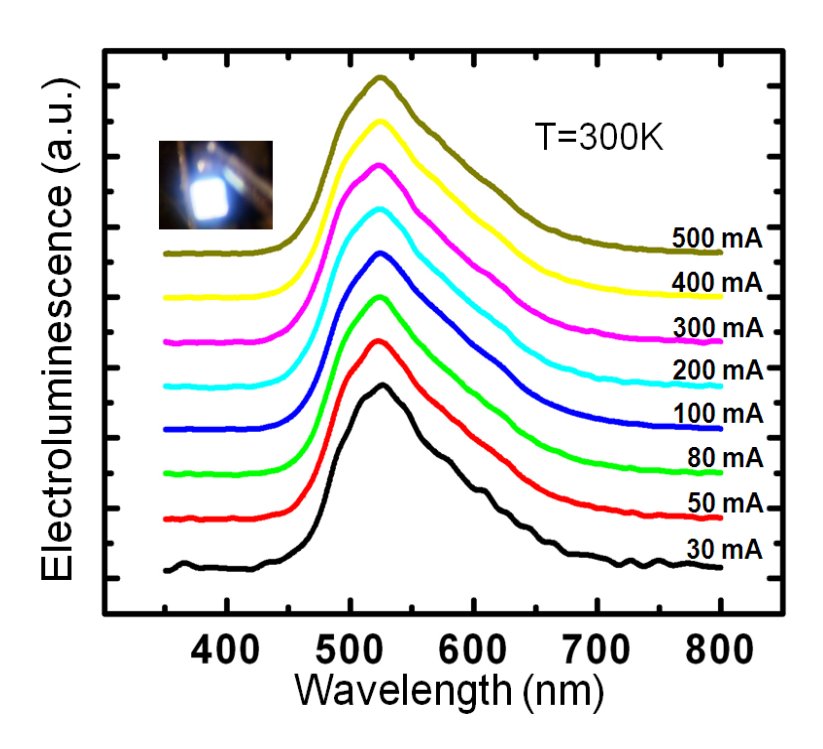


Figure 3.19: Normalized electroluminescence spectra of InGaN/GaN dot-in-a-wire white-emitting LEDs under different injection currents at room temperature. Shown in the inset is the optical microscopy image of the device.

The internal quantum efficiency of the white dot-in-a-wire LED device was also measured under electrical injection. As shown in figure 3.20, an internal quantum efficiency of ~ 36.7% at room temperature was recorded for this LED device under electrical injection. The achievement of relatively high efficiency is attributed to the use of nearly defect free GaN nanowires and the highly effective carrier confinement provided by the quantum dots.

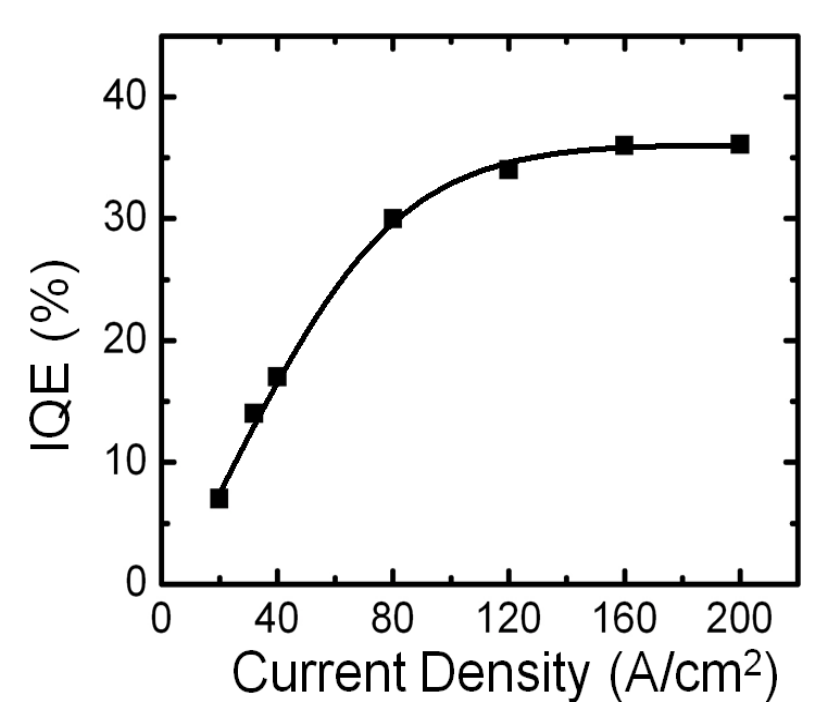


Figure 3.20: Room-temperature internal quantum efficiency of the white InGaN/GaN dot-in-a-wire LED device measured under electrical injection.

The relative external quantum efficiency (EQE) of InGaN/GaN dot-in-a-wire white LEDs was also measured. Illustrated in figure 3.21, the EQE first increases with injection current and stays nearly invariant at relatively high injection currents (> 100 A/cm²). No efficiency degradation was observed for injection currents up to ~ 200A/cm² at room temperature. Compared to conventional InGaN/GaN quantum well LEDs [36, 124, 125, 311], the absence of efficiency droop in InGaN/GaN dot-in-a-wire LEDs is attributed to the drastically reduced dislocation densities and polarization fields associated with these nanoscale heterostructures. However, at relatively high injection levels, the performance of such devices may suffer severely from hot carrier effect [26], including poor hole transport [18] and electron ballistic transport and overflow [27,28], which are described in the following chapters.

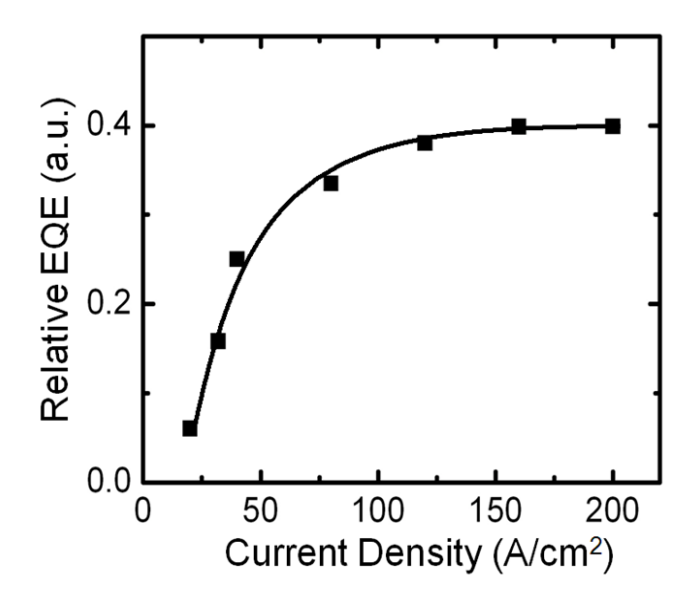


Figure 3.21: Room temperature relative external quantum efficiency of the white LED device, showing negligible efficiency droop up to 200 A/cm² injection current.

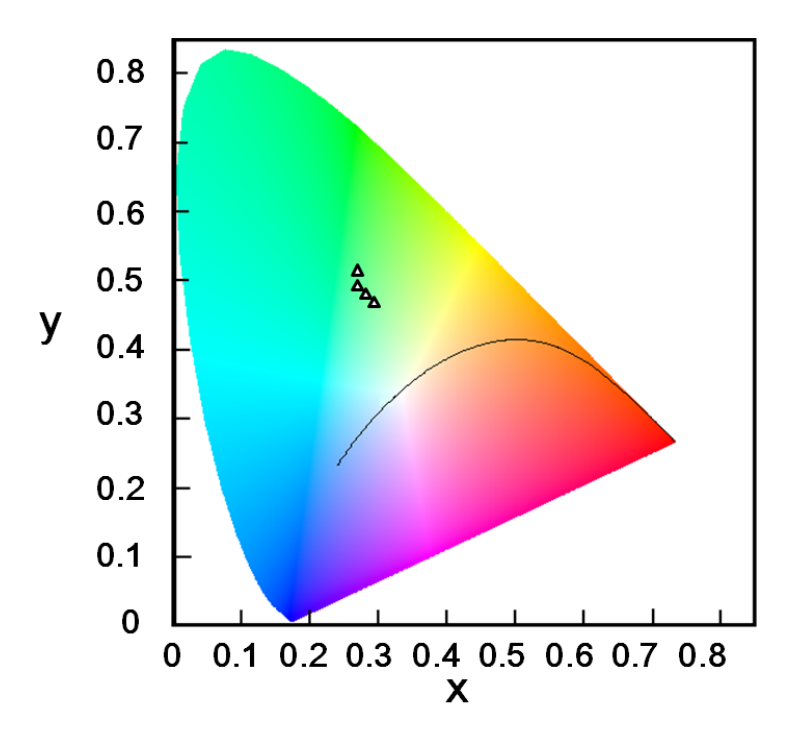


Figure 3.22: CIE chromaticity coordinates of the light emission from InGaN/GaN dot-in-a-wire white LEDs.

Shown in figure 3.22, the output spectrum of the white LED device, measured under injection currents from 100mA to 400mA, are characterized by ≈ 0.26 -0.31 and y ≈ 0.46 -0.51 in the CIE chromaticity coordinates. The variation of light emission with increasing current on the CIE diagram can be partly explained by the quantum-confined Stark effect. Additionally, due to the less efficient hole transport in the device active region, emission from the quantum dot active regions depend strongly on the bias conditions [38]. This unique carrier transport problem will be explained and addressed in detail in chapter 4.

3.4 Conclusion

In summary, we have achieved high performance red-emitting nanowire LEDs grown directly on Si substrates. Moreover, we have demonstrated phosphor-free LEDs by incorporating multiple quantum dots in single GaN nanowires. The devices exhibit relatively high IQE (~ 20-30%) and negligible efficiency degradation at relatively high injection levels (> 200 A/cm²) at room temperature, which is attributed to the superior three-dimensional carrier confinement provided by the InGaN quantum dots and the use of nearly defect-free GaN nanowires. Further improvement in the device performance can be made possible by optimizing the growth conditions and the charge carrier injection process of the dot-in-a-wire nanoscale heterostructures. This work shows the tremendous potential of the unique dot-in-a-wire nanoscale heterostructures in achieving superior performance and low cost LEDs.

Chapter 4: p-Type Modulation Doped InGaN/GaN Dot-in-a-Wire White Light-Emitting Diodes Monolithically Grown on Si(111)

4.1 Introduction

Phosphor-free white light emitting diodes (LEDs), that can be fabricated on low cost, large area substrates and can display high luminous flux, hold immense promise for the emerging solid state lighting. Such devices can be realized monolithically by stacking blue, green and red emitters in a single epitaxial step. They can exhibit much higher quantum efficiency, better color rendering capability, and significantly reduced manufacturing cost and improved reliability, compared to the commercial phosphor-based white LEDs [312]. Although tremendous progress has been made for InGaN/GaN quantum well LEDs, the performance of such devices in the green, yellow, and red wavelength ranges has been plagued by the very low efficiency and "efficiency droop", i.e. the decrease of the external quantum efficiency with increasing current [291]. The underlying mechanism has been extensively investigated. Defects and carrier delocalization [123], polarization field [124, 125], Auger recombination [126], carrier leakage [127], and poor hole transport [128, 313] have been identified as some of the most probable causes. To this end, intensive studies have been performed with the use of various nanostructures, including quantum dots and nanowires [119, 120, 309, 314-317], which can exhibit drastically reduced dislocation densities and polarization field and can provide a greater degree of flexibility for sophisticated device engineering, compared to conventional planar heterostructures. Multi-color emission has been realized by using InGaN/GaN coremulti-shell and well/disk-in-a-wire structures and by exploring various hybrid nanowire heterostructures [119, 120, 315, 318, 319]. More recently, white light emission has been demonstrated in LEDs consisting of compositionally graded

InGaN nanowires [17], InGaN/GaN nanodisks [121], and etched InGaN quantum wells [106].

However, a significant roadblock for the development of nanowire LEDs is the very low quantum efficiency. Due to the lack of three-dimensional carrier confinement, the radiative electron-hole recombination in the commonly reported GaN nanowire LED heterostructures has been severely limited by the presence of unoccupied Ga dangling bond and/or large densities of surface defects along the nonpolar $GaN(1\bar{1}00)$ surface (m-plane), which can lead to a Fermi-level pinning on the nanowire lateral surfaces [285, 287]. Additionally, the device performance is adversely affected by the poor hole injection and transport processes in InGaN/GaN nanoscale heterostructures, caused by the heavy effective mass, small mobility, and low concentration of holes [128, 162, 313]. While electrons can exhibit a relatively uniform distribution across the entire active region, injected holes largely reside in the small region close to the p-doped GaN layer. The highly nonuniform carrier distribution also lead to significantly enhanced Auger recombination and increased electron overflow, further limiting the optical emission efficiency at high injection levels.

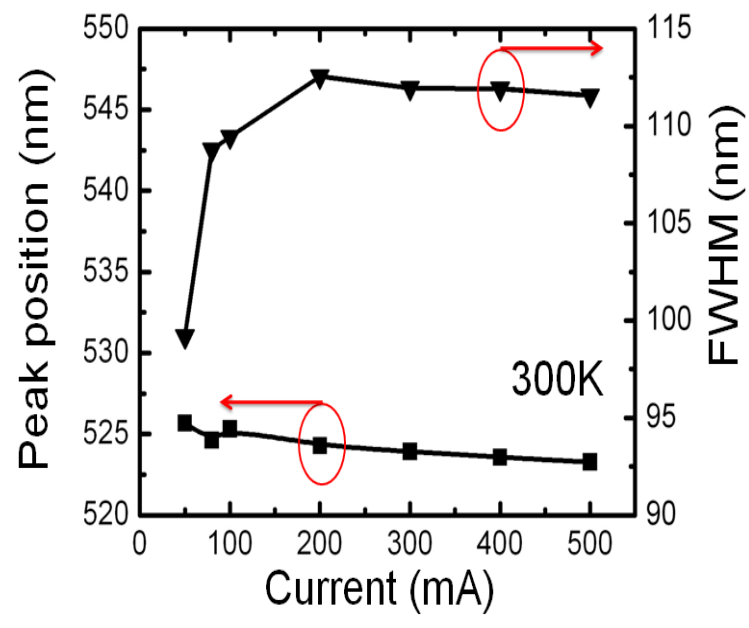


Figure 4.1: Room temperature peak position and full-width-half-maximum of electroluminescence spectra measured from the InGaN/GaN dot-in-a-wire white LEDs.

For the reasons described above, the internal quantum efficiency of the white LEDs described in Chapter 3 is generally limited to ~ 20 to 30% at room temperature. The emission characteristics of such devices are not stable with increasing current. Shown in figure 4.1, there is a blueshift (~ 8 nm) when the injection current is increased from 50 mA to 500 mA, due to the presence of polarization fields and the associated QCSE. Additionally, it is observed that the spectral linewidth of the emission spectra increases rapidly with increasing current, which is a direct reflection of the poor hole transport in the LED device active region. While the electron distribution is more uniform in the quantum dots, holes largely reside in the dots closed to the p-GaN region, leading to highly inhomogeneous carrier distribution in the device active region. The hole concentration is drastically reduced in regions close to the n-GaN. Therefore, light emission is mostly from the quantum dots near the p-GaN region. Furthermore, it is expected that the poor hole transport may become more aggravated under high current injection conditions.

In this regard, special techniques, including p-doped active region, electron blocking layer, and thin InGaN barrier, have been implemented to improve the performance of conventional InGaN/GaN quantum well LEDs [124, 128, 163, 313]. However, such phenomena have not been recognized and addressed in the emerging nanowire LEDs. In this context, we have investigated the epitaxial growth, fabrication, and characterization of self-organized InGaN/GaN dot-in-a-wire LED heterostructures grown on Si(111) substrates that can break the efficiency bottleneck of nanowire devices. Figures 4.2(a) and (b) show the simulated results of hole concentration across the quantum dot active region by using APSYS simulation packages under 1,000 A/cm² current injection level for the un-doped and p-doped LED devices, respectively. In this simulation, LED structures with ten In_{0.25}Ga_{0.75}N quantum wells separated by 3 nm GaN barriers are investigated. We have assumed that nanowire LED devices exhibit drastically reduced dislocation densities, a Shockley-Read lifetime of 10 ns, and an Auger recombination coefficient in the quantum wells of 1×10^{-33} cm⁶/s. The built-in strain in nanowires can be significantly reduced due to the lateral stress relaxation. The polarization charge densities are

assumed to be 25% of the calculated values, and electron and hole mobilities are presumed to be 600 and 5 cm² V⁻¹s⁻¹, respectively.

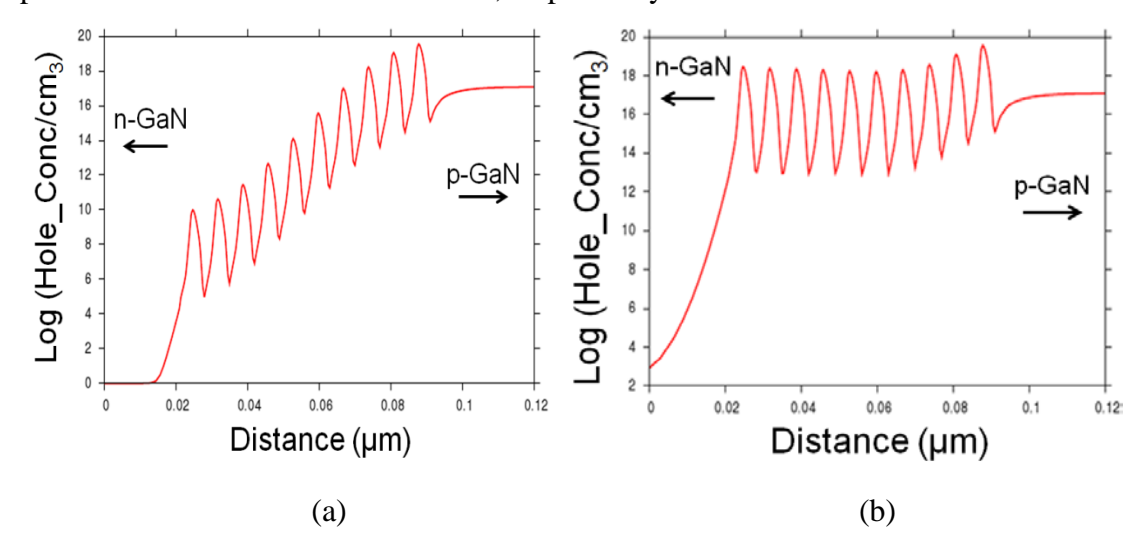


Figure 4.2: Simulated hole concentration across the InGaN/GaN quantum dot active regions for LEDs without (a) and with (b) the usage of p-type modulation doping in InGaN/GaN active regions under 1,000 A/cm² injection current.

Illustrated in figure 4.2(a), the hole concentration is drastically reduced from the quantum dot near the p-GaN segment to the n-GaN region for the LED without using p-type modulation doping technique. For instance, the hole concentration in the quantum dot close to the p-side GaN is virtually nine orders of magnitude higher than that in the last quantum dot which is next to the n-side. The carrier recombination, therefore, mostly occurs within the quantum dots close to the p-GaN region leading to the inefficient radiative recombination in the device active region. However, with the usage of p-type modulation doping technique as shown in figure 4.2(b), the hole distribution is much more uniform across all the active region compared to that of undoped LED device. The carrier recombination in the device active region, consequently, is more effective since all quantum dots can contribute to the electron-hole recombination, which will further lead to reduced electron leakage out of the active region and enhanced LED quantum efficiency. With the use of p-type modulation doping in the quantum dot active region, we have demonstrated phosphor-free white LEDs with a record high ($\sim 56.8\%$) internal quantum efficiency,

which is attributed to the superior carrier confinement provided by the dots and the significantly enhanced hole transport, due to the *p*-type modulation doping.

4.2 Design, Growth and Fabrication of p-doped InGaN/GaN Dot-in-a-Wire LEDs

In this work, we have investigated the design, epitaxial growth, and fabrication of p-doped InGaN/GaN dot-in-a-wire white light LEDs. Illustrated in figure 4.3, the device active region consists of ten vertically aligned InGaN quantum dots, separated by ~ 3 nm GaN barrier layers. The flat energy band diagrams along the wire axial direction and along the lateral direction of the quantum dot active region are also illustrated in figure 4.3. Due to In segregation, the GaN barrier layers also contain a small percentage (~ 5-10%) of In. The resulting thin (~ 3 nm) InGaN barrier layers can enhance the hole injection and transport in the quantum dot active region, thereby leading to more uniform hole distribution, reduced electron leakage, and enhanced internal quantum efficiency at relatively high current levels [163, 320].

To further enhance the hole transport, each quantum dot is modulation doped p-type, which is achieved by incorporating Mg in part of the GaN barrier layer, with the Mg effusion cell temperature at ~ 150 to 200 °C. The technique of modulation p-doping can minimize any deleterious effects associated with the direct Mg incorporation in the dots. As a consequence, no degradation in the optical properties of the p-doped dot-in-a-wire heterostructures was measured, compared to the undoped LED device heterostructures. Figure 4.4 shows the photoluminescence spectra of the p-doped and undoped LED samples, respectively. Both LED structures exhibit nearly identical emission spectra under optical pumping. Other growth conditions are nearly the same as those for the InGaN/GaN dot-in-a-wire white light LEDs described in chapter 3.

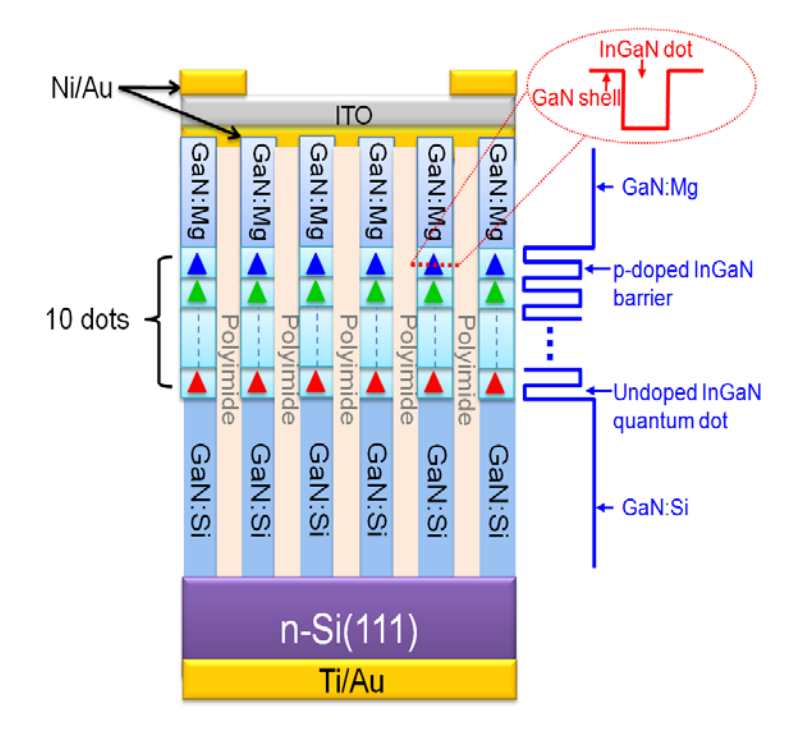


Figure 4.3: Schematic of the p-doped InGaN/GaN dot-in-a-wire LED with the flat band energy shown on the right side.

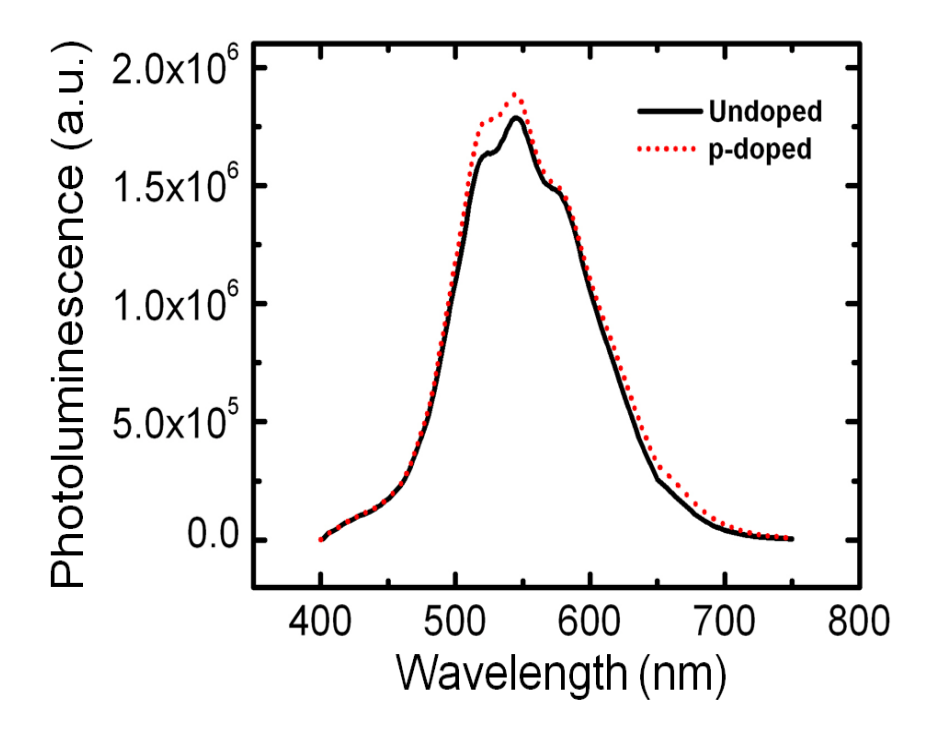


Figure 4.4: Room temperature photoluminescence spectra of p-doped and undoped white LED heterostructures measured under the same optical excitation conditions.

The device fabrication process follows that described in Chapter 3 and is briefly discussed here. The InGaN/GaN nanowire arrays were first planarized using a polyimide resist layer by spin-coating, which was followed by an appropriate dry etching process to reveal the top GaN:Mg sections of the dot-in-a-wire heterostructures. *p*- and *n*-metal contacts, consisting of Ni(5nm)/Au(7nm)/indium tin oxide (ITO) and Ti/Au layers, were then deposited on the exposed wire surface and the backside of the Si substrate, respectively. The fabricated devices with Ni/Au and Ti/Au metal contacts were first annealed at ~ 500 °C for 1 minute in nitrogen ambient. Upon the deposition of the ITO transparent contact, a second annealing step was performed at 300°C in vacuum for ~ 1 hour.

4.3 Results and Discussion

The measured current-voltage characteristics at room temperature, for both the undoped and modulation p-doped dot-in-a-wire LEDs, are shown in figure 4.5. The devices exhibit excellent diode characteristics, with relatively small ($\sim 20-50~\Omega$) series resistances and negligible leakage current under reverse bias. The p-doped nanowire LEDs also show slightly higher current densities, compared to the undoped devices under the same bias conditions. The devices with areas of $0.5\times0.5~\text{mm}^2$ were used for detailed characterization. The optical microscopy image of a fabricated nanowire LED device is shown in the inset of figure 4.5, wherein metallic contact grids were made on the device surface to facilitate the hole transport and injection processes.

Emission characteristics of p-doped InGaN/GaN dot-in-a-wire LEDs were studied. To minimize junction heating effect, pulsed bias conditions, with duty cycles in the range of 0.1% to 5%, were utilized during the measurements. Strong white light emission, illustrated in the inset of figure 4.6, was observed for the *p*-doped dot-in-a-wire LEDs, which is a direct consequence of the polychromatic emission of InGaN/GaN quantum dots, due to the large inhomogeneous broadening. Importantly, emission spectra of the *p*-doped LEDs are nearly invariant with increasing injection currents. Shown in figure 4.6, a very small (~ 4 nm) blueshift was measured for the *p*-

doped dot-in-a-wire LEDs with increasing injection currents, signifying the presence of a very small, or negligible quantum-confined Stark effect.

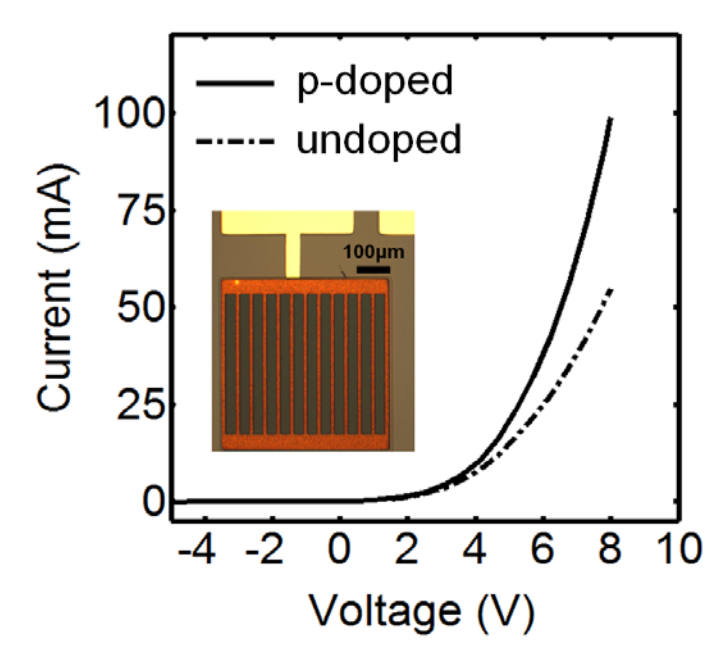


Figure 4.5: Current-voltage characteristics of undoped- and *p*-doped dot-in-a-wire LEDs measured at room temperature. The optical microscopy image of the fabricated dot-in-a-wire LED is shown in the inset.

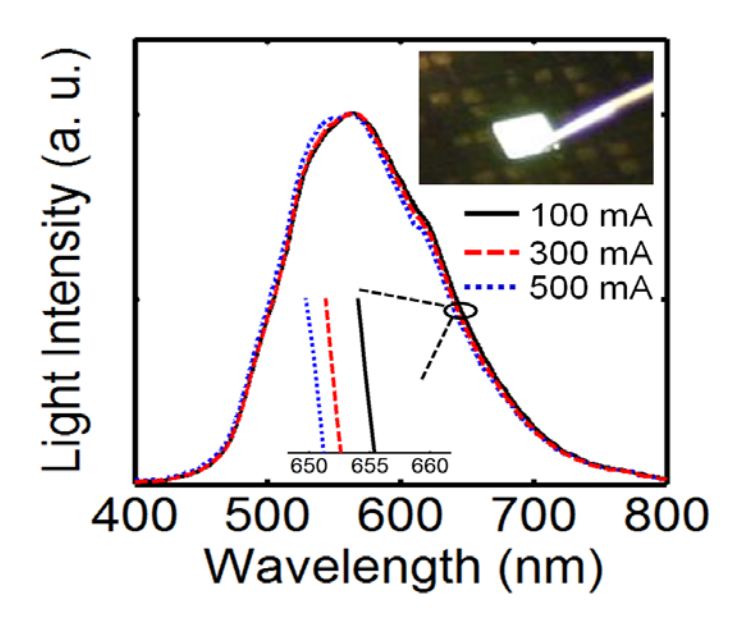


Figure 4.6: Electroluminescence spectra of a *p*-doped InGaN/GaN dot-in-a-wire LED measured at injection currents from 100 to 500 mA under pulsed bias conditions at room temperature. The optical image of the device is shown in the inset.

It is also of interest to notice that their spectral linewidths (full-width-half-maximum – FWHM ~ 136 nm) are comparatively larger than those of the undoped devices (FWHM ~ 110 nm), illustrated in figure 4.7. This is attributed to the more efficient, uniform radiative carrier recombination in the p-doped device active region, compared to the undoped one. With the use of p-type modulation doping, more quantum dots in the device active region can contribute to the light emission, thereby leading to relatively large spectral linewidth. Locations of the light emission on the chromaticity diagram are shown in figure 4.8 for both the undoped (solid triangles) and p-doped (solid circles) LEDs at injection currents from 100 mA to 400 mA. It is seen that the p-doped LEDs exhibit nearly constant CIE chromaticity coordinates (x \approx 0.35 and \approx 0.37) with increasing injection currents, with a correlated color temperature of \sim 4,500 K and fairly high color rendering properties. The undoped LEDs, on the other hand, show varying chromaticity coordinates (\approx 0.26 -0.3 and y \approx 0.46-0.51) in the same current range.

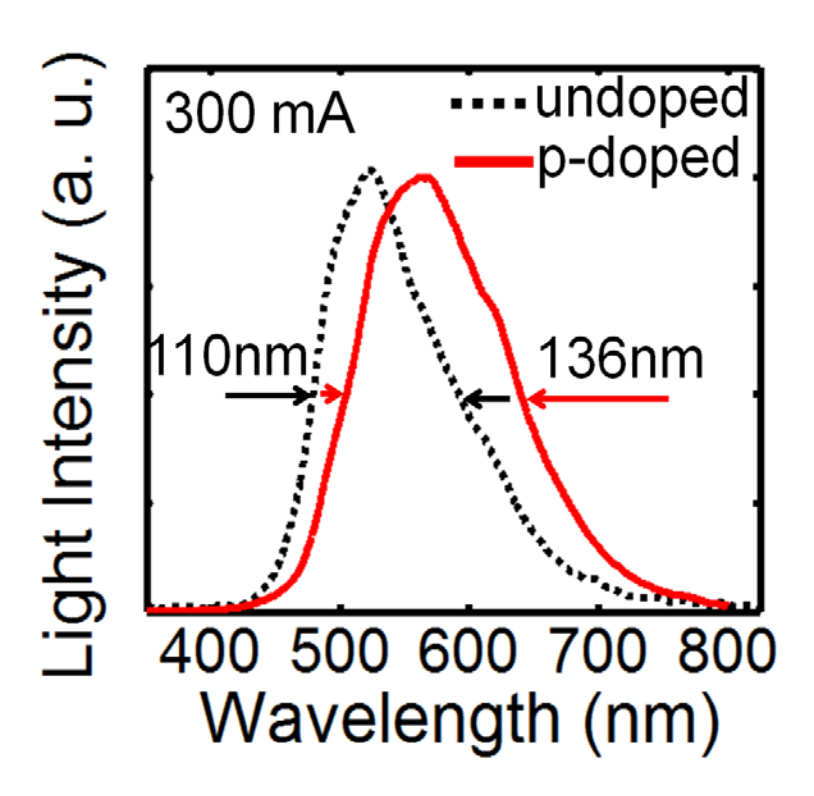


Figure 4.7: Room temperature electroluminescence spectra of p-doped and undoped white LED under an injection current of 300 mA.

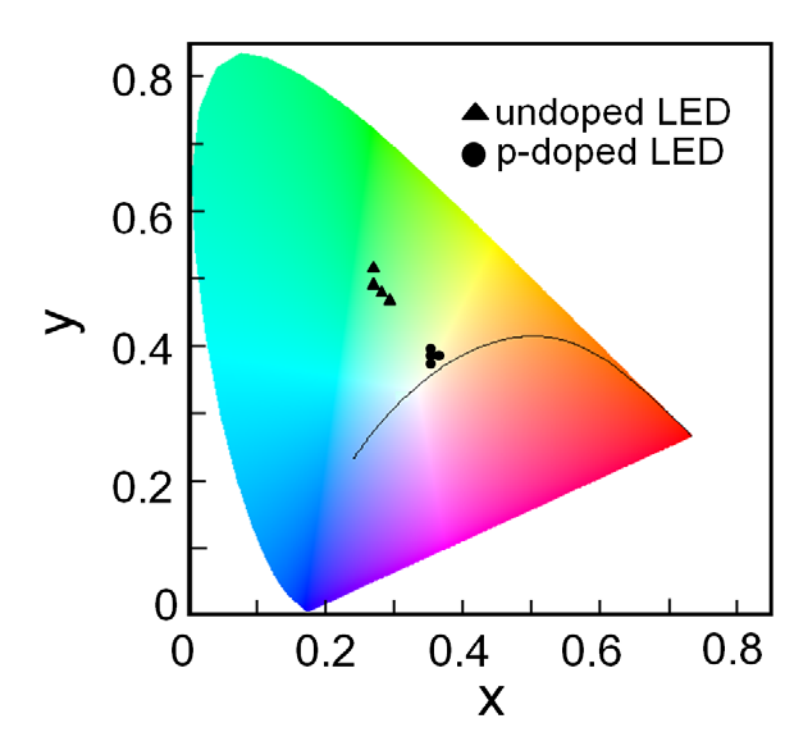


Figure 4.8: 1931 Commission International de l'Eclairage chromaticity diagrams. Location of the light emission for the undoped (triangles) and *p*-doped (circles) dotin-a-wire LEDs are shown at injection currents from 100 mA to 400 mA.

We have further studied the internal quantum efficiency of the undoped and p-doped dot-in-a-wire LEDs. As discussed in Chapter 3, the room-temperature internal quantum efficiency, relative to that at 5 K, is derived by comparing the light intensity measured at these temperatures under the same injection current. The results are shown in figure 4.9 for both the undoped and p-doped dot-in-a-wire LEDs. The internal quantum efficiency first increases with increasing injection currents for both types of devices. It reaches the maximum values of 36.7% and 56.8% at $\sim 130 \text{ A/cm}^2$ and 200 A/cm², for the undoped and p-doped devices, respectively. These values are significantly higher than the internal quantum efficiencies of any previously reported nanowire LEDs under either electrical injection or optical pumping [17, 281]. More importantly, with the use of p-doping, the internal quantum efficiency ($\sim 56.8\%$) shows a more than 50% increase, which is the most efficient phosphor-free white LEDs ever reported.

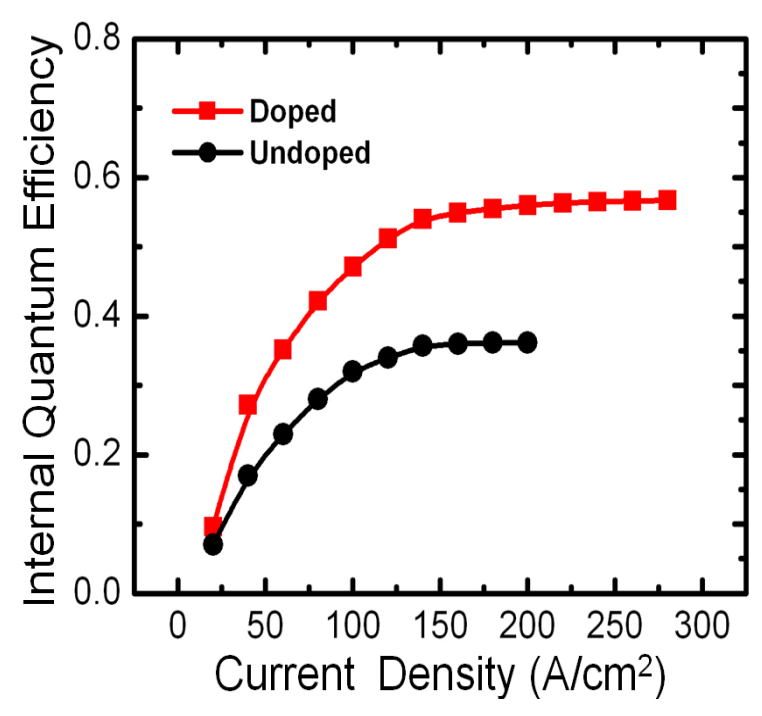


Figure 4.9: Variation of the room temperature internal quantum efficiency of the undoped and *p*-doped dot-in-a-wire LEDs versus injection currents.

Similar results have also been obtained for InGaN/GaN dot-in-a-wire LEDs under optical pumping (λ = 405 nm) with internal quantum efficiency of ~21.7% and 50.2% for the undoped and p-doped dot-in-a-wire LEDs, respectively. The measured results are shown in figure 4.10, which agrees qualitatively well with the values measured under electrical injection. Shown in figure 4.10, a maximum internal quantum efficiency of ~ 50.2% is measured for the p-doped dot-in-a-wire LEDs under optical pumping.

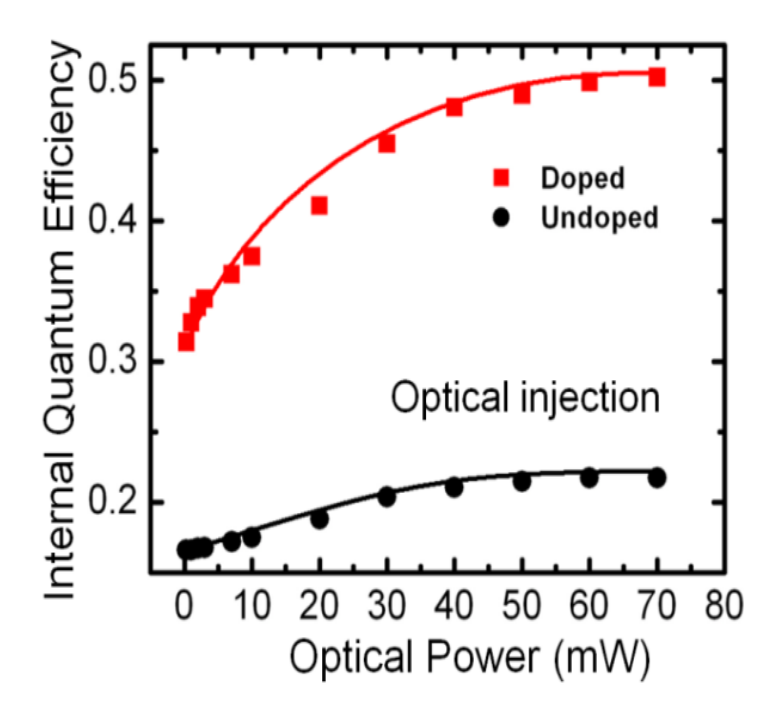


Figure 4.10: Variation of the room temperature internal quantum efficiency of the undoped and p-doped dot-in-a-wire LEDs under different optical pumping power ($\lambda = 405 \text{ nm}$).

Compared to the undoped dot-in-a-wire LEDs, the remarkably high internal quantum efficiency of the *p*-doped white LEDs, as well as their stable emission characteristics, are attributed to the significantly enhanced hole transport in the InGaN quantum dot active region. Poor hole transport, due to their heavy effective mass, has been identified as one of the primary limiting factors for achieving high performance LEDs [128, 313]. In conventional LED heterostructures, injected holes largely reside in the small region close to the *p*-GaN layer, which predominantly determines the emission characteristics. The poor hole transport and injection processes also lead to many undesirable properties, including electron overflow, enhanced Auger recombination, and hot carrier effect. In typical nanowire LED heterostructures, the wire diameters are comparable to, or smaller than the active region thickness. The resulting strong surface scattering, as well as the presence of surface charges, may further aggravate the hole transport and injection processes and deteriorate the device performance. With the use of *p*-doing in the device active

region, enhanced hole transport and, consequently, more uniform, less current dependent hole injection can be achieved, which is consistent with the relatively large spectral linewidth (~ 136nm) measured for the p-doped LEDs, compared to that (~ 110 nm) of the undoped devices wherein optical emission is restricted to a relatively small quantum dot active region close to the p-GaN layer. Consequently, emission characteristics of the p-doped dot-in-a-wire LEDs are governed by the inhomogeneous broadening of the dots, which can be controlled by varying the dot properties during epitaxial growth and can lead to highly stable, robust optical emission with increasing current, compared to other approaches for monolithic white LEDs [163, 321-324]. The very high internal quantum efficiencies for both the undoped and p-doped LEDs are attributed to the significantly reduced nonradiative recombination and carrier leakage, owning to the superior carrier confinement provided by the dot-in-a-wire heterostructures. The improved hole injection and transport processes in the LED active region further reduce carrier leakage, carrier recombination outside of the dots, and hot carrier effect, which explains the drastic increase (>50%) in the internal quantum efficiency, compared to the undoped devices.

To achieve high luminous efficacy, it is critically important to maintain the high efficiency at relatively high injection levels, *i.e.* to minimize or eliminate any efficiency droop. Although reduced efficiency droop has been demonstrated in InGaN/GaN nanowire LEDs, the measured current densities were generally limited to $\sim 50-100$ A/cm² [17, 121]. In this experiment, the light-current characteristics for a p-doped dot-in-a-wire LED were measured up to ~ 300 A/cm². Illustrated in figure 4.11, the relative external quantum efficiency at room temperature for a p-doped dot-in-a-wire LED were measured up to ~ 300 A/cm², showing the presence of a small, or negligible efficiency droop even under relatively high current injection conditions. Detailed studies also confirm that there is no efficiency peak at relatively low injection levels. It is important to notice that these measurements were performed for unpackaged devices without any proper thermal management. Therefore, the intrinsic device performance is expected to be significantly better. To this end, the external quantum efficiency of the p-doped dot-in-a-wire LEDs was measured at 5 K, which

remains nearly invariant for injection current densities as high as 640 A/cm², shown in figure 4.12. The absence of efficiency droop at high injection levels is attributed to the superior carrier confinement provided by the quantum dot heterostructures, the nearly dislocation- and strain-free GaN nanowires, as well as the significantly enhanced hole transport and reduced carrier leakage, due to the *p*-type modulation doping.

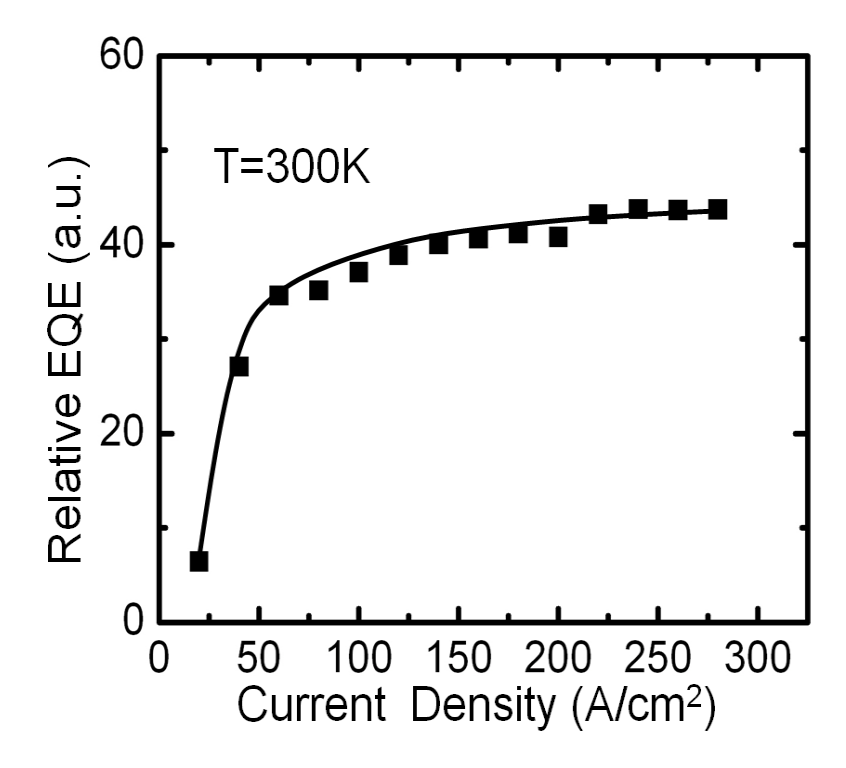


Figure 4.11: Variation of the relative external quantum efficiency versus current density for a *p*-doped dot-in-a-wire LED measured at room temperature.

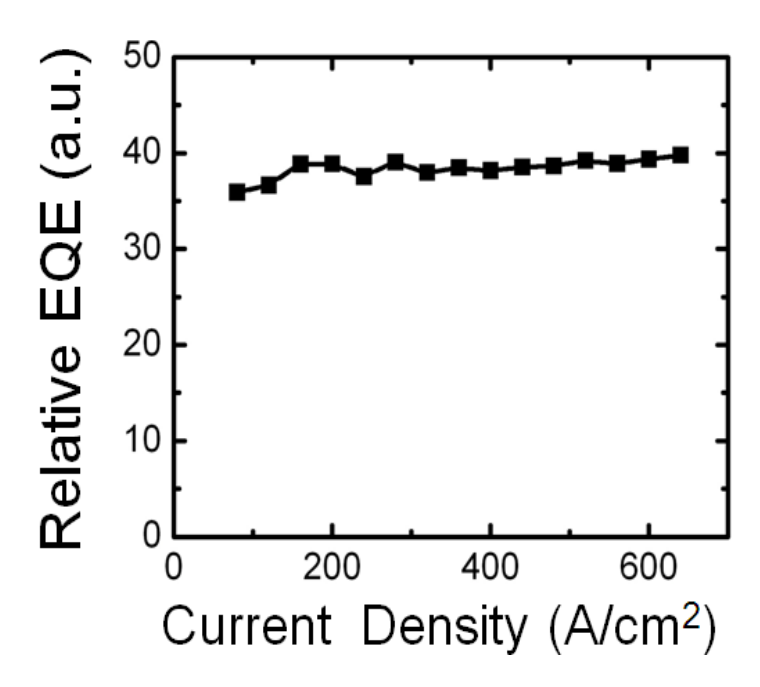


Figure 4.12: Variation of the relative external quantum efficiency versus current density for a *p*-doped dot-in-a-wire LED measured at 5K.

We have also performed detailed measurements on the external quantum efficiency of nanowire LEDs under relatively low injection conditions to examine if there is any efficiency droop. The measured results are detailed in figures 4.13 and 4.14 for injection levels below 25 A/cm², confirming that there is no efficiency degradation at relatively low injection levels for both the undoped and p-doped dotin-a-wire LEDs. These results, in conjunction with that shown in figure 4.11, suggest the presence of small, or negligible efficiency droop in p-doped dot-in-a-wire LEDs under injection current upto ~ 300 A/cm² at room temperature.

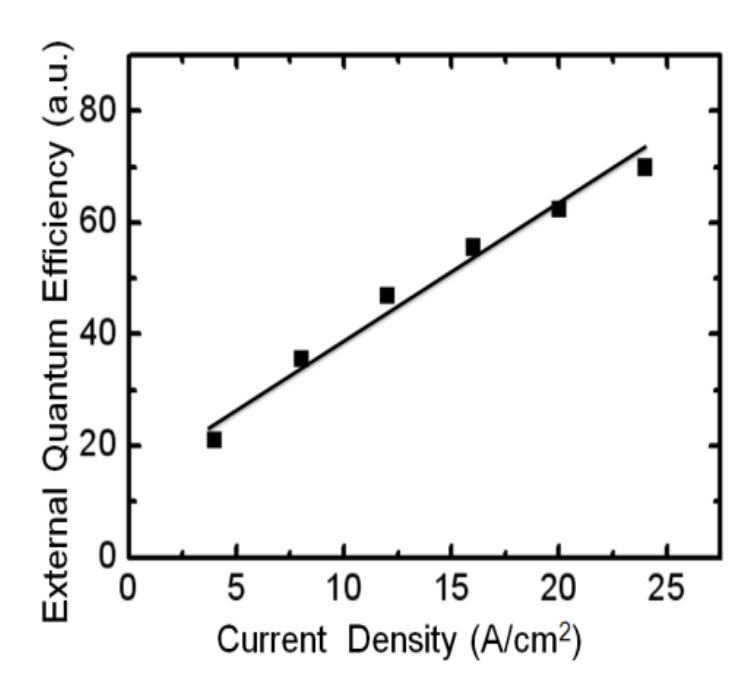


Figure 4.13: Variations of the relative external quantum efficiency with current at relatively low injection levels for the undoped LED.

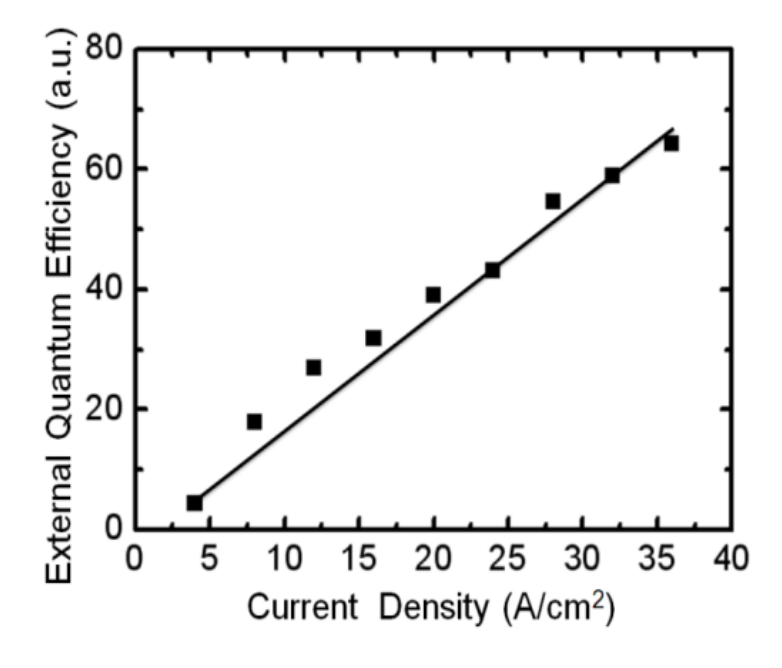


Figure 4.14: Variations of the relative external quantum efficiency with current at relatively low injection levels for the p-doped LED.

4.4 Conclusion

In summary, by significantly enhancing the hole transport in the device active region using p-type modulation doping, we have demonstrated the most efficient phosphorfree white light LEDs ever reported, which exhibit an internal quantum efficiency of $\sim 56.8\%$ at room temperature relative to that measured at 5 K. The p-doped dot-in-awire LEDs also show many desired properties, including highly stable white light emission, nearly zero efficiency droop at injection current densities up to ~ 300 A/cm², and relatively high color rendering properties, that are ideally suited for future smart lighting applications. This work constitutes a significant progress for achieving low cost, high performance phosphor-free white LEDs utilizing nanowire heterostructures.

Chapter 5: Controlling Electron Overflow in Phosphor-Free InGaN/GaN Nanowire White-Light-Emitting Diodes

5.1 Introduction

One of the grand challenges for future solid state lighting is the development of all semiconductor-based white light emitting diodes (LEDs), consisting of monolithically integrated blue, green and red devices, that can exhibit ultrahigh-efficiency, long-term reliability, and tunable color emission. The achievement of such devices using conventional GaN-based planar heterostructures, however, has been severely limited by their low efficiency and efficiency droop in the green to red spectral range, which has been explained by the presence of polarization fields [124, 125], Auger recombination [157], poor hole transport [128], defects/dislocations [325, 326], and/or electron leakage and overflow [124, 127, 327]. In this regard, significant progress has been made in nanowire white LEDs, with the active regions consisting of well/disk-in-a-wire [120, 284], core/shell [299], ternary nanowire [17, 281], and dot-in-a-wire nanoscale heterostructures [16, 38]. In such nanowire devices, mechanisms that may contribute to efficiency degradation, including dislocations, polarization fields, as well as the associated quantum-confined Stark effect (QCSE) [124, 288, 290, 310] can be greatly minimized [15, 16, 115]. Compared to conventional planar heterostructures, however, the performance of such nanoscale LEDs is more susceptible to electron leakage out of the device active region, due to the presence of large densities of states/defects along the wire surface and the onedimensional carrier transport process [168, 285, 287]. The resulting carrier loss and nonradiative carrier recombination severely limit the maximum quantum efficiency achievable at high current injection levels. To date, however, the presence of electron overflow and its predominant effect on the performance of nanowire LEDs has not been reported. Additionally, it has remained a subject of intensive debate on the role of Auger recombination in the performance of GaN-based LEDs [126, 130, 328, 329].

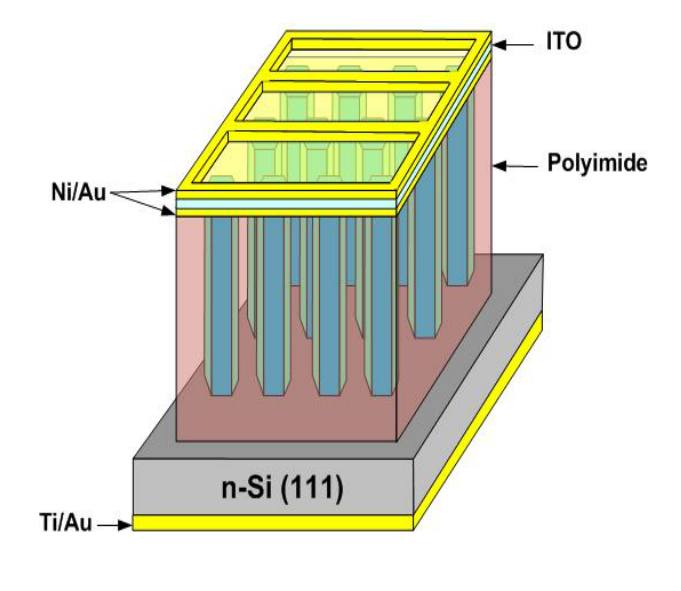
In this study, we have investigated, for the first time, the impact of electron overflow on the performance of nanowire LEDs operating in the entire visible spectral range. Intrinsic white-light emission is achieved by incorporating selforganized InGaN quantum dots, with controlled compositions and sizes, in defect-free GaN nanowires on a single chip. The role of electron overflow on the performance limit of such nanoscale LEDs has been elucidated by characterizing, both experimentally and theoretically, the current-dependent electroluminescence emission of an InGaN/GaN test quantum well embedded between the quantum dot active region and the p-GaN, wherein electrons escaping the quantum dot active region can be correlated with the optical emission from the test well. It is measured that electron overflow is present even under relatively low injection conditions (below the onset of efficiency droop), which, in conjunction with the nonradiative carrier recombination related to the surface states/defects, largely determines the unique emission characteristics of nanowire LEDs. Moreover, we have demonstrated that, with the incorporation of a p-doped AlGaN electron blocking layer between the active region and the p-GaN section, electron overflow can be effectively prevented. The resulting white LEDs can exhibit, for the first time, virtually no efficiency droop up to ~ 2,200 A/cm², thereby providing a highly promising approach for future high-power, all semiconductor-based solid state lighting. This study also provides unambiguous evidence that Auger recombination is not likely the primary mechanism responsible for efficiency droop in GaN-based nanowire LEDs.

5.2 Design, Growth and Fabrication of InGaN/GaN Dot-in-a-Wire LEDs

In this experiment, vertically aligned InGaN/GaN dot-in-a-wire heterostructures were grown on Si(111) substrates by radio-frequency plasma-assisted molecular beam epitaxy under nitrogen rich condition. The device active region contains 10 vertically coupled InGaN/GaN quantum dots. Each InGaN quantum dot has a height of ~ 3 nm and is capped by ~ 3 nm GaN layer. Detailed growth conditions for such dot-in-a-wire

nanoscale heterostructures are described in previous chapters [16, 38]. Figure 5.1(a) shows the schematic of a typical dot-in-a-wire LED device. To investigate the electron overflow phenomena, an InGaN/GaN dot-in-a-wire LED heterostructure, with the incorporation of a p-doped InGaN/GaN test quantum well between the device active region and p-GaN section is grown (LED I shown in figure 5.1(b)). In this design, electrons leaking out of the quantum dots can recombine with holes in the test well, which has smaller In compositions than that of the InGaN/GaN quantum dots. The resulting optical emission can therefore be used to evaluate electron overflow in nanowire LEDs. Additionally, we have designed nanoscale LEDs (LED II) with the incorporation of a p-doped AlGaN electron blocking layer between the LED active region and the InGaN test quantum well, in order to study its effect in preventing electron overflow [330, 331]. Finally, a 3rd LED device that consists of a p-doped AlGaN electron blocking layer, but without the InGaN test well is also investigated. The three nanowire LED designs are schematically shown in figure 5.1(b). The flat energy band diagrams along the nanowire axial dimension are also shown in the insets.

Illustrated in figure 5.2 are the photoluminescence spectra of such nanowire LEDs measured at room temperature. The peak at ~ 550 nm is related to the emission from the quantum dot active region, while the peak at ~ 430 nm is due to the presence of an InGaN test well, which can be measured for the 1st and 2nd nanowire LEDs.



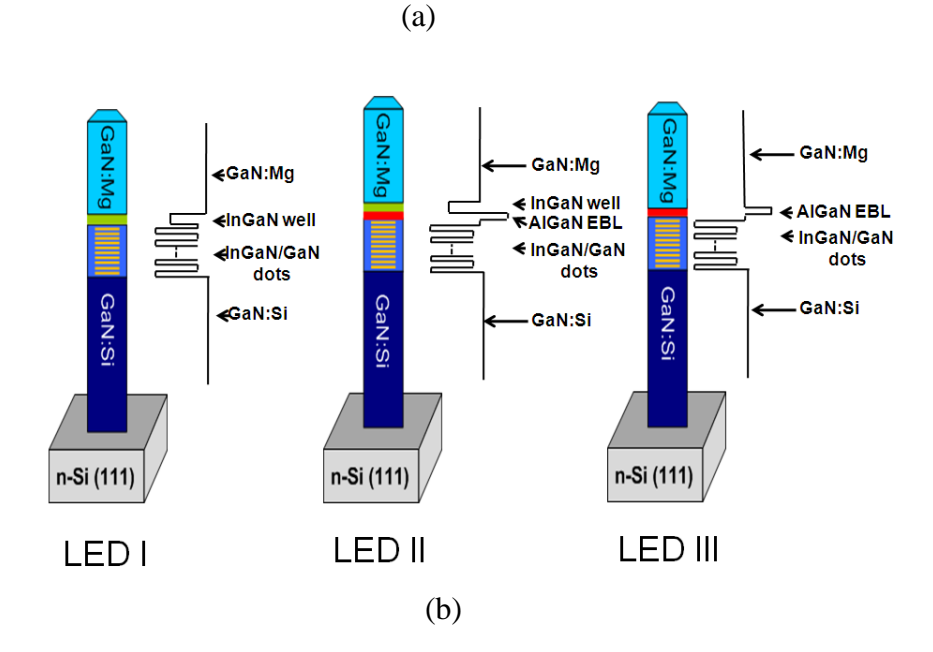


Figure 5.1: (a) Schematic illustration of InGaN/GaN dot-in-a-wire LEDs grown on Si(111) substrates. (b) Illustration of three LED designs. From left to right: InGaN/GaN dot-in-a-wire LEDs with the incorporation of an InGaN test well (LED I), an AlGaN electron blocking layer and an InGaN test well (LED II), and an AlGaN electron blocking layer but no test well (LED III) between the quantum dot active region and the p-GaN section. Flat energy band diagrams for the three LED structures are shown in the insets.

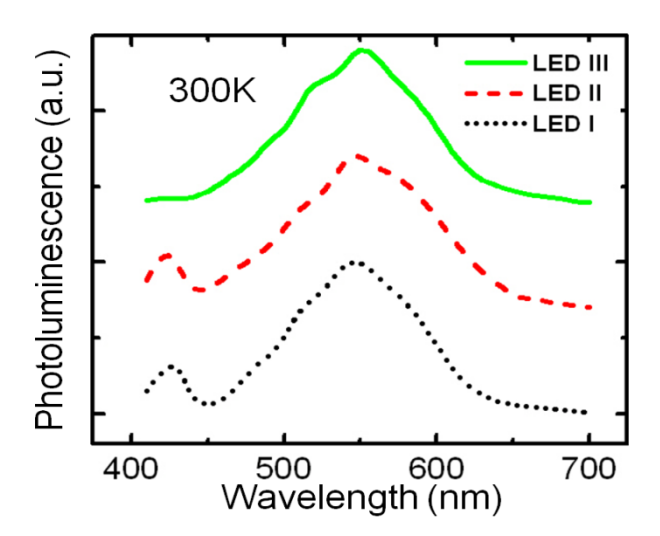


Figure 5.2: Room-temperature photoluminescence spectra of the three LED device heterostructures. The emission peak at ~ 430 nm is due to the presence of the InGaN test well, which can be clearly measured for LEDs I and II.

The dot-in-a-wire LEDs exhibit excellent structural properties. Shown in figure 5.3 is a 45° tilted scanning electron microscopy image of the dot-in-a-wire LED heterostructures grown on Si(111) substrates. The wire diameters and densities are in the range of 30 to 100 nm and $\sim 1\times10^{10}$ cm⁻², respectively. The nanowires are vertically aligned to the substrate and exhibit a high degree of size uniformity.

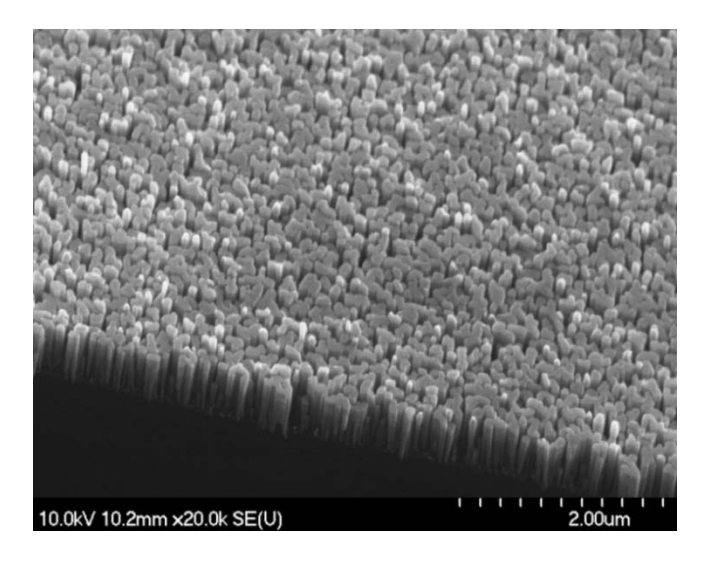
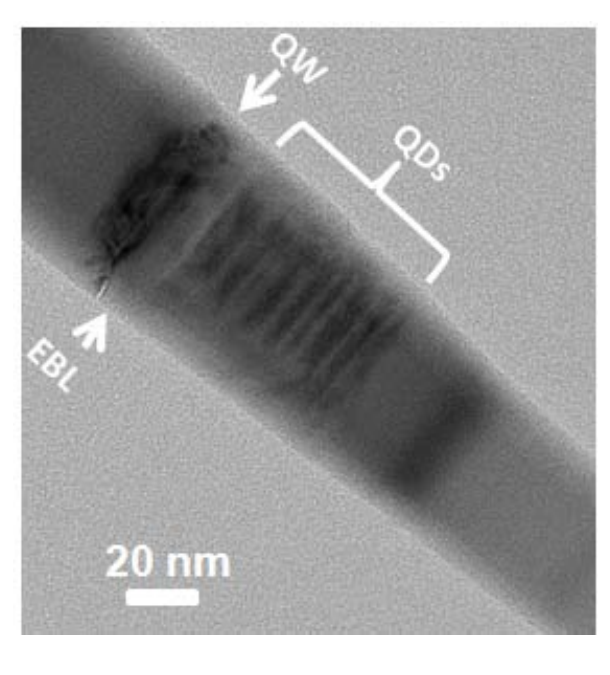


Figure 5.3: A 45° tilted SEM image of the InGaN/GaN dot-in-a-wire LED heterostructure grown on Si(111) substrate.

A CM200 microscope with acceleration voltage of 200 kV was used to obtain bright field transmission electron microscopy (TEM) images. A Titan 80-300 scanning transmission electron microscope (STEM) equipped with an aberration corrector for the image-forming lens was used for annular dark-field imaging and energy dispersive x-ray spectrometry (EDXS) analysis with an electron beam of approximately 0.2 nm in diameter. The Ga and Al K_{α} lines and In L_{α} line were used for the EDXS microanalysis. The TEM image for LED II is shown in figure 5.4(a), wherein the 10 InGaN/GaN quantum dots, the AlGaN electron-blocking layer as well as the InGaN quantum well are identified. There are no extended defects, such as misfit dislocations and stacking faults observed in the view of the current images. InGaN/GaN quantum dots are positioned in the center of the nanowires, due to the strain-induced self-organization. In order to confirm the existence of each region and obtain an estimation of the elemental variations, EDXS analysis together with the annular dark-field image were also performed. The EDXS line profile showing the signal variations of Ga, In and Al across different regions along the growth direction of LED II are displayed in figure 5.4(b). The variation of In signal reveals the existence of the InGaN quantum dots and InGaN quantum well. With the Ga signal from GaN region as a reference and also considering the thickness of the dots along the electron beam traveling path, the maximum In is estimated as ~ 50% constituting group III elements for the dot. Although from simple inspection of the profiles, the In composition of the InGaN quantum well appears higher than the one of the quantum dots, we cannot quantitatively compare the composition of the two structures at this point. Due to the much thinner width of the dots, the finite spatial resolution for EDXS analysis and the possible tilting of the dots away from the electron beam incident direction, the absolute In intensities cannot be directly compared in the two structures and further work is in progress to fully quantify the composition. Nevertheless, qualitative information on the presence of the In and Al have been extracted to confirm the presence of the key components of the device. From the Al signal profile, the AlGaN electron blocking layer is observed between the dot and well region for LED II, shown in figure 5.4(b). The thickness of the electron blocking layer is about 8 nm. In this experiment, the Al composition of the electron blocking

layer is varied from $\sim 8\%$ to 20%. The quality of the nanowire LEDs has been confirmed by the very high internal quantum efficiency ($\sim 30\%$ to 60%) measured at room temperature [16, 38, 332].



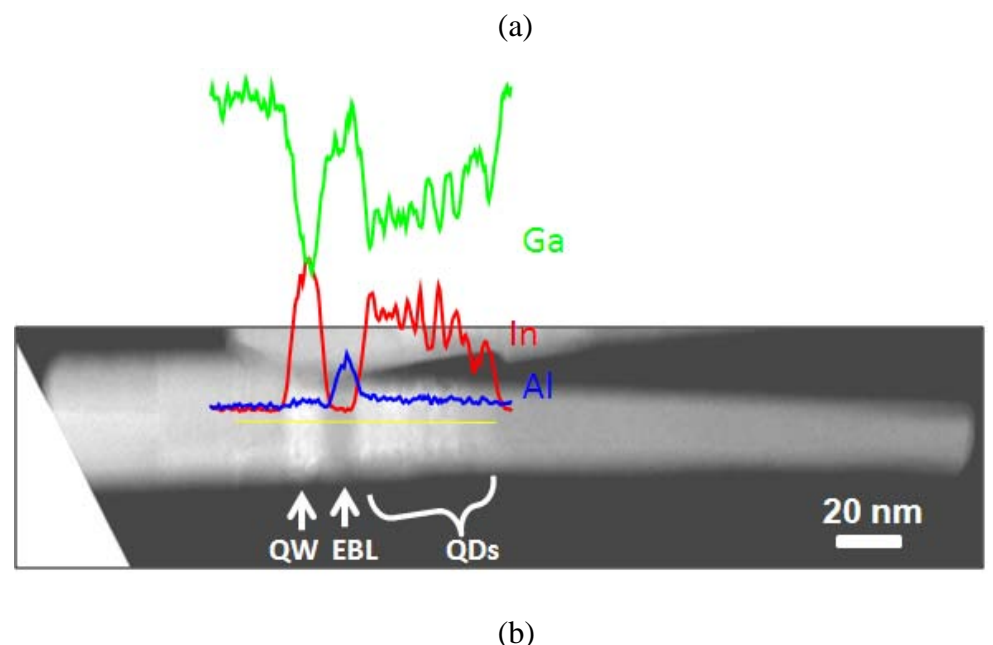


Figure 5.4: (a) Bright field TEM image of InGaN/GaN dot-in-a-wire LED II, wherein the InGaN quantum well (QW), quantum dots (QDs), and AlGaN electron blocking layer (EBL) are identified. (b) Annular dark field TEM image and energy dispersive x-ray spectrometry signals for In, Ga, and Al of LED II.

The nanowire LED fabrication process follows that described in Chapters 3 and 4. The device areas are $\sim 300 \times 300 \, \mu \, \text{m}^2$.

5.3 Results and Discussions

5.3.1 Measurement and Simulation of Electron Overflow in Nanowire LEDs

Emission characteristics of the InGaN/GaN dot-in-a-wire LEDs were studied. Electroluminescence was measured under pulsed biasing condition (~ 0.1% duty cycle) at various temperatures. Figure 5.5 shows the normalized electroluminescence spectra of LED I measured under various injection currents at room, which incorporates an InGaN test well between the device active region and the p-GaN. The peak at ~ 550 nm is related to the emission from the quantum dot active region, which agrees well with the photoluminescence measurements shown in figure 5.2. However, with increasing current, it is seen that the emission at ~ 430 nm becomes progressively stronger, which is attributed to the carrier recombination in the InGaN/GaN test well. This observation confirms that injected electrons can escape from the quantum dot active region and subsequently recombine with holes in the InGaN well. This is the first observation of electron overflow effect in nanowire LEDs. Small blue-shifts of ~ 3 nm and 9 nm are recorded for the emission peaks related to the test well ($\lambda \sim 430$ nm) and the quantum dot active region ($\lambda \sim 550$ nm), respectively. This can be well explained by the QCSE, which becomes more important in InGaN quantum wells/dots with relatively high In compositions. Moreover, we have also observed electroluminescence at ~ 367 nm at high injection currents in InGaN/GaN dot-in-a-wire white LEDs described in chapter 3. Shown in figure 5.6 are the electroluminescence spectra of such devices measured under different injection currents. The presence of emission peaks at ~ 367 nm at high injection current is attributed to electron leakage into the p-GaN region and the subsequent electron-hole recombination. These studies provide an unambiguous evidence for the presence of severe electron overflow in GaN-based nanowire LEDs.

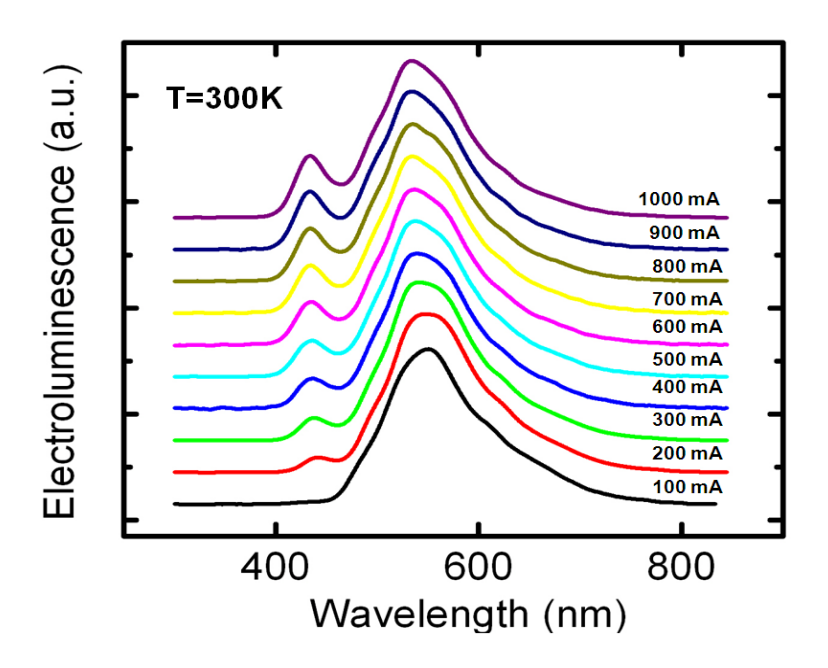


Figure 5.5: Normalized electroluminescence spectra of LED I. This design incorporates ten InGaN/GaN quantum dots in the active region and a GaN/InGaN/GaN test quantum well between the LED active region and p-GaN.

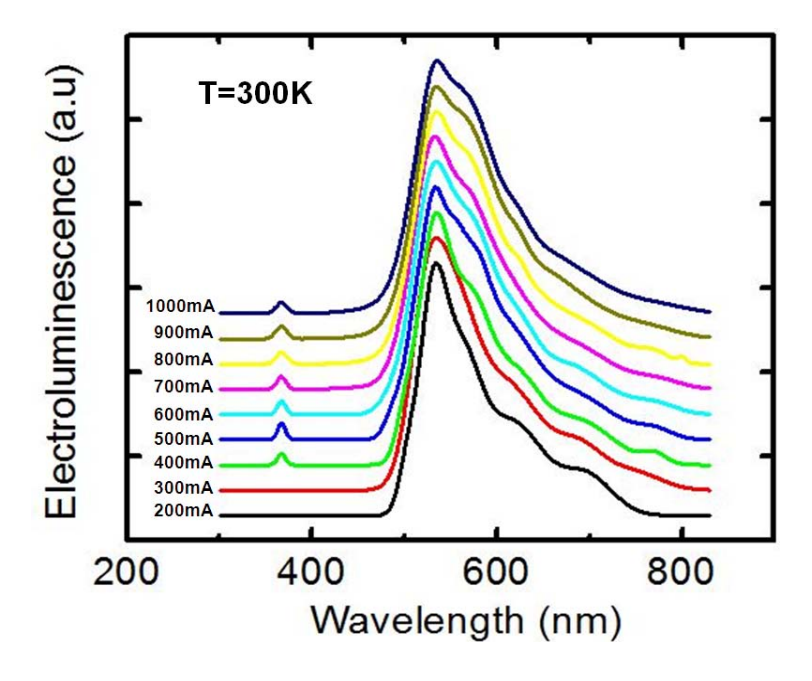


Figure 5.6: Normalized electroluminescence spectra of the InGaN/GaN dot-in-a-wire LED with only ten quantum dots in the active region measured at room temperature.

We have further studied the effect of electron overflow on the performance of nanowire LEDs. Shown in figure 5.7 is the derived normalized relative external quantum efficiency related to the electroluminescence emission from the quantum dot active region as well as that from the test well. It is seen that, for the emission from the test well, the quantum efficiency shows an increasing trend with current, which can be explained by the increased electron overflow and therefore enhanced emission from the test well region with increasing current. For the emission of the quantum dot active region, the relative external quantum efficiency reaches its maximum at ~ 300-400 A/cm² and shows a small drop (~ 6%) with further increasing current up to 1,100 A/cm², which can be explained by the enhanced electron overflow at high injection conditions. Compared to conventional planar LED devices, the quantum efficiency of nanowire LEDs reaches its peak value at much higher current densities (typically > 100 A/cm²), due to the presence of surface states and defects and the associated nonradiative carrier recombination and possibly current leakage along the wire length. It may also be noticed that electron overflow can become appreciably important below such injection levels, evidenced by the presence of emission peak from the test well at current densities of ~ 300 A/cm². It is therefore fair to conclude that the performance of nanowire LEDs is strongly influenced by both the carrier nonradiative recombination along the wire surface and electron overflow.

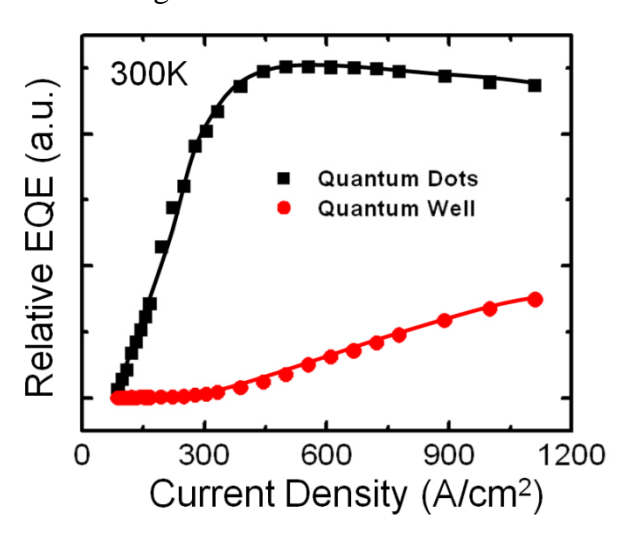


Figure 5.7: Relative external quantum efficiency for emission from the quantum dot active region and from the test well for LED I measured at room temperature.

To systemically study the effect of electron overflow on the performance of InGaN/GaN dot-in-a-wire LEDs, electroluminescence characteristics of LED I were measured under different temperatures. Illustrated in figure 5.8, the emission intensity from the test well becomes comparable to that from the quantum dots at low temperatures, while at room temperature its intensity is only ~ 10% of that from the dots. The measurements were performed at the same current injection condition of ~ 450 A/cm². This indicates electron overflow is significantly enhanced with decreasing temperature, which leads to more severe quantum efficiency drop at lower temperatures.

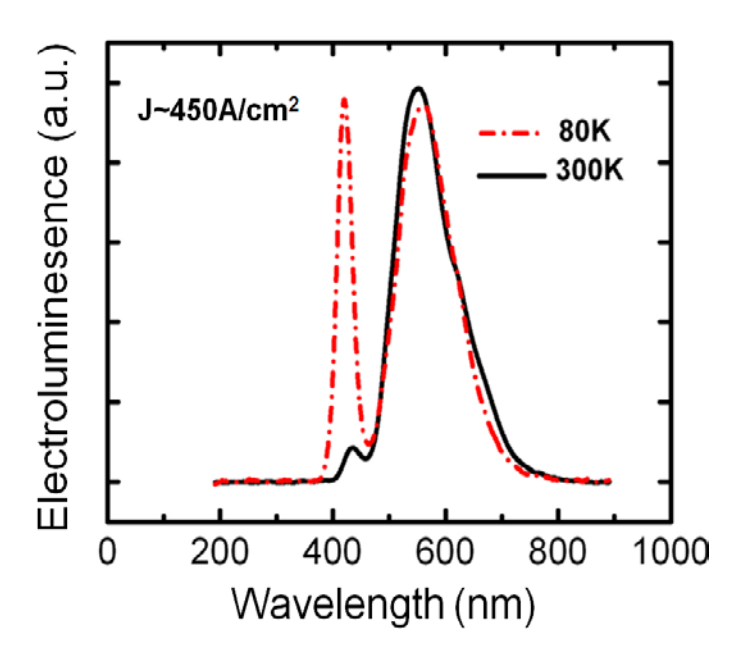


Figure 5.8: Electroluminescence spectra of LED I at 300 K (solid line) and 80 K (dash dot curve) under 450 A/cm² injection current.

Shown in figure 5.9, the estimated efficiency drop is ~ 6%, 10%, and 21% for measurements performed under an injection current of ~ 1,100 A/cm² at 300 K, 200 K, and 80 K, respectively. The increased electron overflow at low temperatures is consistent with recent theoretical studies [165]. At low temperatures, the hole concentration in the p-GaN region is drastically reduced, due to the large activation energy for Mg dopant, thereby leading to reduced hole injection efficiency and further enhanced electron overflow. This is also consistent with the increased device

resistance with decreasing temperatures, which is evident from the current-voltage characteristics measured at different temperatures, shown in figure 5.10. At high temperatures, thermal energy activates Mg-dopants, which can increase hole concentration and injection to the device active regions. Consequently, the carrier distribution is relatively more uniform and electron overflow is reduced. It is also observed that, with decreasing temperature, the peak quantum efficiency shifts to lower current densities, shown in figure 5.9, due to the reduced Shockley-Read-Hall recombination as well as enhanced bimolecular radiative recombination rate. These phenomena can be well simulated by using the following model for the internal quantum efficiency,

$$\eta_i = \frac{BN^2}{AN + BN^2 + f(N)} \tag{5.1}$$

where N is the carrier density in the device active region, and A and B are the Shockley-Read-Hall nonradiative recombination and radiative recombination coefficients, respectively [130, 131]. f(N) represents for any other higher order effects, including Auger recombination and carrier leakage outside of the device active region, which are generally described by $CN^3 + DN^4$. In this study, D is assumed to be zero. The carrier density (N) is related to the injection current density (J) by:

$$J = qW_{QD}[AN + BN^2 + f(N)]$$

where W_{QD} represents the total thickness (~ 25-30 nm) of the quantum dot active region.

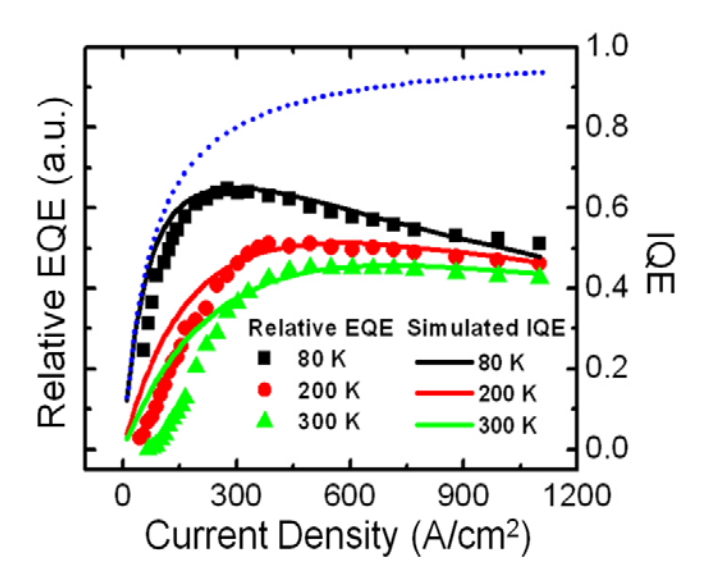


Figure 5.9: Variations of the relative external quantum efficiency (EQE) related to the emission from the quantum dot active region measured at 80, 200, and 300 K. The simulated internal quantum efficiency (IQE) based on the ABF model is also shown for comparison. The dotted blue line is the calculated IQE versus injection currents in the absence of any 3rd or higher order carrier loss mechanisms.

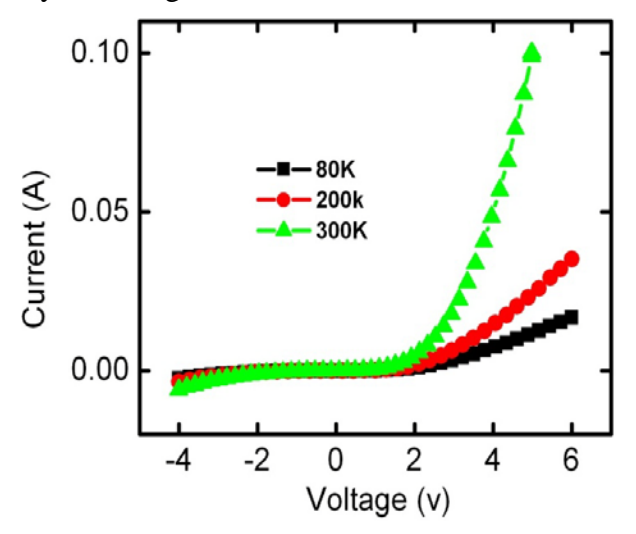


Figure 5.10: Current-voltage characteristics of LED I measured at 300 K, 200K, and 80K, respectively.

Illustrated in figure 5.9, the measured relative external quantum efficiency at various temperatures can be well simulated using this model. The derived values of (A, B, C) are $\sim (2.6 \times 10^8 \text{ s}^{-1}, 6.0 \times 10^{-10} \text{ cm}^3 \text{s}^{-1}, 1.0 \times 10^{-28} \text{ cm}^6 \text{s}^{-1}), (6 \times 10^8 \text{ s}^{-1}, 4 \times 10^{-10} \text{ cm}^3 \text{s}^{-1}, 6 \times 10^{-29} \text{ cm}^6 \text{s}^{-1}), and <math>(7.0 \times 10^8 \text{ s}^{-1}, 3 \times 10^{-10} \text{ cm}^3 \text{s}^{-1}, 4.5 \times 10^{-29} \text{ cm}^6 \text{s}^{-1})$ at 80 K,

200 K, and 300 K, respectively. Additionally, it may be noticed that the quantum efficiency of nanowire LEDs generally reaches its peak value at significantly higher current densities (> 200 A/cm²), compared to those (< 20 A/cm²) of conventional InGaN/GaN quantum well blue LEDs [38, 329, 332, 333]. This observation is consistent with the simulated Shockley-Read-Hall recombination coefficient (A ~ 7×10^8 s⁻¹) at 300 K in the present nanowire LEDs, which is significantly larger than the values commonly employed in InGaN/GaN quantum well blue LEDs [157, 158] and can be partly explained by the significantly enhanced nonradiative surface recombination, due to the very large surface-to-volume ratios of nanowires. This phenonema is further investigated and described in Chapter 6. The commonly observed surface band bending in GaN nanowires [286], as well as the inefficient carrier capture by quantum dots due to hot carrier effect [334, 335], may also contribute considerably to the nonradiative carrier recombination on nanowire surfaces. As a consequence, emission characteristics of nanowire LEDs are predominantly determined by surface-related nonradiative carrier recombination under relatively low carrier injection conditions. In the absence of any 3rd or higher order carrier loss mechanisms, it is further expected that the quantum efficiency should display a small, continuous increase under high injection conditions, illustrated as the dotted blue line in figure 5.9. To date, however, such phenomena have not been observed in nanowire LEDs [17, 38, 329, 332, 336], suggesting the presence of electron overflow or any other high order carrier loss mechanisms, which can lead to either a nearly constant quantum efficiency or efficiency droop under high injection currents.

It has been demonstrated that carrier leakage and electron overflow plays a dominant role in the efficiency droop of GaN based planar LEDs [127, 166, 167, 172], which is directly related to the ineffective electron confinement [337], poor hole transport [338], and even possibly Auger recombination [127] and can be further exasperated by the presence of polarization fields [124]. In this experiment, the more severe efficiency degradation measured at lower temperatures indicates that Auger recombination and Auger-assisted overflow are not likely the primary mechanisms responsible for efficiency droop in nanowire devices, since Auger recombination

coefficient (*C*) generally decreases exponentially with decreasing temperature. This study is also consistent with recent results that Auger recombination is drastically reduced in nearly defect-free GaN-based nanowire devices [329]. Further study on the electron overflow is performed by simulating the band-diagram and carrier distribution in the device active region using the advanced LED device simulation software APSYS (Crosslight Software, 2011). The simulated LED active region consists of ten vertically coupled InGaN quantum dots, separated by ~ 3 nm GaN barrier layers. With an average In composition of ~ 20% in the dots, ~ 10% of the injected current density can leak into the p-GaN region under an injection current density of ~ 1,000 A/cm², illustrated as the black curve in figure 5.11. However, much more severe electron overflow is expected, due to the highly nonuniform In distribution along the lateral dimension of the wires. More importantly, the current path associated with the near-surface GaN region, presented by the black curve in the inset of figure 5.12, can contribute significantly to electron overflow in InGaN/GaN dot-in-a-wire LEDs as well.

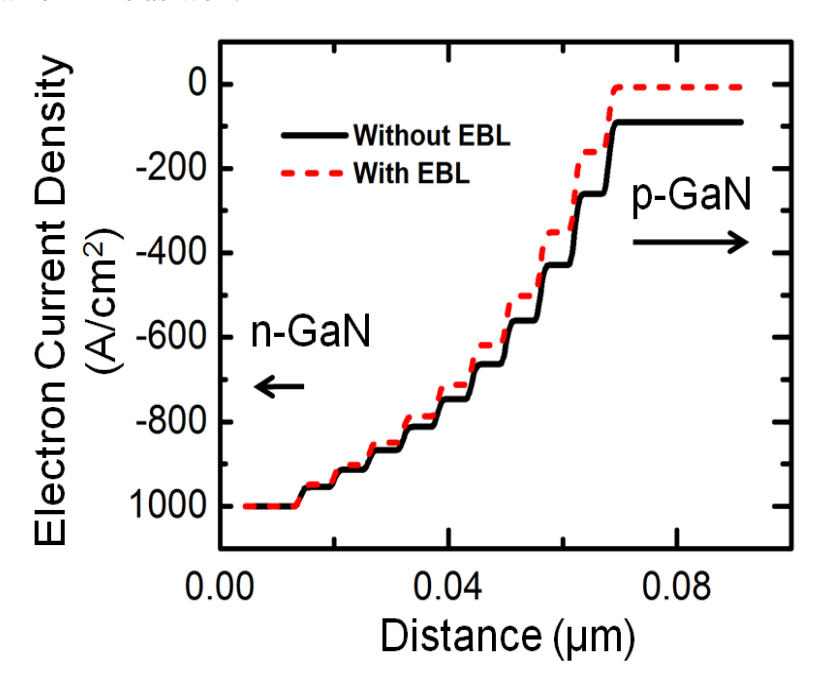


Figure 5.11: Simulated electron current density across the InGaN/GaN quantum dot active region using the APSYS simulation package (Crosslight Software, 2011) with (red dashed curve) and without (black curve) the incorporation of an AlGaN electron blocking layer (EBL).

Simulations were also performed on LED III, wherein a p-doped AlGaN electron blocking layer is incorporated between the quantum dot active region and p-GaN. It can be seen that the electron overflow, through both the quantum dot active region and the near-surface GaN, can be largely eliminated, illustrated as the red dashed curve in figure 5.11 and also in figure 5.12 [330, 331], for Al compositions in the range of ~ 15%. The use of higher Al composition, however, may significantly reduce the hole injection efficiency. Detailed studies also suggest that the use of an electron blocking layer can be significantly more effective in preventing electron overflow in InGaN/GaN nanowire LEDs, due to the drastically reduced polarization fields, compared to conventional InGaN/GaN quantum well devices [127, 339].

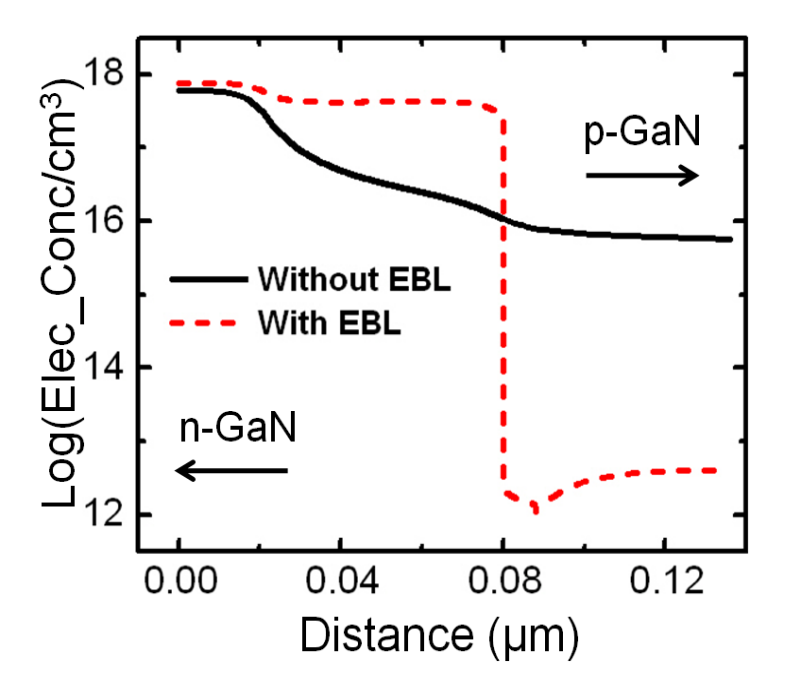


Figure 5.12: The electron density distribution across the near surface GaN region of the nanowire LEDs with (red dashed curve) and without (black curve) the incorporation of an AlGaN electron blocking layer.

5.3.2 Reduced Electron Overflow with the Incorporation of AlGaN Electron Blocking Layer

To enhance the LED performance, it is critically important to minimize electron overflow and to achieve fairly uniform carrier distribution in the device active region. Described in Chapter 4, It has been demonstrated that improved hole transport and injection can be achieved by using the technique of p-type modulation doping in nanowire LEDs [38]. Additionally, the incorporation of an AlGaN electron blocking layer between the device active region and the p-GaN has shown to be highly effective in reducing electron overflow in GaN-based LED and laser heterostructures [330, 331]. To this end, we have investigated the effect of electron blocking layer in nanowire LEDs. Experimentally, the effectiveness of utilizing an AlGaN electron blocking layer in preventing electron overflow in nanowire LEDs is demonstrated by examining the electroluminescence spectra of LED II, wherein an 8 nm Al_{0.15}Ga_{0.85}N electron blocking layer is incorporated between the quantum dot active region and the InGaN test well. The measurements were performed up to very high injection conditions (~ 1,222 A/cm²) at 80 K, 200 K, and 300 K, illustrated in Figure 5.13. Compared to the photoluminescence results shown in figure 5.2, however, only emission from the quantum dot active region ($\lambda_{peak} \sim 550$ nm) can be observed under electrical injection, and any emission from the test well (~ 430 nm) is absent for measurements performed at various injection conditions and temperatures, which confirms the drastically reduced, or eliminated electron overflow by the AlGaN electron blocking layer.

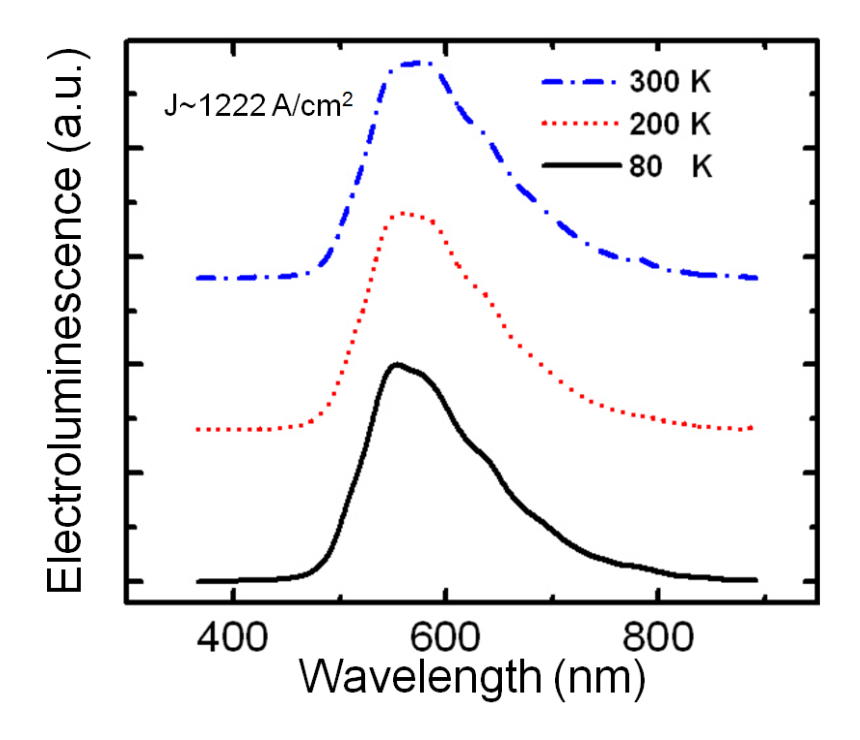


Figure 5.13: Electroluminescence spectra of LED II measured under 1200 mA injection current at 80, 200, and 300 K. Emission peak from the test well is not observed, confirming the drastically reduced, or the absence of electron overflow in the LED devices with the incorporation of an electron blocking layer.

The performance characteristics of LED III, which consists of ten vertically aligned InGaN/GaN quantum dots and an AlGaN electron blocking layer are subsequently investigated. Variations of the relative external quantum efficiency with injection current are measured at 80 K, 200 K, and 300 K, depicted in figure 5.14. It is observed that the quantum efficiency first shows a drastic increase with increasing current, which is directly related to the saturation of defects with increasing carrier density. A very interesting phenomenon, however, is that the quantum efficiency shows a small, continuous increase upto very high injection currents (~ 1,222 A/cm²), which has not been measured in previously reported nanowire LEDs [38, 329]. Such unique characteristics can be well modeled using the ABF model, described by Eqn.

(1), for the LED internal quantum efficiency. Shown in figure 5.14, the calculated internal quantum efficiencies (solid curves) are in excellent agreement with the experimental results. The derived (A, B, C) values are $(7.2 \times 10^7 \text{ s}^{-1}, 6.8 \times 10^{-10} \text{ cm}^3 \text{ s}^{-1}, 1.0 \times 10^{-34} \text{ cm}^6 \text{ s}^{-1})$, $(8.9 \times 10^7 \text{ s}^{-1}, 5.6 \times 10^{-10} \text{ cm}^3 \text{ s}^{-1}, 2.0 \times 10^{-34} \text{ cm}^6 \text{ s}^{-1})$, and $(9.6 \times 10^7 \text{ s}^{-1}, 3.9 \times 10^{-10} \text{ cm}^3 \text{ s}^{-1}, 3.0 \times 10^{-34} \text{ cm}^6 \text{ s}^{-1})$ at 80 K, 200 K, and 300 K, respectively. While the values for A and B are reasonably close to those calculated for LED I, the values for C are nearly five orders of magnitude smaller, confirming the drastic reduction of electron overflow by the AlGaN electron blocking layer. These studies also strongly suggest that Auger recombination plays a very small, or negligible role on the performance of nanowire LEDs, since the Auger coefficient (*C*) is expected to be relatively independent of the incorporation of an AlGaN electron blocking layer.

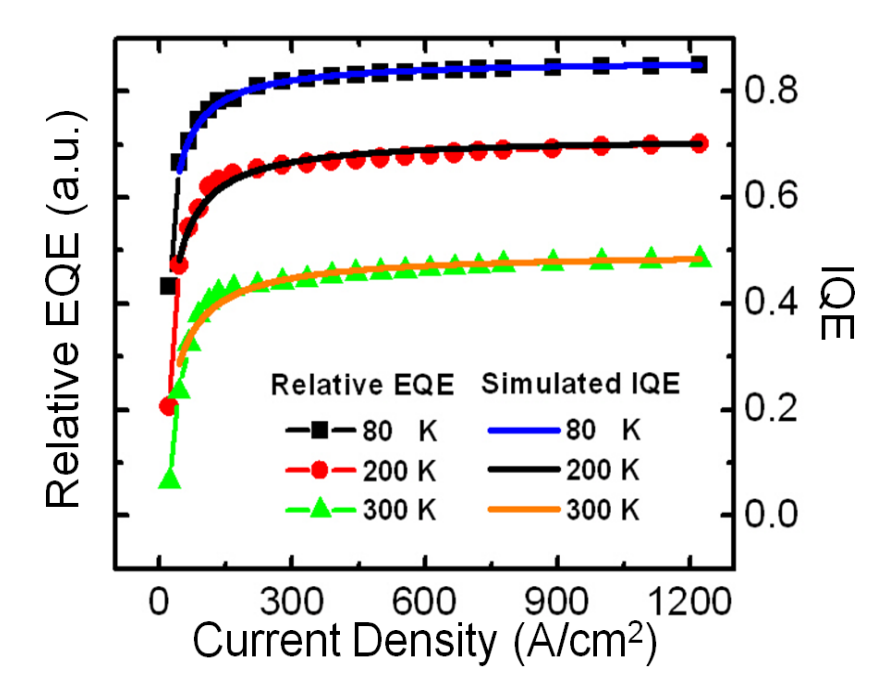


Figure 5.14: Variations of the measured relative external quantum efficiencies of LED III with injection current at 80 K, 200 K, and 300 K. The simulated IQE using the ABF model shows a good agreement with experimental results.

Finally, we have investigated InGaN/GaN dot-in-a-wire LEDs with the incorporation of an AlGaN electron blocking layer as well as the special technique of p-type modulation doping in the device active region. The design and characterization

of p-doped nanowire LEDs were discussed in detail in Chapter 4. As demonstrated previously, the technique of p-type modulation doping can significantly improve the performance of nanowire LEDs by enhancing the hole injection and transport process in the quantum dot active region [38, 338]. Variations of the relative external quantum efficiency with current density at room temperature measured for such nanowire LEDs are shown in figure 5.15. It is seen that the quantum efficiency first shows a significant rise (upto $\sim 400 \text{ A/cm}^2$), followed by small, continuous increase at higher injection conditions. There is virtually no efficiency degradation for injection current density up to $\sim 2,200 \text{ A/cm}^2$. With the use of the ABF model, the values of A, B and C are estimated to be $\sim 2.7 \times 10^8 \text{ s}^{-1}$, $4 \times 10^{-10} \text{ cm}^3 \text{ s}^{-1}$, and $1.0 \times 10^{-34} \text{ cm}^6 \text{ s}^{-1}$, respectively. Additionally, such dot-in-a-wire LEDs can exhibit highly stable white-light emission.

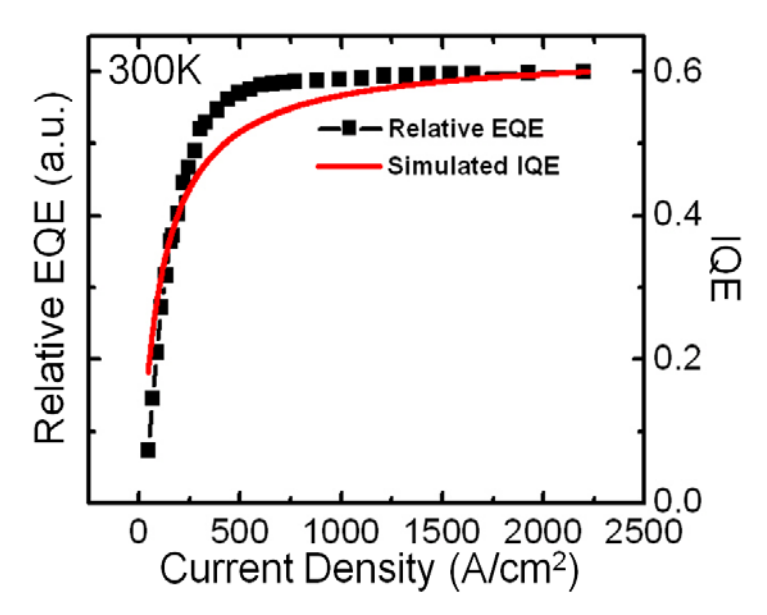


Figure 5.15: Relative external quantum efficiency measured at room temperature for the InGaN/GaN dot-in-a-wire LED with the incorporation of an AlGaN electron blocking layer and p-type modulation doping in the device active region.

Locations of the light emission on the chromaticity diagram are shown in the inset of figure 5.16 under various injection conditions (from $\sim 333~\text{A/cm}^2$ to 1,100 A/cm^2), with the values x and y in the ranges of $\sim 0.33-0.35$ and 0.36-0.38, respectively. The extremely stable white light emission is attributed to the large

inhomogeneous broadening of the dots, the highly uniform carrier distribution in the LED active region, and the drastically reduced QCSE in the nanowire heterostructures.

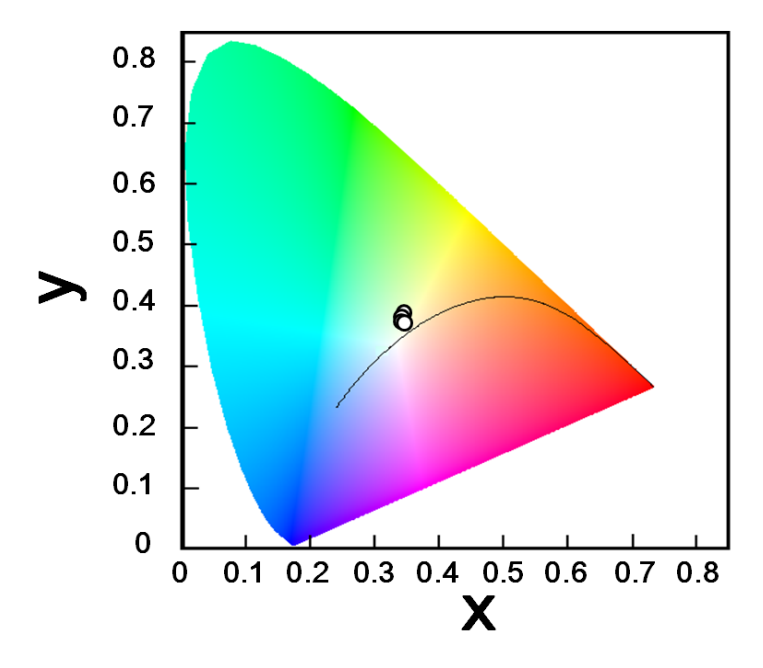


Figure 5.16: the 1931 Commission International de l'Eclairage chromaticity diagram. The device exhibits highly stable emission characteristics, with x and y in the ranges of $\sim 0.33 - 0.35$, and 0.36 - 0.38, respectively.

It is important to notice that, in the current nanowire LEDs, the peak quantum efficiency occurs at relatively high injection levels at room temperature [17, 329, 332, 336], which is largely due to the presence of surface states/defects and energy band bending along the lateral dimension of the wires. Additionally, the incorporation of an AlGaN electron blocking layer may significantly reduce hole injection efficiency, leading to reduced quantum efficiency at relatively low injection currents. It has been recently measured that the electroluminescence intensity in GaN-based LEDs can be drastically reduced, due to the hole blocking effect [340]. It is therefore important to optimize the thickness and compositions of the AlGaN electron blocking layer in order to achieve nanowire LEDs with both high quantum efficiency and negligible efficiency degradation at high injection currents, which is currently under investigation.

5.4 Conclusion

In summary, through extensive theoretical and experimental studies, we have demonstrated unambiguously that the maximum achievable quantum efficiency of GaN-based nanowire LEDs is ultimately limited by electron leakage and overflow, rather than Auger recombination. Detailed temperature-dependent studies further confirm that efficiency droop in nanowire LEDs becomes more severe at lower temperatures, which is directly correlated with the relatively enhanced electron overflow with decreasing temperature. We have further achieved, for the first time, an effective control of electron overflow in phosphor-free InGaN/GaN dot-in-a-wire white LEDs by incorporating a p-doped AlGaN electron blocking layer between the quantum dot active region and the p-GaN. The resulting nanowire LEDs exhibit remarkably stable white-light emission and are virtually free of any efficiency degradation upto ~ 2,200 A/cm². This work has identified and addressed one of the major obstacles of nanowire LEDs for applications in future high power phosphorfree, all-semiconductor based solid state lighting. Detail analysis of nonradiative recombination and the effect of nanowire surface states/defects on the nanowire LED performance is further described in Chapter 6.

Chapter 6: Temperature-Dependent Nonradiative Recombination Processes in GaN-Based Nanowire White-Light-Emitting Diodes on Silicon

6.1 Introduction

GaN-based nanowire light emitting diodes (LEDs) hold promising applications in solid state lighting and full-color flat panel displays. Compared to conventional planar LED heterostructures, the use of nanowires offer several extraordinary advantages, including drastically reduced dislocation densities and polarization fields, enhanced light output efficiency due to the large surface-to-volume ratios, and the compatibility with low cost, large area Si substrates. Emission wavelengths ranging from UV to near-infrared have been demonstrated using GaN-based nanowire heterostructures [115, 284, 309, 332, 341]. More recently, high efficiency phosphor-free white-light emission has been realized by embedding quantum dots, disks, or wells in GaN nanowires [121, 332, 336]. However, the quantum efficiency of currently reported nanowire LEDs generally exhibits a very slow rise with injection current. As a consequence, the peak quantum efficiency of such devices can only be measured under relatively large injection conditions (>100 A/cm²), compared to that (~ 10-20 A/cm²) of conventional InGaN/GaN quantum well blue LEDs [38, 329, 336], indicating the presence of a significant level of nonradiative carrier recombination process [151]. To date, a detailed understanding of such unique emission characteristics and the fundamental carrier loss mechanisms of nanowire LEDs has remained elusive.

It has been generally reported that defects and dislocations [123, 326], Auger recombination [126, 157], electron overflow [124, 167], polarization fields [124, 125], and poor hole transport [128] all play important roles in the output characteristics of GaN-based LEDs. The previous described ABF model (Eqn. 5.1) has been commonly used to study various carrier recombination processes and the

internal quantum efficiency of GaN-based LEDs. The Shockley-Read-Hall (SRH) nonradiative recombination and radiative recombination coefficients are described by A and B, respectively. f(N) is generally used to describe any other higher order carrier loss processes, such as Auger recombination and electron overflow. Mathematically, it can be written as $CN^3 + DN^4$. In nanowire devices, due to the highly effective lateral stress relaxation associated with the large surface areas, it is expected that both the polarization fields and dislocation densities can be significantly reduced. However, the presence of surface states and defects, due to the large surface-to-volume ratios of nanowires, can contribute significantly to the carrier loss in nanowire LEDs. Additionally, it has remained debatable whether Auger recombination plays an important role on the performance of GaN-based devices [126, 329, 342, 343].

In this context, we have performed a detailed investigation of the temperaturedependent carrier recombination processes in GaN-based nanowire LEDs. Selforganized InGaN/GaN quantum dots are incorporated in nearly defect-free GaN nanowires to achieve white-light emission. To evaluate the impact of Auger recombination on the performance of nanowire LEDs, a p-doped AlGaN electron blocking layer is incorporated between the quantum dot active region and the p-GaN region, which can effectively reduce other 3rd or higher order carrier loss mechanisms due to electron overflow. It is observed that efficiency droop is absent in such novel phosphor-free white LEDs in the temperature range from 6 to 440 K. The Auger coefficient is derived to be in the range of $\sim 10^{-34}$ cm⁻⁶s⁻³, or less, which is nearly four orders of magnitude smaller than the commonly reported values in InGaN/GaN quantum well LEDs [126, 157, 159], suggesting that Auger recombination plays an essentially negligible role on the performance of InGaN/GaN dot-in-a-wire LEDs. However, it is observed that the performance of such nanowire LEDs suffers severely from SRH recombination, which accounts for nearly 40% of the total recombination under injection current of ~ 100 A/cm² at room temperature. The carrier nonradiative lifetime is estimated to be in the range of ~ 5.5 ns at room temperature, which correlates well with the surface recombination velocity of GaN and the wire diameters used in this experiment [344]. This work has elucidated the primary carrier loss mechanisms in GaN-based nanowire LEDs and also provides a critical insight for the design and development of practical nanowire devices.

6.2 Experimental Details

In this experiment, phosphor-free InGaN/GaN nanowire white LED, which has the same structure as LED III described in Chapter 5, was used for characterization. The nanowire LED heterostructures were grown by plasma-assisted molecular beam epitaxy without using any foreign metal catalyst. The top and bottom segments of the GaN nanowires are doped p- and n-type using Mg and Si, respectively. The device active region consists of 10 vertically aligned InGaN/GaN quantum dots. Each dot has a height of ~ 3 nm and is capped by ~ 3 nm GaN barrier layer. A p-doped AlGaN electron blocking layer (EBL) is incorporated between the quantum dot active region and the GaN:Mg segment. The use of such an EBL can effectively reduce electron leakage/overflow from the device active region [127, 331, 345, 346]. Detailed growth conditions for the dot-in-a-wire LEDs are described in chapter 3 [38, 332].

Structural properties of this InGaN/GaN dot-in-a-wire heterostructures were characterized by a CM200 microscope with acceleration voltage of 200 kV. Figure 6.1 shows the bright field transmission electron microscopy (TEM) image of a dot-in-a-wire heterostructure, wherein the ten InGaN quantum dots and AlGaN EBL can be clearly indentified. Shown in figure 6.1, the energy dispersive x-ray spectrometry (EDXS) analysis together with the annular dark field image confirm the existence of multiple InGaN/GaN quantum dots. The thickness of the AlGaN EBL is ~ 8 nm and the Al composition of the electron blocking layer is estimated to be ~ 15%. The dot-in-a-wire LED heterostructures exhibit excellent optical properties. Shown in figure 6.2 is the photoluminescence spectrum measured at room temperature using a 405 nm laser. The emission spectrum covers nearly the entire visible wavelength region, with the peak centered at ~ 550 nm. Such dot-in-a-wire nanoscale LED heterostructures can exhibit relatively high internal quantum efficiency (~ 30% to 60%) at room temperature [16, 38, 332].

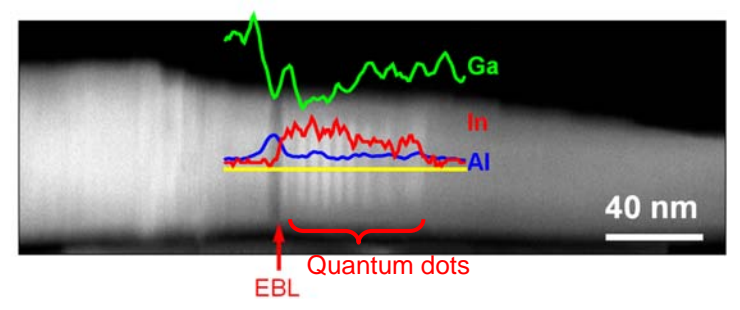


Figure 6.1: Bright field TEM image and EDXS analysis of a single InGaN/GaN dotin-a-wire structure, wherein the AlGaN EBL and InGaN/GaN quantum dots are identified.

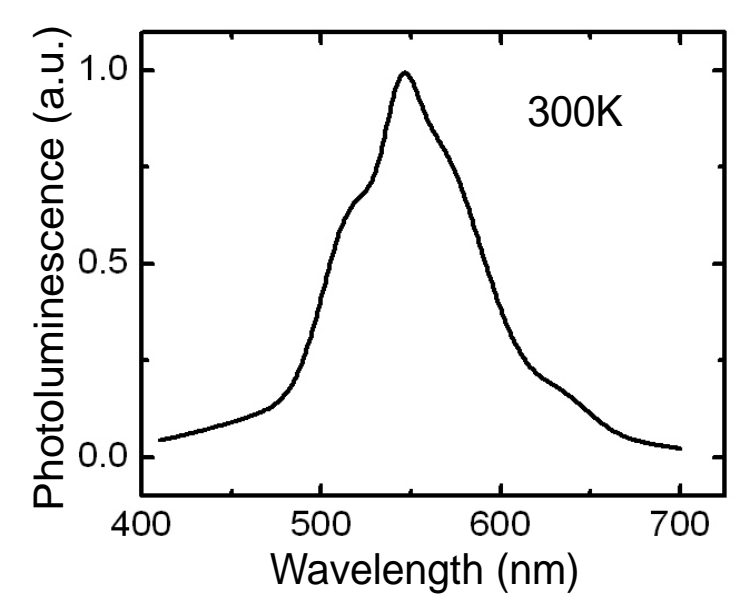


Figure 6.2: Room-temperature photoluminescence spectrum of the dot-in-a-wire LED heterostructure.

6.3 Results and Discussion

Output characteristics of nanowire LEDs with areal size of $\sim 300\times300~\mu\text{m}^2$ were measured under pulsed biasing conditions in the temperature range of 6 K to 440 K. The use of pulsed biasing measurement (duty cycle of $\sim 0.1\%$) can drastically reduce junction heating effect. Figure 6.3 shows the normalized electroluminescence spectra measured under various injection currents at room-temperature.

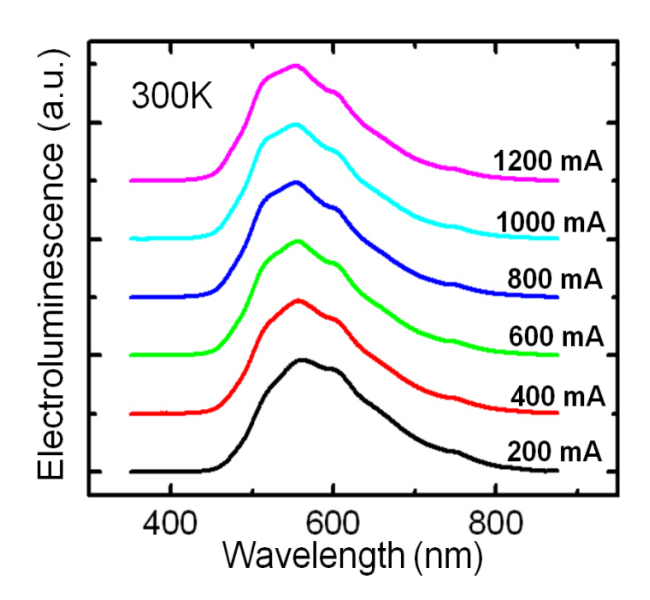


Figure 6.3: Electroluminescence spectra of a phosphor-free InGaN/GaN dot-in-a-wire white LED measured under various injection currents at room temperature.

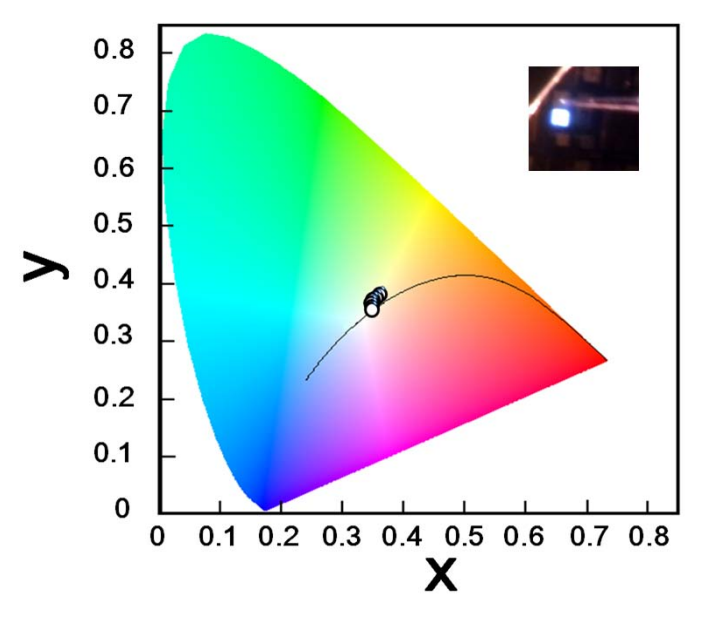


Figure 6.4: Locations of the light emission characteristics shown in the 1931 Commission International de l'Eclairage chromaticity diagram at injection currents from 300 mA to 800 mA. The optical image of the white LED is shown in the inset.

The devices can exhibit strong white-light emission with broad spectral linewidths (full-width-half-maximum ~ 145 nm), due to the compositional variations of the dots in the active region. The device emission characteristics are further

illustrated in the chromaticity diagram under various injection currents (300 mA to 800 mA), shown in figure 6.3. The derived x and y values vary in the ranges of $\sim 0.34 - 0.36$ and 0.36 - 0.38, respectively. The optical image of the white-light LED is also shown in the inset of figure 6.4.

Shown in figure 6.5, variations of the relative external quantum efficiencies with injection currents were measured in the temperature range of 6 K to 440 K, which exhibit two distinct characteristics. The first remarkable feature is that the nanowire white LEDs are free of efficiency droop even under very high injection conditions (up to 1,000 A/cm², or larger), compared to the commonly observed efficiency droop of conventional GaN-based quantum well LEDs [38, 131, 329, 332, 333]. Second, it is seen that with increasing current, there is a very slow rise in the quantum efficiency. For example, the efficiency reaches the maximum value at an injection current density of ~ 280 A/cm² at room temperature, which is nearly a factor of 10 times larger than the commonly reported values for conventional GaN-based quantum well LEDs [124, 157, 347].

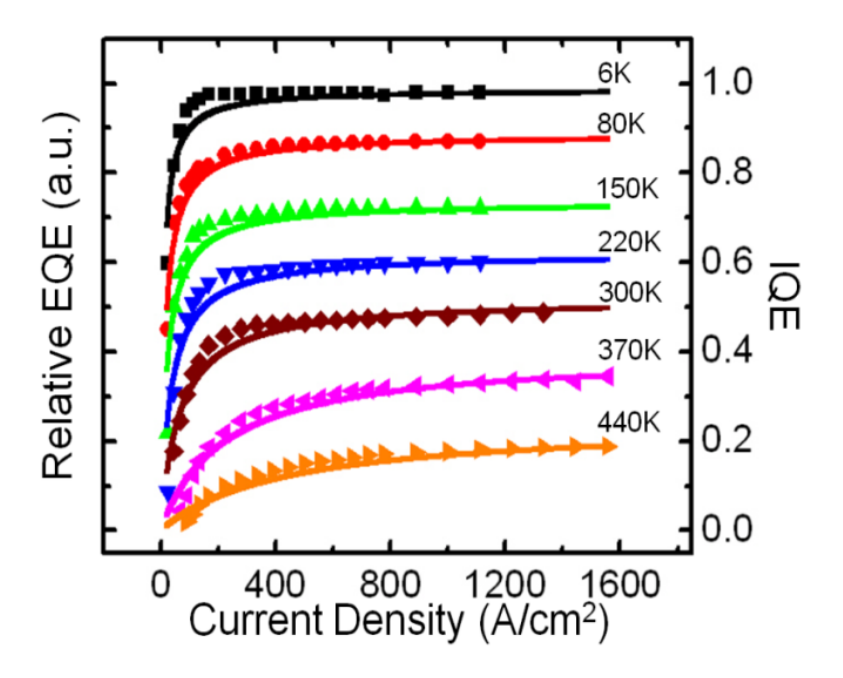


Figure 6.5: Variations of the relative external quantum efficiencies (EQE) with injection current measured in the temperature range of 6 K to 440 K. The simulated internal quantum efficiencies (IQE) using the ABF model are also shown for comparison.

The injection current at which the quantum efficiency reaches ~ 80% of its peak value is plotted as a function of temperature in figure 6.6. It is seen that this critical current density increases significantly with temperature. The very slow rise of the quantum efficiency has been commonly reported in nanowire LEDs [38, 329, 332]. For comparison, the current densities at which conventional blue-emitting InGaN/GaN quantum well LEDs reach their peak efficiency are generally in the range of < 15 A/cm² [124, 333, 347-349], which, together with other reported values of GaN-based nanowire LEDs are also shown in figure 6.6.

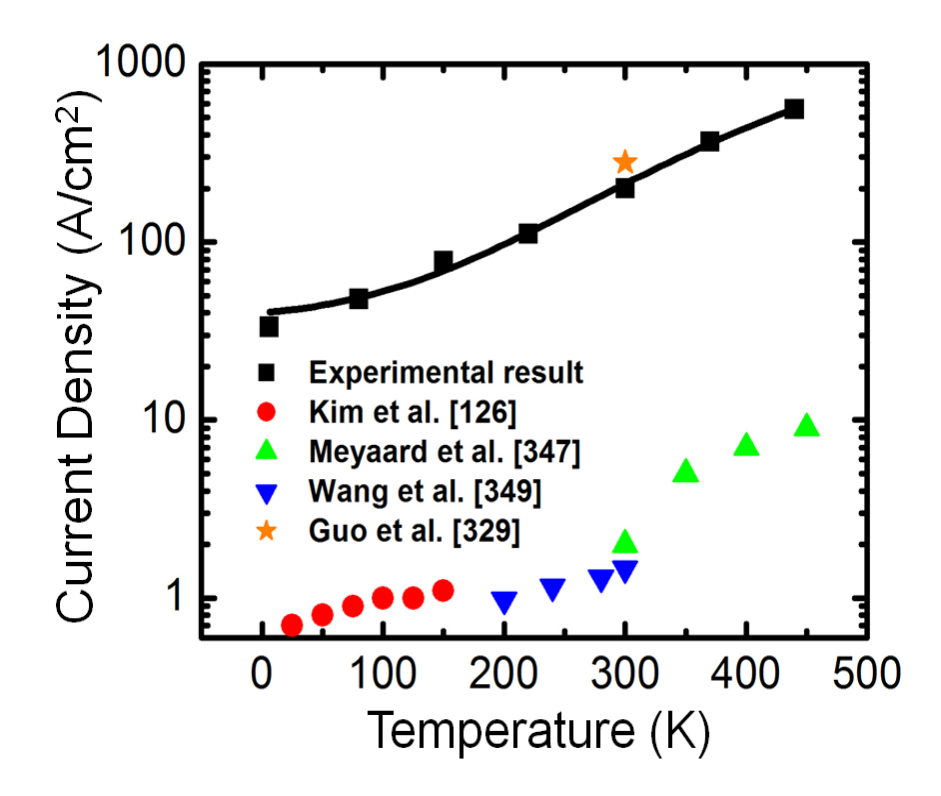


Figure 6.6: Plot of the current densities (solid squares) at which the quantum efficiency reaches ~ 80% of its peak value as a function of temperature. The current densities at which conventional GaN-based quantum well LEDs (solid circles and triangles) and other reported GaN-based nanowire LEDs (star) reach their peak quantum efficiencies are also shown for comparison. The solid circles, upward triangles, downward triangles, and star denote the data obtained from references 126, 347, 349, and 329, respectively.

In order to understand these unique emission characteristics, we have evaluated the radiative and nonradiative recombination processes in GaN-based nanowire LEDs using the internal quantum efficiency model described in Eqn. (5.1). The calculated results are plotted as the solid curves in figure 6.5, which are in excellent agreement with the experimental data. The absence of efficiency droop in the dot-in-a-wire LEDs is first investigated. From the simulation studies, the C coefficient is estimated to be in the range of $\sim 10^{-34}$ cm⁻⁶s⁻¹ and is nearly temperature independent. For conventional GaN-based quantum well LEDs, the presence of efficiency droop is generally attributed to the 3rd or higher order carrier loss mechanisms, including Auger recombination, electron overflow, carrier leakage, and/or polarization fields. For III-nitride nanowire devices, however, strain-induced polarization fields can be drastically reduced, due to the highly effective lateral stress relaxation related to the large surface-to-volume ratios [15, 16, 115]. Additionally, for the present nanowire LED design, an AlGaN EBL layer is incorporated between the quantum dot active region and the p-GaN, which can greatly minimize or largely prevent electron overflow. To further evaluate the significance of Auger recombination, we have compared the derived C coefficient with the commonly reported Auger coefficients in GaN-based materials and devices, shown in Table 6.1. It is seen that the derived C coefficient (~ 10⁻³⁴ cm⁻⁶s⁻¹) in this experiment is nearly four orders of magnitude smaller than the commonly reported values in InGaN quantum well heterostructures [157, 159, 333], thereby suggesting that Auger recombination plays an essentially negligible role on the performance of the present InGaN/GaN dot-in-a-wire LEDs even under relatively high injection conditions. Compared to conventional planar heterostructures, InGaN/GaN nanowire InGaN/GaN quantum well heterostructures are nearly free of defects and dislocations. As a consequence, defectassisted Auger recombination, which may be dominant in conventional planar LED heterostructures, is expected to be negligibly small in nanowire LEDs. This observation is also consistent with recent theoretical and experimental studies [329, 342]. Additionally, the strong carrier confinement offered by the unique dot-in-a-wire nanoscale heterostructure may contribute to the greatly suppressed Auger recombination [350]. It is also important to notice that, without the incorporation of a suitable AlGaN EBL layer, significant electron overflow/carrier leakage was observed in GaN-based nanowire LEDs, as discussed in Chapter 5, which can lead to efficiency droop under relatively high injection conditions.

Table 6.1: List of commonly reported Auger coefficients in InGaN/GaN heterostructures.

Materials	λ (nm)	C (cm ⁶ s ⁻¹)
InGaN/GaN [159]	450	0.35×10 ⁻³⁰
In _{0.22} Ga _{0.78} N/GaN [333]	480	2×10^{-30}
InGaN/GaN [158]	450	1.0×10^{-30}
$In_{0.1}Ga_{0.9}N/GaN$ [157]	410	1.5×10^{-30}
$In_{0.15}Ga_{0.85}N/GaN$ [126]	440	2.0×10^{-30}
InGaN nanowire [329]	500	6.1×10^{-32}
InGaN/GaN disk-in-a-wire [329]	500	4.1×10^{-33}

The slow rising trend of the quantum efficiency observed in nanowire LEDs is directly related to the large SRH recombination. Illustrated in figure 6.7 is the derived contribution of SRH recombination to the total carrier recombination vs. injection current measured at various temperatures. It is seen that the SRH recombination can account for more than 30% of the total recombination even at relatively low temperatures under low injection conditions. With increasing temperature, the SRH recombination becomes appreciably more important. For example, under an injection current of ~ 100 A/cm², the SRH recombination accounts for ~ 8%, 40%, and 80% of the total recombination at 6 K, 300 K, and 440 K, respectively. The significantly enhanced SRH recombination with temperature explains the drastically increased current density at which the quantum efficiency reaches its peak values at elevated temperatures, illustrated in figure 6.6. It also leads to the reduction of the maximum achievable quantum efficiency with increasing temperature, shown in figure 6.5.

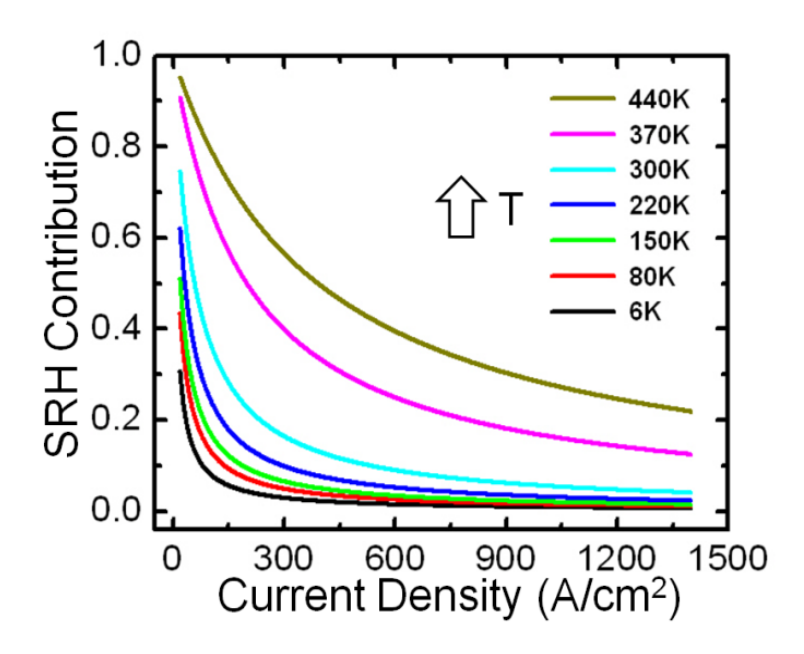


Figure 6.7. Plot of the SRH recombination contribution versus injection current in the temperature range of 6 K to 440 K.

To further understand the significance of SRH recombination, we have plotted the derived A coefficients as a function of temperature, shown in figure 6.8. It is seen that the values of A vary from $\sim 5.5 \times 10^7 \text{ s}^{-1}$ to $4.6 \times 10^8 \text{ s}^{-1}$ from 6 K to 440 K, with the corresponding SRH nonradiative lifetimes in the range of ~ 18.3 ns to 2.2 ns. At room temperature, the A coefficient is approximately 1.8×10^8 s⁻¹, which is significantly larger than the commonly reported values (~ 10⁷ s⁻¹) of conventional InGaN/GaN quantum well LEDs [158, 347, 351]. This observation is in direct contrast to the drastically reduced defect densities associated with nanowire heterostructures. The somewhat unexpected large nonradiative recombination of nanowire LEDs, however, can be qualitatively understood by considering carrier recombination on the lateral surfaces. Due to the extremely large surface-to-volume ratios and the presence of surface states and defects, nonradiative carrier recombination on the wire surfaces may become appreciable. Detailed studies further confirm the presence of band bending on the lateral surfaces of GaN nanowires, which can lead to further enhanced surface recombination [286]. Additionally, the significant nonradiative surface recombination may be related to the hot carrier effect [334, 335], ineffective electron confinement [337], and poor hole transport [128] of GaN-based LED heterostructures as well.

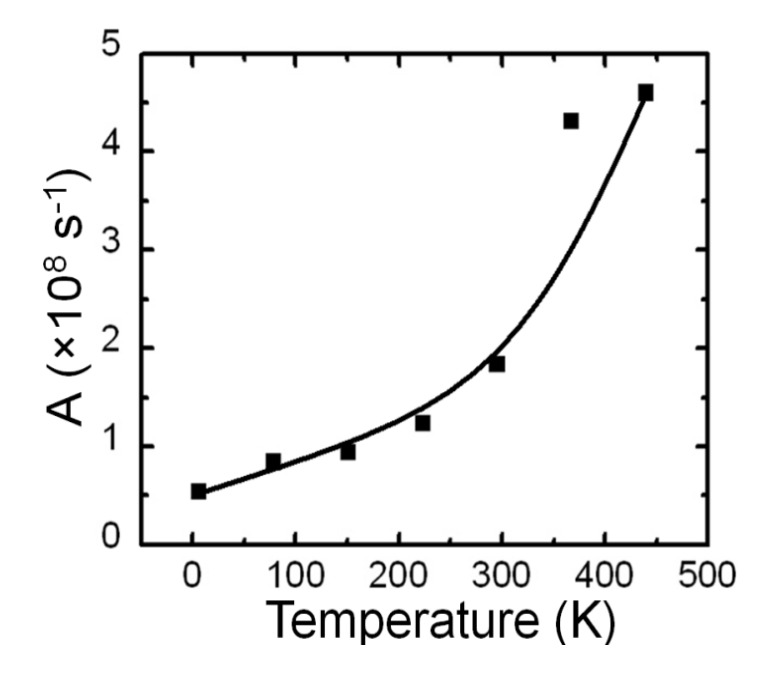


Figure 6.8: Variation of the SRH nonradiative recombination coefficient with temperature

The commonly reported surface recombination velocity on GaN surfaces is in the range of $\sim 10^3$ to 10^4 cm/s [352, 353]. In the present study, the average radius of GaN-nanowires is ~ 40 nm. Therefore, the *A* coefficient, due to carrier surface recombination, is estimated to be in the range of $\sim 10^8$ to 10^9 s⁻¹, which agrees quantitatively well with the simulated results shown in figure 6.8. Variations of the SRH nonradiative lifetime vs. temperature are also plotted in figure 6.9. By comparing this temperature dependence and the following theoretical model,

$$\tau_{nr} = \tau_0 \left(1 + \cosh \frac{E_T - E_{Fi}}{kT} \right)$$

where E_T and E_{Fi} denote the trap energy and the intrinsic Fermi level, respectively, we have derived that the trap energy level is separated from the intrinsic Fermi level by ~ 0.063 eV. However, the exact nature of the trap states and defects needs to be further investigated.

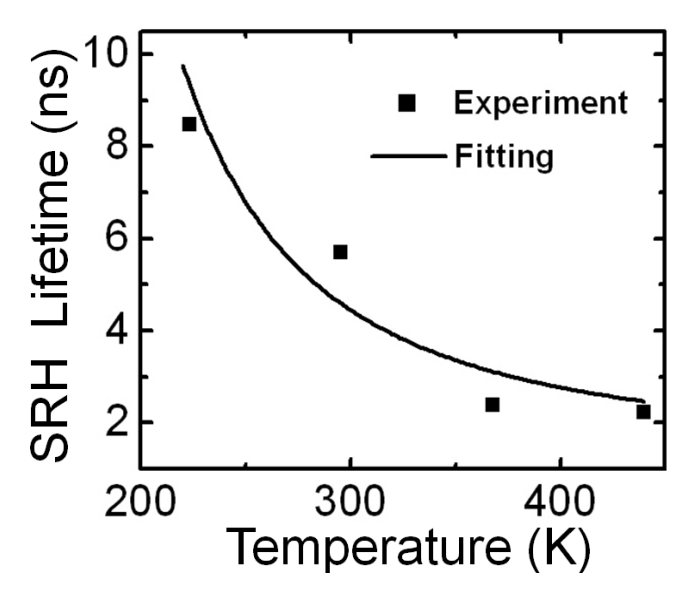


Figure 6.9: The corresponding nonradiative recombination lifetime at different temperatures and the theoretical fit using a trap energy of ~ 0.063 eV separated from the intrinsic Fermi level.

Clearly, the surface SRH recombination, if not remediated, can severely degrade the performance of nanowire LEDs. It can lead to a very slow rise in the quantum efficiency and further limits the maximum achievable efficiency at high injection levels. Consequently, significantly improved device performance can be possibly achieved by embedding the InGaN/GaN dot-in-a-wires in a large bandgap AlGaN shell structure to minimize nonradiative recombination on the wire surfaces [15, 354], while maintaining the benefits associated with the large surface-to-volume ratios of nanowire LEDs.

6.4 Conclusion

In conclusion, through detailed analysis of the temperature- and current-dependent electroluminescence emission of InGaN/GaN nanowire LEDs, we have demonstrated that SRH recombination, due to the large surface-to-volume ratios and the presence of surface states and defects, is largely responsible for the unique characteristics of GaN-based nanowire LEDs. Detailed studies further confirm that, for nanowire LEDs with the incorporation of a suitable EBL, any 3rd or higher order carrier loss mechanisms can become essentially negligible, thereby leading to phosphor-free white LEDs that are free of efficiency droop even under very large injection conditions. This work provides unambiguous evidence that Auger recombination plays an essentially negligible role on the performance of InGaN/GaN dot-in-a-wire LEDs. It further elucidates the role of nonradiative recombination on the performance limit of nanowire LEDs and offers critical insight for the future development of practical nanowire photonic devices.

Chapter 7: InN Nanowires for Photovoltaic Applications

7.1 Introduction

To date, solar cells with the highest efficiencies, ~ 32.0% and 40.7% have been realized in III-V stacked cells and concentrators, respectively [355-361]. Such devices are generally grown on GaAs, InP or Ge substrates, which are prohibitively expensive and, as a result, their terrestrial applications have been very limited. Additionally, the performance of current multi-junction solar cell devices are generally limited by the poor absorption in the energy ranges of 1.0 – 1.2 eV and 2.5 – 3.4 eV [356, 362-364]. The energy band-gap or absorption spectrum of In_xGa_{1-x}N alloy can be continuously varied from 0.7 to 3.4 eV, representing the only semiconductor that can encompass nearly the entire solar spectrum, promising low cost, high efficiency full-solar-spectrum solar cells [84, 365]. One of the most critical, yet missing technology for future III-nitride based full-solar-spectrum solar cells, however, is a functional InN-based single junction device. In this regard, we have studied the epitaxial growth, fabrication and characterization of InN:Mg/i-InN/InN:Si nanowire axial structures on n-type Si(111) substrates and demonstrated the first InN nanowire solar cells [366].

Advantages associated with nanowire solar cells include a direct path for charge carrier transport, a large surface area for better light absorption, and a high possibility for multi-exciton phenomena [15, 86, 89]. InN nanowires, or nanocolumns have been intensively investigated, which exhibit a small direct energy bandgap (~ 0.7 eV), high electron mobility, small effective mass, and large electron saturation velocity [77, 202, 367-378]. InN nanowire heterostructures grown on Si or other substrates can exhibit drastically reduced defect densities, due to the highly effective lateral stress relaxation. In this chapter, we present the first experimental demonstration of InN nanowire solar cells. By employing an *in situ* deposited In seeding layer, we have achieved nearly intrinsic InN nanowires directly on Si(111) substrates by molecular beam epitaxy. The growth and characterization of Si and Mg-doped InN nanowires is

also investigated, which can exhibit superior structural and optical properties, discussed in Chapter 2. We have studied the epitaxial growth, fabrication and characterization of InN:Si/i-InN and InN:Mg/i-InN/InN:Si axial nanowire structures on p-type and n-type Si(111) substrates, respectively. With the use of a CdS surface passivation, InN:Mg/i-InN/InN:Si nanowire homojunction solar cells exhibit a highly promising short-circuit current density of ~ 14.4 mA/cm² and power conversion efficiency of ~ 0.68% under simulated one-sun (AM 1.5G) illumination.

7.2 Growth and Characterization of InN Nanowires

The growth and characterization of InN nanowires has been intensively studied. InN nanowires can be formed using the vapour-liquid-solid growth process, the spontaneous formation under nitrogen-rich conditions, or the selective-area growth on nano-patterned substrates [379-381]. Well-spaced, vertically aligned InN nanowires have been grown on Si and other substrates using plasma-assisted molecular beam epitaxy (MBE) or metal organic chemical vapor deposition. The resulting InN nanowires generally exhibit a wurtzite crystal structure, with the growth direction oriented along the c-axis. However, due to the very low dissociation temperature of InN and the very high surface migration rate of In, conventional growth techniques yield InN nanowires with tapered surface morphology and large densities of stacking faults and dislocation [246, 382, 383], which decrease the carrier diffusion length and severely limit the solar cell efficiency. The wires also exhibit very large size dispersion, with significant variations in the diameters and heights. Additionally, due to the extremely low conduction band minimum of InN, any defects, dislocations or impurities generally form donors, thereby leading to very high electron densities, which are commonly measured in the range of $\sim 1 \times 10^{18}$ cm⁻³, or higher for nominally nondoped InN [228, 245-249]. The resulting n-type degenerate InN nanowires exhibit poor optical properties, characterized by nearly temperature and power invariant photoluminescence emission spectra and photoluminescence peak energies (~ 0.7 – 0.8 eV) considerably larger than the bandgap of InN [245, 246, 384]. The

uncontrolled structural, electrical and optical properties have posed a significant challenge for the rational design and fabrication of InN nanowire solar cells.

The realization of InN nanowire solar cells, as well as many other semiconductor devices, has been further limited by the difficulty in achieving p-type doping. In this regard, Mg-doped InN films and the formation of p-type carriers have been investigated both theoretically and experimentally [251, 385-387]. A Fermi level shift toward the valence band was measured in InN:Mg layers [387], and the possibility of p-type doping is further suggested by electrolyte capacitance-voltage measurements [386, 388]. Free-to-acceptor photoluminescence emission has also been observed in Mg-doped InN, with an activation energy of ~ 61 meV derived for the Mg acceptor [251]. In order to compensate the presence of large electron densities of nominally nondoped InN as well as the associated surface electron accumulation, a relatively high concentration of Mg dopant is required, which, however, may lead to the formation Mg-related, donorlike defects [251, 389, 390]. Additionally, the growth and characterization of InN:Mg nanowires, to the best of our knowledge, has not been reported. It has been observed that the incorporation of Mg can significantly affect the formation and structural properties of GaN nanowires [252, 253]. The presence of Mg can greatly reduce the nanowire nucleation time and enhance the growth rate on the nonpolar surfaces, thereby leading to wires with increased diameters and reduced lengths. Deteriorated crystal structures were further observed at relatively high Mg concentrations.

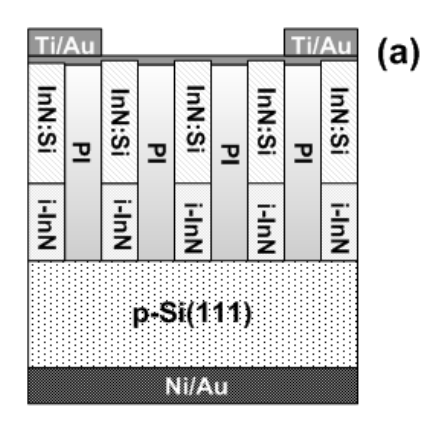
It is therefore important to develop nearly intrinsic InN nanowires as well as InN nanowire p-n junctions, in order to exploit the full potential of InN for third generation photovoltaics. In this context, we have performed a detailed investigation of the MBE growth and characterization of nearly intrinsic and Si- and Mg-doped InN nanowires on Si(111) substrates without using any external metal catalyst, which was discussed in detail in Sec. 2.4 in Chapter 2. Under optimized growth conditions, the wires exhibit nontapered surface morphology and excellent structural and optical properties. An extremely narrow spectral linewidth of ~ 8 meV, compared to the commonly reported values of 50-100 meV for n-type degenerate InN nanowires,

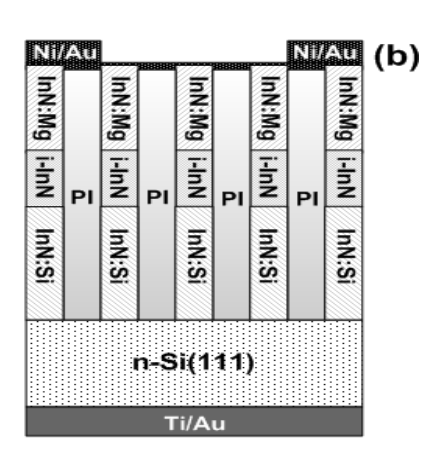
have been achieved for nearly intrinsic InN nanowires. Effects of Si and Mg incorporation on the structural and optical properties of InN nanowires have also been investigated, described in Sec. 2.4.3 in Chapter 2.

7.3 Design and Fabrication of InN Nannowire Solar Cells on Si

Three InN nanowire solar cell designs, schematically illustrated in figures 7.1(a), (b) and (c), have been investigated. In the first approach, shown in figure 7.1(a), the InN nanowire solar cells consist of $\sim 0.3~\mu m$ nondoped and 0.4 μm Si-doped sections, which are grown directly on p-type Si(111) substrates. Such a design does not require the use of p-type InN nanowires, which had not been demonstrated prior to this work. The 2^{nd} and 3^{rd} designs employ InN p-i-n axial homojunctions, illustrated in figures 7.1(b) and (c), which comprise of $\sim 0.8~\mu m$ InN:Si, 0.2 μm nondoped InN, and 0.3 μm InN:Mg sections grown on n-type Si(111) substrates. Compared to the first design, the p-n junction is formed within the wires. It may also be noted that there is a small variation in the thicknesses of the device intrinsic regions, which may not have any major impact on the device efficiency.

One of the primary limitations for semiconductor nanowire devices is the significant nonradiative carrier recombination associated with the presence of surface states, which can be greatly minimized by using core-shell or dot/well-in-a-wire nanoscale heterostructures [16, 309]. In this regard, we have further investigated the use of a CdS passivation technique in the 3rd design. Illustrated in figure 7.1(c), a thin (~ 10 nm) CdS layer is coated on the nanowire surface using a chemical bath deposition method at ~ 70 °C, wherein the bath consists of CdCl₂, NH₄Cl, and NH₄OH, with a molecular proportion of 2:20:20:200 [391]. The resulting CdS layer is nearly intrinsic and exhibits a very high resistivity (~ 10⁶ Ωcm) [392]. Such a passivation/buffer layer has been widely used in the fabrication of CuIn(Ga)Se₂ solar cells and has led to the most efficient (~ 19.9%) thin film solar cells ever reported [393]. Growth conditions for the various nanowire samples have been carefully controlled to achieve high-quality InN nanowires with relatively large diameters (> 150 nm) to effectively enhance the light absorption [394].





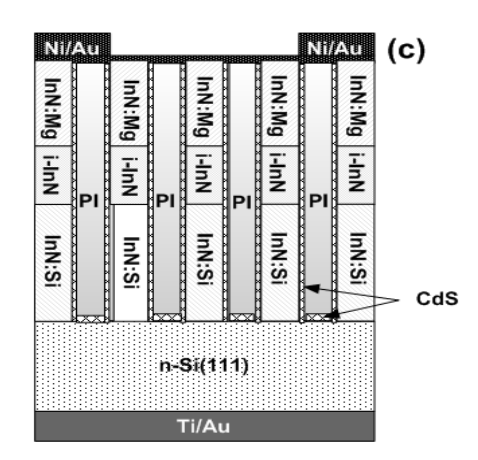
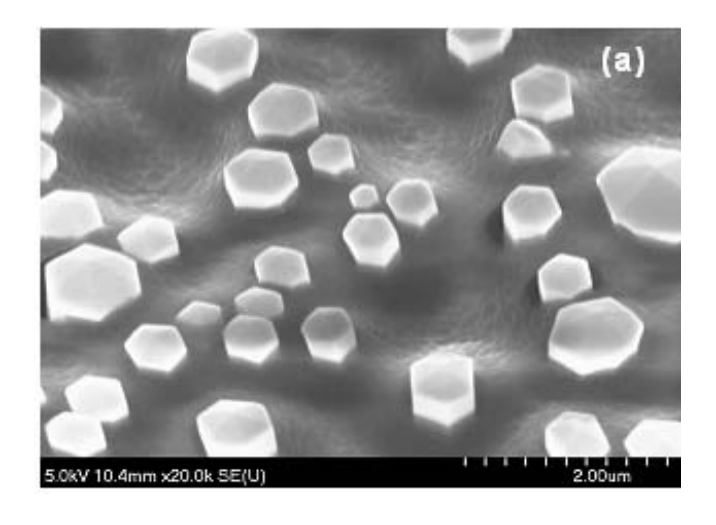


Figure 7.1: Schematic illustrations of (a) InN:Si/i-InN nanowire solar cells grown on p-type Si substrates, (b) InN:Mg/i-InN/InN:Si nanowire solar cells grown on n-type Si substrates, and (c) CdS-passivated InN:Mg/i-InN/InN:Si nanowire solar cells grown on n-type Si substrates.



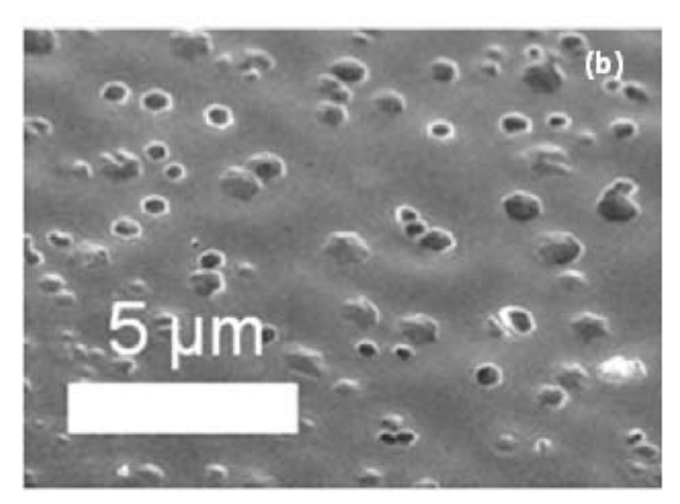


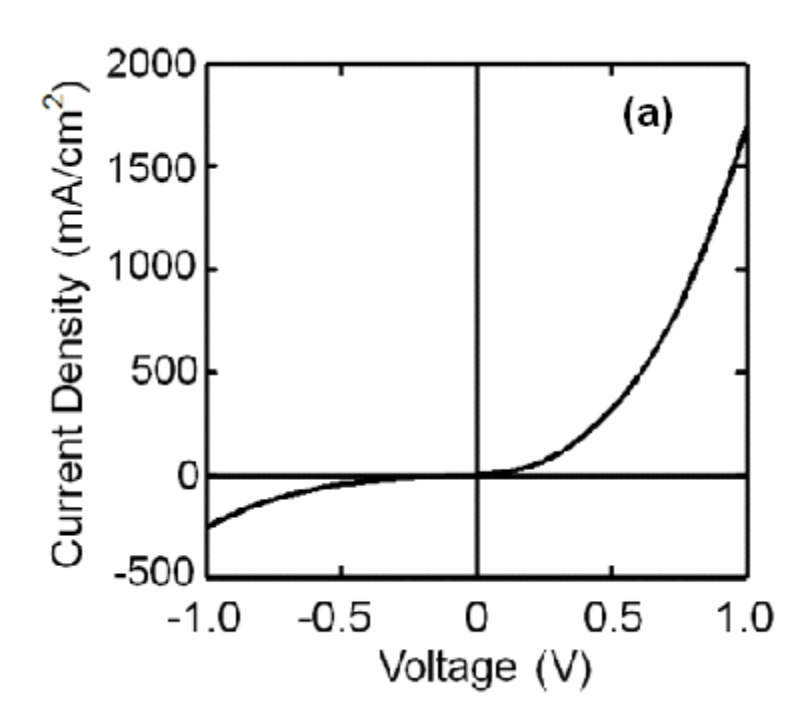
Figure 7.2: 45° scanning electron microscopy images of (a) the InN nanowire ensemble spin-coated with a polyimide layer, with the top region of the wires exposed by dry etching and (b) the polyimide immersed wire ensemble after the deposition of Ni/Au contact layers.

The fabrication process for InN nanowire solar cells on Si is briefly described for the 2^{nd} design. A polyimide resist layer is first spin-coated to fully cover the InN nanowires for surface planarization. The polyimide layer is subsequently etched using O_2 dry-etching until the top region of the wires is exposed, shown in figure 7.2(a). The sample is then flood-exposed with UV light and hard-baked at 350 °C for ~ 30 minutes to cure the polyimide. The top exposed section of the wires is patterned,

using standard photolithography, into cells of various sizes (0.09 mm² up to 1.00 mm²) and a thin Ni/Au (5nm/10nm) p-metal contact is deposited on the cell surface, shown in figure 7.2(b), which is followed by the deposition of thick Ni/Au metal contact layers at the periphery of the devices. Ti/Au (30nm/150nm) layers are then deposited on the backside of the n-Si substrate as the n-metal contact. The sample is annealed at $300 - 400^{\circ}$ C for 60 seconds.

7.4 Results and Discussions

The performance characteristics of InN nanowire solar cells on Si is measured under dark and illuminated (one-sun at AM 1.5G) conditions. Characteristics of the 1st design, i.e. the InN:Si/i-InN/p-Si heterojunction nanowire solar cells is first described. The current-voltage (I-V) response of such devices measured under dark conditions is shown in figure 7.3(a). It is seen that InN/Si nanowire heterojunction design exhibits very poor diode characteristics, with rectifying ratios in the range of ~ 2 to 4 measured at -0.5 V and 0.5 V. At -1 V, a leakage current of more than 100 mA/cm² was observed. As a consequence, no significant photo response was observed. The measured short-circuit current density and energy conversion efficiency is less than 2 mA/cm² and 0.01%, respectively. The underlying mechanism for the extremely poor device performance has been investigated. Due to the very large electron affinity (~ 5.8 eV) of InN, its conduction band minimum is positioned well below the valence band maximum of Si. In addition, a thin ($\sim 2-3$ nm) amorphous layer (SiN_x) is generally formed at the InN/Si misfit interface [238]. The resulting energy-band diagram of the n-InN/i-InN/p-Si heterostructure under thermal equilibrium is schematically shown in figure 7.3(b). The depletion occurs at both sides of the InN/Si junction. It is seen that large densities of electrons accumulate at the InN/Si junction interface, which can readily recombine with holes in the Si valence band and therefore explains the quasi-ohmic behavior observed for the n-InN/i-InN/p-Si heterojunction device under dark conditions. However, the depletion creates a significant barrier to the transport of photogenerated holes, leading to negligible response under illumination.



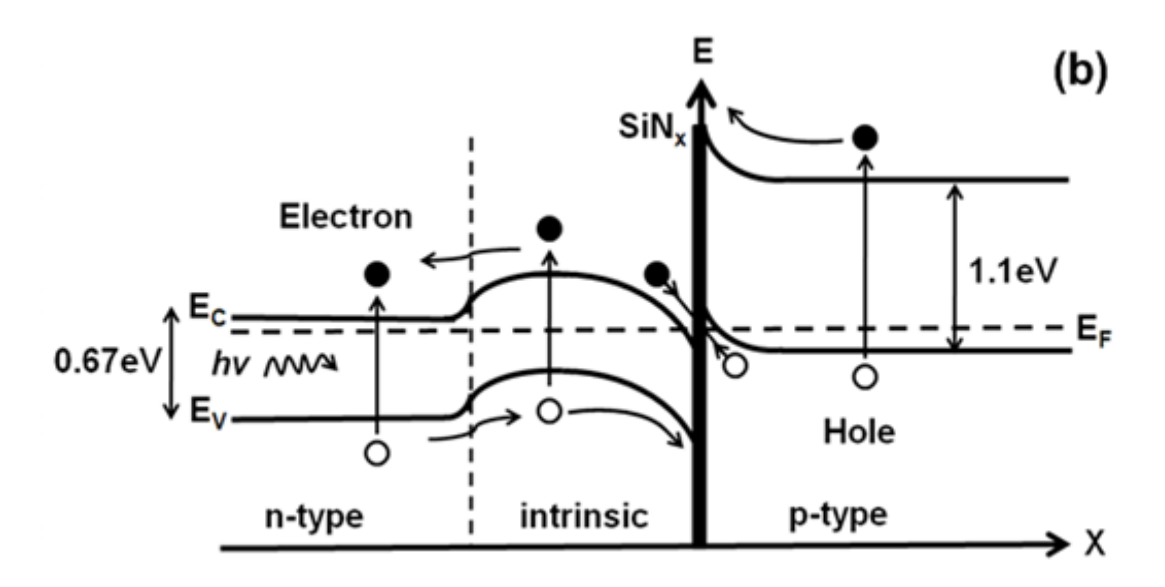
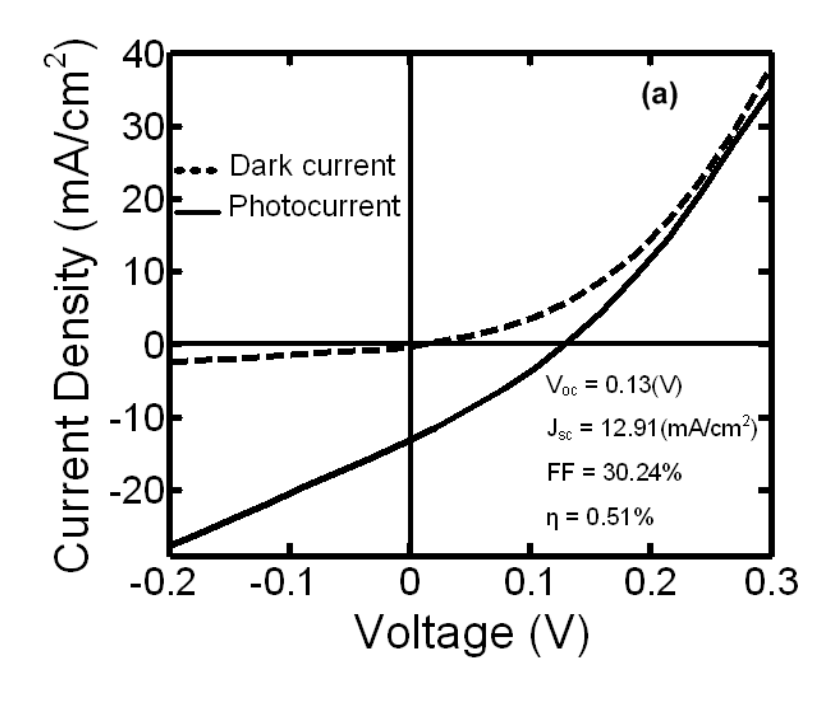


Figure 7.3: (a) I-V response of InN:Si/i-InN nanowire devices on p-Si(111) measured under dark conditions. (b) Schematic of the energy band diagram of the InN:Si/i-InN/p-Si heterojunction under thermal equilibrium. The presence of a thin (\sim 2-3 nm) amorphous SiN_x layer is also illustrated.

Drastically improved device performance, illustrated in figure 7.4(a), has been measured for the 2nd solar cell design grown on n-type Si substrates. Under dark conditions, the InN:Si/i-InN/InN:Mg nanowire device exhibits characteristics of a diode structure, with a significantly improved rectifying ratio (~ 60) measured at -1 and +1 V, which is attributed to the built-in electric field in the p-i-n nanowire homojunction. In addition, a clear photo-response has been consistently observed. Under simulated AM 1.5G illumination, a promising short-circuit current density of ~ 12.91 mA/cm² is obtained for a device area of 1 mm². The measured open-circuit voltage, fill factor, and power conversion efficiency are ~ 0.13 V, 30.2%, and 0.51%, respectively. The functioning of the InN p-i-n axial homojunction solar cells on ntype Si may be explained by the energy-band diagram under thermal equilibrium. Illustrated in figure 7.4(b), it may be noted that the depletion region widths of the InN/Si junction are small, due to the very high doping concentrations in InN and Si. As a consequence, electrons can readily tunnel from InN to Si. Illumination from the top of the nanowires would result in photons with energy larger than $E_{\rm g}$ (InN) to be absorbed by the nanowires. The holes and electrons produced in InN can be promptly collected by the ohmic contacts at the top of the wires and the back contact of the substrate, respectively, thereby generating the observed photocurrent. While photons with energy larger than E_g (Si) could also be absorbed by the substrate when light illuminates onto the Si surface through the gap between the wires, the contribution to the photocurrent is expected to be negligible, due to the presence of a significant barrier to hole transport across the InN/Si heterointerface.



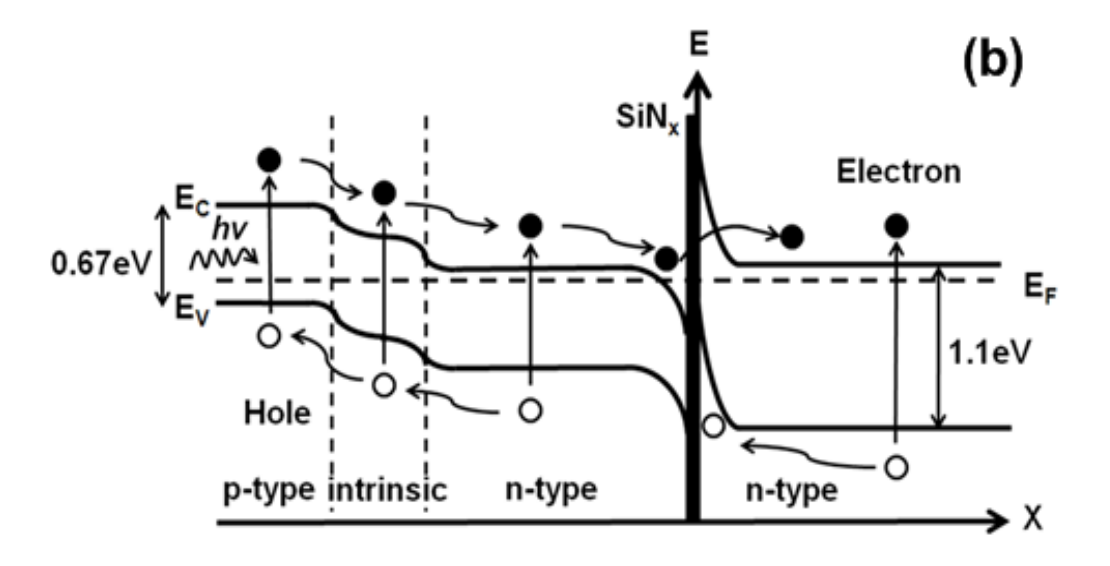


Figure 7.4: (a) I-V characteristics of InN:Mg/i-InN/InN:Si nanowire solar cells grown on n-type Si(111) substrates under dark and illumination (1-sun at AM 1.5G) conditions. (b) Illustration of the corresponding energy band diagram of the nanowire junction under thermal equilibrium.

The performance of the afore-described InN:Si/i-InN/InN:Mg nanowire homojunction solar cells may be severely limited by the presence of surface states, which can be addressed, to a certain extent, with the use of CdS surface passivation [395]. Illustrated in figure 7.5 are the measured I-V curves under dark and illuminated conditions for the 3rd nanowire solar cell design, wherein a thin (~ 10 nm) CdS passivation-layer is incorporated. A reduction in the reverse leakage current and an improvement in the rectifying ratio (~ 150) were measured, compared to identical devices fabricated without the use of any CdS passivation. The improved diode characteristics are attributed to the effective carrier confinement provided by the large bandgap CdS and the suppression of carrier leakage through the wire surface. Under one-sun (AM 1.5G) illumination, the devices exhibit further improved performance, with a short-circuit current density of ~ 14.4 mA/cm², open circuit voltage of 0.14 V, fill factor of 34.0%, and energy conversion efficiency of 0.68%. It may be noted that the measured short-circuit current densities are much larger than the commonly reported values for nanowire solar cells [396-400]. The open-circuit voltage, however, is relatively low, which can be improved by utilizing large bandgap InGaN nanowires and by optimizing the surface passivation and fabrication process.

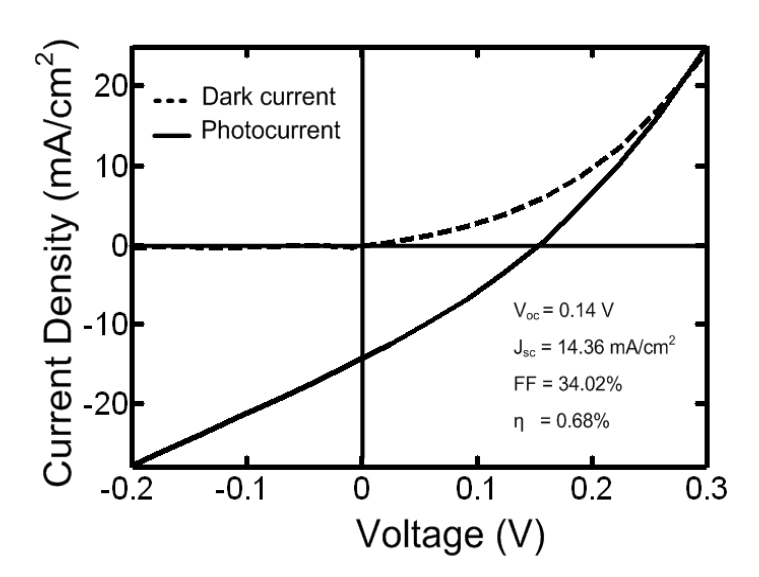


Figure 7.5: I-V characteristics of CdS-passivated InN:Mg/i-InN/InN:Si nanowire solar cells grown on n-type Si(111) substrates under dark and light (1-sun at AM 1.5G) illumination conditions.

The performance of the presently demonstrated InN nanowire solar cells may also be severely limited by the surface electron accumulation of n-type InN and the non-ideal carrier transport across the InN/Si misfit interface, due to the presence of an amorphous SiN_x layer. Improved device performance is therefore expected by utilizing core/shell heterostructures and by employing a planar GaN or InN buffer layer. Additionally, the energy conversion efficiency is practically limited by the very low wire density in this experiment. Shown in figure 7.2(a), the surface coverage of InN nanowires is less than 30%. As a result, a significant portion of the solar radiation cannot be absorbed by InN, and the benefit of light trapping associated with nanowires may be absent as well. Consequently, by optimizing the wire density and diameters, the energy conversion efficiency can be readily increased by a factor of 3, or larger. More importantly, the energy conversion efficiency is expected to improve substantially for InGaN nanowire solar cells with an optimized energy bandgap. The use of coalescent growth for a planar top contact layer will also greatly facilitate the device fabrication and reduce the series resistance [401]. The growth and characterization of high performance InGaN nanowire solar cells on Si, with the use of optimized surface passivation and device fabrication processes, will be investigated in future studies.

7.5 Conclusion

In summary, we have demonstrated the first InN solar cells, consisting of InN:Si/i-InN/InN:Mg nanowire homojunctions on n-type Si(111) substrates, which exhibit a promising short-circuit current density of ~ 14.4 mA/cm² and an energy conversion efficiency of ~ 0.68% under one-sun (AM 1.5G) illumination. Further improvement in the device performance will be investigated by optimizing the growth and fabrication processes. The present work constitutes important progress for the realization of InGaN-based third-generation solar cells. It has also mitigated some of the major barriers for the future development of InN-based nanoelectronic and nanophotonic devices.

Chapter 8: Conclusion and Future Work

8.1 Summary of the Thesis Work

In summary, we have investigated the molecular beam epitaxial growth and characterization of III-Nitride based nanowire heterostructures, including GaN and InN nanowires and InGaN/GaN dot-in-a-wires on Si(111) substrates. We have further demonstrated high performance nanowire LEDs and solar cells with the incorporation of such novel nanowire heterostructures. The significant findings of this thesis are briefly summarized below.

Although tremendous progress has been made for InGaN/GaN quantum well LEDs, the performance of such devices in the green, yellow, and red wavelength ranges has been plagued by the presence of large densities of dislocations. In this context, we have investigated nearly defect-free III-nitride nanowire LEDs. It has been recognized that, due to the presence of unoccupied Ga dangling bonds and surface defects along the GaN nanowire lateral surfaces and the associated nonradiative carrier recombination, the currently reported nanowire LEDs generally exhibit very low quantum efficiency [222, 402]. In this work, we have developed, for the first time in the world, InGaN/GaN dot-in-a-wire nanoscale heterostructures, which can provide superior three-dimensional carrier confinement required for ultrahigh efficiency emission [38]. Moreover, we have demonstrated that the emission wavelengths of such novel nanoscale materials can be controllably varied across nearly the entire visible wavelength range by controlling the sizes and compositions of the dots, which is achieved by varying the growth conditions, including the substrate temperature, growth duration, deposition rate, and In/Ga flux ratios. For example, when grown at relatively low substrate temperatures (~ 550 °C), the In composition in InGaN/GaN quantum dots can reach ~ 50% without the presence of extended defects/dislocations, which can lead to high efficiency emission in the

red/orange wavelength ranges that was not previously possible. High efficiency emission in the blue, green, yellow, and amber wavelength range can also be readily achieved by optimizing the growth conditions. The resulting full-color LEDs can exhibit a relatively high internal quantum efficiency of ~ 20%, or larger at room temperature.

The performance of GaN-based nanowire LEDs has been severely limited by the poor hole transport in the device active region. Due to their large effective mass and small mobility, injected holes are located close to the p-GaN region. The poor hole transport process and the resulting nonuniform carrier distribution in the device active region can further enhance Auger recombination [126] and increase electron overflow [167, 403], thereby limiting the optical emission efficiency at high injection levels. The poor hole transport problem can be effectively addressed by utilizing the special technique of p-type modulation doping in the quantum dot active region. In this regard, we have investigated the design, epitaxial growth, fabrication, and characterization of p-doped InGaN/GaN dot-in-a-wire white LEDs. The p-doped dot-in-a-wire LEDs can exhibit significantly enhanced internal quantum efficiency (\sim 56.8%) at room temperature, which is higher than any previously reported values for GaN-based nanowire LEDs. The devices also show highly stable emission characteristics, with nearly constant CIE chromaticity coordinates (\approx 0.35 and y \approx 0.37), with increasing injection currents.

We have further identified that electron overflow is the primary mechanism responsible for the efficiency droop in nanowire LEDs under high current injection conditions. We have designed, grown, fabricated, and characterized InGaN/GaN dotin-a-wire white-light LEDs with the incorporation of an AlGaN electron blocking layer, which can effectively prevent electron overflow from the device active region. With the use of the special techniques of p-type modulation doping and AlGaN electron blocking, we have demonstrated, for the first time, GaN-based phosphor-free white LEDs that can exhibit virtually zero efficiency droop up to ~ 2,000 A/cm² and highly stable emission characteristics. Such devices are suitable for applications in solid state lighting and full-color displays.

One of the most critical, yet missing technologies for future III-nitride based full-solar-spectrum solar cells is a functional InN-based single junction device. We have investigated the molecular beam epitaxial growth and characterization of nearly intrinsic InN nanowires on Si(111) substrates, which enables a fundamental understanding and precise control of the electrical and optical properties of InN that was not previously possible. We have studied the epitaxial growth, fabrication and characterization of InN:Mg/i-InN/InN:Si nanowire axial structures on n-type Si(111) substrates and demonstrated the first InN nanowire solar cells [366]. We passivated the InN:Mg/i-InN/InN:Si nanowire homojunction solar cells with a CdS layer using a chemical bath deposition method to effectively suppress nonradiative carrier recombination associated with the presence of surface states. Under one-sun (AM 1.5G) illumination, the devices exhibit a short-circuit current density of ~ 14.4 mA/cm², open circuit voltage of 0.14 V, fill factor of 34.0%, and energy conversion efficiency of 0.68%. This work opens up exciting possibilities for InGaN nanowirebased, full solar-spectrum third-generation solar cells. It has also mitigated some of the major barriers for the future development of InN-based nanoelectronic and nanophotonic devices.

8.2 Suggested Future Work

Although significant progress has been made in the growth and characterization of III-nitride nanowire heterostructures and their device applications, many fundamental materials properties of such novel nanomaterials have remained unclear. For example, the achievement of superior quality AlGaN nanowire heterostructures in the ultraviolet wavelength range has remained elusive. For the future work, we therefore propose to perform a fundamental investigation of the epitaxial growth and characteristics of GaN-based nanowire heterostructures and to develop high power white-light LEDs, high efficiency ultraviolet LEDs, as well as multi-junction nanowire solar cells.

8.2.1 High Performance LEDs with Coaxial Nanowire Heterostructures

As discussed in Chapter 6, the Shockley-Read-Hall nonradiative recombination, due to the large surface-to-volume ratios and the presence of surface states and defects, is largely responsible for the unique characteristics of GaN-based nanowire LEDs. The performance of nanowire LEDs can be severely compromised due to the large surface SRH recombination. The quantum efficiency rises up very slowly with increasing current, and the slow rising trend of the quantum efficiency observed in nanowire LEDs is directly related to the large SRH recombination, which further limits the maximum achievable efficiency at high injection levels. Accordingly, significantly improved device performance can be achieved by using effective surface passivation technique. For this approach, a wide bandgap or suitable dielectric material [404-406] should be applied around the nanowire structures to reduce or prevent electrons/holes moving to nanowire surfaces. Nanowire LED quantum efficiency, therefore, can be enhanced due to the reduced/eliminated nonradiative surface recombination. High efficiency nanowire LEDs can be obtained by embedding the InGaN/GaN dot-in-awires in a large bandgap AlGaN shell structure to minimize nonradiative recombination on the wire surfaces [15, 354], while maintaining the benefits associated with the large surface-to-volume ratios of nanowire LEDs. Illustrated in figure 8.1, the InGaN/GaN active region is passivated by an AlN(AlGaN) layer, which can lead to high performance LEDs. This work is currently in progress.

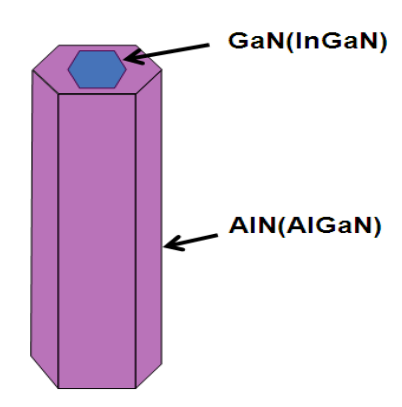


Figure 8.1: Proposed coaxial nanowire heterostructures for high efficiency nanowire based LEDs.

8.2.2 Nanowire LEDs with Significantly Improved Light Extract Efficiency

The external quantum efficiency of an LED is the product of the internal quantum efficiency and the light extraction efficiency. To improve the light extraction efficiency and therefore the optical output of nanowire LEDs, we propose to develop InGaN/GaN dot-in-a-wire LEDs on copper carriers, which can eliminate any optical absorption by the substrates and provide much more effective thermal management. Current commercial LEDs have achieved maximum light extraction efficiency (>70%) by removing the sapphire substrates. We propose to transfer the dot-in-a-wire LEDs on a Cu carrier using the metal-to-metal bonding technique [407, 408]. In this approach, a thin (~ 10 nm) Ni layer is first deposited on the as-grown nanowire surface, followed by the deposition of an Al/Au broadband reflector. The nanowire LED is then bonded onto the Au-coated Cu carrier using the standard lowtemperature metal-to-metal bonding technique. The Si substrate is mechanically polished and chemically etched. The fabrication process of dot-in-a-wire LEDs on Cu carriers is similar to that on Si substrates, except that the Cu carrier is used as p-metal contact while the n-metal contact is placed on the wire top surface. The external quantum efficiency of the fabricated LED devices will be measured using integrated sphere and will be correlated with variations in the device fabrication and data from the structural characterization. Moreover, we will optimize the wire size, density and surface morphology, with the objective to achieve light extraction efficiency of > 50%. The significantly improved light extraction efficiency will lead to nanowire LEDs with an external quantum efficiency of > 45%, compared to the current values (~ 25%) reported for conventional phosphor-based white LEDs.

8.2.3 High Efficiency Ultraviolet Nanowire LEDs

There is a growing awareness that deep ultraviolet (UV) light sources will have a profound impact on environment cleaning. UV light sources are more effective in killing bacteria, virus, and fungi and in damaging pathogens than any other conventional methods. Yet, they are relatively harmless to people. However, the current mercury-based UV lamps are heavy and inefficient, require regular maintenance, and pose a significant health issue due to mercury contained in the

lamp. In this regard, GaN-based LEDs have been intensively investigated which enables the achievement of high efficiency solid state lamps in the visible and UV spectral range. The use of nanowire heterostructures for LED operation offers several additional advantages, including drastically reduced dislocation densities and enhanced light extraction, which will contribute significantly to the efficiency and output power of UV light sources. In addition, such nanowire heterostructures can be grown directly on low cost, large area silicon substrates, thereby drastically reducing the manufacturing cost of deep UV solid state lamps. We therefore propose to develop high efficiency nanowire UV solid state lamps. Self-organized AlGaInN/AlGaN dot-in-a-wire UV LED heterostructures, illustrated in figure 8.2, will be grown on low-resistivity n-type Si(111) substrates, wherein the special techniques of p-doping and electron blocking are also incorporated in the device active region to enhance hole transport and reduce electron overflow, respectively. The bottom and top sections of the wires are doped n- and p-type using Si and Mg, respectively. The device active region consists of six vertically aligned Al_{0.7}Ga_{0.1}In_{0.2}N quantum dots, separated by 3 nm Al_{0.75}Ga_{0.25}N barrier layers. The emission wavelength can be tuned by varying the size of the dots and the compositions in both the dot and barrier layers. With iterations in the design, epitaxial growth, fabrication and characterization, ultrahigh-efficiency (IQE > 60%) deep UV LEDs can be possibly realized, which can address the fundamental materials challenges for realizing practical deep UV solid state lamps.

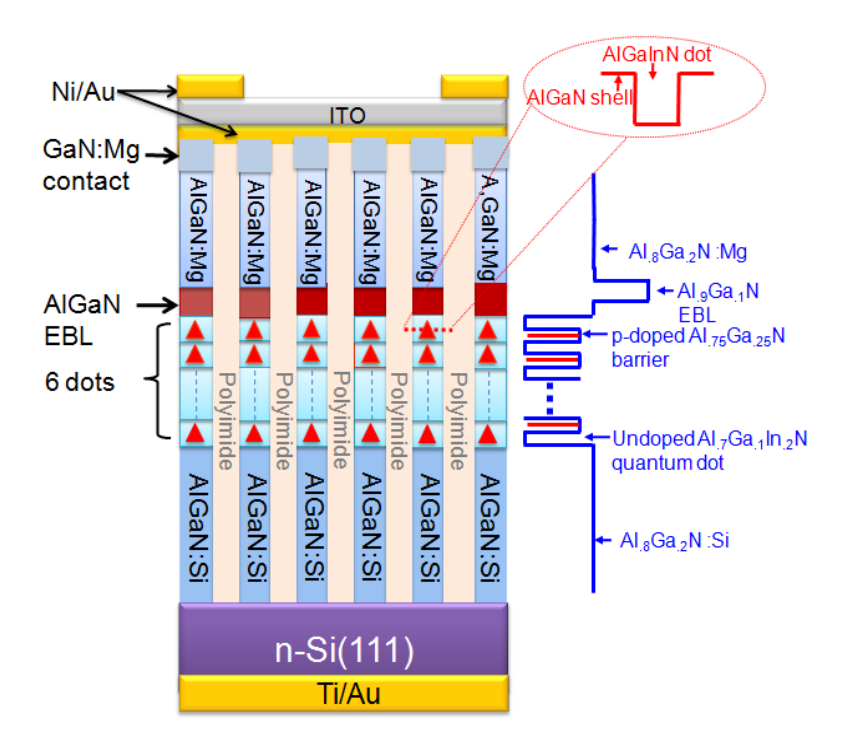


Figure 8.2: Schematic illustration of the proposed AlGaInN/AlGaN deep UV LEDs with the incorporation of the special techniques of electron blocking and modulation p-doing in the device active region for reducing electron overflow and enhancing hole transport, respectively.

8.2.4 High Efficiency III-N Nanowire Solar Cells

We also propose to develop single- and multi-junction InGaN nanowire solar cells on a Si platform. In(Ga)N nanowires will be grown directly on Si substrates under nitrogen rich conditions by molecular beam epitaxy. The proposed single and double junction nanowire solar cells on Si are schematically shown in figure 8.3. Such InGaN nanowire solar cells with broadband absorption spectrum can be achieved by controllably changing the indium and gallium flux during epitaxial growth. By varying the indium and gallium compositions in the nanowire, the nanowire bandgap, or the absorption spectra, can be optimized to achieve solar cells with improved efficiency. Critical to the double-junction device is the formation of n⁺/p⁺ tunnel injection, which can be achieved by optimizing the epitaxial growth conditions,

including the substrate temperature, group III/V ratios, and the dopant (Mg and Si) incorporation.

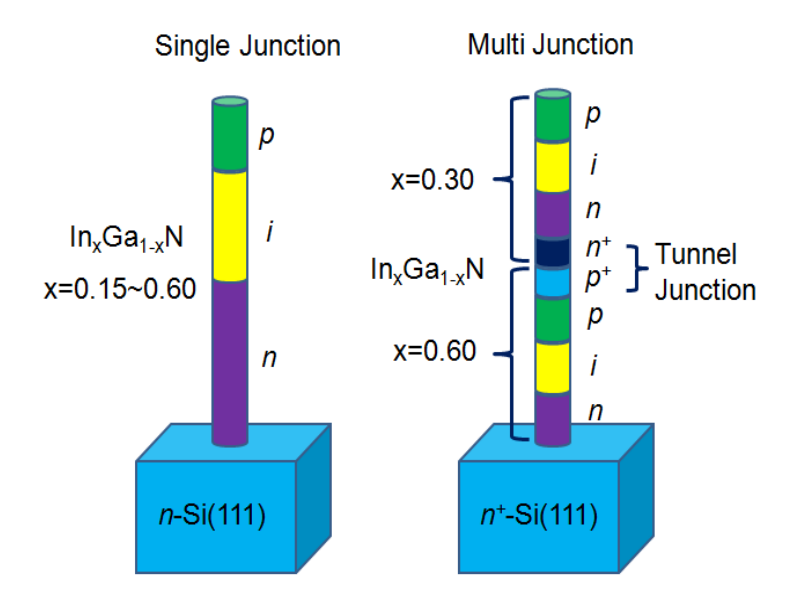


Figure 8.3: Proposed high efficiency single (left) and multi-junction (right) solar cells based on InGaN material system.

Additionally, we propose to develop InGaN/GaN nanowire intermediate band solar cells. In a conventional solar cell, photons with energy below the bandgap cannot be absorbed. In an intermediate band solar cell, however, the presence of an electronic band within the band gap enables the absorption of photons with energy smaller than the bandgap of the semiconductor [409]. Illustrated in figure 8.4(a), electron-hole pairs can be generated with the absorption of sub-band photons, leading to an enhancement in the photocurrent without any voltage degradation. It has been predicted that a limiting efficiency of 63.2% can be achieved in intermediate band solar cells, compared to 40.7% for conventional single gap devices [409]. To realize the full potential of intermediate band solar cells, it is important that the intermediate band is half-filled with electrons and there is negligible nonradiative recombination in the semiconductor. We propose to investigate the design, growth, fabrication, and characterization of InGaN/GaN dot-in-a-wire intermediate band solar cells as shown in figure 8.4(b). An inherent advantage in using quantum dots is the wide range of

tunability that is afforded. Quantum dot size, shape, composition, and barrier material composition can be changed to alter the energy position of the electron and hole states, thereby altering the absorption spectrum. Enhanced response, due to the absorption of sub-band-gap energy photons, has been demonstrated in InAs quantum dot intermediate band solar cells [410]. With the incorporation of optimized quantum dot layers, InGaN-based intermediate band solar cells with significantly improved efficiency, compared to the conventional devices, therefore, is practical.

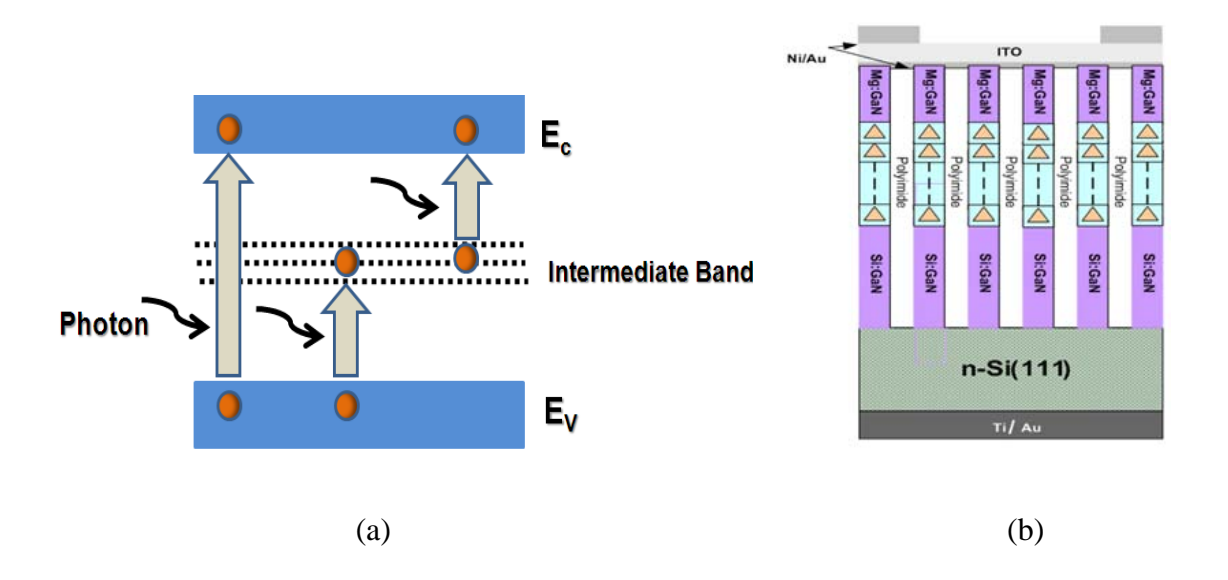


Figure 8.4: (a) Illustration of the energy band diagram in the active region of an intermediate band solar cell. (b) Proposed InGaN based intermediate band solar cells with the utilization of dot-in-a-wire heterostructure.

List of Publications and Copyrights

Refereed and Archival Journal Articles

- 1. <u>H. P. T. Nguyen</u>, M. Djavid, K. Cui, and Z. Mi, "Temperature-dependent nonradiative recombination processes in GaN-based nanowire white-light-emitting diodes on silicon", Nanotechnology, 2012 (submitted).
- 2. <u>H. P. T. Nguyen</u>, K. Cui, S. Zhang, M. Djavid and Z. Mi, "Controlling electron overflow in phosphor-free InGaN/GaN nanowire white-light-emitting diodes", Nano Letters, 2012 (accepted).
- 3. <u>H. P. T. Nguyen</u>, S. Zhang, K. Cui and Z. Mi, "High efficiency InGaN/GaN dot-in-a-wire red light emitting diodes", IEEE Photonics Technology Letters, 24 (2012) 321.
- 4. S. Fathololoumi, <u>H. P. T. Nguyen</u>, and Z. Mi, "Self-organized In(Ga)N nanowire heterostructures and optoelectronic device applications", Nanoscience & Nanotechnology-Asia, 2 (2011) 123.
- 5. <u>H. P. T. Nguyen</u>, K. Cui, S. Zhang, Saeed Fathololoumi and Z. Mi, "Full-color InGaN/GaN dot-in-a-wire light emitting diodes on silicon", Nanotechnology, 22 (2011) 445202.
- 6. <u>H. P. T. Nguyen</u>, S. Zhang, K. Cui, X. Han, S. Fathololoumi, M. Couillard, G. A. Botton, and Z. Mi, "p-type modulation doped InGaN/GaN dot-in-a-wire white-light-emitting diodes monolithically grown on Si(111)", *Nano Letters*, 11 (2011) 1919.
- 7. <u>H. P. T. Nguyen</u>, S. Zhang, K. Cui, X. Han, and Z. Mi^{*} "Molecular beam epitaxial growth, fabrication, and characterization of high efficiency InGaN/GaN dotin-a-wire white light emitting diodes on Si(111)", ECS Transactions, 35 (2011) 41.
- 8. <u>H. P. T. Nguyen</u>, Y.-L Chang, I. Shih and Z. Mi, "InN p-i-n nanowire solar cells on Si", *IEEE J. Sel. Topics Quantum Electron. Nanowires*, 17 (2011) 1062.
- 9. Z. Mi, <u>H. P. T. Nguyen</u>, K. Cui, X. Han, S. Zhang, and Y.-L. Chang, "Prospects and challenges of InN-based nanowire heterostructures and devices integrated on Si", Proc. SPIE 7847, 784702 (2010).

Conference/Meeting Presentations

1. <u>H. P. T. Nguyen</u>, K. Cui, S. Zhang, S. Fathololoumi, R. Wu, and Z. Mi, "High-efficiency phosphor-free InGaN/GaN dot-in-a-wire white-light-emitting diodes on Silicon", *SPIE Photonics West 2012*, San Francisco, California, Jan. 21-26, 2012.

- 2. <u>H. P. T. Nguyen</u>, S. Zhang, K. Cui, S. Fathololoumi and Z. Mi, "Study on the Quantum Efficiency Enhancement in InGaN/GaN Dot-in-a-Wire Light Emitting Diodes Grown by Molecular Beam Epitaxy", *IEEE Photonics Conference (IPC11)*, Arlington, Virginia, October 9-13, 2011.
- 3. Z. Mi, <u>H. P. T. Nguyen</u>, K. Cui, S. Zhang, and S. Fathololoumi, "Ultrahigh-Efficiency Phosphor-Free Nanowire White Light Emitting Diodes Monolithically Grown on Silicon", *15th Canadian Semiconductor Science and Technology Conference*, Vancouver, BC, Canada, Aug. 15-17, 2011.
- 4. <u>H. P. T. Nguyen</u>, S. Zhang, K. Cui, S. Fathololoumi and Z. Mi, "High efficiency phosphor-free InGaN/GaN white light emitting diodes on Silicon", 28th North American Molecular Beam Epitaxy Conference, La Jolla, CA, August 14-17, 2011.
- 5. <u>H. P. T. Nguyen</u>, K. Cui, S. Fathololoumi, X. Han, S. Zhao, Z. Mi, Q. Li, G. Wang, K. Bevan, and H. Guo, "On the surface electron accumulation and Fermi-level pinning at InN nonpolar growth surfaces", *9*th *International Conference on Nitride Semiconductors*, SECC, Glasgow, July 10-15, 2011.
- 6. <u>H. P. T. Nguyen</u>, S. Zhang, K. Cui, X. Han, S. Fathololoumi, and Z. Mi," High-Efficiency p-Doped InGaN/GaN Dot-in-a-Wire White Light Emitting Diodes Monolithically Grown on Si(111)," *9*th International Conference on Nitride Semiconductors, SECC, Glasgow, July 10-15, 2011.
- 7. <u>H. P. T. Nguyen</u>, K. Cui, S. Zhang, X. Han, and Z. Mi, "InGaN/GaN dot-in-a-wire nanoscale heterostructures and high-efficiency light emitting diodes on Si", 5th International Conference on Nanophotonics, Sanghai, China, May 22-26, 2011.
- 8. Z. Mi, <u>H. P. T. Nguyen</u>, K. Cui, Md G. Kibria, D. Wang, and I. Shih, "Harvesting Solar Energy Using Group III-Nitride Nanowires", Photovoltaics Canada-2nd National Scientific Conference, *Ottawa, Canada, May 16 –18, 2011*.
- 9. <u>H. P. T. Nguyen</u>, S. Zhang, K. Cui, X. Han, and Z. Mi, "High Efficiency InGaN/GaN Dot-in-a-Wire Light Emitting Diodes Grown by Molecular Beam Epitaxy on Si(111) Substrate", *the Conference on Lasers and Electro-Optics 2011*, Baltimore Convention Center, Baltimore, Maryland, USA, May 1-6, 2011.
- 10. <u>H. P. T. Nguyen</u>, S. Zhang, K. Cui, X. Han, and Z. Mi, "Molecular beam epitaxial growth, fabrication, and characterization of high efficiency InGaN/GaN dotin-a-wire light emitting diodes on Si(111)," *219th Electrochemical Society Meeting*, Montreal, Canada, May 1-6, 2011
- 11. P. Bianucci, K. Cui, <u>H. P. T. Nguyen</u> and Z. Mi, "Nanoscale infrared sources for spectroscopic analysis of water content in wood fibre networks", *Innovative Green Fiber Products Network 1st Annual Meeting*, Montreal, Quebec, Canada, February 2011,
- 12. Z. Mi, <u>H. P. T. Nguyen</u>, S. Zhang, and K. Cui, "High performance InGaN/GaN dot-in-a-wire light emitting diodes on Si(111)," *IEEE Photonics Society Winter Topical Meeting 2011*, Keystone, CO, Jan. 10-12, 2011.

- 13. Z. Mi, H. P. T. Nguyen, K. Cui, X. Han, S. Zhang, and Y.-L. Chang, "Prospects and challenges of InN-based nanowire heterostructures and devices integrated on Si," *SPIE/COS Photonics Asia*, Beijing, China, Oct. 18-20, 2010.
- 14. Y. L. Chang, F. Li, J. Wang, <u>H. P. T. Nguyen</u>, Z. Mi, "Optical and Electrical Transport Properties of Nearly Intrinsic and Si-Doped InN Nanowires", *Electronic Materials Conference*, Notre Dame, Indiana, US, June 23-25, 2010.
- 15. <u>H. P. T. Nguyen</u>, S. Park, Y. L. Chang, J. L. Wang, I. Shih, and Z. Mi, "Low Cost and High Performance In(Ga)N/CuInSe₂ Heterojunction Solar Cells", *Photonics North 2010 collocated with Photovoltaics Canada-1*st *National Scientific Conference*, Niagara Falls, ON, Canada, June 1 3, 2010.
- 16. Y. L. Chang, <u>H. P. T. Nguyen</u>, I. Shih, and Z. Mi, "Vertically aligned InN p-in nanowire solar cells on Si", *Photonics North 2010 collocated with Photovoltaics Canada-1st National Scientific Conference*, Niagara Falls, ON, Canada, June 1 3, 2010.





Author:









Controlling Electron Overflow in Phosphor-Free InGaN/GaN Nanowire White Light-Emitting

Diodes

Hieu Pham Trung Nguyen et al.

Publication: Nano Letters

Publisher: American Chemical Society

Date: Feb 1, 2012

Copyright © 2012, American Chemical Society

Logged in as: Hieu Pham Trung Nguyen Account #:

3000484859

LOGOUT

PERMISSION/LICENSE IS GRANTED FOR YOUR ORDER AT NO CHARGE

This type of permission/license, instead of the standard Terms & Conditions, is sent to you because no fee is being charged for your order. Please note the following:

- Permission is granted for your request in both print and electronic formats.
- If figures and/or tables were requested, they may be adapted or used in part.
- Please print this page for your records and send a copy of it to your publisher/graduate school.
- Appropriate credit for the requested material should be given as follows: "Reprinted (adapted) with permission from (COMPLETE REFERENCE CITATION). Copyright (YEAR) American Chemical Society." Insert appropriate information in place of the capitalized words.
- One-time permission is granted only for the use specified in your request. No additional uses are granted (such as derivative works or other editions). For any other uses, please submit a new request.

BACK

CLOSE WINDOW

Copyright © 2012 Copyright Clearance Center, Inc. All Rights Reserved. Privacy statement. Comments? We would like to hear from you. E-mail us at customercare@copyright.com













p-Type Modulation Doped InGaN/GaN Dot-in-a-Wire White-

Light-Emitting Diodes

Monolithically Grown on Si(111)

Author: H. P. T. Nguyen et al.

Publication: Nano Letters

Publisher: American Chemical Society

Date: May 1, 2011

Copyright © 2011, American Chemical Society

Logged in as: Hieu Pham Trung Nguyen Account #: 3000484859

LOGOUT

PERMISSION/LICENSE IS GRANTED FOR YOUR ORDER AT NO CHARGE

This type of permission/license, instead of the standard Terms & Conditions, is sent to you because no fee is being charged for your order. Please note the following:

- Permission is granted for your request in both print and electronic formats.
- If figures and/or tables were requested, they may be adapted or used in part.
- Please print this page for your records and send a copy of it to your publisher/graduate school
- Appropriate credit for the requested material should be given as follows: "Reprinted (adapted) with permission from (COMPLETE REFERENCE CITATION). Copyright (YEAR) American Chemical Society." Insert appropriate information in place of the capitalized words.
- One-time permission is granted only for the use specified in your request. No additional uses are granted (such as derivative works or other editions). For any other uses, please submit a new request.

BACK

CLOSE WINDOW

Copyright © 2012 Copyright Clearance Center, Inc. All Rights Reserved. Privacy statement. Comments? We would like to hear from you. E-mail us at customercare@copyright.com







Account Info Help



Title: InN p-i-n Nanowire Solar Cells

on Si

Author: Hieu Pham Trung Nguyen; Yi-Lu

Chang; Ishiang Shih;

Publication: Selected Topics in Quantum

Electronics, IEEE Journal of

Publisher: IEEE

Date: July-Aug. 2011

Copyright © 2011, IEEE

Logged in as: Hieu Pham Trung Nguyen Account #:

3000484859

LOGOUT

Thesis / Dissertaion Reuse

The IEEE does not require individuals working on a thesis to obtain a formal reuse license, however, you may print out this statement to be used as a permission grant:

Requirements to be followed when using any portion (e.g., figure, graph, table, or textual material) of an IEEE copyrighted paper in a thesis:

- 1) In the case of textual material (e.g., using short quotes or referring to the work within these papers) users must give full credit to the original source (author, paper, publication) followed by the IEEE copyright line © 2011 IEEE.
- 2) In the case of illustrations or tabular material, we require that the copyright line © [Year of original publication] IEEE appear prominently with each reprinted figure and/or table.
- 3) If a substantial portion of the original paper is to be used, and if you are not the senior author, also obtain the senior author's approval.

Requirements to be followed when using an entire IEEE copyrighted paper in a thesis:

- 1) The following IEEE copyright/ credit notice should be placed prominently in the references: © [year of original publication] IEEE. Reprinted, with permission, from [author names, paper title, IEEE publication title, and month/year of publication]
- 2) Only the accepted version of an IEEE copyrighted paper can be used when posting the paper or your thesis on-line.
- 3) In placing the thesis on the author's university website, please display the following message in a prominent place on the website: In reference to IEEE copyrighted material which is used with permission in this thesis, the IEEE does not endorse any of [university/educational entity's name goes here]'s products or services. Internal or personal use of this material is permitted. If interested in reprinting/republishing IEEE copyrighted material for advertising or promotional purposes or for creating new collective works for resale or redistribution, please go to http://www.ieee.org/publications/rights/rights_link.html to learn how to obtain a License from RightsLink.

If applicable, University Microfilms and/or ProQuest Library, or the Archives of Canada may supply single copies of the dissertation.

BACK

CLOSE WINDOW

Copyright © 2012 Copyright Clearance Center, Inc., All Rights Reserved. Privacy statement. Comments? We would like to hear from you. E-mail us at customercare@copyright.com





Author:









Title: High-Efficiency InGaN/GaN

Dot-in-a-Wire Red Light-Emitting

Diodes

Nguyen, H. P. T.;Zhang, S.;Cui,

K.;

Publication: IEEE Photonics Technology

Letters
Publisher: IEEE

Date: Feb.15, 2012

Copyright © 2012, IEEE

Logged in as:

Hieu Pham Trung Nguyen

Account #: 3000484859

LOGOUT

Thesis / Dissertaion Reuse

The IEEE does not require individuals working on a thesis to obtain a formal reuse license, however, you may print out this statement to be used as a permission grant:

Requirements to be followed when using any portion (e.g., figure, graph, table, or textual material) of an IEEE copyrighted paper in a thesis:

- 1) In the case of textual material (e.g., using short quotes or referring to the work within these papers) users must give full credit to the original source (author, paper, publication) followed by the IEEE copyright line © 2011 IEEE.
- 2) In the case of illustrations or tabular material, we require that the copyright line © [Year of original publication] IEEE appear prominently with each reprinted figure and/or table.
- 3) If a substantial portion of the original paper is to be used, and if you are not the senior author, also obtain the senior author's approval.

Requirements to be followed when using an entire IEEE copyrighted paper in a thesis:

- 1) The following IEEE copyright/ credit notice should be placed prominently in the references: © [year of original publication] IEEE. Reprinted, with permission, from [author names, paper title, IEEE publication title, and month/year of publication]
- 2) Only the accepted version of an IEEE copyrighted paper can be used when posting the paper or your thesis on-line.
- 3) In placing the thesis on the author's university website, please display the following message in a prominent place on the website: In reference to IEEE copyrighted material which is used with permission in this thesis, the IEEE does not endorse any of [university/educational entity's name goes here]'s products or services. Internal or personal use of this material is permitted. If interested in reprinting/republishing IEEE copyrighted material for advertising or promotional purposes or for creating new collective works for resale or redistribution, please go to http://www.ieee.org/publications/standards/publications/rights/rights link.html to learn how to obtain a License from RightsLink.

If applicable, University Microfilms and/or ProQuest Library, or the Archives of Canada may supply single copies of the dissertation.

BACK

CLOSE WINDOW

Copyright © 2012 Copyright Clearance Center, Inc. All Rights Reserved. Privacy statement. Comments? We would like to hear from you. E-mail us at customercare@copyright.com



"permissions@iop.org" <permissions@iop.org>,

Cc: Bcc:

Subject: Copyright permission

From: Hieu Nguyen <hieu.nguyen3@mail.mcgill.ca> - Wednesday 11/01/2012 18:32

January 11th, 2012

To whom it may concern;

I am completing my PhD thesis entitled "Molecular Beam Epitaxial Growth, Characterization and Device Applications of III-Nitride Nanowire Heterostructures". My thesis includes the papers, submitted/published on Nanotechnology journal. I am an author of these papers. For the copyright issue, the university (McGill University, Montreal, Quebec, Canada) would like to know the journal permits me to reuse these papers in my thesis including the whole manuscripts (figures, tables and writing). Would you please give me your permission and confirm it by sending me an email at hieu.nguyen3@mail.mcgill.ca, I will then enclose your permission letter to my thesis.

I wish to seek copyright permission for the following papers:

1. H. P. T. Nguyen, K. Cui , S. Zhang, Saeed Fathololoumi and Z. Mi, "Full-Color InGan/Gan Dot-in-a-wire Light Emitting Diodes on Silicon", Nanotechnology, 22 (2011) 445202.

2. H. P. T. Nguyen, M. Djavid, K. Cui, and Z. Mi.
Temperature-Dependent Nonradiative Recombination Processes in Gan-Based
Nanowire White-Light-Emitting Diodes on Silicon, submitted (2012).

Not yet accepted for publication

Thank you so much for your consideration.

Yours sincerely,

Hieu Pham Trung Nguyen
Department of Electrical and Computer Engineering,
McGill University
3480 University Street, Montreal, Quebec H3A 2A7, Canada
E-mail: hieu.nguyen3@mail.mcgill.ca
Phone: 514-716-6563

PERMISSION TO REPRODUCE AS REQUESTED IS GIVEN PROVIDED THAT:

(a) the subtained

(b) the source of the material including author, title of article, title of journal, volume number, issue number (if relevant), page range (or first page if this is the only information available), date and publisher is acknowledged.

(c) for material being published electronically, a link back to the original article should be provided (via DOI).

IOP Publishing Ltd Temple Circus

Temple Way BRISTOL

BS1 6BE

Rights & Permissions

Heather McAlinn

From: Hieu Nguyen [hieu.nguyen3@mail.mcgill.ca]
Sent: Wednesday, January 11, 2012 4:06 PM

To: Copyright

Subject: Copyright permission

Follow Up Flag: Follow up Flag Status: Flagged

January 11th, 2012

To whom it may concern;

I wish to seek copyright permission for the following paper:

H. P. T. Nguyen, S. Zhang, K. Cui, X. Han, and Z. Mi, "Molecular beam epitaxial growth, fabrication, and characterization of high efficiency InGaN/GaN dot-in-a-wire white light emitting diodes on Si(111)", ECS Transactions, vol. 35%p. 41 (2011).

Thank you so much for your consideration. Yours sincerely

Hieu Pham Trung Nguyen Department of Electrical and Computer Engineering, McGill University 3480 University Street, Montreal, Quebec H3A 2A7, Canada

E-mail: hieu.nguyen3@mail.mcgill.ca

Phone: 514-716-6563

Permission is granted to include the above-referenced paper in your thesis, provided that you obtain permission of the other individual authors. In the thesis, please acknowledge the authors and the citation given above, and include the words: "Reproduced by permission of ECS — The Electrochemical Society."

Jan. 20, 2012

Ann F. Goedkoop, Director of Publications

Bibliography

- [1] J. Q. Wu, "When group-III nitrides go infrared: New properties and perspectives," J. Appl. Phys., vol. 106, pp. 011101-1 011101-28, 2009.
- [2] J. D. Albrecht, R. P. Wang, P. P. Ruden, M. Farahmand, and K. F. Brennan, "Electron transport characteristics of GaN for high temperature device modeling," *J. Appl. Phys.*, vol. 83, pp. 4777 4781, 1998.
- [3] B. Gelmont, K. Kim, and M. Shur, "Monte-carlo simulation of electron-transport in gallium nitride," *J. Appl. Phys.*, vol. 74, pp. 1818 1821, 1993.
- [4] S. Keller, C. Schaake, N. A. Fichtenbaum, C. J. Neufeld, Y. Wu, K. McGroddy, A. David, S. P. DenBaars, C. Weisbuch, J. S. Speck, and U. K. Mishra, "Optical and structural properties of GaN nanopillar and nanostripe arrays with embedded InGaN/GaN multi-quantum wells," *J. Appl. Phys.*, vol. 100, pp. 054314-1 054314-7, 2006.
- [5] Z. Yarar, "Transport and mobility properties of wurtzite InN and GaN," *Phys. Status Solidi B*, vol. 244, pp. 3711 3718, 2007.
- [6] A. G. Bhuiyan, A. Hashimoto, and A. Yamamoto, "Indium nitride (InN): A review on growth, characterization, and properties," *J. Appl. Phys.*, vol. 94, pp. 2779 2808, 2003.
- [7] M. vanSchilfgaarde, A. Sher, and A. B. Chen, "Theory of AlN, GaN, InN and their alloys," *J. Cryst. Growth*, vol. 178, pp. 8 31, 1997.
- [8] I. Vurgaftman, J. R. Meyer, and L. R. Ram-Mohan, "Band parameters for III-V compound semiconductors and their alloys," *J. Appl. Phys.*, vol. 89, pp. 5815–5875, 2001.
- [9] S. Strite and H. Morkoc, "GaN, AIN, and InN A review," *J. Vac. Sci. Technol.*, *B*, vol. 10, pp. 1237 1266, 1992.
- [10] I. Vurgaftman and J. R. Meyer, "Band parameters for nitrogen-containing semiconductors," *J. Appl. Phys.*, vol. 94, pp. 3675 3696, 2003.
- [11] F. Glas, "Critical dimensions for the plastic relaxation of strained axial heterostructures in free-standing nanowires," *Phys. Rev. B*, vol. 74, pp. 121302-1 121302-4, 2006.
- [12] V. G. Dubrovskii and N. V. Sibirev, "Growth thermodynamics of nanowires and its application to polytypism of zinc blende III-V nanowires," *Phys. Rev. B*, vol. 77, pp. 035414-1 035414-8, 2008.
- [13] P. Yang, R. Yan, and M. Fardy, "Semiconductor nanowire: what's next?," *Nano Lett.*, vol. 10, pp. 1529 –1536, 2010.
- [14] H. J. Joyce, Q. Gao, H. Hoe Tan, C. Jagadish, Y. Kim, J. Zou, L. M. Smith, H. E. Jackson, J. M. Yarrison-Rice, P. Parkinson, and M. B. Johnston, "III-V semiconductor nanowires for optoelectronic device applications," *Prog. Quantum Electron.*, In Press, Corrected Proof.
- [15] F. Qian, Y. Li, S. Gradečak, D. Wang, C. J. Barrelet, and C. M. Lieber, "Gallium nitride-based nanowire radial heterostructures for nanophotonics," *Nano Lett.*, vol. 4, pp. 1975 1979, 2004.

- [16] Y. L. Chang, J. L. Wang, F. Li, and Z. Mi, "High efficiency green, yellow, and amber emission from InGaN/GaN dot-in-a-wire heterostructures on Si(111)," *Appl. Phys. Lett.*, vol. 96, pp. 013106-1 013106-3, 2010.
- [17] W. Guo, M. Zhang, A. Banerjee, and P. Bhattacharya, "Catalyst-Free InGaN/GaN nanowire light emitting diodes grown on (001) silicon by molecular beam epitaxy," *Nano Lett.*, vol. 10, pp. 3355 3359, 2010.
- [18] Y. F. Guo, C. S. Xue, W. J. Liu, H. B. Sun, and Y. P. Cao, "Fabrication of GaN nanowires on Pd-coated sapphire substrates by magnetron sputtering technique," *Mater. Charact.*, vol. 61, pp. 381 385, 2010.
- [19] Q. Li and G. T. Wang, "Improvement in aligned GaN nanowire growth using submonolayer Ni catalyst films," *Appl. Phys. Lett.*, vol. 93, 043119-1 043119-3, 2008.
- [20] R. J. Ellingson, M. C. Beard, J. C. Johnson, P. Yu, O. I. Micic, A. J. Nozik, A. Shabaev, and A. L. Efros, "Highly efficient multiple exciton generation in colloidal PbSe and PbS quantum dots," *Nano Lett.*, vol. 5, pp. 865 871, 2005.
- [21] P. Guyot-Sionnest, "Quantum dots: A new quantum state?," *Nat. Mater.*, vol. 4, pp. 653 654, 2005.
- [22] B. L. Oksengendler, N. N. Turaeva, and A. Zakhidov, "Statistic theory of multiple exciton generation in quantum dot based solar cells. complex phenomena in nanoscale systems," *Springer Netherlands*, pp. 223-228, 2009.
- [23] P. D. Cunningham, J. E. Boercker, E. E. Foos, M. P. Lumb, A. R. Smith, J. G. Tischler, and J. S. Melinger, "Enhanced multiple exciton generation in quasi-one-dimensional semiconductors," *Nano Lett.*, vol. 11, pp. 3476 3481, 2011.
- [24] C. Boney, I. Hernandez, R. Pillai, D. Starikov, A. Bensaoula, M. Henini, M. Syperek, J. Misiewicz, and R. Kudrawiec, "Growth and characterization of InGaN for photovoltaic devices," *35th IEEE Photovoltaic Specialists Conference*, 2010.
- [25] J. W. Ager, L. A. Reichertz, K. M. Yu, W. J. Schaff, T. L. Williamson, M. A. Hoffbauer, N. M. Haegel, and W. Walukiewicz, "InGaN/Si heterojunction tandem solar cells," *33rd IEEE Photovoltaic Specialists Conference*, Vol. 1-4, pp. 110 114, 2008.
- [26] K. T. Chen, C. F. Lin, C. M. Lin, C. C. Yang, and R. H. Jiang, "InGaN-based light-emitting solar cells with a pattern-nanoporous p-type GaN/Mg layer," *Thin Solid Films*, vol. 518, pp. 7377 7380, 2010.
- [27] X. Chen, K. D. Matthews, D. Hao, W. J. Schaff, and L. F. Eastman, "Growth, fabrication, and characterization of InGaN solar cells," *Phys. Status Solidi A*, vol. 205, pp. 1103 1105, 2008.
- [28] R. Dahal, B. Pantha, J. Li, J. Y. Lin, and H. X. Jiang, "InGaN/GaN multiple quantum well solar cells with long operating wavelengths," *Appl. Phys. Lett.*, vol. 94, 063505-1 063505-3, 2009.
- [29] M. Horie, K. Sugita, A. Hashimoto, and A. Yamamoto, "MOVPE growth and Mg doping of In_xGa_{1-x}N (x ~ 0.4) for solar cell," *Sol. Energy Mater. Sol. Cells*, vol. 93, pp. 1013 1015, 2009.

- [30] R. H. Horng, S. T. Lin, Y. L. Tsai, M. T. Chu, W. Y. Liao, M. H. Wu, R. M. Lin, and Y. C. Lu, "Improved conversion efficiency of GaN/InGaN thin-film solar cells," *IEEE Electron. Device Lett.*, vol. 30, pp. 724 726, 2009.
- [31] B. R. Jampana, A. G. Melton, M. Jamil, N. N. Faleev, R. L. Opila, I. T. Ferguson, and C. B. Honsberg, "Design and Realization of Wide-Band-Gap (~ 2.67 eV) InGaN p-n Junction Solar Cell," *IEEE Electron. Device Lett.*, vol. 31, pp. 32 34, 2010.
- [32] B. N. Pantha, J. Y. Lin, and H. X. Jiang, "III-nitride nanostructures for energy generation," *Proc. SPIE: Quantum Sensing and Nanophotonic Devices VII*, vol. 7608, 2010.
- [33] X. H. Zheng, L. J. Tang, D. Y. Zhang, J. R. Dong, and H. Yang, "Effect of contact spreading layer on photovoltaic response of InGaN-based solar cells," *Phys. Status Solidi A*, vol. 208, pp. 199 201, 2011.
- [34] H. Y. Ryu, "Extraction Efficiency in GaN Nanorod Light-emitting Diodes Investigated by Finite-difference Time-domain Simulation," *J. Kor. Phys. Soc.*, vol. 58, pp. 878 882, 2011.
- [35] Y. J. Liu, C. C. Huang, T. Y. Chen, C. S. Hsu, J. K. Liou, and W. C. Liu, "Improved Performance of an InGaN-Based Light-Emitting Diode With a p-GaN/n-GaN Barrier Junction," *IEEE J. Quantum Electron.*, vol. 47, pp. 755–761, 2011.
- [36] L. B. Chang, M. J. Lai, R. M. Lin, and C. H. Huang, "Effect of electron leakage on efficiency droop in wide-well InGaN-based light-emitting diodes," *Appl. Phys. Express*, vol. 4, 012106-1 012106-3, 2011.
- [37] C. H. Chiu, C. C. Lin, D. M. Deng, D. W. Lin, J. C. Li, Z. Y. Li, G. W. Shu, T. C. Lu, J. L. Shen, H. C. Kuo, and K. M. Lau, "Optical and electrical properties of GaN-based light emitting diodes grown on micro- and nano-scale patterned Si substrate," *IEEE J. Quantum Electron.*, vol. 47, pp. 899 906, 2011.
- [38] H. P. T. Nguyen, S. Zhang, K. Cui, X. Han, S. Fathololoumi, M. Couillard, G. A. Botton, and Z. Mi, "p-Type modulation doped InGaN/GaN dot-in-a-wire white-light-emitting diodes monolithically grown on Si(111)," *Nano Lett.*, vol. 11, pp. 1919 1924, 2011.
- [39] A. Tyagi, R. M. Farrell, K. M. Kelchner, C. Y. Huang, P. S. Hsu, D. A. Haeger, M. T. Hardy, C. Holder, K. Fujito, D. A. Cohen, H. Ohta, J. S. Speck, S. P. DenBaars, and S. Nakamura, "AlGaN-cladding free green semipolar GaN based laser diode with a lasing wavelength of 506.4nm," *Appl. Phys. Express*, vol. 4, 011002-1 011002-3, 2011.
- [40] J. Dorsaz, A. Castiglia, G. Cosendey, E. Feltin, M. Rossetti, M. Duelk, C. Velez, J. F. Carlin, and N. Grandjean, "AlGaN-Free Blue III-Nitride Laser Diodes Grown on c-Plane GaN Substrates," *Appl. Phys. Express*, vol. 4, 092102-1 092102-3, 2011.
- [41] Y. Zhang, T. T. Kao, J. P. Liu, Z. Lochner, S. S. Kim, J. H. Ryou, R. D. Dupuis, and S. C. Shen, "Effects of a step-graded Al_xGa_{1-x}N electron blocking layer in InGaN-based laser diodes," *J. Appl. Phys.*, vol. 109, 083115-1 083115-5, 2011.
- [42] T. Sumitomo, M. Ueno, T. Kyono, Y. Enya, Y. Yoshizumi, U. Masanori, Y. Yusuke, S. Yohei, and S. Takamichi, "Nitride-based semiconductor light

- emitting device useful e.g. laser diode comprises gallium-nitride substrate having light emitting layer; and semiconductor region comprising strained contact layer with electrode," EP2276079-A2; US2011012126-A1; JP2011023524-A; KR2011007046-A; CN101958386-A, 2011.
- [43] W. G. Scheibenzuber, U. T. Schwarz, L. Sulmoni, J. Dorsaz, J. F. Carlin, and N. Grandjean, "Recombination coefficients of GaN-based laser diodes," *J. Appl. Phys.*, vol. 109, 093106-1 093106-6, 2011.
- [44] S. J. Chang, T. K. Ko, Y. K. Su, Y. Z. Chiou, C. S. Chang, S. C. Shei, J. K. Sheu, W. C. Lai, Y. C. Lin, W. S. Chen, and C. F. Shen, "GaN-based p-i-n sensors with ITO contacts," *IEEE Sensors J.*, vol. 6, pp. 406 411, 2006.
- [45] D. Starikov, F. Benkabou, N. Medelci, and A. Bensaoula, "Integrated multi-wavelength fluorescence sensors," *Proceedings of the ISA/IEEE Sensors for Industry Conference*, pp. 15 18, 2002.
- [46] D. Starikov, C. Boney, I. Berishev, I. C. Hernandez, and A. Bensaoula, "Radio-frequency molecular-beam-epitaxy growth of III nitrides for microsensor applications," *J. Vac. Sci. Technol. B*, vol. 19, pp. 1404 1408, 2001.
- [47] W. Y. Weng, S. J. Chang, T. J. Hsueh, C. L. Hsu, M. J. Li, and W. C. Lai, "AlInN resistive ammonia gas sensors," *Sensor. Actuat. B-Chem.*, vol. 140, pp. 139 142, 2009.
- [48] J. L. Pau, J. Anduaga, C. Rivera, A. Navarro, I. Alava, M. Redondo, and E. Munoz, "Optical sensors based on III-nitride photodetectors for flame sensing and combustion monitoring," *Appl. Opt.*, vol. 45, pp. 7498 7503, 2006.
- [49] C. Rivera, J. L. Pau, F. B. Naranjo, and E. Munoz, "Novel photodetectors based on InGaN/GaN multiple quantum wells," *Phys. Status Solidi A*, vol. 201, pp. 2658 2662, 2004.
- [50] E. A. Berkman, N. A. El-Masry, A. Emara, and S. M. Bedair, "Nearly lattice-matched n, i, and p layers for InGaN p-i-n photodiodes in the 365-500 nm spectral range," *Appl. Phys. Lett.*, vol. 92, 101118-1 101118-3, 2008.
- [51] P. C. Chang and C. L. Yu, "InGaN/GaN multi-quantum-well ultraviolet photosensors by capping an unactivated Mg-doped GaN layer," *Appl. Phys. Lett.*, vol. 91, 141113-1 141113-32007, 2007.
- [52] S. J. Chang, S. M. Wang, P. C. Chang, C. H. Kuo, S. J. Young, T. P. Chen, S. L. Wu, and B. R. Huang, "GaN Schottky Barrier Photodetectors," *IEEE Sensors J.*, vol. 10, pp. 1609 1614, 2010.
- [53] K. P. Korona, A. Drabinska, J. Borysiuk, and P. Caban, "Nitride-based photodetectors containing quantum wells in tunable electric fields," *J. Optoelectron. Adv. Mater.*, vol. 11, pp. 1108 1114, 2009.
- [54] H. C. Lee, Y. K. Su, J. C. Lin, Y. C. Cheng, S. L. Wu, and Y. D. Jhou, "AlInGaN metal-insulator-semiconductor photodetectors at UV-C 280 nm," *Electrochem. Solid ST*, vol. 12, pp. H357 H360, 2009.
- [55] E. Munoz, "(Al,ln,Ga)N-based photodetectors. Some materials issues," *Phys. Status Solidi B*, vol. 244, pp. 2859 2877, 2007.
- [56] B. S. Kang, F. Ren, B. P. Gila, C. R. Abernathy, and S. J. Pearton, "AlGaN/GaN-based metal-oxide semiconductor diode-based hydrogen gas sensor," *State-of-the-art program on compound semiconductors XL (Sotapocs*

- *Xl) and narrow bandgap optoelectronic materials and devices II*, vol. 2004, pp. 144 151, 2004.
- [57] H. T. Wang, B. S. Kang, F. Ren, R. C. Fitch, J. K. Gillespie, N. Moser, G. Jessen, T. Jenkins, R. Dettmer, D. Via, A. Crespo, B. P. Gila, C. R. Abernathy, and S. J. Pearton, "Comparison of gate and drain current detection of hydrogen at room temperature with AlGaN/GaN high electron mobility transistors," *Appl. Phys. Lett.*, vol. 87, pp. 172105-1 172105-3, 2005.
- [58] J. Schalwig, G. Muller, U. Karrer, M. Eickhoff, O. Ambacher, M. Stutzmann, L. Gorgens, and G. Dollinger, "Hydrogen response mechanism of Pt-GaN Schottky diodes," *Appl. Phys. Lett.*, vol. 80, pp. 1222 – 1224, 2002.
- [59] J. Johnson, Y. H. Choi, A. Ural, W. Lim, J. S. Wright, B. P. Gila, F. Ren, and S. J. Pearton, "Growth and characterization of GaN nanowires for hydrogen sensors," *J. Electron. Mater.*, vol. 38, pp. 490 494, 2009.
- [60] L. C. Tien, P. W. Sadik, D. P. Norton, L. F. Voss, S. J. Pearton, H. T. Wang, B. S. Kang, F. Ren, J. Jun, and J. Lin, "Hydrogen sensing at room temperature with Pt-coated ZnO thin films and nanorods," *Appl. Phys. Lett.*, vol. 87, pp. 222106-1 222106-3, 2005.
- [61] W. Lim, J. S. Wright, B. P. Gila, J. L. Johnson, A. Ural, T. Anderson, F. Ren, and S. J. Pearton, "Room temperature hydrogen detection using Pd-coated GaN nanowires," *Appl. Phys. Lett.*, vol. 93, pp. 072109-1 072109-3, 2008.
- [62] H. T. Wang, T. J. Anderson, F. Ren, C. Z. Li, Z. N. Low, J. Lin, B. P. Gila, S. J. Pearton, A. Osinsky, and A. Dabiran, "Robust detection of hydrogen using differential AlGaN/GaN high electron mobility transistor sensing diodes," *Appl. Phys. Lett.*, vol. 89, pp. 242111-1 242111-3, 2006.
- [63] H. T. Wang, B. S. Kang, F. Ren, L. C. Tien, P. W. Sadik, D. P. Norton, S. J. Pearton, and J. Lin, "Hydrogen-selective sensing at room temperature with ZnO nanorods," *Appl. Phys. Lett.*, vol. 86, pp. 243503-1 243503-3, 2005.
- [64] L. C. Tien, H. T. Wang, B. S. Kang, F. Ren, P. W. Sadik, D. P. Norton, S. J. Pearton, and J. S. Lin, "Room-temperature hydrogen-selective sensing using single Pt-coated ZnO nanowires at microwatt power levels," *Electrochem. Solid-State Lett.*, vol. 8, pp. G230 G232, 2005.
- [65] L. A. Patil, M. D. Shinde, A. R. Bari, and V. V. Deo, "Highly Sensitive Nanostructured SnO₂ Thin Films For Hydrogen Sensing," *International Conference on Advanced Nanomaterials and Nanotechnology (ICANN 2009)*, vol. 1276, pp. 327 334, 2010.
- [66] A. Qurashi, E. M. El-Maghraby, T. Yamazaki, and T. Kikuta, "Catalyst supported growth of In₂O₃ nanostructures and their hydrogen gas sensing properties," *Sens. Actuators B*, vol. 147, pp. 48 54, 2010.
- [67] B. S. Simpkins, K. M. McCoy, L. J. Whitman, and P. E. Pehrsson, "Fabrication and characterization of DNA-functionalized GaN nanowires," *Nanotechnology*, vol. 18, p. 355301 (5pp), 2007.
- [68] A. Ganguly, C.-P. Chen, Y.-T. Lai, C.-C. Kuo, C.-W. Hsu, K.-H. Chen, and L.-C. Chen, "Functionalized GaN nanowire-based electrode for direct label-free voltammetric detection of DNA hybridization," *J. Mater. Chem.*, vol. 19, pp. 928 933, 2009.

- [69] C.-P. Chen, A. Ganguly, C.-H. Wang, C.-W. Hsu, S. Chattopadhyay, Y.-K. Hsu, Y.-C. Chang, K.-H. Chen, and L.-C. Chen, "Label-free dual sensing of DNA molecules using GaN nanowires," *Anal. Chem.*, vol. 81, pp. 36-42, 2008.
- [70] R. S. Chen, H. Y. Chen, C. Y. Lu, K. H. Chen, C. P. Chen, L. C. Chen, and Y. J. Yang, "Ultrahigh photocurrent gain in m-axial GaN nanowires," *Appl. Phys. Lett*, vol. 91, pp. 223106-1 223106-3, 2007.
- [71] R. Calarco, M. Marso, T. Richter, A. I. Aykanat, R. Meijers, A. v.d. Hart, T. Stoica, and H. Lüth, "Size-dependent Photoconductivity in MBE-Grown GaN-Nanowires," *Nano Lett.*, vol. 5, pp. 981 984, 2005.
- [72] L. Rigutti, M. Tchernycheva, A. De Luna Bugallo, G. Jacopin, F. H. Julien, L. F. Zagonel, K. March, O. Stephan, M. Kociak, and R. Songmuang, "Ultraviolet photodetector based on GaN/AlN quantum disks in a single nanowire," *Nano Lett.*, vol. 10, pp. 2939 2943, 2010.
- [73] L. Rigutti, M. Tchernycheva, A. D. L. Bugallo, G. Jacopin, F. H. Julien, R. Songmuang, E. Monroy, S. T. Chou, Y. T. Lin, P. H. Tseng, L. W. Tu, F. Fortuna, L. Zagonel, M. Kociak, and O. Stephan, "GaN/AlN quantum disc single-nanowire photodetectors," *Phys. Stat. Solidi A*, vol. 207, pp. 1323-1327, 2010.
- [74] B. Oksengendler, N. Turaeva, and S. Rashidova, "Statistical theory of multiple exciton generation in quantum dot solar cells," *Appl. Solar Energy*, vol. 45, pp. 162 165, 2009.
- [75] J. Zhu, Z. F. Yu, G. F. Burkhard, C. M. Hsu, S. T. Connor, Y. Q. Xu, Q. Wang, M. McGehee, S. H. Fan, and Y. Cui, "Optical absorption enhancement in amorphous silicon nanowire and nanocone arrays," *Nano Lett.*, vol. 9, pp. 279 282, 2009.
- [76] J. Wu, W. Walukiewicz, K. M. Yu, J. W. Ager, E. E. Haller, H. Lu, W. J. Schaff, Y. Saito, and Y. Nanishi, "Unusual properties of the fundamental band gap of InN," *Appl. Phys. Lett*, vol. 80, pp. 3967 3969, 2002.
- [77] V. Y. Davydov, A. A. Klochikhin, R. P. Seisyan, V. V. Emtsev, S. V. Ivanov, F. Bechstedt, J. Furthmuller, H. Harima, A. V. Mudryi, J. Aderhold, O. Semchinova, and J. Graul, "Absorption and emission of hexagonal InN. Evidence of narrow fundamental band gap," *Phys. Stat. Solidi B*, vol. 229, pp. R1 R3, 2002.
- [78] J. Wu, W. Walukiewicz, K. M. Yu, W. Shan, J. W. Ager, E. E. Haller, H. Lu, W. J. Schaff, W. K. Metzger, and S. Kurtz, "Superior radiation resistance of In_{1-x}Ga_xN alloys: Full-solar-spectrum photovoltaic material system," *J. Appl.Phys.*, vol. 94, pp. 6477 6482, 2003.
- [79] Y. Li, F. Qian, J. Xiang, and C. M. Lieber, "Nanowire electronic and optoelectronic devices," *Mater. Today*, vol. 9, pp. 18 27, 2006.
- [80] F. Qian, S. Gradecak, Y. Li, C. Y. Wen, and C. M. Lieber, "Core/multishell nanowire heterostructures as multicolor, high-efficiency light-emitting diodes," *Nano Lett.*, vol. 5, pp. 2287 2291, 2005.
- [81] T. Kuykendall, P. Ulrich, S. Aloni, and P. Yang, "Complete composition tunability of InGaN nanowires using a combinatorial approach," *Nat. Mater*, vol. 6, pp. 951 956, 2007.

- [82] X. Xiaobin Zhang, Hongling Xiao, Cuibai Yang, and C. Junxue Ran, Qifeng Hou and Jinmin Li, "Simulation of In_{0.65}Ga_{0.35} N single-junction solar cell," *J. Phys. D: Appl. Phys.*, vol. 40, pp. 7335 7338, 2007.
- [83] L. Hsu and W. Walukiewicz, "Modeling of InGaN/Si tandem solar cells," *J. Appl. Phys.*, vol. 104, pp. 024507-1 024507-7, 2008.
- [84] X. Xiaobin Zhang, Hongling Xiao, Cuibai Yang, and C. Junxue Ran, Qifeng Hou, Jinmin Li, and Wang, Z, "Theoretical design and performance of In_xGa_{1-x}N two-junction solar cells," *J. Phys. D: Appl. Phys.*, vol. 41, pp. 245104 (6pp), 2008.
- [85] Y. Dong, B. Tian, T. J. Kempa, and C. M. Lieber, "Coaxial Group HNitride Nanowire Photovoltaics," *Nano Lett.*, vol. 9, pp. 2183 2187, 2009.
- [86] Y. B. Tang, Z. H. Chen, H. S. Song, C. S. Lee, H. T. Cong, H. M. Cheng, W. J. Zhang, I. Bello, and S. T. Lee, "Vertically aligned p-type single-crystalline GaN nanorod arrays on n-type Si for heterojunction photovoltaic cells," *Nano Lett.*, vol. 8, pp. 4191 4195, 2008.
- [87] S. Gradecak, F. Qian, Y. Li, H. G. Park, and C. M. Lieber, "GaN nanowire lasers with low lasing thresholds," *Appl. Phys. Lett.*, vol. 87, pp. 173111-1 173111-3, 2005.
- [88] F. Qian, Y. Li, S. Gradecak, H.-G. Park, Y. Dong, Y. Ding, Z. L. Wang, and C. M. Lieber, "Multi-quantum-well nanowire heterostructures for wavelength-controlled lasers," *Nat. Mater*, vol. 7, pp. 701 706, 2008.
- [89] J. C. Johnson, H.-J. Choi, K. P. Knutsen, R. D. Schaller, P. Yang, and R. J. Saykally, "Single gallium nitride nanowire lasers," *Nat. Mater*, vol. 1, pp. 106 110, 2002.
- [90] H.-J. Choi, J. C. Johnson, R. He, S.-K. Lee, F. Kim, P. Pauzauskie, J. Goldberger, R. J. Saykally, and P. Yang, "Self-organized GaN quantum wire UV lasers," *J. Phys. Chem. B*, vol. 107, pp. 8721 8725, 2003.
- [91] Y. L. Chang, F. Li, A. Fatehi, and Z. Mi, "Molecular beam epitaxial growth and characterization of non-tapered InN nanowires on Si(111)," *Nanotechnology*, vol. 20, pp. 345203 (6pp), 2009.
- [92] S. X. Jin, J. Li, J. Z. Li, J. Y. Lin, and H. X. Jiang, "GaN microdisk light emitting diodes," *Appl. Phys. Lett.*, vol. 76, pp. 631 633, 2000.
- [93] A. V. Maslov and C. Z. Ning, "Reflection of guided modes in a semiconductor nanowire laser," *Appl. Phys. Lett.*, vol. 83, pp. 1237 1239, 2003.
- [94] C. Hahn, Z. Y. Zhang, A. Fu, C. H. Wu, Y. J. Hwang, D. J. Gargas, and P. D. Yang, "Epitaxial growth of InGaN nanowire arrays for light emitting diodes," *ACS Nano*, vol. 5, pp. 3970 3976, 2011.
- [95] T. Y. Tang, C. H. Lin, Y. S. Chen, W. Y. Shiao, W. M. Chang, C. H. Liao, K. C. Shen, C. C. Yang, M. C. Hsu, J. H. Yeh, and T. C. Hsu, "Nitride Nanocolumns for the Development of Light-Emitting Diode," *IEEE Trans. Electron Devices*, vol. 57, pp. 71 78, 2010.
- [96] D. H. Lin, S. C. Shiu, J. S. Huang, C. F. Lin, and Ieee, "Effect of nanowire lengths on polymer-Si nanowire hybrid solar cells," in *35th IEEE Photovoltaic Specialists Conference*, Honolulu, HI, 20 25 June 2010.

- [97] K. Kishino, A. Kikuchi, H. Sekiguchi, and S. Ishizawa, "InGaN/GaN nanocolumn LEDs emitting from blue to red," *Gallium nitride materials and devices II*, vol. 6473, pp. T4730 T4730, 2007.
- [98] M. Kuball, F. H. Morrissey, M. Benyoucef, I. Harrison, D. Korakakis, and C. T. Foxon, "Nano-fabrication of GaN pillars using focused ion beam etching," *Phys. Stat. Solidi A*, vol. 176, pp. 355 358, 1999.
- [99] J. M. Lee, J. W. Choung, J. Yi, D. H. Lee, M. Samal, D. K. Yi, C. H. Lee, G. C. Yi, U. Paik, J. A. Rogers, and W. I. Park, "Vertical pillar-superlattice array and graphene hybrid light emitting diodes," *Nano Lett.*, vol. 10, pp. 2783–2788, 2010.
- [100] J. Y. Liang, H. Chik, A. J. Yin, and J. Xu, "Two-dimensional lateral superlattices of nanostructures: Nonlithographic formation by anodic membrane template," *J. Appl. Phys.*, vol. 91, pp. 2544 2546, 2002.
- [101] I. M. Tiginyanu, V. V. Ursaki, V. V. Zalamai, S. Langa, S. Hubbard, D. Pavlidis, and H. Foll, "Luminescence of GaN nanocolumns obtained by photon-assisted anodic etching," *Appl. Phys. Lett.*, vol. 83, pp. 1551 1553, 2003.
- [102] S. Keller, C. Schaake, N. A. Fichtenbaum, C. J. Neufeld, Y. Wu, K. McGroddy, A. David, S. P. DenBaars, C. Weisbuch, J. S. Speck, and U. K. Mishra, "Optical and structural properties of GaN nanopillar and nanostripe arrays with embedded InGaN/GaN multi-quantum wells," *J. Appl. Phys.*, vol. 100, pp. 054314-1 054314-7, 2006.
- [103] M. Y. Hsieh, C. Y. Wang, L. Y. Chen, M. Y. Ke, and J. J. Huang, "InGaN-GaN nanorod light emitting arrays fabricated by silica nanomasks," *IEEE J. Quantum Electron.*, vol. 44, pp. 468 472, 2008.
- [104] C. Y. Wang, L. Y. Chen, C. P. Chen, Y. W. Cheng, M. Y. Ke, M. Y. Hsieh, H. M. Wu, L. H. Peng, and J. Huang, "GaN nanorod light emitting diode arrays with a nearly constant electroluminescent peak wavelength," *Opt. Express*, vol. 16, pp. 10549 10556, 2008.
- [105] G. W. Quiming Li, Saeed Fathololoumi, Zetian Mi, "Top-down nanorod GaN/InGaN LEDs," *Appl. Phys. Lett., under review*.
- [106] L. Y. Chen, Y. Y. Huang, C. H. Chang, Y. H. Sun, Y. W. Cheng, M. Y. Ke, C. P. Chen, and J. J. Huang, "High performance InGaN/GaN nanorod light emitting diode arrays fabricated by nanosphere lithography and chemical mechanical polishing processes," *Opt. Express*, vol. 18, pp. 7664 7669, 2010.
- [107] M. Q. He, I. Minus, P. Z. Zhou, S. N. Mohammed, J. B. Halpern, R. Jacobs, W. L. Sarney, L. Salamanca-Riba, and R. D. Vispute, "Growth of large-scale GaN nanowires and tubes by direct reaction of Ga with NH₃," *Appl. Phys. Lett.*, vol. 77, pp. 3731 3733, 2000.
- [108] J. Zhang, X. S. Peng, X. F. Wang, Y. W. Wang, and L. D. Zhang, "Micro-Raman investigation of GaN nanowires prepared by direct reaction Ga with NH₃," *Chem. Phys. Lett.*, vol. 345, pp. 372 376, 2001.
- [109] H. Y. Peng, X. T. Zhou, N. Wang, Y. F. Zheng, L. S. Liao, W. S. Shi, C. S. Lee, and S. T. Lee, "Bulk-quantity GaN nanowires synthesized from hot filament chemical vapor deposition," *Chem. Phys. Lett.*, vol. 327, pp. 263 270, 2000.
- [110] X. Duan and C. M. Lieber, "Laser-assisted catalytic growth of single crystal GaN nanowires," *J. Am. Chem. Soc.*, vol. 122, pp. 188 189, 1999.

- [111] E. Calleja, M. A. Sánchez-García, F. J. Sánchez, F. Calle, F. B. Naranjo, E. Muñoz, U. Jahn, K. Ploog, "Luminescence properties and defects in GaN nanocolumns grown by molecular beam epitaxy," *Phys. Rev. B*, vol. 62, pp. 16826 16834, 2000.
- [112] S. A. Dayeh, E. T. Yu, and D. Wang, "III-V nanowire growth mechanism: V/III ratio and temperature effects," *Nano Lett.*, vol. 7, pp. 2486 2490, 2007.
- [113] R. K. Debnath, R. Meijers, T. Richter, T. Stoica, R. Calarco, and H. Luth, "Mechanism of molecular beam epitaxy growth of GaN nanowires on Si(111)," *Appl. Phys. Lett.*, vol. 90, pp. 123117-1 123117-3, 2007.
- [114] P. K. Mohseni, C. Maunders, G. A. Botton, R. R. LaPierre, "GaP/GaAsP/GaP core–multishell nanowire heterostructures on (111) silicon," *Nanotechnology*, vol. 18, p. 445304 (6pp), 2007.
- [115] T. Kuykendall, P. Ulrich, S. Aloni, and P. Yang, "Complete composition tunability of InGaN nanowires using a combinatorial approach," *Nat. Mater.*, vol. 6, pp. 951 956, 2007.
- [116] O. Hayden, A. B. Greytak, and D. C. Bell, "Core-shell nanowire light-emitting diodes," *Adv. Mater.*, vol. 17, pp. 701 704, 2005.
- [117] C. P. T. Svensson, T. Martensson, J. Tragardh, C. Larsson, M. Rask, D. Hessman, L. Samuelson, and J. Ohlsson, "Monolithic GaAs/InGaP nanowire light emitting diodes on silicon," *Nanotechnology*, vol. 19, pp. 305201, 2008.
- [118] K. Tomioka, J. Motohisa, S. Hara, K. Hiruma, and T. Fukui, "GaAs/AlGaAs core multishell nanowire-based light-emitting diodes on Si," *Nano Lett.*, vol. 10, pp. 1639 1644, 2010.
- [119] H.-M. Kim, Y.-H. Cho, H. Lee, S. I. Kim, S. R. Ryu, D. Y. Kim, T. W. Kang, and K. S. Chung, "High-brightness light emitting diodes using dislocation-free indium gallium nitride/gallium nitride multiquantum-well nanorod arrays," *Nano Lett.*, vol. 4, pp. 1059 1062, 2004.
- [120] A. Kikuchi, M. Kawai, M. Tada, and K. Kishino, "InGaN/GaN multiple quantum disk nanocolumn light-emitting diodes grown on (111)Si substrate," *Jpn. J. Appl. Phys.*, vol. 43, pp. L1524 L1526, 2004.
- [121] H. W. Lin, Y. J. Lu, H. Y. Chen, H. M. Lee, and S. Gwo, "InGaN/GaN nanorod array white light-emitting diode," *Appl. Phys. Lett.*, vol. 97, pp. 073101-1 073101-3, 2010.
- [122] S. Nakamura, M. Senoh, and T. Mukai, "p-GaN/n-InGaN/n-GaN double-heterostructure blue-light-emitting diodes," *Jpn. J. Appl. Phys.*, vol. 32, pp. L8 L11, 1993.
- [123] B. Monemar and B. E. Sernelius, "Defect related issues in the "current roll-off" in InGaN based light emitting diodes," *Appl. Phys. Lett.*, vol. 91, pp. 181103-1 181103-3, 2007.
- [124] M. H. Kim, M. F. Schubert, Q. Dai, J. K. Kim, E. F. Schubert, J. Piprek, and Y. Park, "Origin of efficiency droop in GaN-based light-emitting diodes," *Appl. Phys. Lett.*, vol. 91, pp. 183507-1 183507-3, 2007.
- [125] M. F. Schubert, J. Xu, J. K. Kim, E. F. Schubert, M. H. Kim, S. Yoon, S. M. Lee, C. Sone, T. Sakong, and Y. Park, "Polarization-matched GaInN/AlGaInN multi-quantum-well light-emitting diodes with reduced efficiency droop," *Appl. Phys. Lett.*, vol. 93, pp. 041102-1 041102-3, 2008.

- [126] Y. C. Shen, G. O. Mueller, S. Watanabe, N. F. Gardner, A. Munkholm, and M. R. Krames, "Auger recombination in InGaN measured by photoluminescence," *Appl. Phys. Lett.*, vol. 91, pp. 141101-1 141101-3, 2007.
- [127] K. J. Vampola, M. Iza, S. Keller, S. P. DenBaars, and S. Nakamura, "Measurement of electron overflow in 450 nm InGaN light-emitting diode structures," *Appl. Phys. Lett.*, vol. 94, pp. 061116-1 061116-3, 2009.
- [128] J. Q. Xie, X. F. Ni, Q. Fan, R. Shimada, U. Ozgur, and H. Morkoc, "On the efficiency droop in InGaN multiple quantum well blue light emitting diodes and its reduction with p-doped quantum well barriers," *Appl. Phys. Lett.*, vol. 93, pp. 121107-1 121107-3, 2008.
- [129] I. V. Rozhansky and D. A. Zakheim, "Analysis of the causes of the decrease in the electroluminescence efficiency of AlGaInN light-emitting-diode heterostructures at high pumping density," *Semiconductors*, vol. 40, pp. 839–845, 2006.
- [130] H.-Y. Ryu, H.-S. Kim, and J.-I. Shim, "Rate equation analysis of efficiency droop in InGaN light-emitting diodes," *Appl. Phys. Lett.*, vol. 95, pp. 081114-1 081114-3, 2009.
- [131] Q. Dai, Q. F. Shan, J. Wang, S. Chhajed, J. Cho, E. F. Schubert, M. H. Crawford, D. D. Koleske, M. H. Kim, and Y. Park, "Carrier recombination mechanisms and efficiency droop in GaInN/GaN light-emitting diodes," *Appl. Phys. Lett.*, vol. 97, pp. 133507-1 133506-3, 2010.
- [132] F. Bernardini, V. Fiorentini, and D. Vanderbilt, "Spontaneous polarization and piezoelectric constants of III-V nitrides," *Phys. Rev.B*, vol. 56, p. R10024-R10027, 1997.
- [133] O. Ambacher, R. Dimitrov, M. Stutzmann, B. E. Foutz, M. J. Murphy, J. A. Smart, J. R. Shealy, N. G. Weimann, K. Chu, M. Chumbes, B. Green, A. J. Sierakowski, W. J. Schaff, and L. F. Eastman, "Role of spontaneous and piezoelectric polarization induced effects in group-III nitride based heterostructures and devices," *Phys. Stat. Solidi B*, vol. 216, pp. 381–389, 1999.
- [134] A. Hangleiter, J. S. Im, H. Kollmer, S. Heppel, J. Off, and F. Scholz, "The role of piezoelectric fields in GaN-based quantum wells," *MRS Internet J. Nitride Semiconductor Research*, vol. 3, pp. 1998 1999, 1998.
- [135] L. H. Peng, C. W. Chuang, and L. H. Lou, "Piezoelectric effects in the optical properties of strained InGaN quantum wells," *Appl. Phys. Lett.*, vol. 74, pp. 795 797, 1999.
- [136] F. Della Sala, A. Di Carlo, P. Lugli, F. Bernardini, V. Fiorentini, R. Scholz, and J. M. Jancu, "Free-carrier screening of polarization fields in wurtzite GaN/InGaN laser structures," *Appl. Phys. Lett.*, vol. 74, pp. 2002 2004, 1999.
- [137] S. Kalliakos, P. Lefebvre, and T. Taliercio, "Nonlinear behavior of photoabsorption in hexagonal nitride quantum wells due to free carrier screening of the internal fields," *Phys. Rev. B*, vol. 67, pp. 205307-1 205307-10, 2003.
- [138] C. A. Flory and G. Hasnain, "Modeling of GaN optoelectronic devices and strain-induced piezoelectric effects," *IEEE J. Quantum Electron.*, vol. 37, pp. 244 253, 2001.

- [139] J. Piprek, Nitride semiconductor devices. Wiley-VCH, 2007.
- [140] W. Qian, G. S. Rohrer, M. Skowronski, K. Doverspike, L. B. Rowland, and D. K. Gaskill, "Open-core screw dislocations in gan epilayers observed by scanning force microscopy and high-resolution transmission electron-microscopy," *Appl. Phys. Lett.*, vol. 67, pp. 2284 2286, 1995.
- [141] L. T. Romano, B. S. Krusor, and R. J. Molnar, "Structure of GaN films grown by hydride vapor phase epitaxy," *Appl. Phys. Lett.*, vol. 71, pp. 2283–2285, 1997.
- [142] Z. Liliental-Weber, C. Kisielowski, S. Ruvimov, Y. Chen, J. Washburn, I. Grzegory, M. Bockowski, J. Jun, and S. Porowski, "Structural characterization of bulk GaN crystals grown under high hydrostatic pressure," *J. Electron. Mater.*, vol. 25, pp. 1545 1550, 1996.
- [143] X. H. Wu, L. M. Brown, D. Kapolnek, S. Keller, B. Keller, S. P. DenBaars, and J. S. Speck, "Defect structure of metal-organic chemical vapor deposition-grown epitaxial (0001) GaN/Al₂O₃," *J. Appl. Phys.*, vol. 80, pp. 3228–3237, 1996.
- [144] L. Sugiura, K. Itaya, J. Nishio, H. Fujimoto, and Y. Kokubun, "Effects of thermal treatment of low-temperature GaN buffer layers on the quality of subsequent GaN layers," *J. Appl. Phys.*, vol. 82, pp. 4877 4882, 1997.
- [145] E. Arslan, M. K. Ozturk, A. Teke, S. Ozcelik, and E. Ozbay, "Buffer optimization for crack-free GaN epitaxial layers grown on Si(111) substrate by MOCVD," *J. Phys. D: Appl. Phys.*, vol. 41, pp. 155317 (10pp), 2008.
- [146] M. J. Kappers, M. A. Moram, D. V. S. Rao, C. McAleese, and C. J. Humphreys, "Low dislocation density GaN growth on high-temperature AlN buffer layers on (0001) sapphire," *J. Cryst. Growth*, vol. 312, pp. 363–367, 2010.
- [147] M. Mosca, J. L. Reverchon, F. Omnes, and J. Y. Duboz, "Effects of the buffer layers on the performance of (Al,Ga)N ultraviolet photodetectors," *J. Appl. Phys.*, vol. 95, pp. 4367 4370, 2004.
- [148] S. Ruvimov, Z. LilientalWeber, J. Washburn, K. J. Duxstad, E. E. Haller, Z. F. Fan, S. N. Mohammad, W. Kim, A. E. Botchkarev, and H. Morkoc, "TEM structure characterization of Ti/Al and Ti/Al/Ni/Au ohmic contacts for n-GaN,", *III-Nitride, SiC and Diamond Materials for Electronic Devices*. vol. 423, pp. 201 206, 1996,
- [149] H. Amano, M. Kito, K. Hiramatsu, and I. Akasaki, "p-type conduction in mg-doped GaN treated with low-energy electron-beam irradiation (LEEBI)," *Jpn. J. Appl. Phys.*, vol. 28, pp. L2112 L2114, 1989.
- [150] S. Nakamura, T. Mukai, and M. Senoh, "High-power GaN p-n-junction blue-light-emitting diodes," *Jpn. J. Appl. Phys.*, vol. 30, pp. L1998-L2001, Dec 1 1991.
- [151] J. Piprek, "Efficiency droop in nitride-based light-emitting diodes," *Phys. Stat. Solidi A*, vol. 207, pp. 2217 2225, 2010.
- [152] T. Mukai, M. Yamada, and S. Nakamura, "Characteristics of InGaN-based UV/blue/green/amber/red light-emitting diodes," *Jpn. J. Appl. Phys.*, vol. 38, pp. 3976 3981, 1999.

- [153] A. David and M. J. Grundmann, "Droop in InGaN light-emitting diodes: A differential carrier lifetime analysis," *Appl. Phys. Lett.*, vol. 96, pp. 103504-1 103504-3, 2010.
- [154] J.-I. Shim, H. Kim, D.-S. Shin, and H.-Y. Yoo, "An explanation of efficiency droop in InGaN-based light emitting diodes: saturated radiative recombination rate at randomly distributed In-rich active areas," *J. Kor. Phys. Soc.*, vol. 58, pp. 503 508, 2011.
- [155] P. Bhattacharya, "Semiconductor Optoelectronic Devices, 2 ed," *Prentice Hall, Englewood Cliffs, NJ*, 1996.
- [156] J. Piprek, "Semiconductor Optoelectronic Devices: Introduction to Physics and Simulation."
- [157] M. Zhang, P. Bhattacharya, J. Singh, and J. Hinckley, "Direct measurement of auger recombination in In_{0.1}Ga_{0.9}N/GaN quantum wells and its impact on the efficiency of In_{0.1}Ga_{0.9}N/GaN multiple quantum well light emitting diodes," *Appl. Phys. Lett.*, vol. 95, pp. 201108-1 201108-3, 2009.
- [158] M. Meneghini, N. Trivellin, G. Meneghesso, E. Zanoni, U. Zehnder, and B. Hahn, "A combined electro-optical method for the determination of the recombination parameters in InGaN-based light-emitting diodes," *J. Appl. Phys.*, vol. 106, pp. 114508-1 114508-4, 2009.
- [159] A. Laubsch, M. Sabathil, J. Baur, M. Peter, and B. Hahn, "High-Power and High-Efficiency InGaN-Based Light Emitters," *IEEE Trans. Electron Devices*, vol. 57, pp. 79 87, 2010.
- [160] J. H. Zhu, S. M. Zhang, H. Wang, D. G. Zhao, J. J. Zhu, Z. S. Liu, D. S. Jiang, Y. X. Qiu, and H. Yang, "The investigation on carrier distribution in InGaN/GaN multiple quantum well layers," *J. Appl. Phys.*, vol. 109, pp. 093117-1 093117-4, 2011.
- [161] J. P. Liu, J. H. Ryou, R. D. Dupuis, J. Han, G. D. Shen, and H. B. Wang, "Barrier effect on hole transport and carrier distribution in InGaN/GaN multiple quantum well visible light-emitting diodes," *Appl. Phys. Lett.*, vol. 93, pp. 021102-1 021102-3, 2008.
- [162] S.-H. Han, C.-Y. Cho, S.-J. Lee, T.-Y. Park, T.-H. Kim, S. H. Park, S. W. Kang, J. W. Kim, Y. C. Kim, and S.-J. Park, "Effect of Mg doping in the barrier of InGaN/GaN multiple quantum well on optical power of light-emitting diodes," *Appl. Phys. Lett.*, vol. 96, pp. 051113-1 051113-3, 2010.
- [163] X. Ni, Q. Fan, R. Shimada, U. Oezguer, and H. Morkoc, "Reduction of efficiency droop in InGaN light emitting diodes by coupled quantum wells," *Appl. Phys. Lett.*, vol. 93, Oct 27 2008.
- [164] M. C. Tsai, S. H. Yen, Y. C. Lu, and Y. K. Kuo, "Numerical study of blue InGaN Light-emitting diodes with varied barrier thicknesses," *IEEE Photonics Technol. Lett.*, vol. 23, pp. 76 78, 2011.
- [165] J. Piprek and S. Li, "Electron leakage effects on GaN-based light-emitting diodes," *Opt. Quantum Electron.*, vol. 42, pp. 89 95, 2010.
- [166] X. Ni, X. Li, J. Lee, S. Liu, V. Avrutin, Ü. Özgür, H. Morko, and A. Matulionis, "Hot electron effects on efficiency degradation in InGaN light emitting diodes

- and designs to mitigate them," *J. Appl. Phys.*, vol. 108, pp. 033112-1 033112-13, 2010.
- [167] X. Ni, X. Li, J. Lee, S. Liu, V. Avrutin, U. Ozgur, H. Morkoc, A. Matulionis, T. Paskova, G. Mulholland, and K. R. Evans, "The effect of ballistic and quasiballistic electrons on the efficiency droop of InGaN light emitting diodes," *Phys. Status Solidi RRL*, vol. 4, pp. 194 196, 2010.
- [168] I. A. Pope, P. M. Smowton, P. Blood, J. D. Thomson, M. J. Kappers, and C. J. Humphreys, "Carrier leakage in InGaN quantum well light-emitting diodes emitting at 480 nm," *Appl. Phys. Lett.*, vol. 82, pp. 2755 2757, 2003.
- [169] S. Singh, D. Robidas, N. Rohila, S. Pal, and C. Dhanavantri, "Effect of electron blocking layer on efficiency droop in blue InGaN/GaN based light-emitting diodes," *Optoelectron. Adv. Mater. Rapid Commun.*, vol. 4, pp. 1106–1110, 2010.
- [170] J. Piprek, R. Farrell, S. DenBaars, and S. Nakamura, "Effects of built-in polarization on InGaN-GaN vertical-cavity surface-emitting lasers," *IEEE Photonics Technol. Lett.*, vol. 18, pp. 7 9, 2006.
- [171] V. Fiorentini, F. Bernardini, and O. Ambacher, "Evidence for nonlinear macroscopic polarization in III-V nitride alloy heterostructures," *Appl. Phys. Lett.*, vol. 80, pp. 1204 1206, 2002.
- [172] S. H. Han, D. Y. Lee, S. J. Lee, C. Y. Cho, M. K. Kwon, S. P. Lee, D. Y. Noh, D. J. Kim, Y. C. Kim, and S. J. Park, "Effect of electron blocking layer on efficiency droop in InGaN/GaN multiple quantum well light-emitting diodes," *Appl. Phys. Lett.*, vol. 94, pp. 231123-1 231123-3, 2009.
- [173] I. V. Rozhansky and D. A. Zakheim, "Analysis of processes limiting quantum efficiency of AlGaInN LEDs at high pumping," *Phys. Status Solidi A*, vol. 204, pp. 227 230, 2007.
- [174] M. Endo, Z. Jin, S. Kasai, and H. Hasegawa, "Reactive ion beam etching of GaN and AlGaN/GaN for nanostructure fabrication using methane-based gas mixtures," *Jpn. J. Appl. Phys.*, vol. 41, pp. 2689 2693, 2002.
- [175] S.-Y. Park, S. J. Di Giacomo, R. Anisha, P. R. Berger, P. E. Thompson, and I. Adesida, "Fabrication of nanowires with high aspect ratios utilized by dry etching with SF₆:C₄F₈ and self-limiting thermal oxidation on Si substrate," *J. Vac. Sci. Technol.*, *B*, vol. 28, pp. 763 768, Jul 2010.
- [176] Y. L. Chang, F. Li, A. Fatehi, and Z. T. Mi, "Molecular beam epitaxial growth and characterization of non-tapered InN nanowires on Si(111)," *Nanotechnology*, vol. 20, pp. 345203 (6pp), 2009.
- [177] R. K. Debnath, R. Meijers, T. Richter, T. Stoica, R. Calarco, and H. Luth, "Mechanism of molecular beam epitaxy growth of GaN nanowires on Si(111)," *Appl. Phys. Lett.*, vol. 90, pp. 123117-1 123117-3, 2007.
- [178] R. S. Wagner and W. C. Ellis, "Vapor-liquid-solid mechanism of single crystal growth (new method growth catalysis from impurity whisker epitaxial + large crystals si e)," *Appl. Phys. Lett.*, vol. 4, pp. 89 90, 1964.
- [179] J. C. Harmand, G. Patriarche, N. Pere-Laperne, M. N. Merat-Combes, L. Travers, and F. Glas, "Analysis of vapor-liquid-solid mechanism in Au-assisted GaAs nanowire growth," *Appl. Phys. Lett.*, vol. 87, pp. 203101-1 203101-3, 2005.

- [180] W. I. Park, G. Zheng, X. Jiang, B. Tian, and C. M. Lieber, "Controlled synthesis of millimeter-long silicon nanowires with uniform electronic properties," *Nano Lett.*, vol. 8, pp. 3004 3009, 2008.
- [181] W. Braun, V. M. Kaganer, A. Trampert, H.-P. Schönherr, Q. Gong, R. Nötzel, L. Däweritz, and K. H. Ploog, "Diffusion and incorporation: shape evolution during overgrowth on structured substrates," *J. Cryst. Growth*, vol. 227-228, pp. 51 55, 2001.
- [182] S. G. Ihn, J. I. Song, Y. H. Kim, and J. Y. Lee, "GaAs nanowires on Si substrates grown by a solid source molecular beam epitaxy," *Appl. Phys. Lett.*, vol. 89, pp. 053106-1 053106-3, 2006.
- [183] Z. Cai, S. Garzon, M. V. S. Chandrashekhar, R. A. Webb, and G. Koley, "Synthesis and properties of high-quality InN nanowires and nanonetworks," *J. Electron. Mater.*, vol. 37, pp. 585 592, 2008.
- [184] V. Gottschalch, G. Wagner, J. Bauer, H. Paetzelt, and M. Shirnow, "VLS growth of GaN nanowires on various substrates," *J. Cryst. Growth*, vol. 310, pp. 5123 5128, 2008.
- [185] E. Stern, G. Cheng, E. Cimpoiasu, R. Klie, S. Guthrie, J. Klemic, I. Kretzschmar, E. Steinlauf, D. Turner-Evans, E. Broomfield, J. Hyland, R. Koudelka, T. Boone, M. Young, A. Sanders, R. Munden, T. Lee, D. Routenberg, and M. A. Reed, "Electrical characterization of single GaN nanowires," *Nanotechnology*, vol. 16, pp. 2941 2953, 2005.
- [186] S. M. Kang, B. K. Kang, and D. H. Yoon, "Growth and properties of vertically well-aligned GaN nanowires by thermal chemical vapor deposition process," *Mater. Lett.*, vol. 65, pp. 763 765, 2011.
- [187] L. J. Lauhon, M. S. Gudiksen, and C. M. Lieber, "Semiconductor nanowire heterostructures," *Philos. T. Roy. Soc. A*, vol. 362, pp. 1247 1260, 2004.
- [188] L. J. Lauhon, M. S. Gudiksen, D. Wang, and C. M. Lieber, "Epitaxial core-shell and core-multishell nanowire heterostructures," *Nature*, vol. 420, pp. 57 61, 2002.
- [189] B. Tian, X. Zheng, T. J. Kempa, Y. Fang, N. Yu, G. Yu, J. Huang, and C. M. Lieber, "Coaxial silicon nanowires as solar cells and nanoelectronic power sources," *Nature*, vol. 449, pp. 885 889, 2007.
- [190] E. Durgun, N. Akman, C. Ataca, and S. Ciraci, "Atomic and electronic structures of doped silicon nanowires: A first-principles study," *Phys. Rev. B*, vol. 76, p. 245323-1 245323-8, 2007.
- [191] J. Ristic, E. Calleja, S. Fernandez-Garrido, L. Cerutti, A. Trampert, U. Jahn, and K. H. Ploog, "On the mechanisms of spontaneous growth of III-nitride nanocolumns by plasma-assisted molecular beam epitaxy," *J. Cryst. Growth*, vol. 310, pp. 4035 4045, 2008.
- [192] A. P. Vajpeyi, A. O. Ajagunna, G. Tsiakatouras, A. Adikimenakis, E. Iliopoulos, K. Tsagaraki, M. Androulidaki, and A. Georgakilas, "Spontaneous growth of III-nitride nanowires on Si by molecular beam epitaxy," *Microelectron. Eng.*, vol. 86, pp. 812 815, 2009.
- [193] K. A. Bertness, A. Roshko, L. M. Mansfield, T. E. Harvey, and N. A. Sanford, "Mechanism for spontaneous growth of GaN nanowires with molecular beam epitaxy," *J. Cryst. Growth*, vol. 310, pp. 3154 3158, 2008.

- [194] M. A. Sanchez-Garcia, E. Calleja, E. Monroy, F. J. Sanchez, F. Calle, E. Muñoz, and R. Beresford, "The effect of the III/V ratio and substrate temperature on the morphology and properties of GaN- and AlN-layers grown by molecular beam epitaxy on Si(1 1 1)," *J. Cryst. Growth*, vol. 183, pp. 23–30, 1998.
- [195] K. A. Bertness, A. Roshko, N. A. Sanford, J. M. Barker, and A. V. Davydov, "Spontaneously grown GaN and AlGaN nanowires," *J. Cryst. Growth*, vol. 287, pp. 522 527, 2006.
- [196] S. D. Hersee, X. Sun, and X. Wang, "The controlled growth of GaN nanowires," *Nano Lett.*, vol. 6, pp. 1808 1811, 2006.
- [197] J. Gao, R. Chen, D. H. Li, L. Jiang, J. C. Ye, X. C. Ma, X. D. Chen, Q. H. Xiong, H. D. Sun, and T. Wu, "UV light emitting transparent conducting tindoped indium oxide (ITO) nanowires," *Nanotechnology*, vol. 22, pp. 195706 (10pp), 2011.
- [198] T. Schumann, T. Gotschke, F. Limbach, T. Stoica, and R. Calarco, "Selective-area catalyst-free MBE growth of GaN nanowires using a patterned oxide layer," *Nanotechnology*, vol. 22, p. 095603 (6pp), 2011.
- [199] H. Sekiguchi, K. Kishino, and A. Kikuchi, "Ti-mask Selective-Area Growth of GaN by RF-Plasma-Assisted Molecular-Beam Epitaxy for Fabricating Regularly Arranged InGaN/GaN Nanocolumns," *Appl. Phys. Express*, vol. 1, pp. 124002-1 124002-3, 2008.
- [200] K. Kishino, H. Sekiguchi, and A. Kikuchi, "Improved Ti-mask selective-area growth (SAG) by rf-plasma-assisted molecular beam epitaxy demonstrating extremely uniform GaN nanocolumn arrays," *J. Cryst. Growth*, vol. 311, pp. 2063 2068, 2009.
- [201] H. I. H. Lueth. Solid-State Physics, Springer Verlag, 2003.
- [202] T. Stoica, R. Meijers, R. Calarco, T. Richter, and H. Lüth, "MBE growth optimization of InN nanowires," *J. Cryst. Growth*, vol. 290, pp. 241 247, 2006.
- [203] T. L. Tansley and C. P. Foley, "Electron-mobility in indium nitride," *Electron. Lett.*, vol. 20, pp. 1066 1068, 1984.
- [204] J. Q. Wu, "When group-III nitrides go infrared: New properties and perspectives," *J. Appl. Phys.*, vol. 106, pp. 011101-1 011101-28, 2009.
- [205] J. Wu, W. Walukiewicz, W. Shan, K. M. Yu, J. W. Ager, S. X. Li, E. E. Haller, H. Lu, and W. J. Schaff, "Temperature dependence of the fundamental band gap of InN," *J. Appl. Phys.*, vol. 94, pp. 4457 4460, 2003.
- [206] W. Walukiewicz, J. W. Ager, K. M. Yu, Z. Liliental-Weber, J. Wu, S. X. Li, R. E. Jones, and J. D. Denlinger, "Structure and electronic properties of InN and In-rich group III-nitride alloys," *J. Phys. D: Appl. Phys.*, vol. 39, pp. R83–R99, 2006.
- [207] C. G. Van de Walle, J. L. Lyons, and A. Janotti, "Controlling the conductivity of InN," *Phys. Stat. Solidi A*, vol. 207, pp. 1024 1036, 2010.
- [208] L. F. J. Piper, T. D. Veal, C. F. McConville, H. Lu, and W. J. Schaff, "Origin of the n-type conductivity of InN: The role of positively charged dislocations," *Appl. Phys. Lett.*, vol. 88, pp. 252109-1 252109-3, 2006.

- [209] C. S. Gallinat, G. Koblmueller, and J. S. Speck, "The role of threading dislocations and unintentionally incorporated impurities on the bulk electron conductivity of In-face InN," *Appl. Phys. Lett.*, vol. 95, pp. 022103-1 022103-3, 2009.
- [210] G. Pettinari, F. Masia, M. Capizzi, A. Polimeni, M. Losurdo, G. Bruno, T. H. Kim, S. Choi, A. Brown, V. Lebedev, V. Cimalla, and O. Ambacher, "Experimental evidence of different hydrogen donors in n-type InN," *Phys. Rev. B*, vol. 77, pp. 125207-1 125207-6, 2008.
- [211] S. Ruffenach, M. Moret, O. Briot, and B. Gil, "Recent advances in the MOVPE growth of indium nitride," *Phys. Stat. Solidi A*, vol. 207, pp. 9 18, 2010.
- [212] T. Miyajima, S. Uemura, Y. Kudo, Y. Kitajima, A. Yamamoto, D. Muto, and Y. Nanishi, "Determination of the Mg occupation site in MOCVD- and MBE-grown Mg-doped InN using X-ray absorption fine-structure measurements," in *Phys. Status Solidi C*, vol 5, vol. 5, pp. 1665 1667, 2008.
- [213] R. E. Jones, K. M. Yu, S. X. Li, W. Walukiewicz, J. W. Ager, E. E. Haller, H. Lu, and W. J. Schaff, "Evidence for p-type doping of InN," *Phys. Rev. Lett.*, vol. 96, pp. 125505-1 125505-4, 2006.
- [214] X. Wang, S.-B. Che, Y. Ishitani, and A. Yoshikawa, "Growth and properties of Mg-doped in-polar InN films," *Appl. Phys. Lett.*, vol. 90, pp. 201913-1 201913-3, 2007.
- [215] N. Khan, N. Nepal, A. Sedhain, J. Y. Lin, and H. X. Jiang, "Mg acceptor level in InN epilayers probed by photoluminescence," *Appl. Phys. Lett.*, vol. 91, pp. 012101-1 012101-3, 2007.
- [216] J. W. L. Yim, R. E. Jones, K. M. Yu, J. W. Ager, III, W. Walukiewicz, W. J. Schaff, and J. Wu, "Effects of surface states on electrical characteristics of InN and In_{1-x}Ga_xN," *Phys. Rev. B*, vol. 76, pp. 115305-1 115305-9, 2007.
- [217] V. W. L. Chin, T. L. Tansley, and T. Ostochan, "Electron mobilities in gallium, indium, and aluminum nitrides," *J. Appl. Phys.*, vol. 75, pp. 7365 7372, 1994.
- [218] I. Mahboob, T. D. Veal, C. F. McConville, H. Lu, and W. J. Schaff, "Intrinsic electron accumulation at clean InN surfaces," *Phys. Rev. Lett.*, vol. 92, pp. 036804-1 036804-4, 2004.
- [219] P. D. C. King, T. D. Veal, C. F. McConville, F. Fuchs, J. Furthmueller, F. Bechstedt, P. Schley, R. Goldhahn, J. Schoermann, D. J. As, K. Lischka, D. Muto, H. Naoi, Y. Nanishi, H. Lu, and W. J. Schaff, "Universality of electron accumulation at wurtzite c- and a-plane and zinc-blende InN surfaces," *Appl. Phys. Lett.*, vol. 91, pp. 092101-1 092101-3, 2007.
- [220] I. Mahboob, T. D. Veal, L. F. J. Piper, C. F. McConville, H. Lu, W. J. Schaff, J. Furthmuller, and F. Bechstedt, "Origin of electron accumulation at wurtzite InN surfaces," *Phys. Rev. B*, vol. 69, pp. 201307-1 201307-4, 2004.
- [221] P. D. C. King, T. D. Veal, C. F. McConville, F. Fuchs, J. Furthmueller, F. Bechstedt, J. Schoermann, D. J. As, K. Lischka, H. Lu, and W. J. Schaff, "Valence band density of states of zinc-blende and wurtzite InN from x-ray photoemission spectroscopy and first-principles calculations," *Phys. Rev. B*, vol. 77, pp. 115213-1 115213-7, 2008.
- [222] C. G. Van de Walle and D. Segev, "Microscopic origins of surface states on nitride surfaces," *J. Appl. Phys.*, vol. 101, pp. 081704-1 081704-6, 2007.

- [223] C.-L. Wu, H.-M. Lee, C.-T. Kuo, C.-H. Chen, and S. Gwo, "Absence of Fermilevel pinning at cleaved nonpolar InN surfaces," *Phys. Rev. Lett.*, vol. 101, pp. 106803-1 106803-4, 2008.
- [224] Y. M. Chang, Y. L. Hong, and S. Gwo, "Direct probe of the built-in electric field of Mg-doped a-plane wurtzite InN surfaces with time-resolved electric-field-induced second harmonic generation," *Appl. Phys. Lett.*, vol. 93, pp. 131106-1 131106-3, 2008.
- [225] S. Lazic, E. Gallardo, J. M. Calleja, F. Agullo-Rueda, J. Grandal, M. A. Sanchez-Garcia, and E. Calleja, "Raman scattering by longitudinal optical phonons in InN nanocolumns grown on Si(111) and Si(001) substrates," *Physica E*, vol. 40, pp. 2087 2090, 2008.
- [226] E. Calleja, J. Grandal, M. A. Sanchez-Garcia, M. Niebelschuetz, V. Cimalla, and O. Ambacher, "Evidence of electron accumulation at nonpolar surfaces of InN nanocolumns," *Appl. Phys. Lett.*, vol. 90, pp. 262110-1 262110-3, 2007.
- [227] B. Song, J. K. Jian, G. Wang, Z. H. Zhang, M. Lei, H. Q. Bao, and X. L. Chen, "Synthesis, optical and transport properties of single-crystal N-deficient InN nanowires," *Physica E*, vol. 40, pp. 579 584, 2008.
- [228] V. Darakchieva, T. Hofmann, M. Schubert, B. E. Sernelius, B. Monemar, P. O. A. Persson, F. Giuliani, E. Alves, H. Lu, and W. J. Schaff, "Free electron behavior in InN: On the role of dislocations and surface electron accumulation," *Appl. Phys. Lett.*, vol. 94, pp. 022109-1 022109-3, 2009.
- [229] C. H. Liang, L. C. Chen, J. S. Hwang, K. H. Chen, Y. T. Hung, and Y. F. Chen, "Selective-area growth of indium nitride nanowires on gold-patterned Si(100) substrates," *Appl. Phys. Lett.*, vol. 81, pp. 22 24, 2002.
- [230] X. M. Cai, Y. H. Leung, K. Y. Cheung, K. H. Tam, A. B. Djurisic, M. H. Xie, H. Y. Chen, and S. Gwo, "Straight and helical InGaN core-shell nanowires with a high In core content," *Nanotechnology*, vol. 17, pp. 2330 2333, 2006.
- [231] C. K. Chao, J. I. Chyi, C. N. Hsiao, C. C. Kei, S. Y. Kuo, H. S. Chang, and T. M. Hsu, "Catalyst-free growth of indium nitride nanorods by chemical-beam epitaxy," *Appl. Phys. Lett.*, vol. 88, pp. 233111-1 233111-3, 2006.
- [232] J. Grandal, M. A. Sanchez-Garcia, E. Calleja, E. Luna, and A. Trampert, "Accommodation mechanism of InN nanocolumns grown on Si(111) substrates by molecular beam epitaxy," *Appl. Phys. Lett.*, vol. 91, Jul 9 2007.
- [233] C. Denker, J. Malindretos, F. Werner, F. Limbach, H. Schuhmann, T. Niermann, M. Seibt, and A. Rizzi, "Self-organized growth of InN-nanocolumns on p-Si(111) by MBE," *Phys. Status Solidi C*, vol. 5, pp. 1706 1708, 2008.
- [234] D. J. Jang, G. T. Lin, C. L. Hsiao, L. W. Tu, and M. E. Lee, "Auger recombination in InN thin films," *Appl. Phys. Lett.*, vol. 92, pp. 042101-1 042101-3, 2008.
- [235] J. W. Ager, J. Wu, K. M. Yu, R. E. Jones, S. X. Li, W. Walukiewicz, E. E. Haller, H. Lu, and W. J. Schaff, "Group III nitride alloys as photovoltaic materials," *The 4th International Conference on Solid State Lighting*. vol. 5530, pp. 308-315, 2004.
- [236] V. Lebedev, V. Cimalla, T. Baumann, O. Ambacher, F. M. Morales, J. G. Lozano, and D. Gonzalez, "Effect of dislocations on electrical and electron

- transport properties of InN thin films. II. Density and mobility of the carriers," *J. Appl. Phys.*, vol. 100, pp. 094903-1 094903-8, 2006.
- [237] F. Furtmayr, M. Vielemeyer, M. Stutzmann, A. Laufer, B. K. Meyer, and M. Eickhoff, "Optical properties of Si- and Mg-doped gallium nitride nanowires grown by plasma-assisted molecular beam epitaxy," *J. Appl. Phys.*, vol. 104, pp. 074309-1 074309-7, 2008.
- [238] Y. L. Chang, F. Li, A. Fatehi, and Z. T. Mi, "Molecular beam epitaxial growth and characterization of non-tapered InN nanowires on Si(111)," *Nanotechnology*, vol. 20, pp. 345203 (6pp), 2009.
- [239] Y. L. Chang, F. Li, and Z. Mi, "Optimization of the structural and optical quality of InN nanowires on Si(111) by molecular beam epitaxy," *J. Vac. Sci. Technol.,B*, vol. 28, pp. C3B7 C3B11, 2010.
- [240] M. He and S. N. Mohammad, "Novelty and versatility of self-catalytic nanowire growth: A case study with InN nanowires," *J. Vac. Sci. Technol.*, *B*, vol. 25, pp. 940 944, 2007.
- [241] S. N. Mohammad, "Self-catalytic solution for single-crystal nanowire and nanotube growth," *J. Chem. Phys.*, vol. 127, pp. 244702-1 10, 2007.
- [242] E. A. Stach, P. J. Pauzauskie, T. Kuykendall, J. Goldberger, R. He, and P. Yang, "Watching GaN Nanowires Grow," *Nano Lett.*, vol. 3, pp. 867–869, 2003.
- [243] M. Moret, S. Ruffenach, O. Briot, and B. Gil, "The determination of the bulk residual doping in indium nitride films using photoluminescence," *Appl. Phys. Lett.*, vol. 95, pp. 031910-1 031910-3, 2009.
- [244] S. P. Fu, T. T. Chen, and Y. F. Chen, "Photoluminescent properties of InN epifilms," *Semicond. Sci. Technol.*, vol. 21, pp. 244 249, 2006.
- [245] T. Stoica, R. Meijers, R. Calarco, T. Richter, E. Sutter, and H. Luth, "Photoluminescence and intrinsic properties of MBE-grown InN nanowires," *Nano Lett.*, vol. 6, pp. 1541 1547, 2006.
- [246] J. Segura-Ruiz, N. Garro, A. Cantarero, C. Denker, J. Malindretos, and A. Rizzi, "Optical studies of MBE-grown InN nanocolumns: Evidence of surface electron accumulation," *Phys. Rev. B*, vol. 79, pp. 115305-1 115305-9, 2009.
- [247] M. Feneberg, J. Daubler, K. Thonke, R. Sauer, P. Schley, and R. Goldhahn, "Mahan excitons in degenerate wurtzite InN: Photoluminescence spectroscopy and reflectivity measurements," *Phys. Rev. B*, vol. 77, pp. 245207-1 245207-6, 2008.
- [248] A. Janotti and C. G. Van de Walle, "Sources of unintentional conductivity in InN," *Appl. Phys. Lett.*, vol. 92, pp. 032104-1 032104-3, 2008.
- [249] C. G. Van de Walle and J. Neugebauer, "Universal alignment of hydrogen levels in semiconductors, insulators and solutions," *Nature*, vol. 423, pp. 626–628, 2003.
- [250] Y.-L. Chang, Z. Mi, and F. Li, "Photoluminescence properties of a nearly intrinsic single InN nanowire," *Adv. Funct. Mater.*, vol. 20, pp. 4146–4151, 2010.
- [251] X. Q. Wang, S. B. Che, Y. Ishitani, and A. Yoshikawa, "Growth and properties of Mg-doped in-polar InN films," *Appl. Phys. Lett.*, vol. 90, pp. 201913-1 201913-3, 2007.

- [252] F. Furtmayr, M. Vielemeyer, M. Stutzmann, J. Arbiol, S. Estrade, F. Peiro, J. R. Morante, and M. Eickhoff, "Nucleation and growth of GaN nanorods on Si (111) surfaces by plasma-assisted molecular beam epitaxy The influence of Si- and Mg-doping," *J. Appl. Phys.*, vol. 104, pp. 034309-1 034309-7, 2008.
- [253] B. Beaumont, S. Haffouz, and P. Gibart, "Magnesium induced changes in the selective growth of GaN by metalorganic vapor phase epitaxy," *Appl. Phys. Lett.*, vol. 72, pp. 921 923, 1998.
- [254] J. C. Harmand, G. Patriarche, N. Pere-Laperne, M. N. Merat-Combes, L. Travers, and F. Glas, "Analysis of vapor-liquid-solid mechanism in Au-assisted GaAs nanowire growth," *Appl. Phys. Lett.*, vol. 87, pp. 203101-1 203101-3, 2005.
- [255] A. L. Roest, M. A. Verheijen, O. Wunnicke, S. Serafin, H. Wondergem, and E. Bakkers, "Position-controlled epitaxial III-V nanowires on silicon," *Nanotechnology*, vol. 17, pp. S271 – S275, 2006.
- [256] Z. H. Wu, X. Y. Mei, D. Kim, M. Blumin, and H. E. Ruda, "Growth of Aucatalyzed ordered GaAs nanowire arrays by molecular-beam epitaxy," *Appl. Phys. Lett.*, vol. 81, pp. 5177 5179, 2002.
- [257] S. S. Yi, G. Girolami, J. Amano, M. S. Islam, S. Sharma, T. I. Kamins, and I. Kimukin, "InP nanobridges epitaxially formed between two vertical Si surfaces by metal-catalyzed chemical vapor deposition," *Appl. Phys. Lett.*, vol. 89, pp. 133121-1 133121-3, 2006.
- [258] D. K. Gaskill, N. Bottka, and M. C. Lin, "Growth of GaN films using trimethylgallium and hydrazine," *Appl. Phys. Lett.*, vol. 48, pp. 1449–1451, 1986
- [259] L. W. Tu, C. L. Hsiao, T. W. Chi, I. Lo, and K. Y. Hsieh, "Self-assembled vertical GaN nanorods grown by molecular-beam epitaxy," *Appl. Phys. Lett.*, vol. 82, pp. 1601 1603, 2003.
- [260] Y. H. Kim, J. Y. Lee, S. H. Lee, J. E. Oh, and H. S. Lee, "Synthesis of aligned GaN nanorods on Si (111) by molecular beam epitaxy," *Appl. Phys. A*, vol. 80, pp. 1635 1639, 2005.
- [261] Y. H. Kim, J. Y. Lee, S. H. Lee, J. E. Oh, H. S. Lee, and Y. Huh, "Indium-related novel architecture of GaN nanorod grown by molecular beam epitaxy," *Chem. Phys. Lett.*, vol. 412, pp. 454 458, 2005.
- [262] Y. S. Park, C. M. Park, D. J. Fu, T. W. Kang, and J. E. Oh, "Photoluminescence studies of GaN nanorods on Si (111) substrates grown by molecular-beam epitaxy," *Appl. Phys. Lett.*, vol. 85, pp. 5718 5720, 2004.
- [263] M. Tchernycheva, C. Sartel, G. Cirlin, L. Travers, G. Patriarche, J. C. Harmand, L. S. Dang, J. Renard, B. Gayral, L. Nevou, and F. Julien, "Growth of GaN free-standing nanowires by plasma-assisted molecular beam epitaxy: structural and optical characterization," *Nanotechnology*, vol. 18, pp. 385306 (7pp), 2007.
- [264] X. M. Cai, A. B. Djurisic, and M. H. Me, "GaN nanowires: CVD synthesis and properties," *Thin Solid Films*, vol. 515, pp. 984 989, 2006.
- [265] X. H. Chen, J. Xu, R. M. Wang, and D. P. Yu, "High-quality ultra-fine GaN nanowires synthesized via chemical vapor deposition", *Adv. Mater.*, vol. 16, pp. 952 952, 2004.

- [266] A. B. Djurisic, K. H. Tam, Y. F. Hsu, S. L. Zhang, M. H. Xie, and W. K. Chan, "GaN nanowires influence of the starting material on nanowire growth," *Thin Solid Films*, vol. 516, pp. 238 242, 2007.
- [267] T. Y. Kim, S. H. Lee, Y. H. Mo, H. W. Shim, K. S. Nahm, E.-K. Suh, and G. S. Park, "Growth of GaN nanowires on Si substrate using Ni catalyst in vertical chemical vapor deposition reactor (vol 21, pg 257, 2004)," *Korean J. Chem. Eng.*, vol. 23, pp. 1068 1068, 2006.
- [268] C. K. Kuo, C. W. Hsu, C. T. Wu, Z. H. Lan, C. Y. Mou, C. C. Chen, Y. J. Yang, L. C. Chen, and K. H. Chen, "Self-regulating and diameter-selective growth of GaN nanowires," *Nanotechnology*, vol. 17, pp. S332 S337, 2006.
- [269] L. Cerutti, J. Ristic, S. Fernandez-Garrido, E. Calleja, A. Trampert, K. H. Ploog, S. Lazic, and J. M. Calleja, "Wurtzite GaN nanocolumns grown on Si(001) by molecular beam epitaxy," *Appl. Phys. Lett.*, vol. 88, pp. 213114 -1 213114-3, 2006.
- [270] L. H. Robins, K. A. Bertness, J. M. Barker, N. A. Sanford, and J. B. Schlager, "Optical and structural study of GaN nanowires grown by catalyst-free molecular beam epitaxy. I. Near-band-edge luminescence and strain effects," *J. Appl. Phys.*, vol. 101, pp. 113505 -1 113505-8, 2007.
- [271] K. L. Averett, J. E. Van Nostrand, J. D. Albrecht, Y. S. Chen, and C. C. Yang, "Epitaxial overgrowth of GaN nanocolumns," *J. Vac. Sci. Technol.*, *B*, vol. 25, pp. 964 968, 2007.
- [272] Y. S. Park, C. M. Park, I. Hyunsik, S. J. Lee, T. W. Kang, S. H. Lee, and J. E. Oh, "Growth and optical properties on formation of self-assembled GaN nanorod grown on Si(111) substrates," 5th IEEE Conference on Nanotechnology, vol. 2, pp. 499 502, 2005.
- [273] H. W. Seo, Q. Y. Chen, L. W. Tu, M. Chen, X. M. Wang, C. L. Hsiao, Y. J. Tu, L. Shao, O. Lozano, and W. K. Chu, "GaN nanorod assemblies on self-implanted (111) Si substrates," *Microelectron. Eng.*, vol. 83, pp. 1714–1717, 2006.
- [274] S. Ishizawa, H. Sekiguchi, A. Kikuchi, and K. Kishino, "Selective growth of GaN nanocolumns by Al thin layer on substrate," *Phys. Status Solidi B*, vol. 244, pp. 1815 1819, 2007.
- [275] K. Kishino, T. Hoshino, S. Ishizawa, and A. Kikuchi, "Selective-area growth of GaN nanocolumns on titanium-mask-patterned silicon (111) substrates by RF-plasma-assisted molecular-beam epitaxy," *Electron. Lett.*, vol. 44, pp. 819-U55, 2008.
- [276] C. L. Hsiao, L. W. Tu, T. W. Chi, H. W. Seo, Q. Y. Chen, and W. K. Chu, "Buffer controlled GaN nanorods growth on Si(111) substrates by plasma-assisted molecular beam epitaxy," *J. Vac. Sci. Technol., B,* vol. 24, pp. 845–851, 2006.
- [277] L. Largeau, D. L. Dheeraj, M. Tchernycheva, G. E. Cirlin, and J. C. Harmand, "Facet and in-plane crystallographic orientations of GaN nanowires grown on Si(111)," *Nanotechnology*, vol. 19, pp. 155704 (5pp), 2008.
- [278] R. Songmuang, O. Landre, and B. Daudin, "From nucleation to growth of catalyst-free GaN nanowires on thin AlN buffer layer," *Appl. Phys. Lett.*, vol. 91, pp. 251902-1 251902-3, 2007.

- [279] C.-F. Huang, C.-F. Lu, T.-Y. Tang, J.-J. Huang, and C. C. Yang, "Phosphorfree white-light light-emitting diode of weakly carrier-density-dependent spectrum with prestrained growth of InGaN/GaN quantum wells," *Appl. Phys. Lett.*, vol. 90, pp. 151122-1 151122-3, 2007.
- [280] M. Funato, K. Hayashi, M. Ueda, Y. Kawakami, Y. Narukawa, and T. Mukai, "Emission color tunable light-emitting diodes composed of InGaN multifacet quantum wells," *Appl. Phys. Lett.*, vol. 93, pp. 021126-1 021126-3, 2008.
- [281] C. C. Hong, H. Ann, C. Y. Wu, and S. Gwo, "Strong green photoluminescence from InxGa1-xN/GaN nanorod arrays," *Opt. Express*, vol. 17, pp. 17227-17233, 2009.
- [282] R. Calarco, R. J. Meijers, R. K. Debnath, T. Stoica, E. Sutter, and H. Luth, "Nucleation and growth of GaN nanowires on Si(111) performed by molecular beam epitaxy," *Nano Lett.*, vol. 7, pp. 2248 2251, 2007.
- [283] M. A. Tsai, P. C. Yu, C. L. Chao, C. H. Chiu, H. C. Kuo, S. H. Lin, J. J. Huang, T. C. Lu, and S. C. Wang, "Efficiency enhancement and beam shaping of GaN-InGaN vertical-injection light-emitting diodes via high-aspect-ratio nanorod arrays," *IEEE Photonics Technol. Lett.*, vol. 21, pp. 257 259, 2009.
- [284] H. Sekiguchi, K. Kishino, and A. Kikuchi, "Emission color control from blue to red with nanocolumn diameter of InGaN/GaN nanocolumn arrays grown on same substrate," *Appl. Phys. Lett.*, vol. 96, pp. 231104-1 231104-3, 2010.
- [285] M. Bertelli, P. Loptien, M. Wenderoth, A. Rizzi, R. G. Ulbrich, M. C. Righi, A. Ferretti, L. Martin-Samos, C. M. Bertoni, and A. Catellani, "Atomic and electronic structure of the nonpolar GaN(1⁻100) surface," *Phys. Rev. B*, vol. 80, pp. 041306-1 041306-4, 2009.
- [286] S. Chevtchenko, X. Ni, Q. Fan, A. A. Baski, and H. Morkoc, "Surface band bending of a-plane GaN studied by scanning Kelvin probe microscopy," *Appl. Phys. Lett.*, vol. 88, pp. 122104-1 122104-3, 2006.
- [287] C. G. Van de Walle and D. Segev, "Microscopic origins of surface states on nitride surfaces," *J. Appl. Phys.*, vol. 101, pp. 081704-1 081704-6, 2007.
- [288] P. T. Barletta, E. A. Berkman, B. F. Moody, N. A. El-Masry, A. M. Emara, M. J. Reed, and S. M. Bedair, "Development of green, yellow, and amber light emitting diodes using InGaN multiple quantum well structures," *Appl. Phys. Lett.*, vol. 90, pp. 151109-1 15110-3, 2007.
- [289] H. S. Chen, C. F. Lu, D. M. Yeh, C. F. Huang, J. J. Huang, and C. C. Yang, "Orange-red light-emitting diodes based on a prestrained InGaN-GaN quantum-well epitaxy structure," *IEEE Photonics Technol. Lett.*, vol. 18, pp. 2269 2271, 2006.
- [290] B. Damilano, N. Grandjean, J. Massies, L. Siozade, and J. Leymarie, "InGaN/GaN quantum wells grown by molecular-beam epitaxy emitting from blue to red at 300 K," *Appl. Phys. Lett.*, vol. 77, pp. 1268 1270, 2000.
- [291] M. R. Krames, O. B. Shchekin, R. Mueller-Mach, G. O. Mueller, L. Zhou, G. Harbers, and M. G. Craford, "Status and future of high-power light-emitting diodes for solid-state lighting," *J. Disp. Technol.*, vol. 3, pp. 160 175, 2007.
- [292] U. Ozgur, H. Y. Liu, X. Li, X. F. Ni, and H. Morkoc, "GaN-Based Light-Emitting Diodes: Efficiency at High Injection Levels," *Proceedings of The IEEE*, vol. 98, pp. 1180 – 1196, 2010.

- [293] Z. Wang, H. Liang, J. Wang, M. Gong, and Q. Su, "Red-light-emitting diodes fabricated by near-ultraviolet InGaN chips with molybdate phosphors," *Appl. Phys. Lett.*, vol. 89, pp. 071921-1 071921-2, 2006.
- [294] H. Song and S. Lee, "Red light emitting solid state hybrid quantum dot-near-UV GaN LED devices," *Nanotechnology*, vol. 18, pp. 255202 (4pp), 2007.
- [295] Y.-C. Chen, C.-Y. Huang, Y.-K. Su, W.-L. Li, C.-H. Yeh, and Y.-C. Lin, "The hybridization of CdSe/ZnS quantum dot on InGaN light-emitting diodes for color conversion," *IEEE Trans. Nanotechnol.*, vol. 7, pp. 503 507, 2008.
- [296] A. Nishikawa, N. Furukawa, T. Kawasaki, Y. Terai, and Y. Fujiwara, "Room-temperature red emission from light-emitting diodes with Eu-doped GaN grown by organometallic vapor phase epitaxy," *Opt.Mater.*, vol. 33, pp. 1071–1074, 2011.
- [297] A. Nishikawa, T. Kawasaki, N. Furukawa, Y. Terai, and Y. Fujiwara, "Electroluminescence properties of Eu-doped GaN-based red light-emitting diode by OMVPE," *Phys. Status Solidi A*, vol. 207, pp. 1397 1399, 2010.
- [298] S. Neeraj, N. Kijima, and A. K. Cheetham, "Novel red phosphors for solid-state lighting: the system NaM(WO4)_{2-x}(MoO4)_x:Eu³⁺ (M=Gd, Y, Bi)," *Chem. Phys. Lett.*, vol. 387, pp. 2 6, 2004.
- [299] F. Qian, S. Gradecak, Y. Li, C. Wen, and C. Lieber, "Core/multishell nanowire heterostructures as multicolor, high-efficiency light-emitting diodes," *Nano Lett.*, vol. 5, pp. 2287 2291, 2005.
- [300] H. Sekiguchi, K. Kishino, and A. Kikuchi, "Emission color control from blue to red with nanocolumn diameter of InGaN/GaN nanocolumn arrays grown on same substrate," *Appl. Phys. Lett.*, vol. 96, pp. 2311041-1 231104-3, 2010.
- [301] C. C. Hong, H. Ahn, C. Y. Wu, and S. Gwo, "Strong green photoluminescence from In_xGa1-xN/GaN nanorod arrays," *Opt. Express*, vol. 17, pp. 17227-17233, 2009.
- [302] A. Kikuchi, M. Tada, K. Miwa, and K. Kishino, "Growth and characterization of InGaN/GaN nanocolumn LED art. no. 612905," in *Quantum Dots, Particles, and Nanoclusters III.* vol. 6129, K. G. H. D. L. Eyink, Ed., ed, pp. 12905-12905, 2006.
- [303] T. Xu, A. Y. Nikiforov, R. France, C. Thomidis, A. Williams, and T. D. Moustakas, "Blue-green-red LEDs based on InGaN quantum dots grown by plasma-assisted molecular beam epitaxy," *Phys. Status Solidi A*, vol. 204, pp. 2098 2102, 2007.
- [304] N. A. Sanford, P. T. Blanchard, K. A. Bertness, L. Mansfield, J. B. Schlager, A. W. Sanders, A. Roshko, B. B. Burton, and S. M. George, "Steady-state and transient photoconductivity in c-axis GaN nanowires grown by nitrogen-plasma-assisted molecular beam epitaxy," *J. Appl. Phys.*, vol. 107, pp. 034318-1-034318-14, 2010.
- [305] M. Bertelli, P. Loptien, M. Wenderoth, A. Rizzi, R. G. Ulbrich, M. C. Righi, A. Ferretti, L. Martin-Samos, C. M. Bertoni, and A. Catellani, "Atomic and electronic structure of the nonpolar GaN(11–00) surface," *Phys. Rev. B*, vol. 80, pp. 041306-1 041306-4, 2009.

- [306] S. Chevtchenko, X. Ni, Q. Fan, A. A. Baski, and H. Morkoc, "Surface band bending of a-plane GaN studied by scanning Kelvin probe microscopy," *Appl. Phys. Lett.*, vol. 88, pp. 122104-1 122104-3, 2006.
- [307] H. P. T. Nguyen, S. Zhang, K. Cui, A. Korinek, G. Botton, and Z. Mi, "High Efficiency InGaN/GaN Dot-in-a-Wire Red Light Emitting Diodes," *IEEE Photonics Technol. Lett.*, 2011(In Press).
- [308] X. Ni, X. Li, J. Lee, S. Liu, V. Avrutin, U. Ozgur, H. Morkoc, and A. Matulionis, "Hot electron effects on efficiency degradation in InGaN light emitting diodes and designs to mitigate them," *J. Appl. Phys.*, vol. 108, pp. 033112-1 033112-13, 2010.
- [309] F. Qian, S. Gradecak, Y. Li, C.-Y. Wen, and C. M. Lieber, "Core/multishell nanowire heterostructures as multicolor, high-efficiency light-emitting diodes," *Nano Lett.*, vol. 5, pp. 2287 2291, 2005.
- [310] H. Masui, J. Sonoda, N. Pfaff, I. Koslow, S. Nakamura, and S. P. DenBaars, "Quantum-confined Stark effect on photoluminescence and electroluminescence characteristics of InGaN-based light-emitting diodes," *J. Phys. D: Appl. Phys.*, vol. 41, p. 165105 (6pp), 2008.
- [311] S. H. Han, D. Y. Lee, H. W. Shim, G. C. Kim, Y. S. Kim, S. T. Kim, S. J. Lee, C. Y. Cho, and S. J. Park, "Improvement of efficiency droop in InGaN/GaN multiple quantum well light-emitting diodes with trapezoidal wells," *J. Phys. D: Appl. Phys.*, vol. 43, p. 354004 (5pp), 2010.
- [312] M. S. Shur, "Solid-state lighting: Toward superior illumination," *Proceedings of the IEEE*, vol. 93, pp. 1691 1703, 2005.
- [313] I. Rozhansky and D. Zakheim, "Analysis of the causes of the decrease in the electroluminescence efficiency of AlGaInN light-emitting-diode heterostructures at high pumping density," *Semiconductors*, vol. 40, pp. 839–845, 2006.
- [314] Z. Zhong, F. Qian, D. Wang, and C. M. Lieber, "Synthesis of p-Type Gallium Nitride Nanowires for Electronic and Photonic Nanodevices," *Nano Lett.*, vol. 3, pp. 343 346, 2003.
- [315] C.-H. Lee, J. Yoo, Y. J. Hong, J. Cho, Y.-J. Kim, S.-R. Jeon, J. H. Baek, and G.-C. Yi, "GaN/In_{1-x}Ga_xN/GaN/ZnO nanoarchitecture light emitting diode microarrays," *Appl. Phys. Lett.*, vol. 94, pp. 213101 -1 213101-3, 2009.
- [316] A. Pan, R. Liu, M. Sun, and C.-Z. Ning, "Spatial composition grading of quaternary ZnCdSSe alloy nanowires with tunable light emission between 350 and 710 nm on a single substrate," *ACS Nano*, vol. 4, pp. 671 680, 2010.
- [317] Y.-J. Lee, S.-Y. Lin, C.-H. Chiu, T.-C. Lu, H.-C. Kuo, S.-C. Wang, S. Chhajed, J. K. Kim, and E. F. Schubert, "High output power density from GaN-based two-dimensional nanorod light-emitting diode arrays," *Appl. Phys. Lett.*, vol. 94, pp. 141111-1 141111-3, 2009.
- [318] X.-M. Zhang, M.-Y. Lu, Y. Zhang, L.-J. Chen, and Z. L. Wang, "Fabrication of a high-brightness blue-light-emitting diode using a ZnO-nanowire array grown on p-GaN thin film," *Adv.Mater.*, vol. 21, pp. 2767 2770, 2009.
- [319] S. Xu, C. Xu, Y. Liu, Y. Hu, R. Yang, Q. Yang, J.-H. Ryou, H. J. Kim, Z. Lochner, S. Choi, R. Dupuis, and Z. L. Wang, "Ordered Nanowire Array

- Blue/Near-UV Light Emitting Diodes," *Adv. Mater.*, vol. 22, pp. 4749–4753, 2010.
- [320] Y. Sheng-Horng, T. Meng-Lun, T. Miao-Chan, C. Shu-Jeng, and K. Yen-Kuang, "Investigation of Optical Performance of InGaN MQW LED With Thin Last Barrier," *IEEE Phot. Tech. Lett.*, vol. 22, pp. 1787 1789, 2010.
- [321] B. Damilano, A. Dussaigne, J. Brault, T. Huault, F. Natali, P. Demolon, P. De Mierry, S. Chenot, and J. Massies, "Monolithic white light emitting diodes using a (Ga,In)N/GaN multiple quantum well light converter," *Appl. Phys. Lett.*, vol. 93, pp. 101117-1 101117-3, 2008.
- [322] C. B. Soh, W. Liu, J. H. Teng, S. Y. Chow, S. S. Ang, and S. J. Chua, "Cool white III-nitride light emitting diodes based on phosphor-free indium-rich InGaN nanostructures," *Appl. Phys. Lett.*, vol. 92, pp. 261909-1 261909-3, 2008.
- [323] Y. J. Lee, P. C. Lin, T. C. Lu, H. C. Kuo, and S. C. Wang, "Dichromatic InGaN-based white light emitting diodes by using laser lift-off and wafer-bonding schemes," *Appl. Phys. Lett.*, vol. 90, pp. 161115-1 161115-3, 2007.
- [324] M. Ueda, T. Kondou, K. Hayashi, M. Funato, Y. Kawakami, Y. Narukawa, and T. Mukai, "Additive color mixture of emission from InGaN/GaN quantum wells on structure-controlled GaN microfacets," *Appl. Phys. Lett.*, vol. 90, pp. 171907-1 171907-3, 2007.
- [325] B. Monemar and B. E. Sernelius, "Defect related issues in the "current roll-off" in InGaN based light emitting diodes," *Appl. Phys. Lett.*, vol. 91, pp. 181103-1 181103-3, 2007.
- [326] Y. Yang, X. A. Cao, and C. H. Yan, "Investigation of the nonthermal mechanism of efficiency roll-off in InGaN light-emitting diodes," *IEEE Trans. Electron Devices*, vol. 55, pp. 1771–1775, 2008.
- [327] X. Ni, X. Li, J. Lee, S. Liu, V. Avrutin, U. Ozgur, H. Morkoc, A. Matulionis, T. Paskova, G. Mulholland, and K. R. Evans, "InGaN staircase electron injector for reduction of electron overflow in InGaN light emitting diodes," *Appl. Phys. Lett.*, vol. 97, pp. 031110-1 031110-3, 2010.
- [328] F. Bertazzi, M. Goano, and E. Bellotti, "A numerical study of Auger recombination in bulk InGaN," *Appl. Phys. Lett.*, vol. 97, pp. 231118-1 231118-3, 2010.
- [329] W. Guo, M. Zhang, P. Bhattacharya, and J. Heo, "Auger Recombination in III-Nitride Nanowires and Its Effect on Nanowire Light-Emitting Diode Characteristics," *Nano Lett.*, vol. 11, pp. 1434-1438, 2011.
- [330] R. C. Tu, C. J. Tun, S. M. Pan, C. C. Chuo, J. K. Sheu, C. E. Tsai, T. C. Wang, and G. C. Chi, "Improvement of near-ultraviolet InGaN-GaN light-emitting diodes with an AlGaN electron-blocking layer grown at low temperature," *IEEE Photonics Technol. Lett.*, vol. 15, pp. 1342-1344, 2003.
- [331] Y. K. Kuo and Y. A. Chang, "Effects of electronic current overflow and inhomogeneous carrier distribution on InGaN quantum-well laser performance," *IEEE J. Quantum Electron.*, vol. 40, pp. 437 444, 2004.
- [332] H. P. T. Nguyen, K. Cui, S. Zhang, S. Fathololoumi, and Z. Mi, "Full-color InGaN/GaN dot-in-a-wire light emitting diodes on silicon," *Nanotechnology*, vol. 22, p. 445202, 2011.

- [333] S. C. Ling, T. C. Lu, S. P. Chang, J. R. Chen, H. C. Kuo, and S. C. Wang, "Low efficiency droop in blue-green m-plane InGaN/GaN light emitting diodes," *Appl. Phys. Lett.*, vol. 96, pp. 231101-1 231101-3, 2010.
- [334] P. Bhattacharya and Z. Mi, "Quantum-dot optoelectronic devices," *Proc. IE IEEE*, vol. 95, pp. 1723 1740, 2007.
- [335] Ü. Özgür, X. Ni, X. Li, J. Lee, S. Liu, S. Okur, V. Avrutin, A. Matulionis, and H. Morkoç, "Ballistic transport in InGaN-based LEDs: impact on efficiency," *Semicond. Sci. Technol.*, vol. 26, p. 014022, 2011.
- [336] W. Guo, A. Banerjee, P. Bhattacharya, and B. S. Ooi, "InGaN/GaN disk-innanowire white light emitting diodes on (001) silicon," *Appl. Phys. Lett.*, vol. 98, pp. 193102-1 193102-3, 2011.
- [337] I. V. Rozhansky and D. A. Zakheim, "Analysis of processes limiting quantum efficiency of AlGaInN LEDs at high pumping," *Phys. Status Solidi A*, vol. 204, pp. 227 230, 2007.
- [338] J. Q. Xie, X. F. Ni, Q. Fan, R. Shimada, U. Ozgur, and H. Morkoc, "On the efficiency droop in InGaN multiple quantum well blue light emitting diodes and its reduction with p-doped quantum well barriers," *Appl. Phys. Lett.*, vol. 93, pp. 121107-1 121107-3, 2008.
- [339] J. Piprek, "Efficiency droop in nitride-based light-emitting diodes," *Phys. Status Solidi A*, vol. 207, pp. 2217 2225, 2010.
- [340] S. Grzanka, G. Franssen, G. Targowski, K. Krowicki, T. Suski, R. Czernecki, P. Perlin, and M. Leszczynski, "Role of the electron blocking layer in the low-temperature collapse of electroluminescence in nitride light-emitting diodes," *Appl. Phys. Lett.*, vol. 90, pp. 103507-1 103507-3, 2007.
- [341] H. Sekiguchi, K. Kato, J. Tanaka, A. Kikuchi, and K. Kishino, "Ultraviolet GaN-based nanocolumn light-emitting diodes grown on n-(111) Si substrates by rf-plasma-assisted molecular beam epitaxy," *Phys. Status Solidi A*, vol. 205, pp. 1067 1069, 2008.
- [342] E. Kioupakis, P. Rinke, K. T. Delaney, and C. G. V. d. Walle, "Indirect Auger recombination as a cause of efficiency droop in nitride light-emitting diodes," *Appl. Phys. Lett.*, vol. 98, pp. 161107-1 161107-3, 2011.
- [343] F. Bertazzi, M. Goano, and E. Bellotti, "A numerical study of Auger recombination in bulk InGaN," *Appl. Phys. Lett.*, vol. 97, pp. 231118-1 23118-3, 2010.
- [344] K. A. Bertness, N. A. Sanford, and A. V. Davydov, "GaN Nanowires Grown by Molecular Beam Epitaxy," *IEEE J. Sel. Top. Quantum Electron.*, vol. 17, pp. 847 858, 2011.
- [345] S. Grzanka, G. Franssen, G. Targowski, K. Krowicki, T. Suski, R. Czernecki, P. Perlin, and M. Leszczynski, "Role of the electron blocking layer in the low-temperature collapse of electroluminescence in nitride light-emitting diodes," *Appl. Phys. Lett.*, vol. 90, pp. 103507-1 103507-3, 2007.
- [346] T. Ru-Chin, T. Chun-Ju, P. Shyi-Ming, C. Chang-Cheng, J. K. Sheu, T. Ching-En, W. Te-Chung, and C. Gou-Chung, "Improvement of near-ultraviolet InGaN-GaN light-emitting diodes with an AlGaN electron-blocking layer grown at low temperature," *IEEE Photonics Technol. Lett.*, vol. 15, pp. 1342 1344, 2003.

- [347] D. S. Meyaard, Q. Shan, Q. Dai, J. Cho, E. F. Schubert, M.-H. Kim, and C. Sone, "On the temperature dependence of electron leakage from the active region of GaInN/GaN light-emitting diodes," *Appl. Phys. Lett.*, vol. 99, pp. 041112-1 041112-3, 2011.
- [348] H. J. Chung, R. J. Choi, M. H. Kim, J. W. Han, Y. M. Park, Y. S. Kim, H. S. Paek, C. S. Sone, Y. J. Park, J. K. Kim, and E. F. Schubert, "Improved performance of GaN-based blue light emitting diodes with InGaN/GaN multilayer barriers," *Appl. Phys. Lett.*, vol. 95, pp. 241109-1 241109-3, 2009.
- [349] C. H. Wang, J. R. Chen, C. H. Chiu, H. C. Kuo, Y. L. Li, T. C. Lu, and S. C. Wang, "Temperature-Dependent Electroluminescence Efficiency in Blue InGaN-GaN Light-Emitting Diodes With Different Well Widths," *IEEE Photonics Technol. Lett.*, vol. 22, pp. 236 238, 2010.
- [350] G. E. Cragg and A. L. Efros, "Suppression of Auger Processes in Confined Structures," *Nano Lett.*, vol. 10, pp. 313 317, 2010.
- [351] Z. Liu, T. Wei, E. Guo, X. Yi, L. Wang, J. Wang, G. Wang, Y. Shi, I. Ferguson, and J. Li, "Efficiency droop in InGaN/GaN multiple-quantum-well blue light-emitting diodes grown on free-standing GaN substrate," *Appl. Phys. Lett.*, vol. 99, pp. 091104-1 091104-3, 2011.
- [352] Y.-J. Lin, W.-X. Lin, C.-T. Lee, and F.-T. Chien, "Changes in optical and electrical properties and surface recombination velocity of n-type GaN due to (NH4)2Sx treatment," *Solid State Commun.*, vol. 137, pp. 257 259, 2006.
- [353] M. Boroditsky, I. Gontijo, M. Jackson, R. Vrijen, E. Yablonovitch, T. Krauss, C.-C. Cheng, A. Scherer, R. Bhat, and M. Krames, "Surface recombination measurements on III-V candidate materials for nanostructure light-emitting diodes," *J. Appl. Phys.*, vol. 87, pp. 3497 3504, 2000.
- [354] A.-L. Bavencove, D. Salomon, M. Lafossas, B. Martin, A. Dussaigne, F. Levy, B. Andre, P. Ferret, C. Durand, J. Eymery, L. S. Dang, and P. Gilet, "Light emitting diodes based on GaN core/shell wires grown by MOVPE on n-type Si substrate," *Electron. Lett*, vol. 47, pp. 765 767, 2011.
- [355] R. R. King, D. C. Law, K. M. Edmondson, C. M. Fetzer, G. S. Kinsey, H. Yoon, R. A. Sherif, and N. H. Karam, "40% efficient metamorphic GaInP/GaInAs/Ge multijunction solar cells," *Appl. Phys. Lett.*, vol. 90, 183516-1 183516-3, 2007.
- [356] R. R. King, D. C. Law, K. M. Edmondson, C. M. Fetzer, G. S. Kinsey, H. Yoon, D. D. Krut, J. H. Ermer, R. A. Sherif, and N. H. Karam, "Advances in high-efficiency III-V multijunction solar cells," *Adv. Opt. Electron.*, vol. 2007, pp. 29523 (8pp), 2007.
- [357] J. F. Geisz, S. Kurtz, M. W. Wanlass, J. S. Ward, A. Duda, D. J. Friedman, J. M. Olson, W. E. McMahon, T. E. Moriarty, and J. T. Kiehl, "High-efficiency GaInP/GaAs/InGaAs triple-junction solar cells grown inverted with a metamorphic bottom junction," *Appl. Phys. Lett.*, vol. 91, pp. 023502-1 023502-3, 2007.
- [358] M. Yamaguchi, "Multi-junction solar cells and novel structures for solar cell applications," *Physica E*, vol. 14, pp. 84 90, 2002.
- [359] M. Yamaguchi, "III-V compound multi-junction solar cells: present and future," *Sol. Energy Mater. Sol. Cells*, vol. 75, pp. 261 269, 2003.

- [360] M. Yamaguchi, T. Takamoto, and K. Araki, "Super high-efficiency multi-junction and concentrator solar cells," *Sol. Energy Mater. Sol. Cells*, vol. 90, pp. 3068 3077, 2006.
- [361] M. Yamaguchi, T. Takamoto, A. Khan, M. Imaizumi, S. Matsuda, and N. J. Ekins-Daukes, "Super-high-efficiency multi-junction solar cells," *Prog. Photovoltaics*, vol. 13, pp. 125 132, 2005.
- [362] C. M. Fetzer, H. Yoon, R. R. King, D. C. Law, T. D. Isshiki, and N. H. Karam, "1.6/1.1 eV metamorphic GaInP/GaInAs solar cells grown by MOVPE on Ge," *J. Cryst. Growth*, vol. 276, pp. 48 56, 2005.
- [363] D. C. Law, R. R. King, H. Yoon, M. J. Archer, A. Boca, C. M. Fetzer, S. Mesropian, T. Isshiki, M. Haddad, K. M. Edmondson, D. Bhusari, J. Yen, R. A. Sherif, H. A. Atwater, and N. H. Karam, "Future technology pathways of terrestrial III-V multijunction solar cells for concentrator photovoltaic systems," *Sol. Energy Mater. Sol. Cells*, vol. 94, pp. 1314 1318, 2010.
- [364] A. Martí and G. L. Araújo, "Limiting efficiencies for photovoltaic energy conversion in multigap systems," *Sol. Energy Mater. Sol. Cells*, vol. 43, pp. 203 222, 1996.
- [365] X. M. Cai, S. W. Zeng, and B. P. Zhang, "Fabrication and characterization of InGaN p-i-n homojunction solar cell," *Appl. Phys. Lett.*, vol. 95, pp. 173504-1 173504-3, 2009.
- [366] H. P. T. Nguyen, Y. L. Chang, I. Shih, and Z. Mi, "InN p-i-n Nanowire Solar Cells on Si," *IEEE J. Sel. Top. Quantum Electron.*,vol. 17, pp. 1062-1069, 2011.
- [367] J. Wu, W. Walukiewicz, K. M. Yu, J. W. Ager, E. E. Haller, H. Lu, and W. J. Schaff, "Small band gap bowing in In_{1-x}Ga_xN alloys," *Appl. Phys. Lett.*, vol. 80, pp. 4741 4743, 2002.
- [368] M. C. Johnson, C. J. Lee, E. D. Bourret-Courchesne, S. L. Konsek, S. Aloni, W. Q. Han, and A. Zettl, "Growth and morphology of 0.80 eV photoemitting indium nitride nanowires," *Appl. Phys. Lett.*, vol. 85, pp. 5670 5672, 2004.
- [369] T. Stoica, R. J. Meijers, R. Calarco, T. Richter, E. Sutter, and H. Lueth, "Photoluminescence and intrinsic properties of MBE-grown InN nanowires," *Nano Lett.*, vol. 6, pp. 1541 1547, 2006.
- [370] C. H. Shen, H. Y. Chen, H. W. Lin, S. Gwo, A. A. Klochikhin, and V. Y. Davydov, "Near-infrared photoluminescence from vertical InN nanorod arrays grown on silicon: Effects of surface electron accumulation layer," *Appl. Phys. Lett.*, vol. 88, pp. 253104-1 253104-3, 2006.
- [371] T. Richter, C. Bloemers, H. Lueth, R. Calarco, M. Indlekofer, M. Marso, and T. Schaepers, "Flux quantization effects in InN nanowires," *Nano Lett.*, vol. 8, pp. 2834 2838, 2008.
- [372] Y.-S. Lu, C.-C. Huang, J. A. Yeh, C.-F. Chen, and S. Gwo, "InN-based anion selective sensors in aqueous solutions," *Appl. Phys. Lett.*, vol. 91, pp. 202109-1 202109-3, 2007.
- [373] C. Bloemers, T. Schaepers, T. Richter, R. Calarco, H. Lueth, and M. Marso, "Phase-coherent transport in InN nanowires of various sizes," *Phys. Rev. B*, vol. 77, pp. 201301-1 201301-4, 2008.

- [374] E. Calleja, J. Grandal, M. A. Sanchez-Garcia, M. Niebelschuetz, V. Cimalla, and O. Ambacher, "Evidence of electron accumulation at nonpolar surfaces of InN nanocolumns," *Appl. Phys. Lett.*, vol. 90, pp. 262110-1- 262110-3, 2007.
- [375] E. Calleja, J. Ristic, S. Fernandez-Garrido, L. Ceruffi, M. A. Sanchez-Garcia, J. Grandal, A. Trampert, U. Jahn, G. Sanchez, A. Griol, and B. Sanchez, "Growth, morphology, and structural properties of group-III-nitride nanocolumns and nanodisks," *Phys. Status Solidi B*, vol. 244, pp. 2816 2837, 2007.
- [376] J. Grandal, M. A. Sanchez-Garcia, E. Calleja, E. Luna, and A. Trampert, "Accommodation mechanism of InN nanocolumns grown on Si(111) substrates by molecular beam epitaxy," *Appl. Phys. Lett.*, vol. 91, pp. 021902-1 021902-3, 2007.
- [377] S. Vaddiraju, A. Mohite, A. Chin, M. Meyyappan, G. Sumanasekera, B. W. Alphenaar, and M. K. Sunkara, "Mechanisms of 1D crystal growth in reactive vapor transport: Indium nitride nanowires," *Nano Lett.*, vol. 5, pp. 1625 1631, 2005.
- [378] C. Denker, J. Malindretos, F. Werner, F. Limbach, H. Schuhmann, T. Niermann, M. Seibt, and A. Rizzi, "Self-organized growth of InN-nanocolumns on p-Si(111) by MBE," *Phys. Status Solidi C*, vol 5, pp. 1706 1708, 2008.
- [378] Z. Cai, S. Garzon, M. Chandrashekhar, R. Webb, and G. Koley, "Synthesis and properties of high-quality InN nanowires and nanonetworks," *J. Electron. Mater.*, vol. 37, pp. 585 592, 2008.
- [380] C. Chao, J. Chyi, C. Hsiao, C. Kei, S. Kuo, H. Chang, and T. Hsu, "Catalyst-free growth of indium nitride nanorods by chemical-beam epitaxy," *Appl. Phys. Lett.*, vol. 88, pp. 233111-1 233111-3, 2006.
- [381] C. Liang, L. Chen, J. Hwang, K. Chen, Y. Hung, and Y. Chen, "Selective-area growth of indium nitride nanowires on gold-patterned Si(100) substrates," *Appl. Phys. Lett.*, vol. 81, pp. 22 24, 2002.
- [382] T. Stoica, R. Meijers, R. Calarco, T. Richter, and H. Luth, "MBE growth optimization of InN nanowires," *J. Cryst. Growth*, vol. 290, pp. 241–247, 2006.
- [383] J. Grandal, M. Sanchez-Garcia, E. Calleja, E. Luna, and A. Trampert, "Accommodation mechanism of InN nanocolumns grown on Si(111) substrates by molecular beam epitaxy," *Appl. Phys. Lett.*, vol. 91, pp. 021902-1 021902-3, 2007.
- [384] E. Calleja, J. Grandal, M. Sanchez-Garcia, M. Niebelschutz, V. Cimalla, and O. Ambacher, "Evidence of electron accumulation at nonpolar surfaces of InN nanocolumns," *Appl. Phys. Lett.*, vol. 90, pp. 262110-1 262110-3, 2007.
- [385] J. H. Song, T. Akiyama, and A. J. Freeman, "Stabilization of bulk p-type and surface n-type carriers in Mg-doped InN [253] films," *Phys. Rev. Lett.*, vol. 101, pp. 186801-1 186801-4, 2008.
- [386] P. A. Anderson, C. H. Swartz, D. Carder, R. J. Reeves, S. M. Durbin, S. Chandril, and T. H. Myers, "Buried p-type layers in Mg-doped InN," *Appl. Phys. Lett.*, vol. 89, pp. 184104-1 184104-3, 2006.
- [387] R. Kudrawiec, T. Suski, J. Serafinczuk, J. Misiewicz, D. Muto, and Y. Nanishi, "Photoreflectance of InN and InN: Mg layers: An evidence of Fermi level shift

- toward the valence band upon Mg doping in InN," *Appl. Phys. Lett.*, vol. 93, pp.131917-1 121917-3, 2008.
- [388] R. E. Jones, K. M. Yu, S. X. Li, W. Walukiewicz, J. W. Ager, E. E. Haller, H. Lu, and W. J. Schaff, "Evidence for p-type doping of InN," *Phys. Rev. Lett.*, vol. 96, pp. 125505-1 125505-3, 2006.
- [389] I. Mahboob, T. Veal, C. McConville, H. Lu, and W. Schaff, "Intrinsic electron accumulation at clean InN surfaces," *Phys. Rev. Lett.*, vol. 92, pp. 036804-1 036804-3, 2004.
- [390] C. L. Wu, H. M. Lee, C. T. Kuo, C. H. Chen, and S. Gwo, "Absence of Fermilevel pinning at cleaved nonpolar InN surfaces," *Phys. Rev. Lett.*, vol. 101, pp. 106803-1 106803-4, 2008.
- [391] H. Du, I. Shih, and C. Champness, "Monocrystalline CulnSe₂ photovoltaic cell of superior performance," *J. Vac. Sci. Technol. A*, vol. 22, pp. 1023–1026, 2004.
- [392] K. S. Ramaiah, V. S. Raja, A. K. Bhatnagar, R. D. Tomlinson, R. D. Pilkington, A. E. Hill, S. J. Chang, Y. K. Su, and F. S. Juang, "Optical, structural and electrical properties of tin doped indium oxide thin films prepared by spraypyrolysis technique," *Semicond. Sci. Technol.*, vol. 15, pp. 676 683, 2000.
- [393] M. A. Contreras, B. Egaas, K. Ramanathan, J. Hiltner, A. Swartzlander, F. Hasoon, and R. Noufi, "Progress toward 20% efficiency in Cu(In,Ca)Se₂ polycrystalline thin-film solar cells," *Prog. Photovoltaics*, vol. 7, pp. 311 316, 1999.
- [394] J. S. Li, H. Y. Yu, S. M. Wong, X. C. Li, G. Zhang, P. G. Q. Lo, and D. L. Kwong, "Design guidelines of periodic Si nanowire arrays for solar cell application," *Appl. Phys. Lett.*, vol. 95, pp. 243113-1 243113-3, 2009.
- [395] O. V. Galan, J. V. Larramendi, I. Riech, G. Pena, A. Iribarren, J. Aguilar-Hernandez, and G. Contreras-Puente, "Characterization of the passivation of CdS thin films grown by chemical bath deposition on InP," *Semicond. Sci. Technol.*, vol. 17, pp. 1193 1197, 2002.
- [396] W. Wei, X. Y. Bao, C. Soci, Y. Ding, Z. L. Wang, and D. Wang, "Direct Heteroepitaxy of Vertical InAs Nanowires on Si Substrates for Broad Band Photovoltaics and Photodetection," *Nano Lett.*, vol. 9, pp. 2926 2934, 2009.
- [397] Y. Tang, Z. Chen, H. Song, C. Lee, H. Cong, H. Cheng, W. Zhang, I. Bello, and S. Lee, "Vertically Aligned p-Type Single-Crystalline GaN Nanorod Arrays on n-Type Si for Heterojunction Photovoltaic Cells," *Nano Lett.*, vol. 8, pp. 4191 4195, 2008.
- [398] J. A. Czaban, D. A. Thompson, and R. R. LaPierre, "GaAs Core-Shell Nanowires for Photovoltaic Applications," *Nano Lett.*, vol. 9, pp. 148–154, 2009
- [399] Y. J. Dong, B. Z. Tian, T. J. Kempa, and C. M. Lieber, "Coaxial Group III-Nitride Nanowire Photovoltaics," *Nano Lett.*, vol. 9, pp. 2183 2187, 2009.
- [400] L. Tsakalakos, J. Balch, J. Fronheiser, B. Korevaar, O. Sulima, and J. Rand, "Silicon nanowire solar cells," *Appl. Phys. Lett.*, vol. 91, pp. 233117-1 233117-3, 2007.
- [401] V. Consonni, M. Knelangen, U. Jahn, A. Trampert, L. Geelhaar, and H. Riechert, "Effects of nanowire coalescence on their structural and optical

- properties on a local scale," *Appl. Phys. Lett.*, vol. 95, pp. 241910-1 241910-3, 2009.
- [402] M. Bertelli, P. Loptien, M. Wenderoth, A. Rizzi, R. G. Ulbrich, M. C. Righi, A. Ferretti, L. Martin-Samos, C. M. Bertoni, and A. Catellani, "Atomic and electronic structure of the nonpolar GaN(11⁻00) surface," *Phys. Rev. B*, vol. 80, pp. 115324-1 115324-7, 2009.
- [403] K. J. Vampola, M. Iza, S. Keller, S. P. DenBaars, and S. Nakamura, "Measurement of electron overflow in 450 nm InGaN light-emitting diode structures," *Appl. Phys. Lett.*, vol. 94, pp. 061116-1 061116-3, 2009.
- [404] G. L. Martinez, M. R. Curiel, B. J. Skromme, and R. J. Molnar, "Surface recombination and sulfide passivation of GaN," *J. Electron. Mater.*, vol. 29, pp. 325 331, 2000.
- [405] M. Higashiwaki, N. Onojima, T. Matsui, and T. Mimura, "Effects of SiN passivation by catalytic chemical vapor deposition on electrical properties of AlGaN/GaN heterostructure field-effect transistors," *J. Appl. Phys.*, vol. 100, pp. 033714-1 033714-6, 2006.
- [406] P. Kordos, P. Kudela, D. Gregusova, and D. Donoval, "The effect of passivation on the performance of AlGaN/GaN heterostructure field-effect transistors," *Semicond. Sci. Technol.*, vol. 21, pp. 1592 1596, 2006.
- [407] R. H. Horng, C. T. Pan, T. Y. Tsai, and D. S. Wuu, "Transferring thin film GaN LED epi-structure to the Cu substrate by chemical lift-off technology," *Elec. Sol. Stat. Lett.*, vol. 14, pp. H281 H284, 2011.
- [408] T. Egawa and B. A. B. A. Shuhaimi, "High performance InGaN LEDs on Si (111) substrates grown by MOCVD," *J. Phys. D: Appl. Phys.*, vol. 43, pp. 345008 (8pp), 2010.
- [409] N. Lopez, A. Marti, A. Luque, C. Stanley, C. Farmer, and P. Diaz, "Experimental analysis of the operation of quantum dot intermediate band solar cells," *J. Sol. Energy Engineer.*, vol. 129, pp. 319 322, 2007.
- [410] R. B. Laghumavarapu, M. El-Emawy, N. Nuntawong, A. Moscho, L. F. Lester, and D. L. Huffaker, "Improved device performance of InAs/GaAs quantum dot solar cells with GaP strain compensation layers," *Appl. Phys. Lett.*, vol. 91, pp. 24315-1 234115-3, 2007.